



UNIVERSITÀ
DEGLI STUDI
FIRENZE

DOTTORATO DI RICERCA IN
SCIENZE CHIMICHE

CICLO XXVII

COORDINATORE Prof. Goti Andrea

"From Advanced Materials to Sustainable Metal-Free Catalysts *via* Tailored Chemical Decorations of Carbon Nanostructures"

Settore Scientifico Disciplinare CHIM/06

Dottorando

Dott. Tuci Giulia

(firma)

Tutore

Dott. Giambastiani Giuliano

(firma)

Coordinatore

Prof. Goti Andrea

(firma)

Anni 2012/2014

Index

1. Introduction	1
1.1 Covalent functionalization	3
1.1.1 Amidation/esterification reactions	3
1.1.2 Direct functionalization of CNT side walls and tips	4
1.1.2.1 Side wall halogenation, hydrogenation and epoxydation	5
1.1.2.2 Cycloaddition reactions	5
1.1.2.3 Reactions with radical species.....	7
1.2 Non-covalent functionalization	7
1.3 Multimodal and versatile CNTs decoration	8
1.4 Doping of CNTs: creating efficient and powerful metal-free catalysts...10	
1.5 Objects of the Thesis	13
References.....	15
2. “Click” on Tubes: a Versatile Approach Towards Multimodal Functionalization of SWCNTs.....	21
2.1 Abstract.....	21
2.2 Introduction.....	22
2.3 Results and Discussion.....	24
2.3.1 Characterization of the f_{I-IV}-SWCNTs samples (7-10) and their deprotected counterparts (11-12).....	29
2.3.2 Hetero-decoration of SWCNTs	36
2.4 Conclusions	40
2.5 Experimental Section.....	41

2.5.1 General Considerations	41
2.5.2 Material Characterization and Analyses Conditions.....	42
2.5.3 Synthesis of 4-azidoaniline (1).....	43
2.5.4 General procedure for the “homogeneous” CuAAC “click” reaction between the model phenylazide and the alkynes 3-6.....	44
2.5.5 Functionalization of SWCNTs with 4-azidoaniline (1).....	45
2.5.6 General procedure for the CuAAC reaction on azido- decorated f_{N_3} -SWCNTs 2 – homo and hetero-functionalization.....	45
2.5.7 Removal of the Boc-protecting group from either homo- or hetero-decorated f -SWCNTs.....	46
2.5.8 Removal of the Pht-protecting group from either homo- or hetero-decorated f -SWCNTs.....	46
2.5.9 Preparation of $f_{III(OH)}$ -SWCNTs (11) from the β -D- glucopyranoside derivative f_{III} -SWCNTs sample (9).....	47
2.5.10 Cyclic voltammetry (CV) measurements	47
2.5.11 General procedure for the <i>Kaiser</i> test on Boc-protected and Pht-protected homo/hetero-decorated samples.....	47
References and Notes.....	49
3. “Click” on MOFs: a Versatile Tool for the Multimodal Derivatization of N_3-decorated Metal Organic Frame works	53
3.1 Abstract	53
3.2 Introduction.....	54
3.3 Results and Discussion	55
3.3.1 MOF homo-decoration	60
3.3.2 MOF hetero-decoration	69
3.4 Conclusions.....	77
3.5 Experimental Section.....	77

3.5.1 General Considerations.....	77
3.5.2 Material Characterization and Analyses Conditions	78
3.5.3 Preparation of MIXMOF-5-NH ₂	79
3.5.4 Preparation of UMCM-1-NH ₂	79
3.5.5 Preparation of MIXMOF-5-N ₃	79
3.5.6 Preparation of UMCM-1-N ₃	80
3.5.7 General procedure for the homo-(hetero)-PSM of N ₃ -MOFs <i>via</i> CuAAC chemistry	80
3.5.8 ¹ H NMR characterization of MOF's reagents and derivatives	81
References and Notes.....	82
4. A Hetero-bi-Functional Spacer for the Smart Engineering of Carbon-based Nanostructures	85
4.1 Abstract.....	85
4.2 Introduction.....	85
4.3 Results and Discussion.....	87
4.3.1 Synthesis of the hetero-bi-functional spacer 3	87
4.3.2 Reactivity study on the hetero-bi-functional cross-linker 3 in homogeneous phase.....	88
4.3.3 Homo- and hetero-decoration of <i>f</i> _{N₃} -SWCNTs; towards multifunctional carbon nanotube platforms	90
4.4 Conclusions	101
4.5 Experimental Section.....	102
4.5.1 General Considerations.....	102
4.5.2 Material characterization and analyses conditions	102
4.5.3 Synthesis of 3-(tritylthio)propionic acid (1)	104
4.5.4 Synthesis of N-(prop-2-ynyl)-3-(tritylthio)propanamide (2).....	104

4.5.5	Synthesis of N-(prop-2-ynyl)-3-(pyridin-2-yl)disulfanylpropanamide (3)	105
4.5.6	Synthesis of the alkyne-BODIPy derivative 18	105
4.5.7	Homogeneous CuAAC reaction on 3 with the azido-BODYPy-derivative 6.....	106
4.5.8	General procedure for the homo- and hetero-derivatization of phenyl-azido decorated SWCNTs via CuAAC reaction.....	106
4.5.9	General procedure for the disulfide cleavage on 3, 7 and the SWCNT composite 14 by a model dithiol and subsequent monitoring of the reaction course by UV-vis measurement	107
4.5.10	Covalent grafting of the L-aminoacid 10 [<i>N</i> -(<i>tert</i> -Butoxycarbonyl)-L-cysteine methyl ester] on 3 to give 11	108
4.5.11	Covalent grafting of the L-aminoacid 10 [<i>N</i> -(<i>tert</i> -Butoxycarbonyl)-L-cysteine methyl ester] on 7 to give 12.....	108
4.5.12	Covalent grafting of the L-aminoacid 10 [<i>N</i> -(<i>tert</i> -Butoxycarbonyl)-L-cysteine methyl ester] on 14 to give f_{SSCy} -SWCNTs (16)	109
	References and Notes.....	110
5.	Tailoring Carbon Nanotube N-Dopants while Designing Metal-Free Electrocatalysts for the Oxygen Reduction Reaction in Alkaline Medium	113
5.1	Abstract	113
5.2	Introduction.....	113
5.3	Results and Discussion	114
5.4	Conclusions.....	126
5.5	Experimental Section.....	126
5.5.1	General Considerations	126
5.5.2	Material characterization and analyses conditions	127

5.5.3	General procedure for the <i>ex-situ</i> MWCNTs functionalization <i>via</i> aryldiazonium salt chemistry	129
5.5.4	Acid-base titration of N-decorated samples 2 and 4	129
5.5.5	Electrochemical data processing	130
	References.....	132
6.	Chemically Functionalized Carbon Nanotubes with Pyridine Groups as Easily Tunable N-decorated Nanomaterials for the Oxygen Reduction Reaction in Alkaline Medium	135
6.1	Abstract.....	135
6.2	Introduction.....	135
6.3	Results and Discussion.....	139
6.3.1	Synthesis and characterization of the N-functionalized MW@N ₁₋₆ samples	140
6.3.2	Electrochemical tests on MW@N ₁₋₆ samples as electrocatalysts for the ORR.....	146
6.4	Conclusions	155
6.5	Experimental Section.....	156
6.5.1	General Considerations.....	156
6.5.2	Material characterization and analyses conditions	157
6.5.3	General procedure for the <i>ex-situ</i> MWCNTs functionalization <i>via</i> aryldiazonium salt chemistry	159
6.5.4	Electrochemical data processing	160
6.5.5	Acid-base titration of N-CNMs MW@N ₁₋₆	160
6.5.6	Computational Details.....	161
	References and Notes.....	162
	List of abbreviations	167
	Acknowledgements	171

1. Introduction

Beyond the natural allotropic forms of carbon (amorphous carbon, diamond and graphite), in the last decades other carbon-based nanomaterial were discovered and gained great interest due to their novel properties and unique chemico-physical features. Nowadays, the most studied carbon nanomaterials are fullerene,¹ carbon nanotubes² and graphene³ (Figure 1.1).

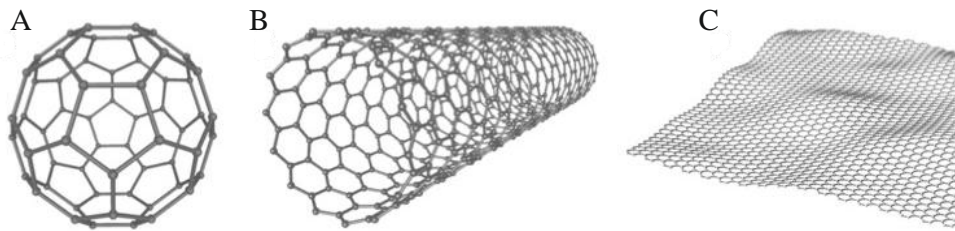


Figure 1.1. Different carbon-based nanomaterials: A) fullerene, B) carbon nanotube, C) graphene.

Carbon nanotubes (CNTs) were described for the first time by Iijima in 1991.² They can be conceived as graphene sheets rolled up to form long hollow cylindrical structures; depending on the way to wrap the graphene sheet it's possible to obtain CNTs with different chiralities. The circumference of a CNT is described by the chiral vector \mathbf{C} defined as a combination of two integers (n , m) and the basis vectors of the graphene sheet⁴ (eq. 1.1):

$$\mathbf{C} = n\mathbf{a} + m\mathbf{b} \equiv (n,m) \quad (\text{eq. 1.1})$$

When $n = m$ nanotubes possess an armchair structure, when $n = 0$ they get a zigzag geometry while in all other cases (when n and m have different values) nanotubes present a chiral structure (Figure 1.2).

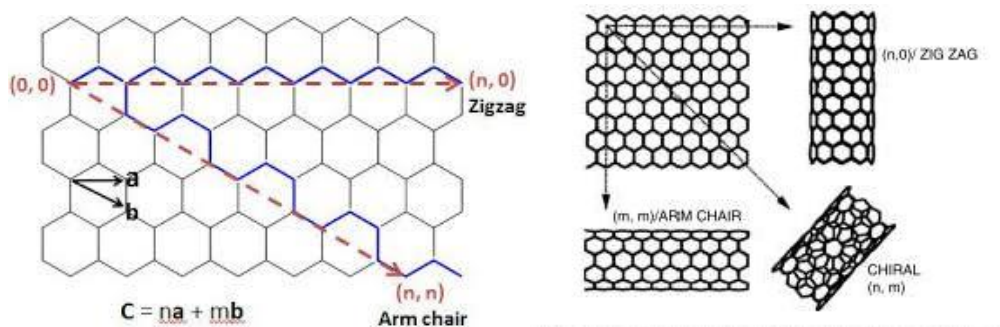


Figure 1.2. (left) Schematic representation of CNTs formation by wrapping a graphene sheet. (right) Different chiralities of CNTs obtained by rolling a graphene sheet.

Carbon nanotubes can be classified into two different categories: single-walled carbon nanotubes (SWCNTs) and multi-walled carbon nanotubes (MWCNTs) depending if they consist in a single shell of graphene or in a structure constituted by multiple concentric tubes (Figure 1.3).

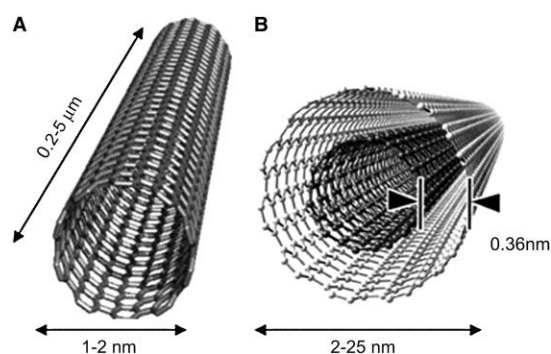


Figure 1.3. A) Single-walled carbon nanotube (SWCNT). B) Multi-walled carbon nanotube (MWCNT).

SWCNTs typically show a diameter between 1 and 2 nm, while MWCNTs diameter normally ranges between 2 and 25 nm even if there are cases where it can reach 100 nm. The length of CNTs is instead in the size of micrometers.

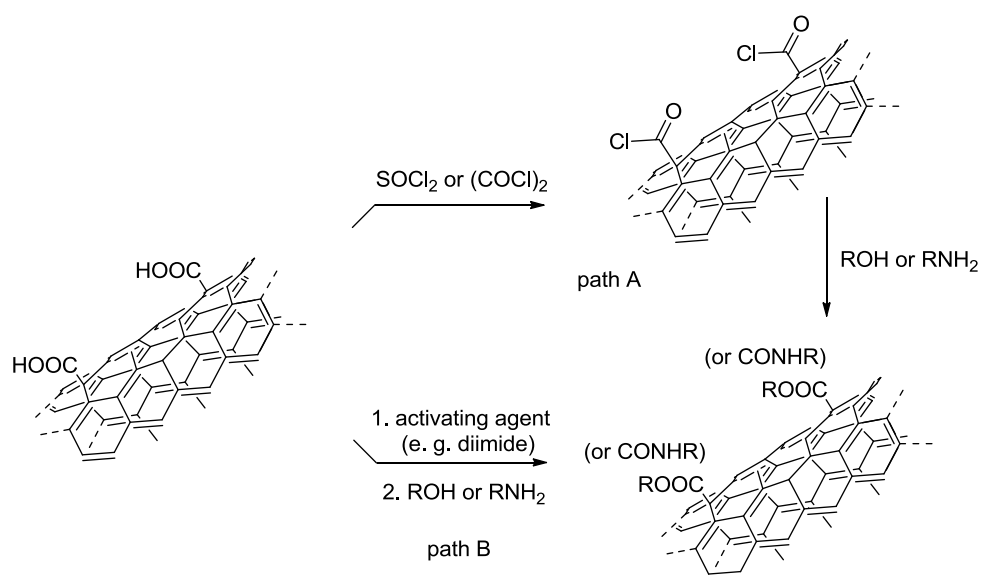
Thanks to their unique mechanical, thermal and electrical properties, CNTs have received growing attention for applications in materials science, nanotechnology and medicinal chemistry.^{5,6,7} However, the strong Van der Waals interactions between the nanotubes cause the formation of bundles that are at the origin of the lack of solubility of pristine CNTs, both in organic and aqueous media. This aspect represents the major drawback for their use in practical applications; however, the possibility to functionalize the nanomaterial in different ways with various techniques and strategies permits to obtain an increase of miscibility and processability of CNTs in the most common

media. The several approaches that have been developed to functionalize CNTs can be divided into two main categories: the covalent and the non-covalent (exohedral or endohedral) approach.⁸

1.1 Covalent functionalization

1.1.1 Amidation/esterification reactions

One main approach in the field of chemical functionalization of CNTs consists in their acidic and oxidative treatment, such as in a mixture of nitric and sulphuric acid under sonication, which leads to the formation of defective, opened and short nanotubes (less than 500 nm in length). The as-prepared materials possess oxygenated functionalities, mainly carboxylic groups,⁹ that represent reactive groups susceptible to undergo further functionalization in the presence of alcohols or amines to give the corresponding esters or amides, respectively¹⁰ (Scheme 1.1).



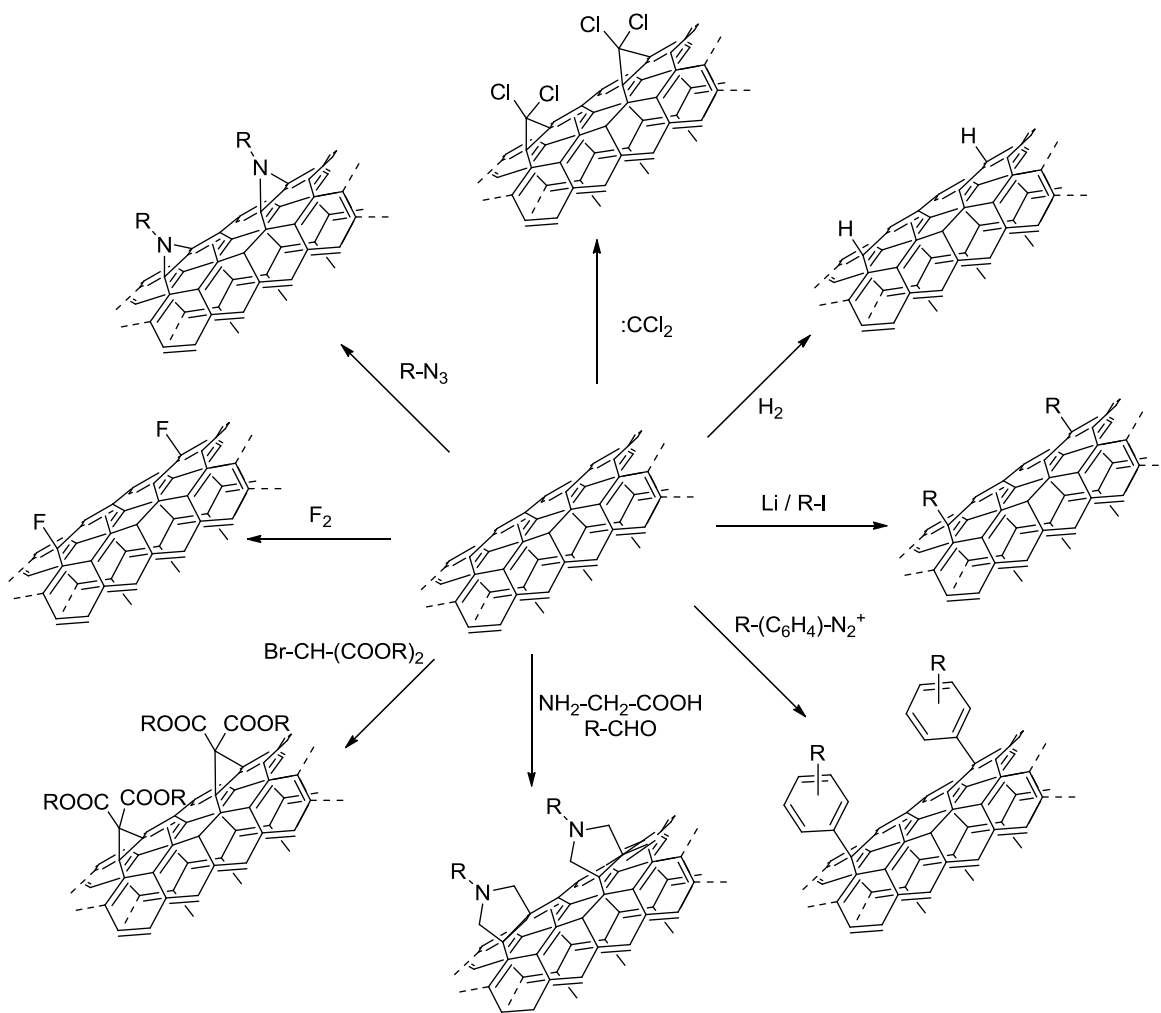
Scheme 1.1. Amidation and/or esterification of carboxylic groups through acyl chloride intermediates (path A) or through the employment of activating agents (path B).

In 1998 Smalley and co-workers first reported the functionalization of oxidized SWCNTs through amidation, using thionyl chloride to convert the carboxylic functions in reactive sites for the coupling with a thiolated undecylamine and the subsequent anchoring of the carbon nanomaterial to a gold substrate.⁹ In a similar way, Chen et al. functionalized oxidized CNTs with long chain alkylamines (after acylation treatment)

and obtained for the first time a material soluble in organic solvents.¹¹ The same reaction can be conducted using carbodiimide-based coupling agents as DCC (N,N'-dicyclohexylcarbodiimide) or EDC (1-ethyl-3-(3-dimethylaminopropyl)carbodiimide) in the presence of NHS (N-hydroxy succinimide) or HOBt (1-hydroxy-benzotriazole) that allow to perform the amidation/esterification reaction under milder conditions.

1.1.2 Direct functionalization of CNT sidewalls and tips

Highly reactive species are required in order to perturb the graphitic Csp² network and functionalize CNT sidewalls and tips. On this ground, several synthetic methodologies grew up in the last decades (Scheme 1.2).⁸



Scheme 1.2. Different approaches to CNTs chemical functionalization.

1.1.2.1 Sidewall halogenation, hydrogenation and epoxydation

It is possible to obtain F-decorated CNT sidewalls through a thermal treatment of CNTs in the presence of elemental fluorine.¹² The reaction is very useful because upon treatment with organolithium or Grignard reagents the fluorine atoms can be easily replaced by alkyl groups.¹³ Moreover, several nucleophilic species such as diamines or diols have been reported to react with fluorinated CNTs.¹⁴

Chlorination and bromination of CNTs were also accomplished through an electrochemical oxidation of the appropriate inorganic salts.¹⁵

Hydrogenation of CNTs has been performed upon treatment with Li or Na in liquid NH₃ (Birch reduction);¹⁶ the as-prepared materials show thermal stability till 400 °C.

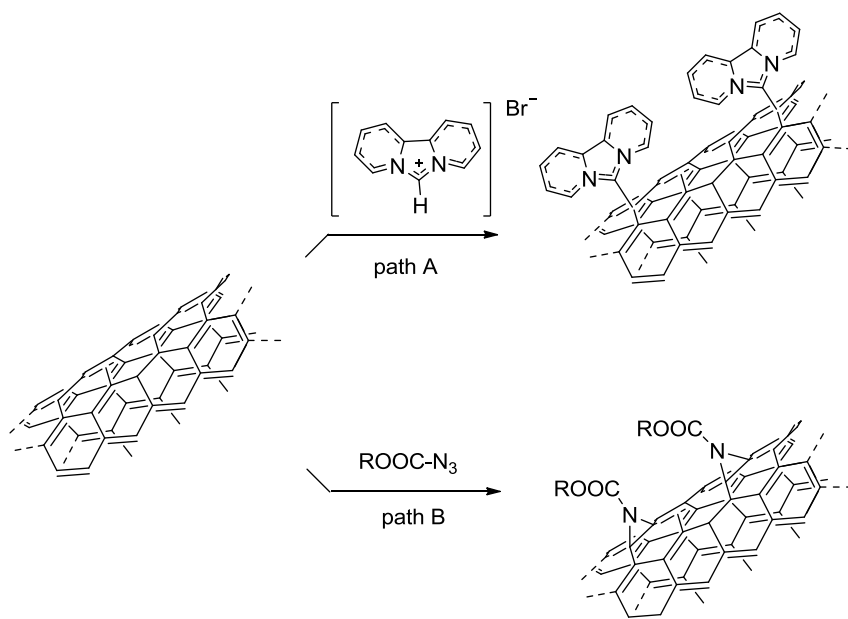
CNTs can be also decorated with epoxy groups using strong oxidizing agents such as *m*-CPBA (*meta*-chloroperbenzoic acid), dioxiranes or a mixture of ReMeO₃ and H₂O₂.¹⁷ The as-formed epoxy groups can be further derivatized by reaction with nucleophiles, e. g. amines.¹⁸

1.1.2.2 Cycloaddition reactions

Carbenes cycloaddition was reported for the first time by Haddon and co-workers.¹⁹ The reactive species were generated *in-situ* using a mixture of chloroform/sodium hydroxide or using phenyl (bromodichloro methyl) mercury. The as-obtained dichlorocarbene efficiently reacts with CNT sidewalls thus forming cyclopropane rings.

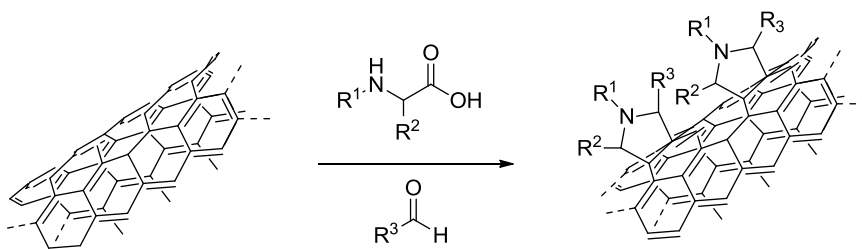
The Bingel cyclopropanation has also been reported to modified CNTs sidewalls.²⁰ In this case, the carbene species is originated *in-situ* from diethylbromomalonate in the presence of DBU (1,8-diazobicyclo[5,4,0]-undecene).

Hirsch and co-workers also reported a nucleophilic addition of carbenes on CNTs with the formation of zwitterionic adducts (Scheme 1.3, path A).²¹ Another important reaction investigated by the same group is the thermal functionalization of CNTs by nitrene species produced *in-situ* (Scheme 1.3, path B).²² Starting from an alkyl azidoformate derivative, a thermal decomposition of the azide leads to the formation of the reactive alkoxycarbonylnitrene through nitrogen elimination. The cycloaddition of the as-produced nitrene to the CNT sidewalls resulted in the formation of alkoxycarbonylaziridino derivatives. Hirsch and co-workers demonstrated also the feasibility of this reaction using different types of alkyl chains, such as oligoethylenic derivatives, crown ethers and dendrimers that increase the dispersibility of the functionalized materials.



Scheme 1.3. Path A: nucleophilic addition of carbenes to CNTs. Path B: functionalization of CNTs by *in-situ* produced nitrene species.

An important and versatile approach to the CNTs functionalization is the azomethine ylides cycloaddition reported for the first time by Prato and co-workers.²³ The reactive species is thermally generated *in-situ* by condensation of aldehydes and α -amino acids forming pyrrolidine rings fused to the CNTs network (Scheme 1.4).



Scheme 1.4. CNTs functionalization by *in-situ* generated azomethine ylides.

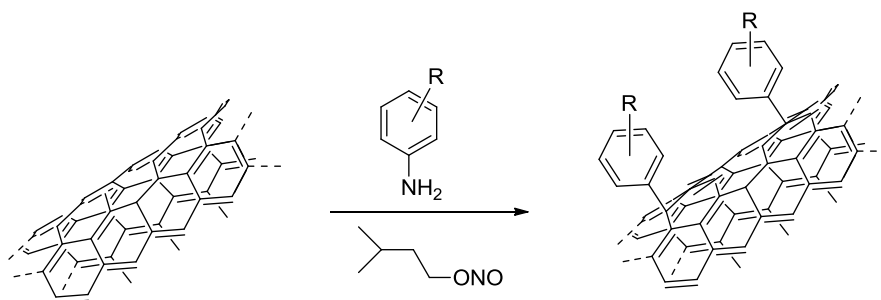
More recently, the same reaction was reported to proceed under solvent-free microwave irradiation.²⁴ In principle, as shown in Scheme 1.4, a wide and virtually infinite variety of groups can be anchored to CNTs making this approach highly versatile.

Thinking to CNTs Csp^2 network as a dienophile, a Diels-Alder cycloaddition was performed with *o*-quinodimethane generated *in-situ*, as reported by Delgado and co-workers.²⁵

Other 1,3-dipolar cycloaddition were reported employing other reactive species such as nitrile imines²⁶ and nitrones.²⁷

1.1.2.3 Reactions with radical species

The addition of radicals on SWCNTs sidewalls has been reported for the first time by Tour's group using aryl diazonium salts.²⁸ The reactive aryl diazonium salt species can also be generated *in-situ* from the corresponding aniline derivative using NaNO_2 ²⁹ or an organic nitrite like the isopentyl nitrite (Scheme 1.5).³⁰



Scheme 1.5. Functionalization of CNTs by *in-situ* formed aryl diazonium species.

A variety of different reaction conditions has been reported later, such as solvent-free³¹ or microwave assisted³² functionalization procedures. Also in this case the synthetic protocol allows to bring at the CNTs surface a large range of different aromatic groups.

Thermal and photochemical approaches has also been reported for the covalent CNTs sidewall functionalization with radicals. For example a thermal decomposition of alkyl or aryl peroxide was reported to generate radical species able to covalently decorate the CNTs network,³³ while photoinduced homolytic dissociation of alkyl iodide precursors was accomplished to perform perfluoroalkyl radical additions.³⁴

1.2 Non-covalent functionalization

An alternative approach to bring functional groups and/or to enhance the CNTs dispersibility in organic and aqueous solvents is the non-covalent functionalization, regulated by interactions mainly based on Van der Waals forces, hydrophobic interactions and π - π stacking.

In order to obtain stable suspensions of CNTs in both organic and aqueous solutions the use of polymers, aromatic compounds, surfactants and biomolecules have been

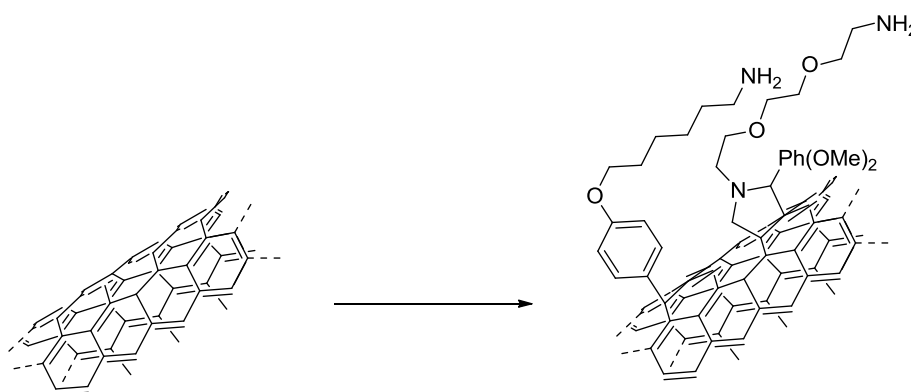
explored. The first example of CNTs functionalization with polymers was reported by Xu and co-workers performing an *in-situ* polymerization of phenylacetylene that led to the CNTs easy dispersion in common organic media.³⁵ Nakashima and co-workers³⁶ showed that different aromatic ammonium derivatives were able to disperse SWCNTs; among them, pyrene-based compounds demonstrated to be good candidates to solubilize this type of nanomaterial.³⁷ Exploiting this property, Harada and co-workers³⁸ functionalized SWCNTs with β -cyclodextrins anchored to pyrene compounds obtaining hybrid materials soluble in aqueous solutions. Great interest has also been devoted to CNTs interactions with biopolymers;⁸ in particular, DNA was found to be efficient in dispersing CNTs in aqueous solutions generating DNA-SWCNTs adducts that result stable for months thanks to the interaction of the nucleotide bases with the CNTs graphitic walls.³⁹

An alternative and less common approach to functionalize carbon nanotubes is the encapsulation of molecules inside the tubes cavity (endohedral functionalization). The first example dealt with the possibility to fill CNTs with fullerenes,⁴⁰ but later other organic and inorganic molecules have been employed. For example, Kataura and co-workers⁴¹ studied the possibility to encapsulate conjugated dyes, such as carotene, in the inner cavity of CNTs but also metal halides have been introduced inside nanotubes⁴² (e. g. the encapsulation of radioactive NaI has been used for *in vivo* localization and imaging of SWCNTs⁴³).

1.3 Multimodal and versatile CNTs decoration

CNTs have attracted great attention in the last years as they have potential applications in different fields, from nanomedicine for drug delivery,⁴⁴ therapy and imaging,⁴⁵ to their use as catalytic materials in specific fields of renewable energies technology.⁴⁶ CNT sidewall and tip decoration with organic functional groups represents the only way to exploit their unique properties more conveniently but, in spite of the huge number of CNT functionalization protocols developed,⁸ the efficient synthesis of flexible and versatile systems still represents a challenge. In particular, one main point is to impart multimodality to CNTs through the anchoring of different molecules, possibly under mild reaction conditions and avoiding undesired side-processes or conflicting side-reactions between the decorating groups. Several approaches have been successfully applied to CNTs multiple functionalization taking

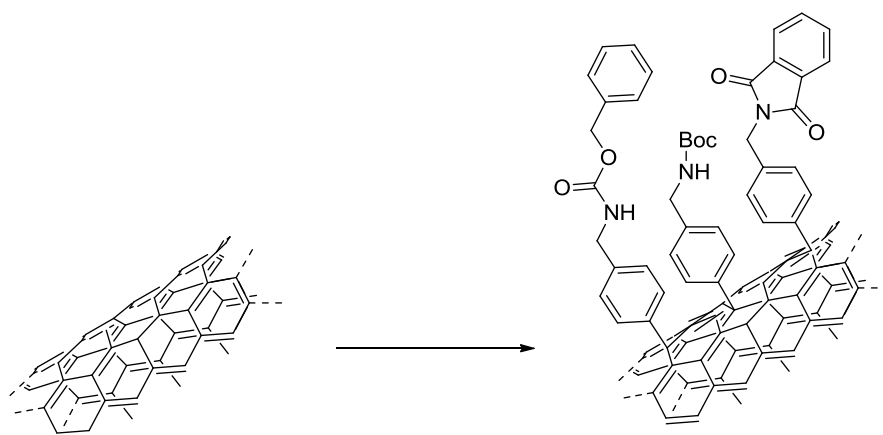
advantage of well-established protocols. The first example was the site-selective functionalization of the opposite tube ends on vertically aligned MWCNTs exposed to different photoreactive solutions.⁴⁷ Later, different synthetic strategies and combinations of organic protocols were exploited;⁴⁸ in particular, there are several examples including double azomethine ylide cycloaddition,⁴⁹ double amidation reaction on oxidized CNTs⁵⁰ or double aryl diazonium salt reaction.⁵¹ Another possibility is to tune the reaction conditions to perform a combination of different functionalization approaches such as amidation and cycloaddition reaction,⁵² or aryldiazonium salt reaction and azomethine ylide cycloadditions^{24b,53} (Scheme 1.6).



Scheme 1.6. Functionalization of CNTs through a combination of azomethine ylides cycloaddition and aryl diazonium salt reaction.

Also non-covalent functionalization protocols has been used to perform multifunctionalization and impart multimodality to the final nanomaterials. One of the first examples was reported by Dai and co-workers using two different PEG-chains decorated with different terminal functionalities,⁵⁴ but there are also strategies based on a combination of non-covalent and covalent approaches; for example, Liu and co-workers performed an amidation reaction followed by the loading of an aromatic species interacting with CNTs by π - π stacking.⁵⁵

A step-forward towards the easy and smart engineering of carbon nanomaterials is the covalent anchoring of masked functionalities bearing orthogonally cleavable protecting groups;^{49b,52,56} for example, a one-pot triple functionalization with different aryldiazonium derivatives was reported to bring at the CNTs surface three masked benzylamines groups that can be orthogonally and selectively deprotected under specific conditions (Scheme 1.7).⁵⁶ The sequential removal of the amines protecting groups allows the grafting of different molecules of interest imparting multimodality to the final nanomaterial.



Scheme 1.7. One-pot triple CNTs functionalization through aryl diazonium salt cycloaddition

Another relevant strategy to design flexible CNT platforms is the incorporation of functionalities containing cleavable bonds for the controlled release of specific molecules under appropriate chemical and/or biological settings.⁵⁷ For example, Prato and co-workers decorated CNTs surface with an anticancer compound through a peptide-based linker to facilitate a controlled release of the drug from CNTs by an enzymatic cleavage.^{57b} Other examples include CNTs functionalization with groups bearing disulfide bonds that can be easily cleaved by pH changes⁵⁸ and/or reducing agents.^{57a}

In spite of the huge efforts devoted in the last years to conceive different synthetic strategies and protocols, making CNTs (and complex carbon-based nanomaterials in general) flexible platforms through their efficient, facile and multiple functionalization, still represents a priority to be properly faced in order to widen the application of these unique nanomaterials in different technological and biomedical fields.

1.4 Doping of CNTs: creating efficient and powerful metal-free catalysts

In the last few years, great attention was focused to the doping of CNTs with heteroatoms. Indeed, CNTs application in various catalytic reactions requires their chemical modification in order to tune and whenever possible control their ultimate physico-chemical properties. Most importantly CNT doping is expected to render these nanomaterials capable to coordinate different substrates and drive catalytic transformations efficiently. The natural choice for CNTs doping is nitrogen⁵⁹ since it differs by only one additional valence electron from a carbon atom and may provide

additional π -electrons in the Csp^2 graphitic network. However, there are several examples of doping with other heteroelements such as boron,⁶⁰ phosphorus,⁶¹ sulphur⁶² or even selenium.⁴⁶ The insertion of an alien atom breaks the electroneutrality typical of the CNTs sp^2 network and transform them either in interesting supports for growing metal nanoparticles (NPs) or in metal-free systems suitable for promoting specific catalytic transformations.

One of the main advantages in employing doped CNTs as supports for metal NPs is a stronger interaction with the metal NPs themselves respect to pristine CNTs, that implies a minor metal leaching and a minor tendency to the NPs sinterization.⁶³ In this way the catalytic activity of the NPs/CNTs system is maintained through several catalytic trials and the heterogeneous catalyst can be recycled many times. Moreover, the donor atoms present at the nanostructure surface also represent valuable nucleation site for NPs, allowing for the synthesis of small and monodispersed metal systems.

In many cases, due to the high cost of metal-based catalysts (particularly those based on platinum group metals – PGMs) and their scarce abundance in nature, doped CNTs have attracted the interest of many research groups for their ability to replace efficiently metal-based systems of the state-of-the-art for promoting (as metal-free catalysts) important catalytic processes.⁶⁴ There are several catalytic reactions where they exhibit good performances including selective alcohol oxidation,⁶⁵ oxidative dehydrogenation of aromatic hydrocarbons and alkanes,^{64a,66} selective oxidation of H_2S ,⁶⁷ oxidation of cyclohexane,⁶⁸ acetylene hydrochlorination⁶⁹ and Knoevenagel condensation.⁷⁰ However, the largest area of employment of doped-CNTs as metal-free catalysts is the clean and sustainable energy sector,⁷¹ *e.g.* in photovoltaic applications⁷² and lithium ion batteries,⁷³ but one of the main field in which doped-CNTs, and in particular nitrogen doped-CNTs (N-CNTs), have proved to be very promising and attracting systems is the electrochemical oxygen reduction reaction (ORR) in fuel cells cathodes.⁴⁶ Indeed, the development of alternative and green energy sources has become a priority because of the increasing global energy demand and the environmental impact of traditional energy sources;⁷⁴ on this ground, fuel cells are clean and highly efficient devices able to directly convert chemical energy from a fuel (*e.g.* hydrogen or alcohols) into electrical energy. The main drawback for the large scale application and commercialization of fuel cells is the high cost and poor durability of platinum-based catalysts, that are, to date, the most active catalysts for ORR. Thus, in the last few years, many research

efforts have been devoted to the development of efficient, durable and inexpensive alternatives to platinum.^{64,75}

The first example of N-doped CNTs used as efficient electrocatalysts in ORR was reported by Dai and co-workers in 2009.⁷⁶ They demonstrated that N-CNTs show a catalytic activity comparable to that observed with the commercially available Pt/C in alkaline media. The main reason to this remarkable ORR activity is that, while pristine CNTs are composed of neutral C-C bonds with high chemical inertness, N-doped CNTs present C-N bonds that are permanently polarized with weak negative charges localized on N atoms and weak positive charges on C atoms. These latter facilitate the O₂ absorption, the initial step for the ORR process, while the locally increased electron density on N atoms promotes a charge transfer to the adsorbed O₂ molecules that reduces the dissociation energy barrier weakening the O-O bond and favouring the reduction process. Moreover, while the simple employment of pristine CNTs translates into a 2e⁻ reduction process with formation of hydrogen peroxide as the main product,⁷⁷ the introduction of a heteroatom (mostly nitrogen) in the Csp² network leads to very efficient metal-free catalysts for ORR able to foster a prevalent 4e⁻ reducing path with formation of water as the main reduction product.

This revolutionary discovery quickly focused great interest on carbon-based catalysts for ORR and therefore huge efforts have been devoted to the synthesis of either mono-dimensional (1D) or bi-dimensional (2D) nitrogen-doped carbon nanomaterials and to fully exploit their catalytic ability to promote ORR both on a theoretical⁷⁸ and experimental⁷⁹ ground. Many different methods have been developed for the synthesis of N-doped carbon nanomaterials. The most widely used technique is the *in-situ* Chemical Vapour Deposition (CVD) approach.⁸⁰ This process is commonly used to produce CNTs through a thermal decomposition (600–1200 °C) of a hydrocarbon vapour in the presence of a metal catalyst, typically Fe or Co, on alumina supports. To prepare N-doped CNTs a nitrogen source (*e.g.* ammonia) is added in the hydrocarbon flow obtaining N-doped CNTs with different types of nitrogen functionalities embedded in the Csp² network.⁸¹ Alternative approaches start from already synthesized CNTs and achieve the nitrogen doping through different post-treatments such as ion implantation with N₂⁺,⁸² thermal annealing of CNTs in the presence of different nitrogen sources⁸³ or reduction with N-containing reducing agents.⁸⁴

Anyway, none of the above synthetic methodologies is able to control the nitrogen species formed and, as a result, all the nanomaterials produced contain, at the same

time, a wide variety of different nitrogen species (pyridine, pyrrolic, quaternary and nitrogen oxide groups), as shown in Figure 1.4.^{46,85}

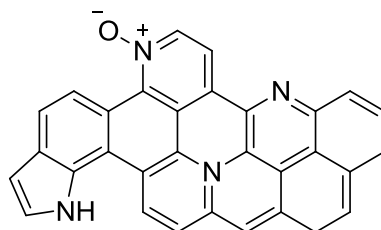


Figure 1.4. Different nitrogen species typically present in N-doped CNTs.

The coexistence of different nitrogen species makes extremely hard to identify which is the real nature of the active sites in N-doped CNTs.⁷⁹ Only a partial control on the degree and type of N-doping can be achieved through an accurate optimization of the CVD synthetic conditions⁸⁶ or through a thermal post-synthetic treatment on already prepared N-CNTs, but in all cases a simple adjustment of the different N-species relative concentration is achieved.⁸⁷ The result is that the role of the different N-functionalities on the catalytic efficiency of N-doped CNTs still remains unclear and it is at the origin of controversial debates in the scientific community, sometimes producing even conflicting literature results.⁸⁸

The in-depth comprehension of the real nature of the N-containing active species would represent an important step-forward towards the understanding of the underlying ORR mechanism and a fundamental starting point for the design, synthesis and development of stable and efficient metal-free electrocatalysts for their application on a large scale.

1.5 Objects of the Thesis

In the first part of the thesis an original, efficient and versatile approach to the convenient and facile functionalization of carbon nanotubes capable of imparting multimodality to these fundamental nanostructures, is described. In particular, the strategy developed takes advantage from the well established Cu-mediated acetylene-azide coupling (CuAAC) reaction applied to phenylazido-functionalized CNTs for their convenient homo-/hetero-decoration using different organic/organometallic frameworks bearing terminal acetylene pendant arms. The mild reaction conditions required, the high chemoselectivity and functional group tolerance of the CuAAC approach make the

protocol highly versatile for CNT single step multidecoration, avoiding those drawbacks resulting from the application of different and subsequent organic functionalization methods. The protocol has been properly applied for the synthesis of optically traceable nanocarriers through the smart and easy hetero-decoration of CNTs with a fluorescent probe and a new bifunctional linker designed for the facile and controllable conjugation of complex (bio)molecules.

The CuAAC protocol has been conveniently extended from monodimensional carbon nanomaterials to other complex structures such as Metal Organic Frameworks (MOFs), imparting multimodality to these porous, crystalline 3D organometallic coordination polymers and demonstrating the general applicability of the developed method.

In the second part of the work, an energy- and atom-saving process to the production of tailored N-doped and catalytically active metal-free carbon nanostructures, has been set up. The N-decoration of multiwalled carbon nanotubes occurs *via* chemical functionalization under mild reaction conditions and generates effective catalysts for the oxygen reduction reaction in alkaline medium. Our *ex-situ* approach allows a precise control of the N-containing groups representing a unique tool for shedding light on the complex structure-reactivity relationship of N-doped carbon nanomaterials in ORR and a unique model for an in-depth understanding of the underlying reduction mechanism.

References

- ¹ H. W. Kroto, J. R. Heath, S. C. O'Brien, R. F. Curl, R. E. Smalley, *Nature* **1985**, *318*, 162.
- ² S. Iijima, *Nature* **1991**, *354*, 56.
- ³ K. S. Novoselov, A. K. Geim, S. V. Morozov, D. Jiang, Y. Zhang, S. V. Dubonos, I. V. Grigorieva, A. A. Firsov, *Science* **2004**, *306*, 666.
- ⁴ S. Iijima, T. Ichihashi, *Nature* **1993**, *363*, 603.
- ⁵ P. M. Ajayan, *Chem. Rev.* **1999**, *99*, 1787. b) R. H. Baughman, A. A. Zakhidov, W. A. de Heer, *Science* **2002**, *297*, 787.
- ⁶ a) D. M. Guldi, N. Martín in *Carbon Nanotubes and Related Structures: Synthesis, Characterization, Functionalization and Applications* (Eds.: D. M. Guldi, N. Martín), Publisher: Wiley-VCH, **2010**, pp. 562. ISBN: 978-3-527-32406-4. b) S. Yellampalli in *Carbon Nanotubes – Synthesis, Characterization, Application* (Ed.: S. Yellampalli), Publisher: InTech, **2011**, pp. 514. ISBN: 978-953-307-497-9.
- ⁷ a) A. Krüger in *Carbon Materials and Nanotechnology* (Ed.: A. Krüger), Publisher: Wiley-VCH, **2010**, pp. 490. ISBN: 978-3-527-31803-2. b) S. Bianco in *Carbon Nanotubes – From Research to Applications* (Ed.: S. Bianco), Publisher: InTech, **2011**, pp. 358. ISBN: 978-953-307-500-6.
- ⁸ a) D. Tasis, N. Tagmatarchis, A. Bianco, M. Prato, *Chem. Rev.* **2006**, *106*, 1105. b) P. Singh, S. Campidelli, S. Giordani, D. Bonifazi, A. Bianco, M. Prato, *Chem. Soc. Rev.* **2009**, *38*, 2214. c) N. Karousis, N. Tagmatarchis, *Chem. Rev.* **2010**, *110*, 5366.
- ⁹ J. Liu, A. G. Rinzler, H. Dai, J. H. Hafner, R. K. Bradley, P. J. Boul, A. Lu, T. Iverson, K. Shelimov, C. B. Huffman, F. Rodriguez-Macias, Y.-S. Shon, T. R. Lee, D. T. Colbert, R. E. Smalley, *Science* **1998**, *280*, 1253.
- ¹⁰ H. Li, R. B. Martin, B. A. Harruff, R. A. Carino, L. F. Allard, Y.-P. Sun, *Adv. Mater.* **2004**, *16*, 896.
- ¹¹ J. Chen, M. A. Hamon, H. Hu, Y. Chen, A. M. Rao, P. C. Eklund, R. C. Haddon, *Science* **1998**, *282*, 95.
- ¹² E. T. Mickelson, C. B. Huffman, A. G. Rinzler, R. E. Smalley, R. H. Hauge, J. L. Margrave, *Chem. Phys. Lett.* **1998**, *296*, 188.
- ¹³ a) P. J. Boul, J. Liu, E. T. Mickelson, C. B. Huffman, L. M. Ericson, I. W. Chiang, K. A. Smith, D. T. Colbert, R. H. Hauge, J. L. Margrave, R. E. Smalley, *Chem. Phys. Lett.* **1999**, *310*, 367. b) R. K. Saini, I. W. Chiang, H. Peng, R. E. Smalley, W. E. Billups, R. H. Hauge, J. L. Margrave, *J. Am. Chem. Soc.* **2003**, *125*, 3617.
- ¹⁴ a) J. L. Stevens, A. Y. Huang, H. Peng, I. W. Chiang, V. N. Khabashesku, J. L. Margrave, *Nano Lett.* **2003**, *3*, 331. b) L. Zhang, V. U. Kiny, H. Peng, J. Zhu, R. F. M. Lobo, J. L. Margrave, V. N. Khabashesku, *Chem. Mater.* **2004**, *16*, 2055.
- ¹⁵ E. Unger, A. Graham, F. Kreupl, M. Liebau, W. Hoenlein, *Curr. Appl. Phys.* **2002**, *2*, 107.
- ¹⁶ S. Pekker, J.-P. Salvetat, E. Jakab, J.-M. Bonard, L. Forro, *J. Phys. Chem. B.* **2001**, *105*, 7938.

-
- 17 a) D. Ogrin, A. R. Barron, *J. Mol. Cat.* **2006**, *244*, 267. b) D. Ogrin, J. Chattopadhyay, A. K. Sadana, W. E. Billups, A. R. Barron, *J. Am. Chem. Soc.* **2006**, *128*, 11332. c) W. Yuan, M. B. Chan-Park, *ACS Appl. Mater. Interfaces* **2012**, *4*, 2065.
- 18 C. Annese, L. D'Accolti, G. Giambastiani, A. Mangone, A. Milella, G. Tuci, C. Fusco, *Eur. J. Org. Chem.* **2014**, 1666.
- 19 H. Hu, B. Zhao, M. A. Hamon, K. Kamaras, M. E. Itkis, R. C. Haddon, *J. Am. Chem. Soc.* **2003**, *125*, 14893.
- 20 a) K. S. Coleman, S. R. Bailey, S. Fogden, M. L. H. Green, *J. Am. Chem. Soc.* **2003**, *125*, 8722. b) K. A. Worsley, K. R. Moonosawmy, P. Kruse, *Nano Lett.* **2004**, *4*, 1541.
- 21 a) A. Hirsch, *Angew. Chem., Int. Ed.* **2002**, *41*, 1853. b) A. Hirsch, O. Vostrowsky, *Top. Curr. Chem.* **2005**, *245*, 193. c) M. Holzinger, O. Vostrowsky, A. Hirsch, F. Hennrich, M. Kappes, R. Weiss, F. Jellen, *Angew. Chem. Int. Ed.* **2001**, *40*, 4002.
- 22 a) F. Hennrich, M. Kappes, A. Hirsch, *J. Am. Chem. Soc.* **2003**, *125*, 8566. b) M. Holzinger, J. Steinmetz, D. Samaille, M. Glerup, M. Paillet, P. Bernier, L. Ley, R. Graupner, *Carbon* **2004**, *42*, 941.
- 23 a) V. Georgakilas, K. Kordatos, M. Prato, D. M. Guldi, M. Holzinger, A. Hirsch, *J. Am. Chem. Soc.* **2002**, *124*, 760. b) N. Tagmatarchis, M. Prato, *J. Mater. Chem.* **2004**, *14*, 437.
- 24 a) F. G. Brunetti, M. A. Herrero, J. de M. Muñoz, S. Giordani, A. Díaz-Ortiz, S. Filippone, G. Ruaro, M. Meneghetti, M. Prato, E. Vázquez, *J. Am. Chem. Soc.* **2007**, *129*, 14580. b) N. Rubio, M. A. Herrero, A. de la Hoz, M. Meneghetti, M. Prato, E. Vázquez, *Org. Biomol. Chem.* **2010**, *8*, 1936.
- 25 J. L. Delgado, P. de la Cruz, F. Langa, A. Urbina, J. Casado, J. T. Lopez Navarrete, *Chem. Commun.* **2004**, 1734.
- 26 a) M. Alvaro, P. Atienzar, P. de la Cruz, J. L. Delgado, H. Garcia, F. Langa, *J. Phys. Chem. B* **2004**, *108*, 12691. b) Y. Wang, Z. Iqbal, S. Mitra, *Carbon* **2005**, *43*, 1015.
- 27 a) G. Ghini, L. Luconi, A. Rossin, C. Bianchini, G. Giambastiani, S. Cicchi, L. Lascialfari, A. Brandi, A. Giannasi, *Chem. Commun.* **2010**, *46*, 252. b) G. Giambastiani, S. Cicchi, A. Giannasi, L. Luconi, A. Rossin, F. Mercuri, C. Bianchini, A. Brandi, M. Melucci, G. Ghini, P. Stagnaro, L. Conzatti, E. Passaglia, M. Zoppi, T. Montini, P. Fornasiero, *Chem. Mater.* **2011**, *23*, 1923.
- 28 J. L. Bahr, J. Yang, D. V. Kosynkin, M. J. Bronikowski, R. E. Smalley, J. M. Tour, *J. Am. Chem. Soc.* **2001**, *123*, 6536.
- 29 J. J. Stephenson, J. L. Hudson, S. Azad, J. M. Tour, *Chem. Mater.* **2006**, *18*, 374.
- 30 B. K. Price, J. M. Tour, *J. Am. Chem. Soc.* **2006**, *128*, 12899.
- 31 C. A. Dyke, J. M. Tour, *Chem. Eur. J.* **2004**, *10*, 812.
- 32 S. P. Economopoulos, N. Karousis, G. Rotas, G. Pagona, N. Tagmatarchis, *Curr. Org. Chem.* **2011**, *15*, 1121.
- 33 a) H. Peng, P. Reverdy, V. N. Khabashesku, J. L. Margrave, *Chem. Commun.* **2003**, 362. b) P. Umek, J. W. Seo, K. Hernadi, A. Mrzel, P. Pechy, D. D. Mihailovic, L. Forro, *Chem. Mater.* **2003**, *15*, 4751.

- 34 a) T. Nakamura, M. Ishihara, T. Ohana, A. Tanaka, Y. Koga, *Chem. Commun.* **2004**, 1336. b) T. Nakamura, M. Ishihara, T. Ohana, A. Tanaka, Y. Koga, *Diamond Relat. Mater.* **2004**, *13*, 1971.
- 35 B. Z. Tang, H. Xu, *Macromolecules* **1999**, *32*, 2569.
- 36 Y. Tomonari, H. Murakami, N. Nakashima, *Chem. Eur. J.* **2006**, *12*, 4027.
- 37 a) N. Nakashima, Y. Tomonari, H. Murakami, *Chem. Lett.* **2002**, 638. b) H. Durmaz, A. Dag, U. Tunca, G. Hizal, *J. Polym. Sci. Pol. Chem.* **2012**, *50*, 2406.
- 38 T. Ogoshi, Y. Takashima, H. Yamaguchi, A. Harada, *J. Am. Chem. Soc.* **2007**, *129*, 4878.
- 39 H. Cathcarth, V. Nicolosi, J. M. Hughes, W. J. Blau, J. M. Kelly, S. J. Quinn, J. N. Coleman, *J. Am. Chem. Soc.* **2008**, *130*, 12734.
- 40 A. N. Khlobystov, D. A. Britz, G. A. D. Briggs, *Acc. Chem. Res.* **2005**, *38*, 901.
- 41 K. Yanagi, K. Iakoubovskii, H. Matsui, H. Matsuzaki, H. Okamoto, Y. Miyata, Y. Maniwa, S. Kazaoui, N. Minami, H. Kataura, *J. Am. Chem. Soc.* **2007**, *129*, 4992.
- 42 J. S. Bendall, A. Ilie, M. E. Welland, J. Sloan, M. L. H. Green, *J. Phys. Chem. B* **2006**, *110*, 6569.
- 43 S. Y. Hong, G. Tobias, K. T. Al-Jamal, B. Ballesteros, H. Ali-Boucetta, S. Lozano-Perez, P. D. Nellist, R. B. Sim, C. Finucane, S. J. Mather, M. L. H. Green, K. Kostarelos, B. G. Davis, *Nat. Mater.* **2010**, *9*, 485.
- 44 a) Z. Liu, K. Chen, C. Davis, S. Sherlock, Q. Cao, X. Chen, H. Dai, *Cancer Res.* **2008**, *68*, 6652. b) Z. Liu, S. Tabakman, K. Welsher, H. Dai, *Nano Res.* **2009**, *2*, 85.
- 45 a) Z. Liu, A. C. Fan, K. Rakhra, S. Sherlock, A. Goodwin, X. Chen, Q. Yang, D. W. Felsher, H. Dai, *Angew. Chem. Int. Ed. Engl.* **2009**, *48*, 7668. b) K. Kostarelos, A. Bianco, M. Prato, *Nat. Nanotechnol.* **2009**, *4*, 627. c) A. Ruggiero, C. H. Villa, J. P. Holland, S. R. Sprinkle, C. May, J. S. Lewis, D. A. Scheinberg, M. R. McDevitt, *Int. J. Nanomedicine* **2010**, *5*, 783.
- 46 Z. Yang, H. Nie, X. Chen, X. Chen, S. Huang, *J. Power Sources* **2013**, *236*, 238.
- 47 K. M. Lee, L. Li, L. Dai, *J. Am. Chem. Soc.* **2005**, *127*, 4122.
- 48 G. Lamanna, A. Battigelli, C. Ménard-Moyon, A. Bianco, *Nanotechnol. Rev.* **2012**, *1*, 17.
- 49 a) M. R. McDevitt, D. Chattopadhyay, B. J. Kappel, J. S. Jaggi, S. R. Schiffman, C. Antczak, J. T. Njardarson, R. Brentjens, D. A. Scheinberg, *J. Nucl. Med.* **2007**, *48*, 1180. b) G. Pastorin, W. Wu, S. Wieckowski, J.-P. Briand, K. Kostarelos, M. Prato, A. Bianco, *Chem. Commun.* **2006**, 1182.
- 50 W. Wu, R. Li, X. Bian, Z. Zhu, D. Ding, X. Li, Z. Jia, X. Jiang, Y. Hu, *ACS Nano* **2009**, *3*, 2740.
- 51 J. J. Stephenson, J. L. Hudson, A. D. Leonard, B. K. Price, J. M. Tour, *Chem. Mater.* **2007**, *19*, 3491.
- 52 W. Wu, S. Wieckowski, G. Pastorin, M. Benincasa, C. Klumpp, J.-P. Briand, R. Gennaro, M. Prato, A. Bianco, *Angew. Chem. Int. Ed.* **2005**, *44*, 6358.
- 53 F. G. Brunetti, M. A. Herrero, J. De M. Muñoz, A. Díaz-Ortiz, J. Alfonsi, M. Meneghetti, M. Prato, E. Vázquez, *J. Am. Chem. Soc.* **2008**, *130*, 8094.
- 54 Z. Liu, W. Cai, L. He, N. Nakayama, K. Chen, X. Sun, X. Chen, H. Dai, *Nat. Nanotechnol.* **2007**, *2*, 47.

-
- 55 C. L. Lay, H. Q. Liu, H. R. Tan, Y. Liu, *Nanotechnology* **2010**, *21*, 065101.
- 56 C. Ménard-Moyon, C. Fabbro, M. Prato, A. Bianco, *Chem. Eur. J.* **2011**, *17*, 3222.
- 57 a) N. W. S. Kam, Z. Liu, H. Dai, *J. Am. Chem. Soc.* **2005**, *127*, 12492. b) C. Samorí, H. Ali-Boucetta, R. Sainz, C. Guo, F. M. Toma, C. Fabbro, T. da Ros, M. Prato, A. Bianco, *Chem. Commun.* **2010**, *46*, 1494.
- 58 J. Chen, S. Chen, X. Zhao, L. V. Kuznetsova, S. S. Wong, I. Ojima, *J. Am. Chem. Soc.* **2008**, *130*, 16778.
- 59 W. J. Lee, U. N. Maiti, J. M. Lee, J. Lim, T. H. Han, S. O. Kim, *Chem. Commun.* **2014**, *50*, 6818.
- 60 E. A. Ekimov, V. A. Sidorov, E. D. Bauer, N. N. Mel'nik, N. J. Curro, J. D. Thompson, S. M. Stishov, *Nature* **2004**, *428*, 542.
- 61 Y. Zhang, T. Mori, J. Ye, M. Antonietti, *J. Am. Chem. Soc.* **2010**, *132*, 6294.
- 62 Z. Yang, Z. Yao, G. Li, G. Fang, H. Nie, Z. Liu, X. Zhou, X. A. Chen, S. Huang, *ACS Nano* **2011**, *6*, 205.
- 63 a) K. Chizari, I. Janowska, M. Houille, I. Florea, O. Ersen, T. Romero, P. Bernhardt, M. J. Ledoux, C. Pham-Huu, *Appl. Catal. A: General* **2010**, *380*, 72. b) J. Hu, J. Shi, S. Li, Y. Qin, Z.-X. Guo, Y. Song, D. Zhu, *Chem. Phys. Lett.* **2005**, *401*, 352.
- 64 a) D. Su, J. Zhang, B. Frank, A. Thomas, X. Wang, J. Paraknowitsch, R. Schlögl, *ChemSusChem* **2010**, *3*, 169. b) D. Yu, E. Nagelli, F. Du, L. Dai, *J. Phys. Chem. Lett.* **2010**, *1*, 2165.
- 65 a) J. Long, X. Xie, J. Xu, Q. Gu, L. Chen, X. Wang, *ACS Catal.* **2012**, *2*, 622. b) J. Luo, F. Peng, H. Wang, H. Yu, *Catal. Commun.* **2013**, *39*, 44.
- 66 C. Chen, J. Zhang, B. Zhang, C. Yu, F. Peng, D. Su, *Chem. Commun.* **2013**, *49*, 8151.
- 67 K. Chizari, A. Deneuve, O. Ersen, I. Florea, Y. Liu, D. Edouard, I. Janowska, D. Begin, C. Pham-Huu, *ChemSusChem* **2012**, *5*, 102.
- 68 a) H. Yu, F. Peng, J. Tan, X. Hu, H. Wang, J. Yang, W. Zheng, *Angew. Chem., Int. Ed.* **2011**, *50*, 3978. b) X. Yang, H. Yu, F. Peng, H. Wang, *ChemSusChem* **2012**, *5*, 1213.
- 69 K. Zhou, B. Li, Q. Zhang, J.-Q. Huang, G.-L. Tian, J.-C. Jia, M.-Q. Zhao, G.-H. Luo, D. S. Su, F. Wei, *ChemSusChem* **2014**, *7*, 723.
- 70 S. van Dommele, K. P. de Jong, J. H. Bitter, *Chem. Commun.* **2006**, *46*, 4859.
- 71 D. S. Su, S. Perathoner, G. Centi, *Chem. Rev.* **2013**, *113*, 5782.
- 72 J. M. Lee, J. S. Park, S. H. Lee, H. Kim, S. Yoo, S. O. Kim, *Adv. Mater.* **2011**, *23*, 629.
- 73 J. Yang, J. Wang, X. Li, D. Wang, J. Liu, G. Liang, M. Gauthier, Y. Li, D. Geng, R. Li, X. Sun, *J. Mater. Chem.* **2012**, *22*, 7537.
- 74 a) R. A. Costa, J. R. Camacho, *J. Power Sources* **2006**, *161*, 1176. b) J. M. Andujar, F. Segura, *Renew. Sustain. Energy Rev.* **2009**, *13*, 2309.
- 75 a) S. Minhua in: *Electrocatalysis in Fuel Cells, A Non- and Low-Platinum Approach*, (Ed.: S. Minhua), Publisher: Springer, London **2013**, pp. 327. b) N. M. Markovic, T. J. Schmidt, V. Stamenkovic, P. N. Ross, *Fuel Cells* **2001**, *1*, 105. c) Z. Chen, D. Higgins, A. Yu, L. Zhang, J.

-
- Zhang, *Energy Environ. Sci.* **2011**, *4*, 3167. d) M. Chisaka, Y. Suzuki, T. Iijima, Y. Sakurai, *J. Phys. Chem. C* **2011**, *115*, 20610.
- 76 K. Gong, F. Du, Z. Xia, M. Durstock, L. Dai, *Science* **2009**, *323*, 760.
- 77 I. Kruusenberg, J. Leis, M. Arulepp, K. J. Tammeveski, *J. Solid State Electrochem.* **2010**, *14*, 1269.
- 78 a) K.-Y. Yeh, M. J. Janik, *J. Comput. Chem.* **2011**, *32*, 3399. b) M. Kaukonen, A. V. Krasheninnikov, E. Kauppinen, R. M. Nieminen, *ACS Catal.* **2013**, *3*, 159. c) S. Ni, Z. Li, J. Yang, *Nanoscale* **2012**, *4*, 1184.
- 79 a) Y. Zheng, Y. Jiao, M. Jaroniec, Y. G. Jin, S. Z. Qiao, *Small* **2012**, *8*, 3550. b) C. Z. Zhu, S. J. Dong, *Nanoscale* **2013**, *5*, 1753. c) D.-W. Wang, D. Su, *Energy Environ. Sci.* **2014**, *7*, 576.
- 80 M. Kumar, Y. Ando, *J. Nanosci. Nanotechnol.* **2010**, *10*, 3739.
- 81 E. J. Biddinger, D. von Deak, U. S. Ozkan, *Top. Catal.* **2009**, *52*, 1566.
- 82 C. Morant, J. Andrey, P. Prieto, D. Mendiola, J. M. Sanz, E. Elizalde, *Phys. Status Solidi A* **2006**, *203*, 1069.
- 83 a) C. D. Higgins, J. Wu, W. Li, Z. Chen, *Electrochim. Acta* **2012**, *59*, 8. b) S. M. Unni, S. Devulapally, N. Karjulea, S. Kurungot, *J. Mater. Chem.* **2012**, *22*, 23506. c) A. Morozan, P. Jegou, M. Pinault, S. Campidelli, B. Jousset, S. Palacin, *ChemSusChem* **2012**, *5*, 647.
- 84 a) H. Yang, C. Shan, F. Li, D. Han, Q. Zhang, L. Niu, *Chem. Commun.* **2009**, 3880. b) S. Park, Y. Hu, Y. O. Hwang, S. E. Lee, L. B. Casabianca, W. Cai, J. R. Potts, H. W. Ha, S. Chen, J. Oh, S. O. Kim, Y. H. Kim, Y. Ishii, R. S. Ruoff, *Nature Commun.* **2012**, *3*, 638.
- 85 H. T. Liu, Y. Q. Liu, D. B. Zhu, *J. Mater. Chem.* **2011**, *21*, 3335.
- 86 a) K. Chizari, A. Vena, L. Laurentius, U. Sundararaj, *Carbon* **2014**, *68*, 369. b) S. van Dommele, A. Romero-Izquierdo, R. Brydson, K. P. de Jong, J. H. Bitter, *Carbon* **2008**, *46*, 138.
- 87 a) T. Sharifi, G. Hu, X. Jia, T. Wågberg, *ACS Nano* **2012**, *10*, 8904. b) P. H. Matter, L. Zhang, U. S. Ozkan, *J. Catal.* **2006**, *239*, 83.
- 88 a) L. Lai, J. R. Potts, D. Zhan, L. Wang, C. K. Poh, C. Tang, K. Gong, Z. Shen, J. Linc, R. S. Ruoff, *Energy Environ. Sci.* **2012**, *5*, 7936. b) S. Kundu, T. C. Nagaiah, W. Xia, Y. Wang, S. van Dommele, J. H. Bitter, M. Santa, G. Grundmeier, M. Bron, W. Schuhmann, M. Muhler, *J. Phys. Chem. C* **2009**, *113*, 14302. c) H. Niwa, K. Horiba, Y. Harada, M. Oshima, T. Ikeda, K. Terakura, J.-I. Ozaki, S. Miyata, *J. Power Sources* **2009**, *187*, 93. d) B. Zheng, J. Wang, F. B. Wang, X. H. Xia, *Electrochem. Commun.* **2013**, *28*, 24. e) H. B. Li, W. J. Kang, L. Wang, Q. L. Yue, S. L. Xu, H. S. Wang, J. F. Liu, *Carbon* **2013**, *54*, 249.

2. “Click” on Tubes: a Versatile Approach Towards Multimodal Functionalization of SWCNTs

2.1 Abstract

Organic functionalization of carbon nanotube sidewalls is a tool of primary importance in material science and nanotechnology, equally from a fundamental and an applicative point of view.^{1,2} In this chapter, an efficient and versatile approach to the organic/organometallic functionalization of single-walled carbon nanotubes (SWCNTs) capable of imparting multimodality to these fundamental nanostructures, is described. Our strategy takes advantage from well established Cu-mediated acetylene-azide coupling (CuAAC) reactions applied to phenylazido-functionalized SWCNTs for their convenient homo-/hetero-decoration using a number of organic/organometallic frameworks, or mixture thereof, bearing terminal acetylene pendant arms. The phenylazido-decorated SWCNTs are prepared by chemoselective arylation of the CNT sidewalls with diazonium salts under mild conditions, and subsequently used for the copper-mediated cycloaddition protocol in the presence of terminal acetylenes. The latter reaction is performed in one-step using either single acetylene derivatives or equimolar mixtures of terminal alkynes bearing either similar functional groups (masked with orthogonally cleavable protecting groups) or easily distinguishable functionalities (on the basis of complementary analytical/spectroscopic techniques). All the materials and intermediates have been characterized with respect to their most relevant aspects/properties, through TEM microscopy, thermogravimetric analysis coupled with MS analysis of volatiles (TG-MS), elemental analysis, cyclic voltammetry (CV), Raman and UV-vis spectroscopy. The functional loading and related chemical grafting of both primary amino- and ferrocene-decorated SWCNTs have been spectroscopically (UV-vis – *Kaiser* test) and electrochemically (CV) determined, respectively.

2.2 Introduction

Since their discovery,³ carbon nanotubes (CNTs)⁴ have received growing attention in nanotechnology because of their unique mechanical, thermal and electrical properties.⁵ At present, CNTs are among the nanomaterials with the largest impact on a wide range of technological applications:^{1,2} from nanocomposite materials with improved chemico-physical properties⁶ to biology⁷ and nanomedicine⁸ for drug delivery and imaging. Due to their scarce processability and miscibility in the most common media, both covalent and non-covalent functionalization approaches have been extensively investigated in the last few years. CNT sidewalls and tips decoration with organic functional groups has allowed scientists to exploit the unique properties of these macromolecular systems more conveniently. Indeed, the development of new methodologies for the covalent functionalization of CNTs, aimed at integrating these nanomaterials into more complex functional structures, has recently emerged as an area of great interest.⁹ Despite the chemical inertness of the CNT sidewalls, relevant examples of organic functionalization have been successfully addressed.⁹ Among them, reactions with nitrenes,¹⁰ nucleophilic carbenes,¹¹ diazonium salts,¹² bromomalonates,¹³ free radicals¹⁴ and 1,3-dipoles^{15,16,17,18,19a} have been widely documented on both experimental⁹ and theoretical ground. In spite of that, making complex carbon nanostructures such as SWCNTs and/or MWCNTs flexible platforms for the efficient/facile and multiple functionalization of their sidewalls and tips, still represents a priority to be properly faced. In particular, one main challenging issue is to impart multimodality to these systems by exploiting the whole CNT surface for the anchoring of different molecules, possibly under mild reaction conditions and avoiding undesired side-processes or conflicting side-reactions between the decorating groups.

Different synthetic approaches have been successfully applied to the CNT multifunctionalization, all of them taking advantage of well-established organic strategies: from the combination of different organic protocols¹⁹ and the covalent anchoring of masked functionalities bearing orthogonally cleavable protecting groups^{19d,20} to site-selective functionalization of the opposite tube ends on vertically aligned multi-walled carbon nanotubes (VA-MWCNTs) exposed to different photoreactive solutions.²¹ In this chapter is described a versatile and efficient organometallic approach to the (multi)functionalization of SWCNTs starting from

covalently modified nanomaterials bearing phenylazido pendant arms. Their subsequent exposure to terminal acetylenes under Cu^I-mediated conditions (CuAAC reaction) allows for the convenient homo- and/or hetero-decoration of the CNT sidewalls with organic/organometallic fragments or mixture thereof. Reactions described hereafter are found to be highly efficient in producing differently functionalized carbon nanomaterials, even at relatively low reaction temperatures (85 °C), setting the way for a versatile approach towards the CNT sidewall multifunctionalization. Moreover, the azide-alkyne cycloaddition reaction is compatible with various solvents and functional groups^{22,23} and the produced triazole functionality is chemically stable, with structural and functional properties similar to those of the (most common) amide bond. Accordingly, click chemistry represents a promising and original choice for boarding molecular systems on the “CNT skeleton”, thus imparting multimodality to the final carbon nanomaterials.^{24,25,26}

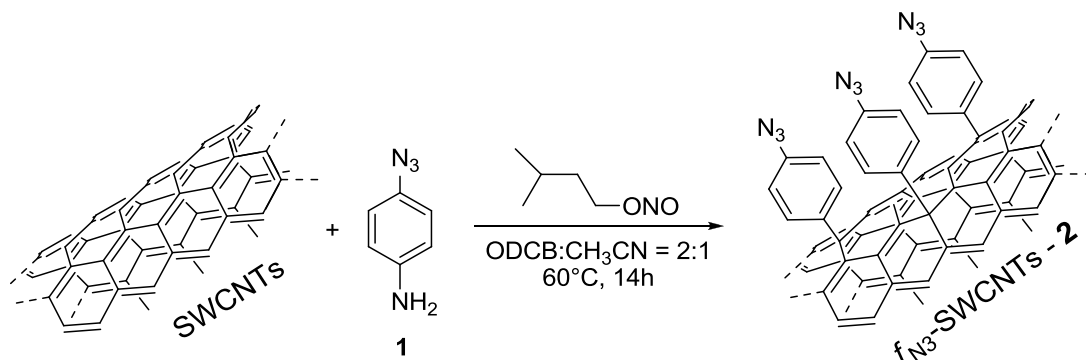
Alkynes containing either orthogonally cleavable protecting groups or chemical functional groups imparting well-defined redox properties to the final carbon nanomaterials have been selected; this choice was motivated by the need of controlling the course of the functionaliation process and the degree of the final functionalization loading through complementary chemical/spectroscopic and electrochemical measurements.

Such an approach to the functionalization of carbon nanostructures aims at providing chemists with “flexible platforms” (phenylazido-decorated SWCNTs) to be used for “mild” organic/organometallic (multi)decoration. In addition, the high functional group tolerance of the CuAAC protocol makes this approach highly suitable for imparting multimodality (hetero-decoration) to carbon nanostructures. Indeed, a one-step cycloaddition using acetylene mixtures can be conveniently used to bring different molecules on the tube board, minimizing those potential drawbacks resulting from the application of different (and subsequent - multi-step) organic functionalization protocols.

All homo- and hetero-functionalized materials presented hereafter have been characterized by thermogravimetric-MS analysis, FT-IR, Raman spectroscopy and TEM microscopy. Cyclic voltammetry (CV) and ninhydrin (*Kaiser*) test were finally used (whenever applicable) to calculate the functional loading.

2.3 Results and Discussion

Our approach to the (multi)functionalization of carbon nanostructures relies on the preliminary derivatization of the CNT sidewalls and tips with 4-azidoaniline (**1**) under classical Tour conditions²⁷ (Scheme 2.1).



Scheme 2.1. Synthesis of the arylazido-decorated f_{N_3} -SWCNTs (**2**) sample.

The reaction proceeds chemoselectively in *o*-dichlorobenzene/acetonitrile (ODCB/ CH_3CN) through the *in-situ* generation of aryldiazonium salts affording the arylazido-decorated f_{N_3} -SWCNTs (**2**). The 4-azidoaniline (**1**) is entirely recovered with no apparent decomposition of the azido group once the reaction is carried out in the absence of the proper alkyl nitrite (blank test). Furthermore, the azido group does not show any functionalization tendency even under harsher reaction conditions (ODCB $140^\circ C$ for prolonged reaction times) that might enhance its chemical reactivity (nitrene formation after a thermally-induced N_2 elimination).^{10,11}

In a typical procedure, the chemoselective arylazidation proceeds smoothly at $60^\circ C$, affording the f_{N_3} -SWCNTs material. Successive sonication/centrifugation/washing cycles and filtration through a $0.2\text{-}\mu m$ -pore inorganic membrane (AnodiscTM) have been used to recover the functionalized sample; the collected solid (**2**) was dried under vacuum and stored under N_2 atmosphere without decomposition per months. The thermal stability of the azido-functionalized material (**2**) was established according to the following thermal-stress test; the solid sample is maintained under stirring at $60^\circ C$ on-air overnight with no apparent alteration. Furthermore, the extremely high C/N ratio of **2** makes it a relatively safe, handling and harmless, azido-containing material.²⁸

This chemistry produces highly-functionalized samples and can be conveniently performed on a relatively large scale (up to 200 mg of SWCNTs *per run*). Evidence of

the sidewall functionalization is firstly obtained by comparing the TGA profiles of pristine and functionalized materials (Figure 2.1); a weight loss of 6.84 % is calculated in the 40-700 °C temperature range.^{20a}

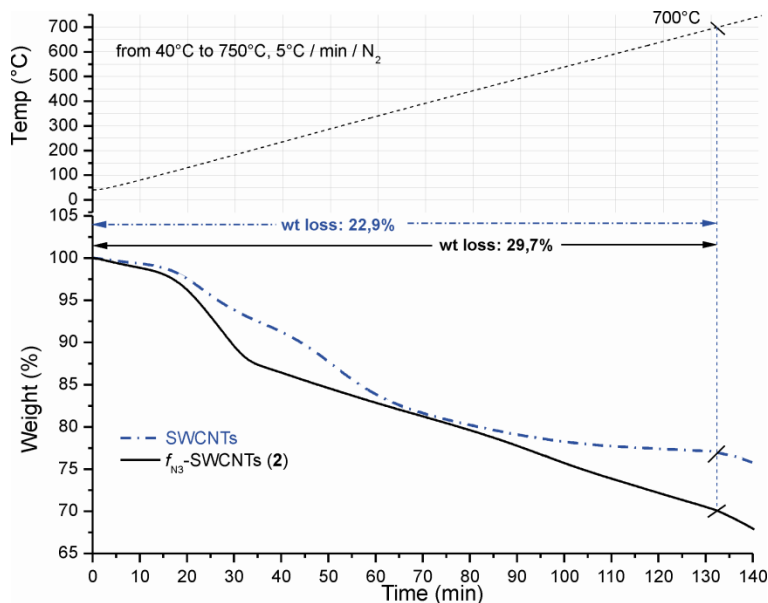


Figure 2.1. TGA profiles of pristine SWCNTs and f_{N_3} -SWCNTs (**2**).

The N and C quantitative elemental analysis (pristine SWCNTs: N, 0.26; C, 63.34; f_{N_3} -SWCNTs **2**: N, 6.95; C, 64.55) also provides evidence of the occurred functionalization.²⁹ According to these data, it can be roughly inferred that one phenylazido group is present every 80-90 C atoms of the CNT, hence about 0.58 mmol of $-C_6H_4-N_3$ per 1g of **2** are covalently tethered to the sidewalls. Additional evidence of the phenylazido decoration at the CNT sidewalls is unambiguously provided by the FT-IR spectrum of **2** (Figure 2.2). A relatively intense asymmetric stretching $\nu(N_3)$ close to 2100 cm^{-1} together with its symmetric counterpart falling around 1290 cm^{-1} are indicative of azido pendant groups.³⁰

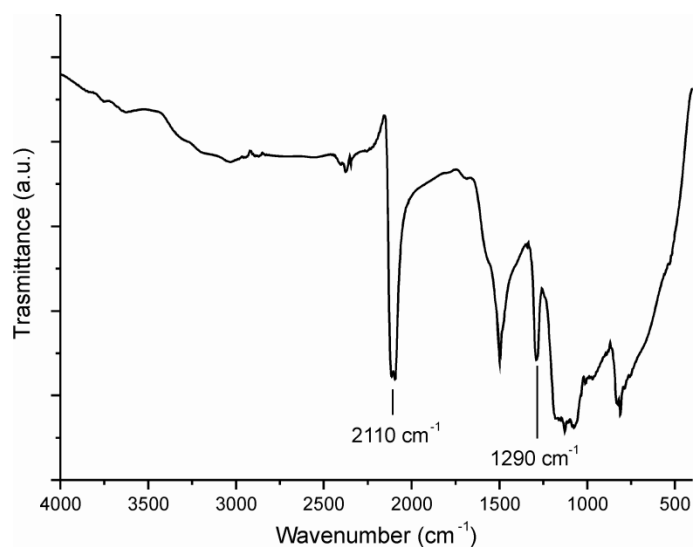


Figure 2.2. FT-IR spectrum of f_{N_3} -SWCNTs (**2**).

The f_{N_3} -SWCNTs sample does not show any appreciable improvement of its solubility/dispersibility in either polar (DMF, EtOH) or apolar (toluene) organic solvents compared to the pristine material. On the other hand, TEM analysis of the former sample reveals a higher deaggregation degree of the CNT bundles throughout the whole scanned area (Figure 2.3).

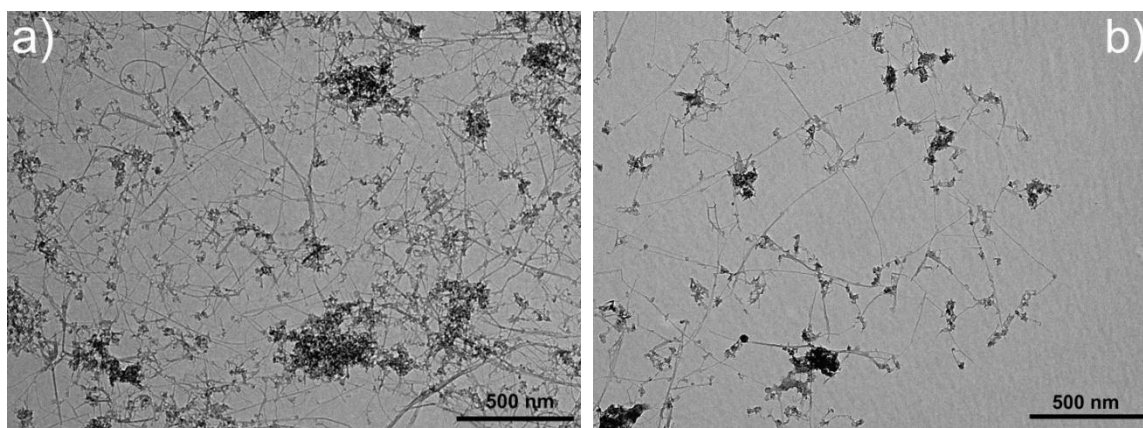


Figure 2.3. TEM micrographs of a) pristine SWCNTs and b) f_{N_3} SWCNTs (**2**) prepared by drop casting previously sonicated suspensions (EtOH) over copper grids coated with a Formvar film (FF200-Cu - Formvar film only).

Raman spectroscopy has been finally used for the characterization of **2**; an increased intensity of the disorder-induced mode (D-band) at 1314 cm^{-1} together with an overall reduction of the peak's intensity of the RBMs (between 75 and 250 cm^{-1}), are unambiguously indicative of the occurred sidewall derivatization (Figure 2.4).^{18,19,31,32}

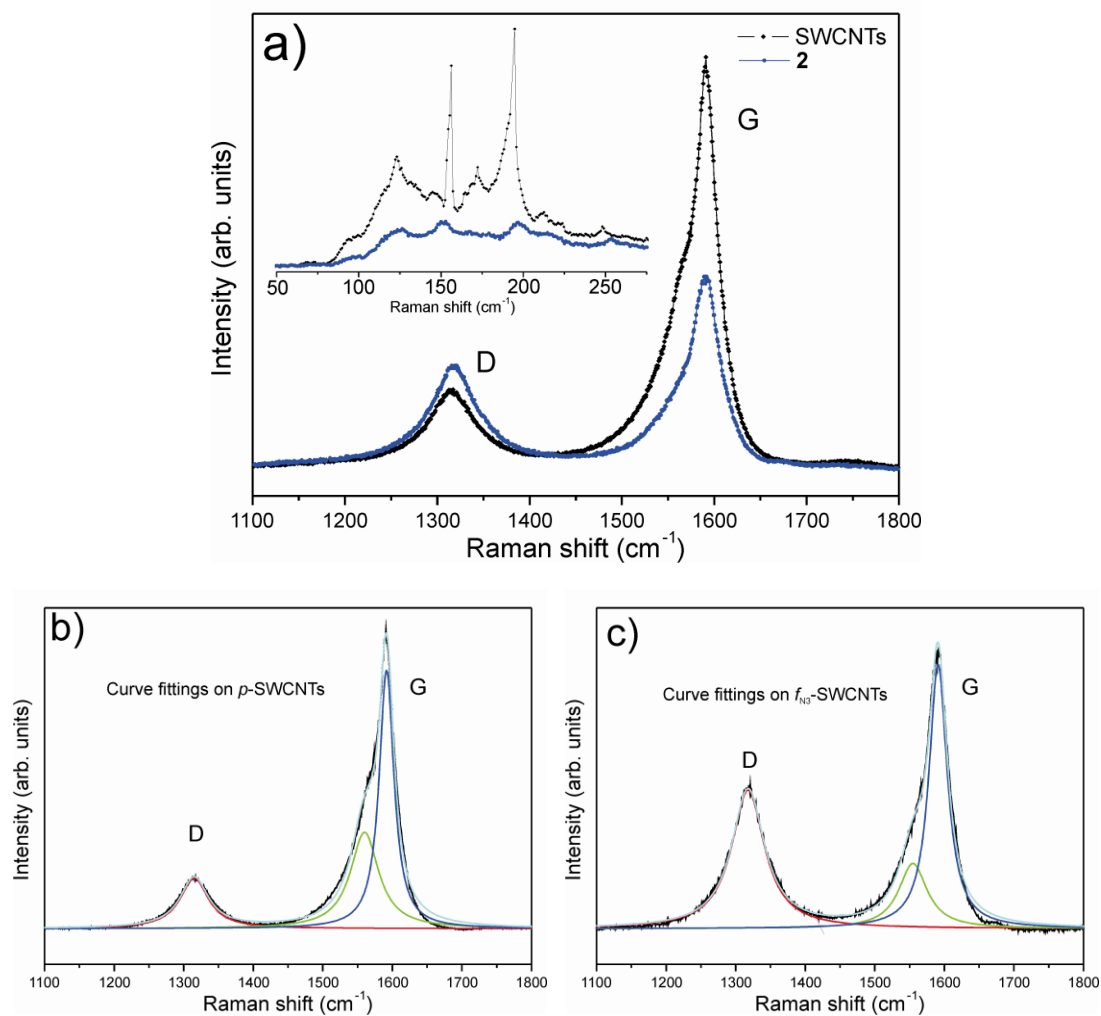


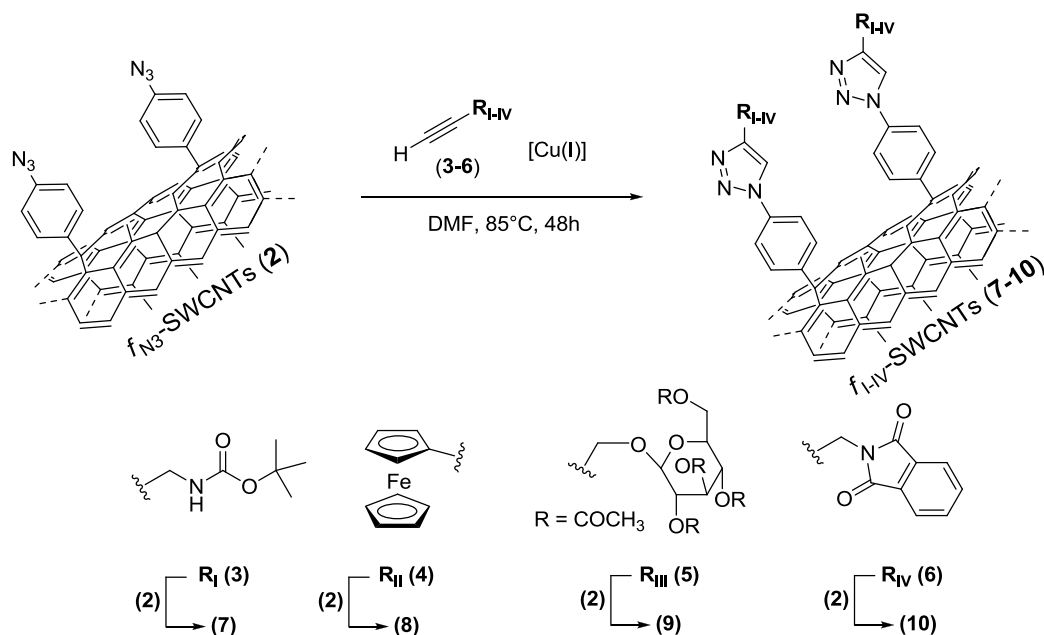
Figure 2.4. a) Raman spectra of f_{N_3} SWCNTs (**2**) vs. pristine SWCNTs and their respective curve fittings b) and c).

From a closer examination of the spectra reported it can be easily inferred that the functionalization increased the (I_D/I_G) intensity ratio from 0.34 (for pristine SWCNTs) to 0.66 (for **2**), suggesting a substantial sp^2 CNT sidewall perturbation after the functionalization (Figure 2.4b and 2.4c).

The as-synthesized f_{N_3} -SWCNTs (**2**) are exploited as a versatile starting material for the convenient CNT sidewall (multi)decoration, using organic and/or organometallic reagents bearing terminal alkyne pendant arms. Our strategy towards the (post)functionalization of **2** relied upon an efficient Cu^I -mediated azide-alkyne cycloaddition protocol (CuAAC).^{22a,23b,33} A conceptually related but complementary approach has been recently proposed by Adronov and co-workers;²⁵ polymer-nanotube conjugates are prepared from alkyne-decorated SWCNTs and azido-terminated polystyrenes employing different $Cu(I)$ precursors. Campidelli, Guldi *et al.* have used a

similar Cu-mediated strategy for the CNT-chemical grafting of azido end-capped zinc-phthalocyanines.³⁴

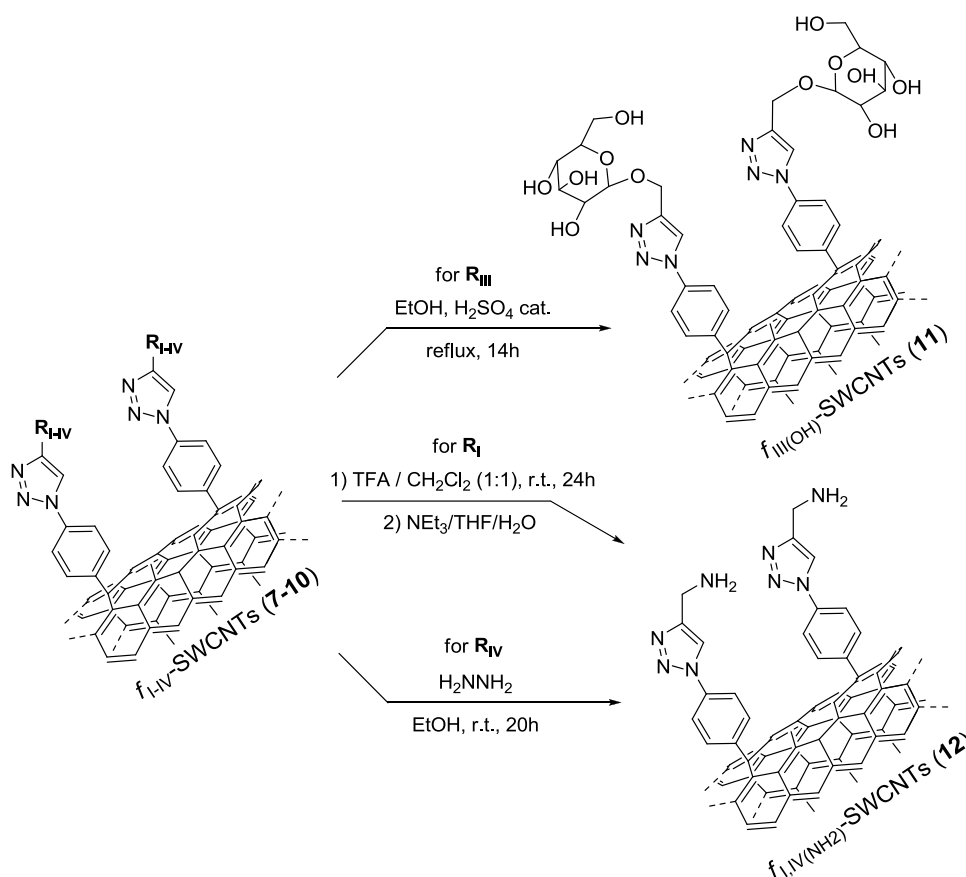
Our approach for the facile (post)functionalization of **2** is summarized in Scheme 2.2. According to that, a series of alkyne-terminated organic/organometallic compounds $\text{HC}\equiv\text{C}-\text{R}_{\text{I-IV}}$ (**3-6**) have been successfully coupled via CuAAC reaction using either $\text{CuSO}_4/\text{Na-ascorbate}$ ³⁵ or the organosoluble $(\text{EtO})_3\text{PCuI}$ as metal sources.^{36,37}



Scheme 2.2. CuAAC reaction between arylazido-decorated f_{N_3} -SWCNTs (**2**) and alkyne-terminated organic/organometallic compounds (**3-6**).

In a typical procedure, terminal alkynes **3-6** and the f_{N_3} -SWCNTs (**2**) are reacted in degassed DMF at 85°C for two days in the presence of $\text{CuSO}_4/\text{Na-ascorbate}$ (10 mol% Cu:alkyne ratio). Attempts to improve the functionalization degree by replacing $\text{CuSO}_4/\text{Na-ascorbate}$ with the organosoluble $[(\text{EtO})_3\text{PCuI}]$ in DMF resulted unsuccessful for almost all the scrutinized acetylene derivatives,³⁸ except for the ethynylferrocene **4** (Table 2.1, entry 2).

All functionalized samples (**7-10**) undergo successive sonication/centrifugation/washing cycles and filtration through a $0.2\text{-}\mu\text{m}$ -pore inorganic membrane (Anodisc™) before being dried under vacuum. Afterwards, compounds **7**, **9** and **10** undergo chemical deprotection to give either the hydroxy- (**11**) or the amine-decorated (**12**) carbon nanomaterials (Scheme 2.3).



Scheme 2.3. Preparation of hydroxy- (11) and primary amine-decorated (12) carbon nanostructures.

According to Scheme 2.3, a complete deacetylation of the β -D-glucopyranoside **9** is achieved by refluxing the CNT-tethered tetraacetyl-sugar in acidic (H_2SO_4 cat.) ethanol overnight to afford the glycoconjugate derivative $f_{III(OH)}$ -SWCNTs (11).³⁹ Acidic conditions have been also used to remove the Boc protecting group (TFA/ CH_2Cl_2), while ethanolic hydrazine is employed to cleave the orthogonal phthalimide framework; both procedures are used to generate primary amine groups at the CNT-sidewall [$f_{I,IV(NH_2)}$ -SWCNT (12)].²⁰

2.3.1 Characterization of the f_{I-IV} -SWCNTs samples (7-10) and their deprotected counterparts (11-12)

The functionalized carbon nanomaterials **7-10** and their derivatives $f_{III(OH)}$ - and $f_{I,IV(NH_2)}$ -SWCNTs (11-12) have been characterized by different chemical (*Kaiser test*, solubility tests, elemental analysis) spectroscopic/spectrometric (FT-IR, TGA-MS, Raman) and morphological (TEM) techniques. Evidence of the occurred Cu-mediated

azide-alkyne cycloaddition is primarily achieved by comparing the TGA profiles of the pristine SWCNTs with those of the functionalized materials.

In particular, **7** and **10** (Figure 2.5, left) show a weight loss of 9.9 and 15.7 % respectively, in the 40-700 °C temperature range (calculated as the weight difference between the TGA profiles of **7/10** and the pristine sample). As a result, one may conclude that the cycloaddition reactions proceed smoothly with both alkynes under Cu-mediated conditions (*ca.* 85 % and 95 % yield respectively, calculated referring to the –C₆H₄-N₃ loading on the *f*_{N₃}-SWCNTs sample – see also Table 2.1, entries 1 and 4). Similarly, **8** and **9** (Figure 2.5, right) show a weight loss of 9.7 and 27.3 % respectively, consistent with an azide/alkyne cycloaddition reaction taking place with *ca.* 78 and 95 % yield respectively (Table 2.1, entries 2 and 3).

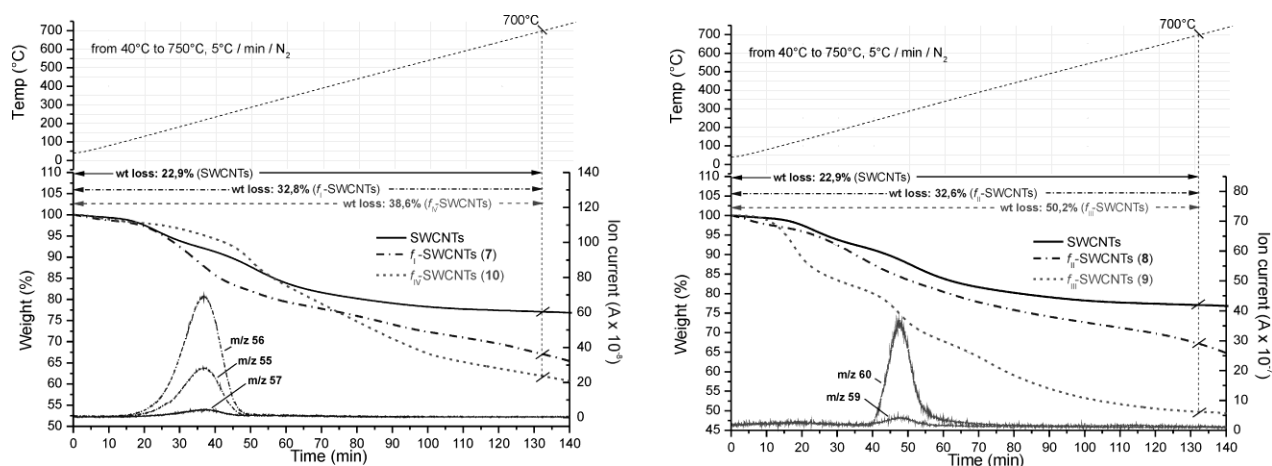


Figure 2.5. TGA profiles of pristine SWCNTs and *f*_{I-IV}-SWCNTs in the 40-700 °C temperature range. MS analysis of selected volatiles are reported for **7** (left) and **9** (right).

A mass analysis performed on the low molecular weight volatiles (from 25 amu to 125 amu) generated during the thermogravimetric tests is used to obtain further qualitative information on the composition of selected functionalized samples. In particular, the thermal decomposition and rearrangement (below 300 °C) of both *t*-butoxyl groups at the N-Boc protected cycloadduct **7** and the acetyl fragments at **9** are evidenced by isobutene (*m/z* 56 M⁺; *m/z* 55 M⁺ - 1; *m/z* 57 M⁺ + 1 – Figure 2.5, left) and acetic acid (*m/z* 60 M⁺; *m/z* 59 M⁺ - 1 – Figure 2.5, right) evolution; for both samples neither additional decomposition paths nor other significant mass fragmentations are observed in the same temperature range.

FT-IR spectra of the functionalized materials show characteristic broad bands between 1740 and 1630 cm^{-1} , unambiguously attributed to $\nu(\text{C}=\text{O})$ vibrational modes of carbamate, acetyl and phthalimide moieties in **7**, **9** and **10**, respectively; in addition, the almost complete suppression of the intense $\nu(\text{N}_3)$ asymmetric stretching (close to 2100 cm^{-1}) for all *f*-derivatives (**7-10**) is an additional proof of evidence of the occurred Cu-mediated azide-alkyne cycloaddition (Figure 2.6).

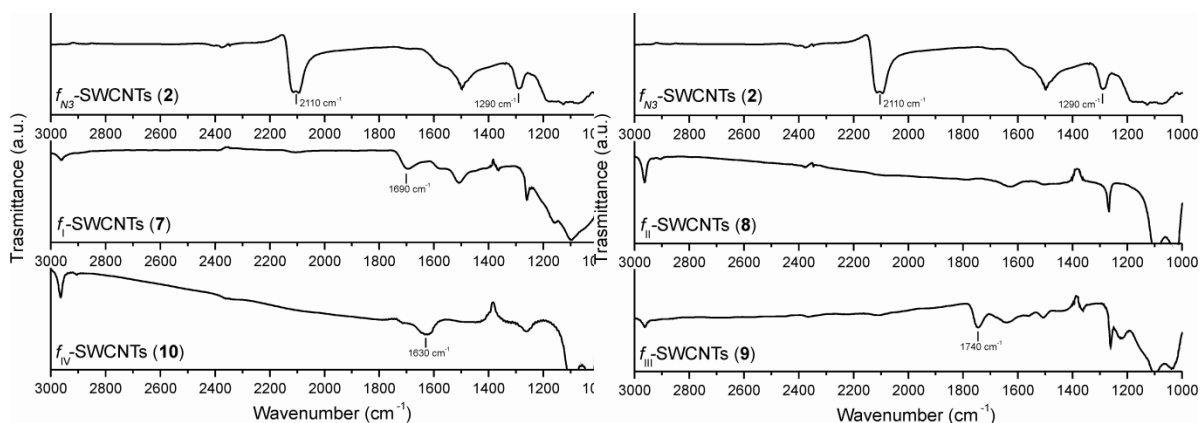


Figure 2.6. FT-IR spectra of: (left) f_{N_3} -SWCNTs (**2**), f_{I} -SWCNTs (**7**), and f_{IV} -SWCNTs (**10**); (right) f_{N_3} -SWCNTs (**2**), f_{II} -SWCNTs (**8**), and f_{III} -SWCNTs (**9**).

Raman spectra recorded on the (post)functionalized samples **7-10** do not show any relevant modification of the $I_{\text{D}}/I_{\text{G}}$ ratio measured for **2**. This is consistent with the absence of additional perturbations at the CNT sp^2 network after the post-derivatization of the tethered phenylazido moieties under CuAAC conditions.

Primary amine-decorated SWCNTs (**12**) are prepared by successive Boc and Pht deprotection at **7** and **10**, under acidic ($\text{CF}_3\text{COOH}/\text{CH}_2\text{Cl}_2$, r.t.) and ethanolic hydrazine (H_2NNH_2 , EtOH, r.t.) environment, respectively (Scheme 2.3). The primary amine loading on both samples are determined using the colorimetric *Kaiser* test and the measured values are reported in Table 2.1, entries 5 and 7. The TGA profile of the deprotected $f_{\text{I}(\text{NH}_2)}$ sample together with the complete disappearance of the typical isobutene evolution in the 100-300 $^\circ\text{C}$ temperature range (Figure 2.7, left) are consistent with a complete Boc removal under acidic conditions. According to that, a complete suppression of the $\nu(\text{C}=\text{O})$ stretching mode is also evidenced on the FT-IR spectrum of the deprotected material (Figure 2.8, left). On the contrary, the TGA profile of $f_{\text{IV}(\text{NH}_2)}$ sample as well as its FT-IR spectrum (a broad band around 1630 cm^{-1} is still present

after the hydrazine treatment) are indicative of a partial deprotection of the Pht moiety (Figures 2.7 and 2.8, right).

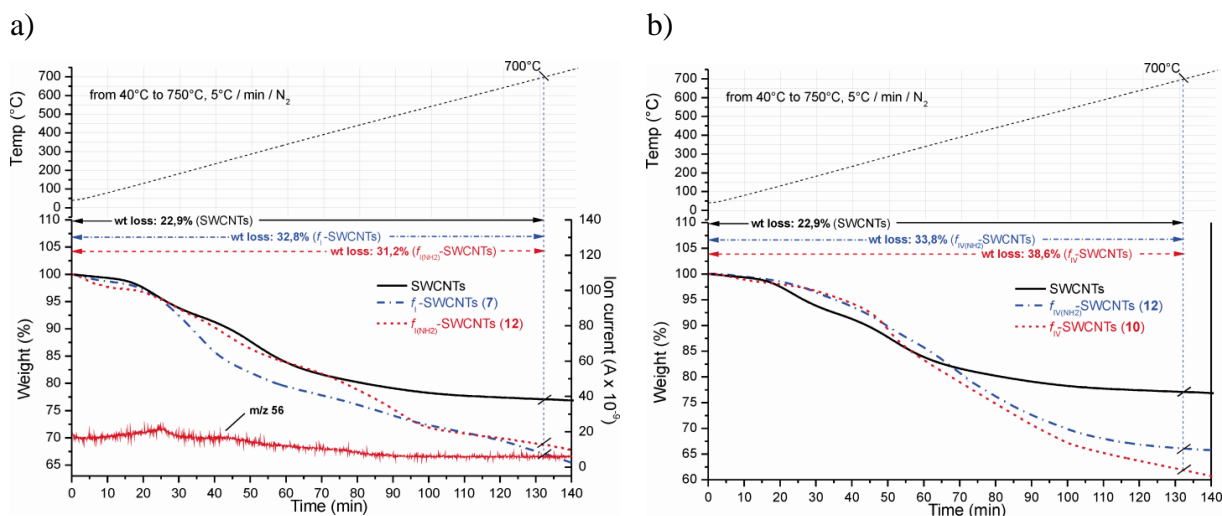


Figure 2.7. TGA profiles of a) f_{I} -SWCNTs (**7**) and b) f_{IV} -SWCNTs (**10**) together with their Boc/Pht deprotected counterparts (**12**). Mass analysis of volatiles [isobutene (m/z 56 M^+)] of the Boc-deprotected sample $f_{\text{I}(\text{NH}_2)}$ SWCNT (**12**) was also reported to highlight the protecting group removal.

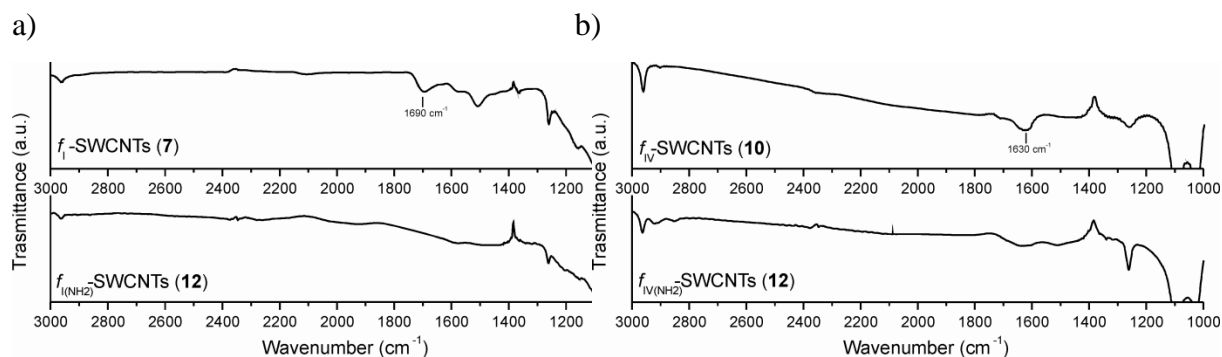


Figure 2.8. FT-IR of a) f_{I} -SWCNTs (**7**) and b) f_{IV} -SWCNTs (**10**) and their (Boc/Pht)-deprotected counterparts (**12**).

No significant changes in the final material characterization (FT-IR, TGA profiles) are observed when harsher deprotection conditions (40 °C, 96 h) are employed. As a support of this (qualitative) information, the more difficult Phthalimide removal from **10** is evidenced by the lower free-amine loading measured by the ninhydrin (*Kaiser*) test on the $f_{\text{IV}(\text{NH}_2)}$ sample (Table 2.1, entry 7). For both the amino-decorated samples ($f_{\text{I}(\text{NH}_2)}$ and $f_{\text{IV}(\text{NH}_2)}$ - **12**), the *Kaiser* test shows a lower functionalization loading compared to that estimated from the thermogravimetric profiles. Notably, the relatively

high difference in the free-amine loading measured between the $f_{\text{I}(\text{NH}_2)}$ and $f_{\text{IV}(\text{NH}_2)}$ samples (Table 2.1, entry 5 vs. 7) is likely due to the incomplete deprotection of **10** under alcoholic hydrazine conditions; other reasons, including detrimental π - π interactions between the CNT sidewalls and the protecting Phtalimide moieties,²⁰ hampering the regular efficiency of the CuAAC protocol, can be reasonably ruled out. As a matter of fact, both *N*-protected propargylamine (**3** and **6**) undergo highly efficient cycloadditions under Cu-mediated conditions (Table 2.1, entries 1 and 4).

Table 2.1. Loading capacity of *f*-SWCNTs

Entry	<i>f</i> -material	“Clicked” molecule loading (mmol/g) ^{a,d} [%] ^{b,d}	Measured loading (mmol/g) [functional group]
1	f_{I} -SWCNT (7)	(0.49) [85]	-
2	f_{II} -SWCNT (8)	(0.45) [78]	0.38 ^{c,d} ; 049 ^{c,e} [ferrocene]
3	f_{III} -SWCNT (9)	(0.55) [95]	-
4	f_{IV} -SWCNT (10)	(0.55) [95]	-
5	$f_{\text{I}(\text{NH}_2)}$ -SWCNT (12)	(0.49) [>99]	0.34 ^{d,f} [NH ₂]
6	$f_{\text{III}(\text{OH})}$ -SWCNT (11)	(0.55) [>99]	-
7	$f_{\text{IV}(\text{NH}_2)}$ -SWCNT (12)	n.d.	0.12 ^{d,f} [NH ₂]

^aAs calculated from the TGA profiles, assuming a phenylazido loading [$-\text{C}_6\text{H}_4\text{N}_3$] of 0.58 mmol·g⁻¹ of f_{N_3} -SWCNTs (**2**). ^bmol% of reacted phenylazido groups, as calculated from the TGA weight losses. ^cAs calculated from cyclic voltammetric data. ^dCuSO₄/Na-ascorbate as metal source. ^e(EtO)₃PCuI as metal source. ^fAs calculated from the *Kaiser* test.

Cyclic voltammetry (CV) is used to quantify the ferrocene loading on sample **8**. Figure 2.9 shows the CV data obtained from **8** as measured in a 1 M aqueous perchloric acid solution. Well-defined redox peaks (centered at $E^0 = +0.37$ V – forward scan; $E^0 = +0.32$ V – backward scan vs. Ag/AgCl/KCl(sat.)) are observed.

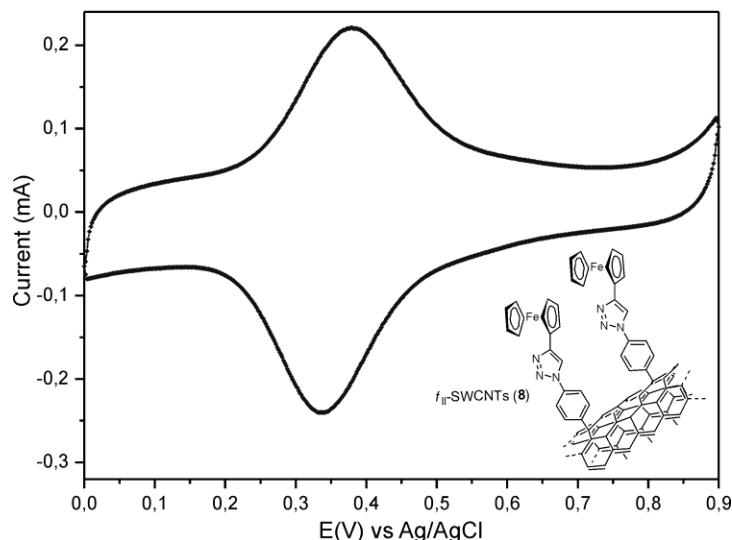


Figure 2.9. Cyclic voltammetry of **8** recorded at 100 mV/s as scan rate.

The peak current is found to vary linearly with the scan rate (from 20 mV/s to 400 mV/s), that is consistent with a real ferrocene surface grafting.⁴⁰ Anodic and cathodic peaks (160 mV full-width measurements at half maximum; +76 %) larger than the ideal Nernstian width⁴¹ suggest possible interactions between the ferrocene units.⁴² The charge measured under the reduction and oxidation peaks (as obtained from samples prepared at different concentrations of **8**) is consistent with a 2.1 wt. % iron content (see section 2.5); these data translate into 0.38 mmol of grafted ethynylferrocene (**4**) per gram of f_{II} -SWCNT derivative (**8**), in fairly good accord with the TGA outcomes (Table 2.1, entry 2).

Classical deacetylation conditions are finally used to prepare hydroxyl-decorated SWCNTs (**11**) from the polyacetylated material **9** and the reaction course is investigated by TGA-MS and FT-IR spectroscopy. While only a partial deacetylation of **9** is observed by heating the sugar-decorated sample **9** in acidic EtOH (EtOH, HCl cat.), a complete acetyl deprotection is obtained under harsher reaction conditions (refluxing EtOH, H₂SO₄ cat.). TGA-MS analysis and FT-IR spectroscopy of **11** are consistent with the occurrence of a complete transesterification and the subsequent generation of the hydroxyl-decorated nanomaterials (Scheme 2.3 and Figure 2.10).

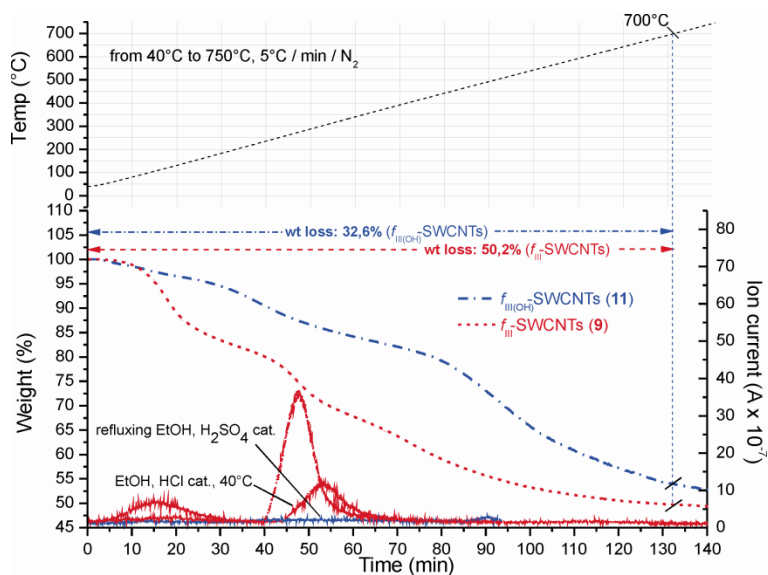


Figure 2.10. TGA profiles of f_{III} -SWCNTs (**9**) and their $f_{\text{III(OH)}}$ (**11**) counterpart. Mass analysis of volatiles [acetic acid (m/z 60 M^+)] was also used to follow the deacetylation process till completeness, under different reaction conditions.

Most importantly, **11** shows enhanced solubility in protic polar solvents (EtOH) compared to precursor **9** (Figure 2.11); stable inks (up to 1.5 mg/mL of EtOH) with no apparent CNTs rebundling for days are conveniently prepared upon simple sample sonication (Figure 2.11a). A direct comparison of TEM images recorded on **9** and **11** (from EtOH solution/suspension) clearly shows a high deaggregation degree for the latter sample (Figure 2.11b). No appreciable changes of either tube diameters (from 3 to 8 nm as measured in the smaller CNT bundles) or tube lengths (from 50 nm to several micrometers) are observed throughout the whole scanned area for both samples, before and after deacetylation.

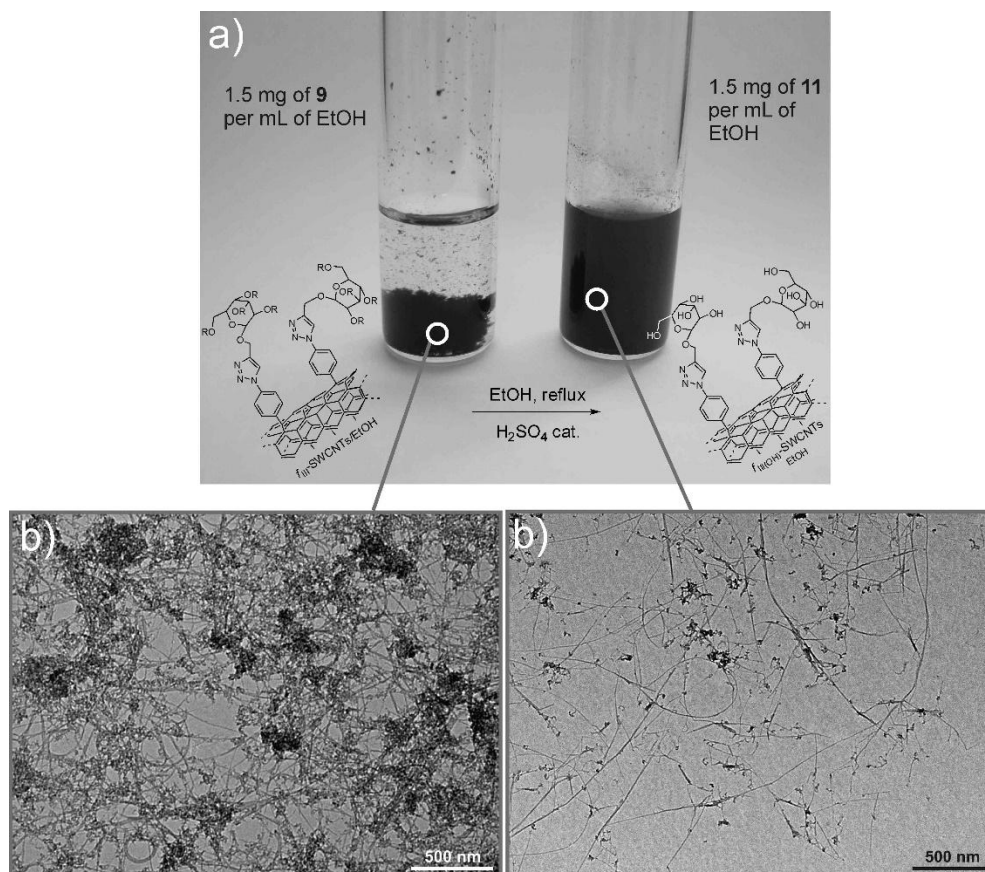


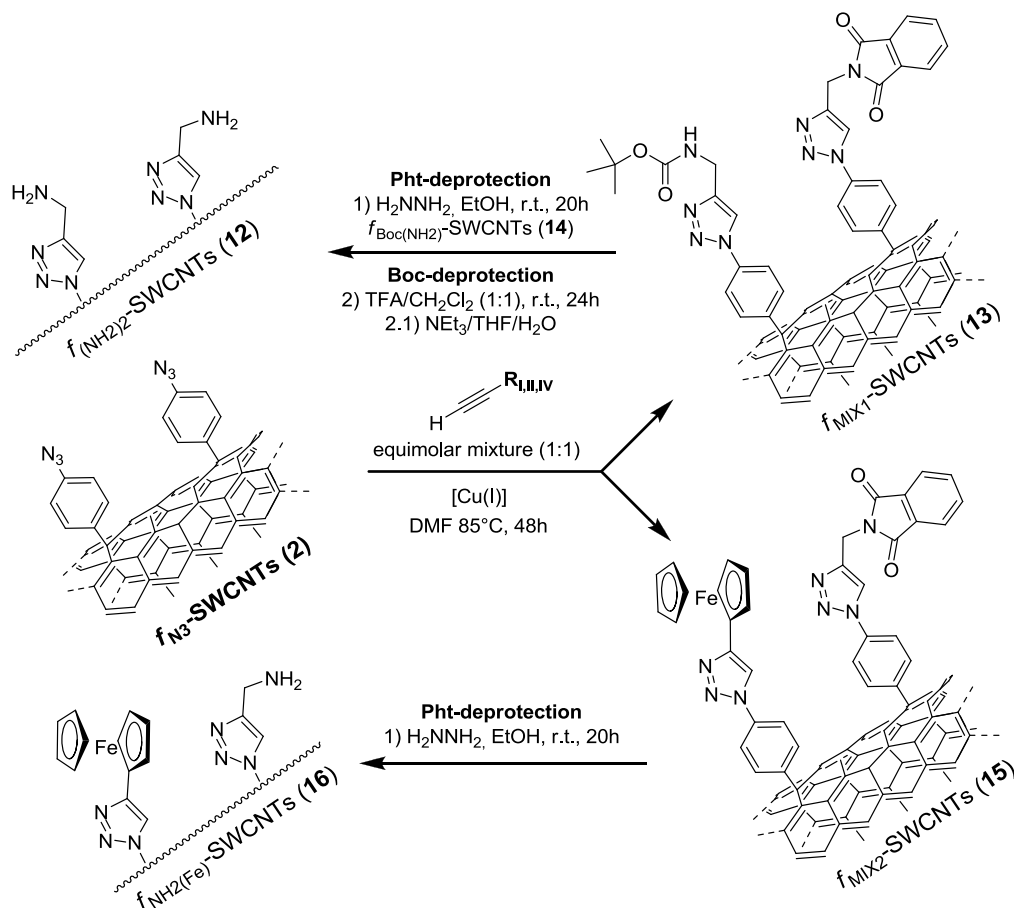
Figure 2.11. a) Solubility of f_{III} -SWCNTs (**9**) vs. $f_{III(OH)}$ -SWCNTs (**11**) in EtOH and related b) TEM micrographs.

2.3.2 Hetero-decoration of SWCNTs

Our approach to the CNT decoration via CuAAC chemistry has also been applied to mixtures of acetylene end-capped molecules, thus imparting multimodality to the final functionalized nanomaterials. Hetero-decorated SWCNTs are prepared by reaction of the arylazido f_{N3} -SWCNTs (**2**) in the presence of equimolar amounts of two selected acetylenes (Scheme 2.4). In all the hetero-functionalization experiments the total amount (mmol) of the acetylenes in the initial mixture was kept equal to that used in the homo-decoration experiments.⁴³ Acetylene mixtures have been selected in order to bring on the SWCNT board either the same functional groups but masked with orthogonally cleavable protecting groups, or different functional groups distinguishable on the basis of complementary analytical/spectroscopic techniques.

In a typical experiment, an equimolar mixture of **3** and **6** are reacted with the arylazido f_{N3} -SWCNTs (**2**) under CuAAC conditions (Scheme 2.4).⁴³ Successive and multiple sonication/centrifugation/washing cycles are accomplished on the hetero-

functionalized material **13** (f_{MIX1} -SWCNTs), to remove the unreacted alkynes and physisorbed reagents. The f_{MIX2} -SWCNTs material **15** is prepared similarly by reacting **2** with an equimolar amount of alkynes **4** and **6** under Cu-mediated conditions, followed by identical work-up procedures. Filtration/washing through a 0.2- μm -pore inorganic membrane (AnodiscTM) is finally used to recover both mix-decorated samples; the solids are finally dried under vacuum up to constant weight and stored in air without any apparent decomposition per months.



Scheme 2.4. Hetero-decoration of SWCNTs using equimolar mixtures of terminal alkynes and subsequent removal of Boc and Pht-protecting groups.

According to the “deprotection” procedures described above for the homo-decorated samples (**7**, **9** and **10**), all mixed functionalized materials (**13** and **15**) undergo sequential cleavage protocols (Boc and Pht removal) to give the free-amine decorated samples **12**, **14** and **16**; UV-vis measurements (*Kaiser* test) and cyclic voltammetry (CV) are finally used to calculate the achieved functionalization loading. TGA and FT-IR spectra recorded on both the mixed decorated samples and their deprotected counterparts were used for qualitative investigation only. TGA spectra are reported on Figure 2.12.

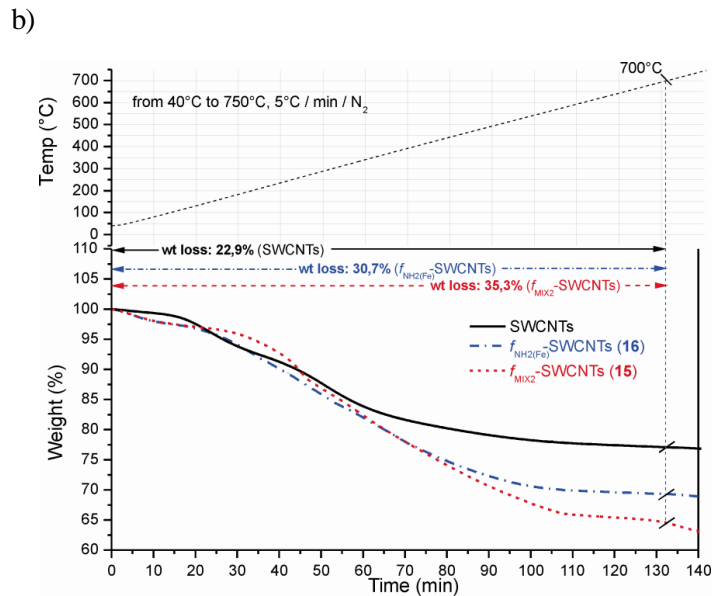
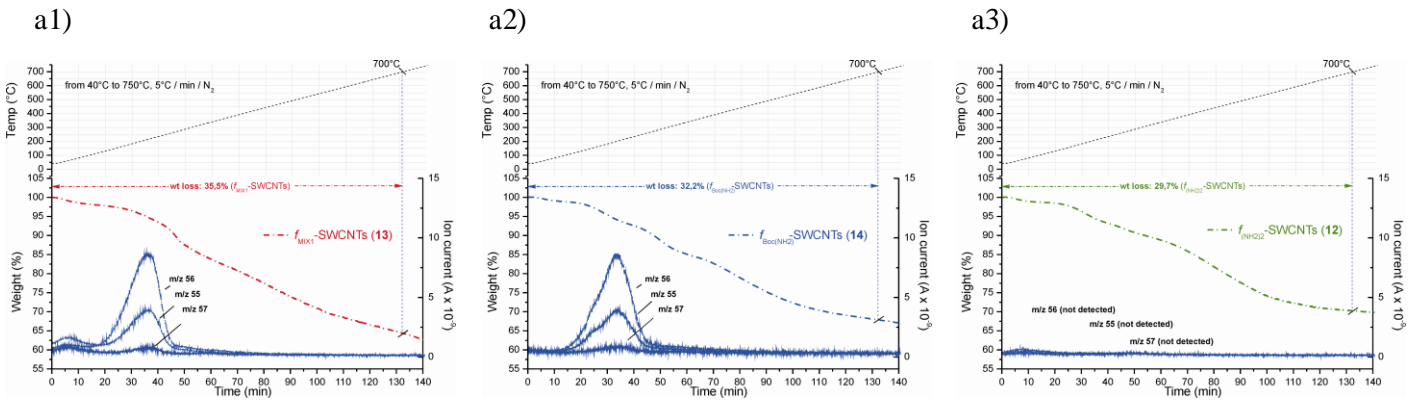
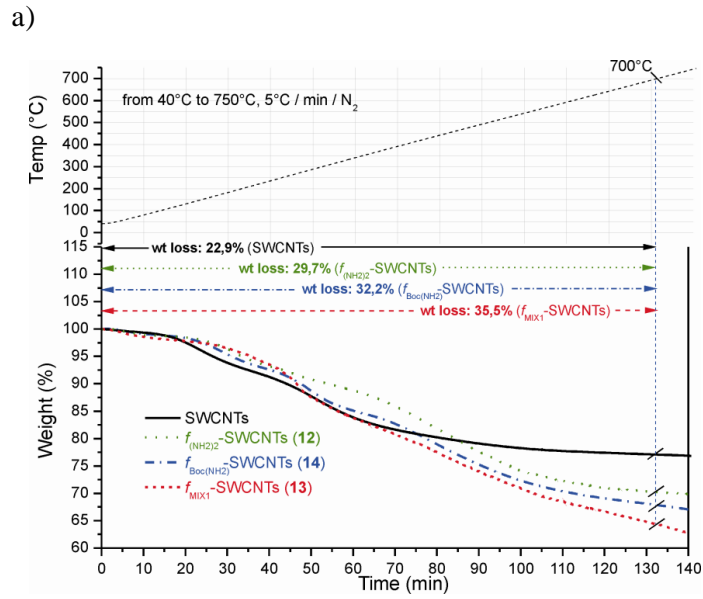


Figure 2.12. TGA profiles of a) f_{MIX1} (13) and b) f_{MIX2} -SWCNTs (15) compared to their (mono/bis)deprotected counterparts (12, 14 and 16). Figures a1)-a3) reports the mass analysis of volatiles [isobutene (m/z 56 M^+ ; m/z 55 $M^+ - 1$ and m/z 57 $M^+ + 1$) as observed for f_{MIX1} (13), $f_{Boc(NH_2)}$ (14) and $f_{(NH_2)_2}$ (12) samples, respectively.

Sample **13** is sequentially treated under “basic” (ethanolic hydrazine) and acid conditions in order to orthogonally remove both amino-protecting groups. Firstly, the Pht group is cleaved upon treatment with hydrazine in ethanol at room temperature to give the intermediate **14**; subsequently, the latter material undergoes classical acidic conditions to remove the Boc framework, affording **12**. For each deprotection step, the samples are submitted to work-up procedures identical to those described above for the relative homo-decorated/deprotected SWCNTs. The mono- and bis-deprotected samples from **13** ($f_{\text{Boc}(\text{NH}_2)}$ -SWCNTs, **14** and $f_{(\text{NH}_2)_2}$ -SWCNTs, **12**) are spectroscopically characterized with respect to their amine-free loading, using the colorimetric *Kaiser* test; the respective $-\text{NH}_2$ contents are summarize in Table 2.2 (entry 1).

Table 2.2. Loading capacity of f_{MIX1} - and f_{MIX2} SWCNTs^a

Entry	<i>f</i> -material	Pht ^b	Boc ^b	Ferrocene	Total
		NH ₂ loading		loading	loading ^{c,d}
		(mmol/g) ^c		(mmol/g) ^c	(mmol/g)
1	f_{MIX1} -SWCNTs	0.09	0.16 ^e	-	0.25
2	f_{MIX2} -SWCNTs	0.08	-	0.23	0.31

^aPrepared using CuSO₄ (10 mol%)/Na-ascorbate as Cu(I) source. ^bProtecting group removed ^cAs spectroscopically determined from the colorimetric *Kaiser* test. ^dAs calculated from cyclic voltammetry. ^e Calculated as loading difference between the total loading and the NH₂ loading measured by the only Pht deprotection.

Cyclic voltammetry and UV-vis spectroscopy are finally used to determine the functionalization loading on the f_{MIX2} -SWCNTs (**15**) sample.⁴⁴ The functionalization loading of **15**, as measured spectroscopically and electrochemically on the monodeprotected material ($f_{\text{NH}_2(\text{Fe})}$ -SWCNTs) **16**, is summarized in Table 2.2, entry 2. Similarly to **8**, the CV profile recorded for **16** shows larger anodic and cathodic peaks (180 mV; + 90 % compared to the ideal Nernstian width⁴¹) and a peak current varying linearly with the scan rate (from 20 mV/s to 400 mV/s). The charge measured under the reduction and oxidation peaks (as obtained from samples prepared at different concentrations of **16**) is consistent with a 1.3 wt. % iron content (see section 2.5), this accounting for *ca.* 0.23 mmol of grafted ferrocene per gram of **16** (Figure 2.13).

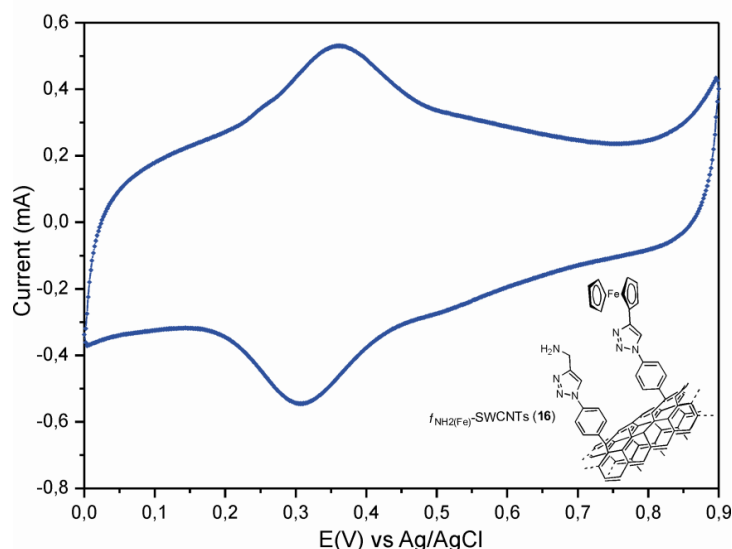


Figure 2.13. CV curve of the $f_{\text{NH}_2(\text{Fe})}$ -SWCNTs (**16**) sample.

As one may infer from Table 2.2, equimolar alkyne mixtures result (overall) into slightly lower functionalization degrees (compared to those calculated for the homo-decorated samples).⁴³ In spite of that, the “free-amino” and “ferrocene” functional loading is found to decrease almost linearly while reducing the molar amount of the respective alkynes. This result is of crucial importance, because it allows for a convenient tuning of the functional groups at the SWCNT sidewalls just varying the molar ratio of each alkyne in the reactive mixture.

2.4 Conclusions

In this chapter we have described an original approach to the convenient and facile homo- and hetero-decoration of single-walled carbon nanotubes. Our methodology relies on flexible and versatile “CNT platforms” chemoselectively decorated with aryl-azido pendant arms. Joining the latter functionalities with differently substituted terminal acetylenes (or mixture thereof), under classical CuAAC conditions, allowed for a single-step homo- and hetero-functionalization/derivatization of the CNT sidewalls. Azidated CNTs represent safe and stable substrates (high C/N ratio) for the CNT sidewall (multi)decoration, avoiding those drawbacks resulting from the application of different and subsequent organic functionalization protocols. Indeed, they allow for operating mildly under the popular “click chemistry” conditions with a variety of

reactive alkynes. Additionally, the bio-orthogonal character of the click reaction makes this approach highly desirable for conjugating CNTs and biomolecules.⁴⁵

Accordingly, examples of homo- and hetero-functionalization of SWCNTs have been presented; model acetylene reagents, featured by either the same functional groups but masked with orthogonally cleavable protecting groups or by easily distinguishable moieties (on the basis of complementary analytical/spectroscopic techniques), were employed. Free amino- and alcohol decorated SWCNTs have been prepared by reacting the aryl-azido functionalized CNTs with N-protected propargylamine and tetra-O-acetyl-beta-D-glucopyranoside acetylene derivatives, respectively; protecting groups removal (Boc, Pht or Ac) has been conveniently achieved under standard deprotection conditions. The functional group loading was estimated according to the TGA-MS profile and elemental analysis; when possible, they were measured more precisely using either UV-vis spectroscopy (*Kaiser* test for primary amine groups) or electrochemical titrations (CVs) for the functionalized materials containing redox active groups.

All the functionalized materials and intermediates were characterized according to their most relevant properties using TEM microscopy, thermogravimetric analysis coupled with MS analysis of volatiles, elemental analysis, cyclic voltammetry, Raman and UV-vis spectroscopy.

Finally, the established applicability of the aryldiazonium chemistry (our first step in the production of f_{N_3} -SWCNT “platforms”) to the arylation to different types of CNTs^{20a,27} [in terms of diameter, number of walls (SWCNTs, MWCNTs) and length (pristine and shortened CNTs)] and carbon nanostructures, widens the applicability range of our protocol.

2.5 Experimental Section

2.5.1 General Considerations

All manipulations were carried out under dry nitrogen atmosphere using standard Schlenk-type techniques. Nitrogen ($\geq 99.999\%$ from Rivoira) was dried through a CaCl_2 column and deoxygenated with an oxisorb cartridge from Messer Griesheim prior to use. Dry DMF (dimethylformamide) and ODCB (orthodichlorobenzene) were prepared according to the literature procedures⁴⁶ and stored over 4 Å molecular sieves under a nitrogen atmosphere. Acetonitrile was obtained by means of an MBraun Solvent

Purification System. Pristine SWCNTs were purchased from Nanocyl S. A. (Nanocyl™ 1100, average diameter and length: 2 nm and several nm, respectively). The 4-azidoaniline **1** was prepared according to modified literature procedures⁴⁷ (half gram *per* single batch) and stored under N₂ atmosphere at 5 °C without decomposition. N-Boc-propargylamine, Ethynylferrocene, 2-Propynyl-tetra-O-acetyl-beta-D-glucopyranoside and N-Propargylphthalimide were purchased from commercial suppliers. The phenylazide (C₆H₅)N₃ for “model” homogeneous CuAAC screening tests (see section 2.5.4), was prepared according to literature procedures.⁴⁸ Unless otherwise stated, all other chemicals/solvents were obtained from commercial suppliers and used as received without further purification.

Samples sonication was carried out using an Elma S15 Elmasonic sonicator bath (37 kHz) cooling the samples in a water/ice mixture throughout the sample treatment. CNT filtration was accomplished using inorganic Anopore™ membranes/filters – Anodisc™ 47, Whatman with 0.2 µm pore size.

All measurements carried out on pristine SWCNTs and functionalized materials (f-SWCNTs) were conducted on samples which underwent identical washing/sonication/filtration work-up procedures.

2.5.2 Material Characterization and Analyses Conditions

Thermogravimetric analysis (TGA) was performed under N₂ atmosphere (50 mL/min) on an EXSTAR Thermo Gravimetric Analyzer (TG/DTA) Seiko 6200 coupled with a ThermoStar™ GSD 301 T (TGA-MS) for MS gas analysis of volatiles.

Transmission Electron Microscopy (TEM) analysis of modified and unmodified CNTs was performed by a Philips CM12 microscope operating at 120 kV, on samples prepared by drop casting previously sonicated suspensions (EtOH) over copper grids coated with a Formvar film (FF200-Cu - Formvar film only). TEM images were recorded with a CCD camera (Gatan 791).

Raman spectra were measured using the 647.1 nm emission of a Kr ion laser source, accordingly to the preferential reactivity of aryldiazonium derivatives with metallic SWCNTs.^{34,49} The scattered radiation was collected in a back scattering geometry, dispersed using the single stage configuration of a triple Raman spectrometer (Trivista TR555) equipped with a 900 grooves/mm grating and recorded by a liquid nitrogen cooled CCD detector. The beam profile was cleaned by a spatial filter and Rayleigh

scattering was filtered out using Notch filters. The spectral resolution was 1.7 cm^{-1} . The incident laser power on the sample was lower than 0.4 mW and any damage of the sample due to the laser was carefully checked and excluded. The Raman spectra were collected in order to detect the presence and strength of the G and D modes.³¹ The G mode, which is located at around 1590 cm^{-1} , is characteristic of the sp^2 in-plane bond-stretching motion of pairs of carbon atoms in graphite-like structures. The D mode, which is forbidden in perfect graphite, is found at around 1320 cm^{-1} and becomes active only in the presence of disorder.³¹ All recorded curves were fitted using Lorentzian line-shapes and the intensity ratios (namely I_D/I_G) were calculated from the fitted areas of the D and G bands.^{31,50,51} According to the literature,⁵¹ D- and G-peak intensities were used for the calculation of the I_D/I_G ratios.

FT-IR spectroscopy was performed on a Perkin-Elmer Spectrum BX FT-IR spectrophotometer and all CNT samples were prepared by mixing spectroscopic grade KBr with pristine SWCNTs or *f*-SWCNTs (2-3 wt. %) and analyzed in the $400\text{-}4000\text{ cm}^{-1}$ range (600-800 scans) with a resolution of 1 cm^{-1} . For all reported FT-IR spectra, SWCNTs (2-3 wt. %)/KBr were used as background and directly subtracted from the spectra of the functionalized (*f*-SWCNTs) samples.

NMR spectra of all organic products and intermediates were obtained on either a Bruker Avance 300 MHz instrument or a Bruker Avance DRX-400 spectrometer. Chemical shifts are reported in ppm (δ) relative to TMS and referenced to the chemical shifts of residual solvent resonances.

Elemental analyses were performed using a Thermo FlashEA 1112 Series CHNS-O elemental analyzer with an accepted tolerance of ± 0.4 units.

Cyclic voltammetry (CV) experiments were conducted on a Princeton 2273A potentiostat/galvanostat, using a three-electrode arrangement with a saturated Ag/AgCl/KCl reference electrode and a platinum wire as counter electrode.

UV-vis measurements were performed on a CARY VARIAN 4000 Spectrometer.

2.5.3 Synthesis of 4-azidoaniline (1)

4-bromoaniline (0.5 g, 2.91 mmol), NaN_3 (0.378 g, 5.82 mmol), Na-ascorbate (0.03 g, 0.15 mmol) and CuI (0.055 g, 0.29 mmol) were put in sequence into a two-necked 25 mL flask equipped with a magnetic stir bar and a reflux condenser. The mixture was then dissolved in 5 mL of a EtOH:H₂O = 7:3 mixture and degassed through several

freeze-pump thaw cycles. N,N-dimethylethylenediamine (0.048 mL, 0.44 mmol) was added in one portion and the mixture was stirred for 3 h at 80 °C. Afterwards, the reaction was cooled at room temperature and diluted with water (20 mL). The mixture was extracted with CHCl₃ (5 x 20 mL) and the collected organic phases were washed with brine and then water before being dried over Na₂SO₄. The organic solvent was removed under vacuum and the resulting crude product was purified by flash chromatography [silica gel (eluent: CH₂Cl₂)] to give 0.288 g of pure **1** in 74 % yield. ¹H NMR (400 MHz, CD₂Cl₂) δ (ppm): 3.73 (bs, 2H), 6.69-6.71 (2H), 6.85-6.87 (2H).

2.5.4 General procedure for the “homogeneous” CuAAC “click” reaction between the model phenylazide and the alkynes 3-6

To a solution of the model phenylazide (0.05 g, 0.42 mmol) in dry and degassed DMF (2 mL), the proper alkyne (0.5 mmol), CuSO₄ (0.003 g, 0.02 mmol) and Na-ascorbate (0.008 g, 0.04 mmol) were added in sequence. The reaction mixture was stirred at room temperature overnight and then quenched with water. The reaction mixture was extracted with Et₂O (3 x 15 mL) and the collected organic phases washed twice with water (2 x 30 mL). The organic layer was then dried with Na₂SO₄ and concentrated at reduced pressure. The crude material was purified by flash chromatography over silica gel (eluent: petroleum ether/Et₂O = 1/1 for cycloadducts with **3** and **4**; EtOAc/petroleum ether = 80/20 for cycloadducts with **5** and **6**) to give the pure product. Identical conditions were used with the organosoluble P(OEt)₃CuI (5 mol% respect to the reactive alkyne) instead of the CuSO₄(5 mol%)/Na-ascorbate system. No appreciable differences were observed in the isolated yields whatever copper(I) source used under homogeneous conditions. **Cycloadduct with alkyne 3** (C₁₄H₁₈N₄O₂): yield 80 %. ¹H NMR (400 MHz, CDCl₃) δ (ppm): 1.42 (s, 9H), 4.46 (s, 2H), 5.36 (bs, 1H), 7.39-7.42 (1H), 7.47-7.51 (2H), 7.68-7.70 (2H), 8.00 (1H). ¹³C{¹H} NMR (100 MHz, CDCl₃) δ (ppm): 28.5, 36.1, 79.9, 120.3, 128.8, 129.4, 129.9, 137.2, 156.1; **Cycloadduct with alkyne 4** (C₁₈H₁₅N₃Fe): yield 82 %. ¹H NMR (400 MHz, CDCl₃) δ (ppm): 4.12 (s, 5H), 4.34 (2H), 4.79 (2H), 7.42-7.46 (1H), 7.52-7.56 (2H), 7.77-7.79 (2H), 7.89 (1H); ¹³C{¹H} NMR (100 MHz, CDCl₃) δ (ppm): 66.7, 68.8, 69.6, 74.9, 116.5, 120.3, 128.5, 129.7, 137.1, 147.6; **Cycloadduct with alkyne 5** (C₂₃H₂₇N₃O₁₀): yield 87 %. ¹H NMR (300 MHz, CD₂Cl₂) δ (ppm): 1.97 (s, 6H), 2.01 (s, 3H), 2.06 (s, 3H), 3.78 (ddd, ³J = 9.9 Hz, ³J = 4.8 Hz, ³J = 2.4 Hz, 1H), 4.11-4.31 (2H), 4.75 (d, ³J = 8.4 Hz, 1H), 4.85-4.89

(1H), 4.95-5.01 (2H), 5.08 (t, $^3J = 8.4$ Hz, 1H), 5.21 (t, $^3J = 9.9$ Hz, 1H), 7.44-7.49 (1H), 7.53-7.58 (2H), 7.73-7.76 (2H), 8.02 (1H). $^{13}\text{C}\{^1\text{H}\}$ NMR (75 MHz, CD_2Cl_2) δ (ppm): 20.4, 20.4, 20.4, 20.5, 61.8, 62.8, 68.3, 71.2, 72.0, 72.6, 100.0, 120.5, 121.2, 128.8, 129.8, 137.1, 144.8, 169.3, 169.4, 169.9, 170.5; **Cycloadduct with alkyne 6** ($\text{C}_{17}\text{H}_{12}\text{N}_4\text{O}_2$): yield 86 %. ^1H NMR (400 MHz, CD_2Cl_2) δ (ppm): 5.07 (s, 2H), 7.46-7.50 (1H), 7.54-7.58 (2H), 7.73-7.74 (2H), 7.77-7.80 (2H), 7.89-7.91 (2H), 8.10 (1H); $^{13}\text{C}\{^1\text{H}\}$ NMR (100 MHz, CD_2Cl_2) δ (ppm): 33.0, 120.5, 121.3, 123.3, 123.4, 128.7, 129.7, 132.1, 134.2, 134.3, 187.7.

2.5.5 Functionalization of SWCNTs with 4-azidoaniline (1)

SWCNTs (100 mg) were weighed into a two-necked 250 mL flask and suspended in 80 mL of dry and degassed ODCB. The suspension was sonicated for 15 min and then treated with a degassed acetonitrile solution (40 mL) of the 4-azidoaniline **1** (200 mg). Afterwards, isopentyl nitrite (0.30 mL, 2.3 mmol) was added in one portion and the suspension was further sonicated for 10 min. The mixture was maintained under stirring in nitrogen atmosphere and heated at 60 °C for 14 hours, then cooled to room temperature and diluted with ethylacetate (50 mL). The mixture was then sonicated for 10 minutes and centrifuged in order to recover the solid residue. The latter was then washed three times with dichloromethane, each time sonicated for 10 min and separated from the supernatant by centrifugation. The solid residue was suspended in dichloromethane, sonicated for 15 min and filtered through a 0.2 μm -pore filter. The collected material (f_{N_3} -SWCNTs - **2**) was then dried under vacuum to constant weight. The azido-decorated SWCNTs were then stored under nitrogen atmosphere at room temperature.

2.5.6 General procedure for the CuAAC reaction on azido-decorated f_{N_3} -SWCNTs **2** – homo and hetero-functionalization

In a typical procedure, f_{N_3} -SWCNTs - **2** (20 mg) were weighed into a two-necked 25 mL flask and suspended in 3 mL of dry and degassed DMF. The suspension was sonicated for 15 min and then treated with proper alkyne(s) (0.17 mmol), CuSO_4 (3 mg, 0.017 mmol) and Na-ascorbate (7 mg, 0.034 mmol). The mixture was then sonicated for 10 min and heated at 85 °C for 48 h, under stirring and under nitrogen atmosphere. Additional sonication cycles (2 x 10 min) were done on the mixture after 8 and 16

hours. The final mixture underwent an identical work-up procedure to that described above for **2**. The recovered solid was dried under vacuum at 50 °C to constant weight. All *f*-SWCNT samples were stored on air at room temperature. The same procedure was followed also for the hetero-derivatization protocol except for using equimolar mixture (0.085 mmol + 0.085 mmol) of the two reactive alkynes.

CuAAC experiments with the organosoluble metal source P(OEt)₃CuI (10 mol% respect to the reactive alkyne) instead of the CuSO₄(10 mol%)/Na-ascorbate system, were accomplished similarly to the procedure described above.

2.5.7 Removal of the Boc-protecting group from either homo- or hetero-decorated *f*-SWCNTs

In a typical procedure, *f*-SWCNTs (20 mg) were suspended in 5 mL of a TFA/CH₂Cl₂ (1:1) solution and sonicated for 15 min. The mixture was maintained under stirring at room temperature for 24 h till completeness, diluted with ethylacetate, sonicated for 10 min and centrifugated to remove the supernatant. The collected solid was finally suspended in a Et₃N/THF/H₂O 1:20:2 mixture (20 mL), sonicated for 10 min and maintained under stirring overnight before being filtered through a 0.2 μm-pore filter and washed twice with EtOH (2 x 20 mL) and CH₂Cl₂ (2 x 20 mL). The resulting solid sample underwent an identical work-up procedure to that described above for the *f*_{N3}-SWCNTs. The recovered material was dried under vacuum at 50 °C to constant weight. All deprotected samples were stored on air at room temperature. Amine loadings were measured spectroscopically (UV-vis) using the colorimetric *Kaiser* test (see section 2.5.11).

2.5.8 Removal of the Pht-protecting group from either homo- or hetero-decorated *f*-SWCNTs

In a typical procedure, *f*-SWCNTs (20 mg) were suspended in 22 mL of ethanol and sonicated for 15 min. Then hydrazine hydrate (0.08 mL, 1.6 mmol) was added and the suspension was sonicated for further 10 min. The reaction mixture was stirred at room temperature for 20 h, then diluted with ethylacetate, sonicated for 10 min and centrifugated to remove the supernatant. The solid residue underwent an identical work-up procedure to that described above for the *f*_{N3}-SWCNTs. The recovered material was dried under vacuum at 50 °C to constant weight. All deprotected samples were stored on

air at room temperature. Amine loadings were measured spectroscopically (UV-vis) using the colorimetric *Kaiser* test (see section 2.5.11).

2.5.9 Preparation of $f_{\text{III(OH)}}$ -SWCNTs (11) from the β -D-glucopyranoside derivative f_{III} -SWCNT sample (9)

f_{III} -SWCNTs (20 mg) were weighed into a 25 mL flask, suspended in 5 mL of ethanol and sonicated for 15 min. Then 2-3 drops of sulphuric acid (98 %) were added and the mixture was further sonicated for 10 min. Afterwards, the suspension was stirred at the EtOH reflux temperature for 24 h, then diluted with a large excess of ethylacetate (30 mL), sonicated for 10 min and centrifuged as to remove the supernatant. The collected solid residue was then washed three times with dichloromethane, each time sonicated for 10 min and separated from the supernatant by centrifugation. The solid residue **11** was finally suspended in dichloromethane, sonicated for 15 min, filtered through a 0.2 μm -pore filter and dried under vacuum at 50 °C to constant weight.

2.5.10 Cyclic voltammetry (CV) measurements

The cyclic voltammetric measurements were carried out in a 1 M aqueous perchloric acid solution, using Ag/AgCl/KCl_{sat.} as reference electrode and a Pt wire as counterelectrode. A 1 wt. % ethanol suspension of carbon nanotubes (f -SWCNTs) was put on a glassy-carbon electrode ($A = 0.1963 \text{ cm}^2$) and covered with 2.6 μL of a 0.5 wt. % solution of nafion in EtOH. Unless otherwise stated, samples were analyzed at 50 mV/s. For all scrutinized samples, the peak current was found to vary linearly with the scan rate from 20 mV/s to 400 mV/s. Each measure was repeated up to 6 times using different sample loadings (from 2 mg to 7 mg of 1 wt. % CNT suspension deposited on the glassy-carbon electrode) and the resulting peak areas were properly correlated (by means of a linear regression curve) with the relative iron loadings.

2.5.11 General procedure for the *Kaiser* test on Boc-protected and Pht-protected homo/hetero-decorated samples

Primary amine loadings were measured spectroscopically using the “classical” colorimetric *Kaiser* conditions.^{20a,52} Three standard solutions were prepared as follows:
a: 10 g of phenol in 20 mL of absolute EtOH.

b: 2 mL of potassium cyanide 1 mM (aqueous solution) dissolved in 98 mL of pyridine.

c: 1 g of ninhydrin in 20 mL of absolute EtOH.

200 μg of carbon nanotubes (*f*-SWCNTs) were carefully weighted using a Sartorius 4503 microbalance ($d = 0.001 \text{ mg}$) and treated in sequence with 75 μL of solution (a), 100 μL of solution (b) and 75 μL of solution (c). The resulting dispersion was sonicated in a water bath until complete CNTs disaggregation. Afterwards, the mixture was heated at 120 $^{\circ}\text{C}$ for 5 min and immediately diluted with 4750 μL of a 60 % (v/v) EtOH solution. After centrifugation at 14000 rpm, the supernatant was analyzed by UV-vis spectroscopy. The absorbance at 570 nm was correlated to the amount of free amine functional groups present at the CNTs surface using the following equation:

$$\text{NH}_2 \text{ loading (mmol/g)} = \frac{[\text{Abs}_{\text{sample}} - \text{Abs}_{\text{blank}}] \times \text{dilution (mL)} \times 10^3}{\epsilon (\text{M}^{-1} \text{cm}^{-1}) \times \text{sample weight (mg)} \times \text{optical path (cm)}}$$

Dilution was fixed to 5 mL and extinction coefficient (ϵ) was 15000 $\text{M}^{-1} \text{cm}^{-1}$. The blank absorption was measured exactly in the same way but without CNTs.

References and Notes

- ¹ a) D. M. Guldi, N. Martín in *Carbon Nanotubes and Related Structures: Synthesis, Characterization, Functionalization, and Applications* (Eds.: D. M. Guldi, N. Martín), Publisher: Wiley-VCH, **2010**, pp. 562. ISBN: 978-3-527-32406-4. b) S. Yellampalli in *Carbon Nanotubes - Synthesis, Characterization, Applications* (Ed.: S. Yellampalli), Publisher: InTech, **2011**, pp. 514. ISBN: 978-953-307-497-9.
- ² a) A. Krüger in *Carbon Materials and Nanotechnology* (Ed. A. Krüger), Publisher: Wiley-VCH, 2010, pp. 490. ISBN: 978-3-527-31803-2. b) S. Bianco in *Carbon Nanotubes – From Research to Applications* (Ed.: S. Bianco), Publisher: InTech, 2011, pp. 358. ISBN: 978-953-307-500-6.
- ³ S. Iijima, *Nature* **1991**, *354*, 56.
- ⁴ M. Monthieux, V. L. Kuznetsov, *Carbon* **2006**, *44*, 1621.
- ⁵ a) P. M. Ajayan, *Chem. Rev.* **1999**, *99*, 1787-1799. b) R. H. Baughman, A. A. Zakhidov, W. A. de Heer, *Science* **2002**, *297*, 787.
- ⁶ a) T. Kashiwagi, E. Grulke, J. Hilding, R. Harris, W. Awad, J. Douglas, *Macromol. Rapid. Commun.* **2002**, *23*, 761. b) C. F. Kuan, W. J. Chen, Y. L. Li, C. H. Chen, H. C. Kuan, C. L. Chiang, *J. Phys. Chem. Solids* **2010**, *71*, 539. c) M. T. Byrne, Y. K. Gun'ko, *Adv. Mater.* **2010**, *22*, 1672. d) S. H. Park, P. R. Bandaru, *Polymer* **2010**, *51*, 5071. e) N. G. Sahoo, S. Rana, J. W. Cho, L. Li, S. H. Chan, *Prog. Polym. Sci.* **2010**, *35*, 837.
- ⁷ N. Saito, Y. Usui, K. Aoki, N. Narita, M. Shimizu, K. Hara, N. Ogiwara, K. Nakamura, N. Ishigaki, H. Kato, S. Taruta, M. Endo, *Chem. Soc. Rev.* **2009**, *38*, 1897.
- ⁸ K. Kostarelos, A. Bianco, M. Prato, *Nat. Nanotechnol.* **2009**, *4*, 627.
- ⁹ a) N. Karousis, N. Tagmatarchis, D. Tasis, *Chem. Rev.* **2010**, *110*, 5366. b) A. Hirsch, O. Vostrowsky, *Top. Curr. Chem.* **2005**, *245*, 193.
- ¹⁰ M. Holzinger, J. Abraham, P. Whelan, R. Graupner, L. Ley, F. Hennrich, M. Kappes, A. Hirsch, *J. Am. Chem. Soc.* **2003**, *125*, 8566.
- ¹¹ M. Holzinger, O. Vostrowsky, A. Hirsch, F. Hennrich, M. Kappes, R. Weiss, F. Jellen, *Angew. Chem. Int. Ed.* **2001**, *40*, 4002.
- ¹² J. L. Bahr, J. Yang, D. V. Kosynkin, M. J. Bronikowski, R. E. Smalley, J. M. Tour, *J. Am. Chem. Soc.* **2001**, *123*, 6536.
- ¹³ K. S. Coleman, S. R. Bailey, S. Fogden, M. L. H. Green, *J. Am. Chem. Soc.* **2003**, *125*, 8722.
- ¹⁴ P. Umek, J. W. Seo, K. Hernadi, A. Mrzel, P. Pechy, D. D. Mihailovic, L. Forro, *Chem. Mater.* **2003**, *15*, 4751.
- ¹⁵ a) V. Georgakilas, K. Kordatos, M. Prato, D. M. Guldi, M. Holzinger, A. Hirsch, *J. Am. Chem. Soc.* **2002**, *124*, 760. b) N. Tagmatarchis, M. Prato, *J. Mater. Chem.* **2004**, *14*, 437.
- ¹⁶ M. Alvaro, P. Atienzar, P. de la Cruz, J. L. Delgado, H. Garcia, F. Langa, *J. Phys. Chem. B* **2004**, *108*, 12691.
- ¹⁷ Y. Wang, Z. Iqbal, S. Mitra, *Carbon* **2005**, *43*, 1015.

- 18 a) G. Ghini, L. Luconi, A. Rossin, C. Bianchini, G. Giambastiani, S. Cicchi, L. Lascialfari, A. Brandi, A. Giannasi, *Chem. Commun.* **2010**, 46, 252. b) G. Giambastiani, S. Cicchi, A. Giannasi, L. Luconi, A. Rossin, F. Mercuri, C. Bianchini, A. Brandi, M. Melucci, G. Ghini, P. Stagnaro, L. Conzatti, E. Passaglia, M. Zoppi, T. Montini, P. Fornasiero, *Chem. Mater.* **2011**, 23, 1923.
- 19 a) F. G. Brunetti, M. A. Herrero, J. de M. Muñoz, A. Diaz-Ortiz, J. Alfonsi, M. Meneghetti, M. Prato, E. Vázquez, *J. Am. Chem. Soc.* **2008**, 130, 8094. b) C. Samorí, H. Ali-Boucetta, R. Sainz, C. Guo, F. M. Toma, C. Fabbro, T. da Ros, M. Prato, K. Kostarelos, A. Bianco, *Chem. Commun.* **2010**, 46, 1494. c) J. J. Stephenson, J. L. Hudson, A. D. Leonard, B. K. Price, J. M. Tour, *Chem. Mater.* **2007**, 19, 3491. d) N. Rubio, M. A. Herrero, A. de la Hoz, M. Meneghetti, M. Prato, E. Vázquez, *Org. Biomol. Chem.* **2010**, 8, 1936. e) G. Lamanna, A. Battigelli, C. Ménard-Moyon, A. Bianco, *Nanotechnol. Rev.* **2012**, 1, 17.
- 20 a) C. Ménard-Moyon, C. Fabbro, M. Prato, A. Bianco, *Chem. Eur. J.* **2011**, 17, 3222. b) G. Pastorin, W. Wu, S. Wieckowski, J.-P. Briand, K. Kostarelos, M. Prato, A. Bianco, *Chem. Commun.* **2006**, 1182. c) W. Wu, S. Wieckowski, G. Pastorin, M. Benincasa, C. Klumpp, J.-P. Briand, R. Gennaro, M. Prato, A. Bianco, *Angew. Chem. Int.* **2005**, 44, 6358.
- 21 K. M. Lee, L. Li, L. Dai, *J. Am. Chem. Soc.* **2005**, 127, 4122.
- 22 a) V. V. Rostovtsev, L. G. Green, V. V. Fokin, K. B. Sharpless, *Angew. Chem.* **2002**, 114, 2708; *Angew. Chem. Int. Ed.* **2002**, 41, 2596. b) X. Li, *Chem. Asian J.* **2011**, 6, 2606.
- 23 a) C. W. Tornøe, M. Meldal in *The Wave of the Future* (Ed.: M. Lebl, R. A. Houghten), San Diego: American Peptide Society and Kluwer Academic Publishers, **2001**, 263. b) C. W. Tornøe, C. Christensen, M. Meldal, *J. Org. Chem.* **2002**, 67, 3057.
- 24 For a review paper on ‘click’ chemistry in material science see: a) W. H. Binder, R. Sachsenhofer, *Macromol. Rapid Commun.* **2007**, 28, 15. b) G. Clavé, S. Campidelli, *Chem. Sci.* **2011**, 2, 1887.
- 25 H. Li, F. Cheng, A. M. Duft, A. Adronov, *J. Am. Chem. Soc.* **2005**, 127, 14518.
- 26 L. Lascialfari, C. Vinattieri, G. Ghini, L. Luconi, D. Berti, M. Mannini, C. Bianchini, A. Brandi, G. Giambastiani, S. Cicchi, *Soft. Matter.* **2011**, 7, 10660.
- 27 a) J. L. Bahr, J. M. Tour, *Chem. Mater.* **2001**, 13, 3823. b) C. A. Dyke, J. M. Tour, *J. Am. Chem. Soc.* **2003**, 125, 1156. c) C. A. Dyke, J. M. Tour, *Nano Letters* **2003**, 3, 1215. d) J. L. Hudson, M. J. Casavant, J. M. Tour, *J. Am. Chem. Soc.* **2004**, 126, 11158. e) C. A. Dyke, M. P. Stewart, F. Maya, J. M. Tour, *Synlett* **2004**, 1, 155. f) B. K. Price, J. L. Hudson, J. M. Tour, *J. Am. Chem. Soc.* **2005**, 127, 14867. g) B. K. Price, J. M. Tour, *J. Am. Chem. Soc.* **2006**, 128, 12899. h) C. D. Doyle, J. M. Tour, *Carbon* **2009**, 47, 3215.
- 28 S. Bräse, C. Gil, K. Knepper, V. Zimmermann, *Angew. Chem. Int. Ed.* **2005**, 44, 5188.
- 29 The elemental analysis provides an overvalued functionalization loading although within the same order of magnitude as calculated from the TGA profile.
- 30 E. Lieber, C. N. Ramachandra Rao, T. S. Chao, C. W. W. Hoffman, *Anal. Chem.* **1957**, 29, 916.
- 31 A. C. Ferrari, J. Robertson, *Phys. Rev. B* **2000**, 61, 14095.

-
- 32 R. Graupner, *J. Raman Spectrosc.* **2007**, *38*, 673.
- 33 a) R. Huisgen, *Proc. Chem. Soc.*, London, **1961**, 357. b) S. Kamijo, T. Jin Y. Yamamoto, *Tetrahedron Lett.* **2004**, *45*, 689. c) M. V. Gil, M. J. Arévalo, Ó. López, *Synthesis* **2007**, *11*, 1589. d) J. F. Lutz, *Angew. Chem. Int. Ed.* **2007**, *46*, 1018. e) P. Appukkutan, W. Dehaen, V. V. Fokin, E. Van der Eycken, *Org. Lett.* **2004**, *6*, 4223.
- 34 a) S. Campidelli, B. Ballesteros, A. Filoramo, D. Diaz Diaz, G. de la Torre, T. Torres, G. M. Aminur Rahman, C. Ehli, D. Kiessling, F. Werner, V. Sgobba, D. M. Guldi, C. Cioffi, M. Prato, J.-P. Bourgoïn, *J. Am. Chem. Soc.* **2008**, *130*, 11503. b) B. Palacin, H. Le Khanh, B. Joussetme, P. Jegou, A. Filoramo, C. Ehli, D. M. Guldi, S. Campidelli, *J. Am. Chem. Soc.* **2009**, *131*, 15394. c) K. Hy Le Ho, L. Rivier, B. Joussetme, P. Jégou, A. Filoramo, S. Campidelli, *Chem. Commun.* **2010**, *46*, 8731.
- 35 For CuAAC reactions using CuSO₄/Na-ascorbate as catalyst see ref 22a and P. Wu, V. V. Fokin *Aldrichim. Acta* **2007**, *40*, 7.
- 36 a) N. Pietrzik, C. Schips, T. Ziegler, *Synthesis* **2008**, *4*, 519. b) For CuAAC reactions using (EtO)₃PCuI as catalyst see: F. Pérez-Balderas, M. Ortega-Muñoz, J. Morales-Sanfrutos, F. Hernández-Mateo, F. G. Calvo-Flores, J. A. Calvo-Asín, J. Isac-García, F. Santoyo-González, *Org. Lett.* **2003**, *5*, 1951.
- 37 The CuI/DBU/DMF system was additionally screened as the most effective protocol reported in the literature (see ref. 25) for “click” couplings on SWCNTs. For related Huisgen-type conditions see also: K. D. Bodine, D. Y. Gin, M. S. Gin, *J. Am. Chem. Soc.* **2004**, *126*, 1638. The latter conditions did not gave (in our hands) any relevant difference compared to either CuSO₄/Na-ascorbate/DMF or (EtO)₃PCuI/DMF protocol conditions.
- 38 The efficiency of each metal source (CuSO₄/Na-ascorbate vs. [(EtO)₃PCuI], 10 mol% respect to the alkyne) in the CuAAC reaction on **2** was evaluated (in DMF) for all selected acetylene derivatives (**3-6**). TGA profiles of cycloadducts (**7-10**) in combination with electrochemical (CV) and spectroscopic (UV-vis) characterizations of **8** and **11-12**, respectively, were used to quantify the metal source effectiveness.
- Both copper sources were successfully used under homogeneous CuAAC conditions (catalytic) while studying the reactivity of all selected alkynes (**3-6**) with the model Ph-N₃ as reagent. Homogeneous conditions did not reveal any appreciable difference between the two selected catalytic systems (in term of isolated yields).
- 39 N. E. Bryamova, M. V. Ovchiunikov, L. V. Backinowski, N. K. Kochetov, *Carbohydr. Res.* **1983**, *124*, C8.
- 40 An almost linear increases of the $\Delta(E_{ox}^p - E_{red}^p)$ up to a maximum of 54 mV was recorded on the CVs measured at different scan rates (25-400 mV/s). Such a trend was reasonably ascribed to whatever kinetic irreversibility of the electrochemical process.
- 41 A. J. Bard, L. R. Faulkner, *Electrochemical Methods: Fundamentals and Applications*, 2nd ed.; Wiley, New York, **2001**, p. 591.

-
- 42 No peaks corresponding to the ferrocene redox couple were observed when f_{N_3} -SWCNTs were treated with ethylferrocene in the absence of the Cu^I source – blank test.
- 43 For both homo- and hetero-functionalization the alkyne content was always used in excess respect to the azido-groups available at the SWCNT sidewalls ($\approx 15 : 1$). No apparent improvements of the functionalization loading (homo-decoration experiments) were observed while increasing the fixed amount (mmol) of the alkyne reagent.
- 44 The Pht-protected propargylamine **6** is used instead of the Boc protected counterpart **3** because of the scarce stability of the ferrocene moiety under acidic deprotection environments.
- 45 a) J. A. Prescher, C. R. Bertozzi, *Nat. Chem. Biol.* **2005**, *1*, 13. b) J. M. Baskin, C. R. Bertozzi, *QSAR Comb. Sci.* **2007**, *11*, 1211.
- 46 D. D. Perrin, W. L. F. Armarego, D. R. Perrin, *Purification of laboratory chemicals, 2nd Edition*; Pergamon Press, **1980**; Vol. 1.
- 47 a) M. A. Fazio, O. P. Lee, D. I. Schuster, *Org. Lett.* **2008**, *10*, 4979. For spectroscopic characterization of **1** see also: b) W. Zhu, D. Ma, *Chem. Commun.* **2004**, 888.
- 48 K. Barral, A. D. Moorhouse, J. E. Moses, *Org. Lett.* **2007**, *9*, 1809.
- 49 a) M. S. Strano, C. A. Dyke, M. L. Ursey, P. W. Barone, M. J. Allen, H. W. Shan, C. Kittrell, R. H. Hauge, J. M. Tour, R. E. Smalley, *Science* **2003**, *301*, 1519. b) C. A. Dyke, M. P. Stewart, J. M. Tour, *J. Am. Chem. Soc.* **2005**, *127*, 4497.
- 50 A. C. Ferrari, J. Robertson, *Phys. Rev. B* **2001**, *64*, 075414.
- 51 M. M. Lucchese, F. Stavale, E. H. Martins Ferreira, C. Vilani, M. V. O. Moutinho, R. B. Capaz, C. A. Achete, A. Jorio, *Carbon* **2010**, *48*, 1592.
- 52 E. Kaiser, R. L. Colescott, C. D. Bossinger, P. I. Cook, *Anal. Biochem.* **1970**, *34*, 595.

3. “Click” on MOFs: a Versatile Tool for the Multimodal Derivatization of N₃-decorated Metal Organic Frameworks

3.1 Abstract

The CuAAC protocol developed for the smart and multimodal functionalization of carbon nanotubes can be easily and usefully extended to other complex materials such as Metal Organic Frameworks (MOFs), 3D coordination polymers obtained from the combination of multidentate organic linkers with metal-based inorganic units. Post-synthetic modification (PSM) has been exploited for the preparation of two novel N₃-decorated MOFs, namely UMCM-1-N₃ [Zn₄O(N₃tpa)(btb)_{4/3}; N₃tpa²⁻ = 2-azidoterephthalate; btb³⁻ = 4,4',4''-benzene-1,3,5-triyl-tribenzoate] and MIXMOF-5-N₃ [Zn₄O(N₃tpa)_{0.4}(tpa)_{2.6}; tpa²⁻ = terephthalate], featured by both different azido functional group content and crystalline structure. Subsequently, the as-synthesized materials were further transformed through an efficient and versatile approach capable of imparting multimodality to these porous organic-inorganic polymers. Cu-mediated acetylene-azide coupling (CuAAC; “click” reaction) has been performed in a single step, under optimized conditions, with complete azido → triazole conversion using either single acetylene derivatives or mixtures of reactive terminal alkynes in variable molar fractions to give homo- and hetero-derivatized MOFs. An accurate control of the relative percentages of the functional groups in the final hetero-functionalized materials is conveniently achieved through a fine tuning of the starting acetylene mixtures molar ratio. All MOFs derivatives have been characterized through thermogravimetric analysis coupled with MS analysis of volatiles (TG-MS), powder X-ray diffraction (PXRD), FT-IR spectroscopy and ¹H NMR spectroscopy of the digested functionalized samples. Fluorescence studies on properly labeled (dye-functionalized) MOFs have been used for the first time to assess the statistical distribution of the “reactive probe” throughout the bulk material.

3.2 Introduction

The chemistry of metal-organic frameworks (MOFs), crystalline coordination polymers obtained from the combination of multidentate organic linkers with inorganic units, has seen a tremendous boost in the last two decades.¹ Their unique properties like high surface area, chemical/thermal stability and tunable pore size, have opened new perspectives in gas storage and separation,² catalysis,³ and medicinal chemistry.⁴ The virtually infinite choice of spacers available to build MOFs is the most versatile feature of this class of materials, when searching for practical applications. In the last few years, the discovery of new chemical protocols for the introduction of more than one functional group within the same material (multimodality) has become the main target in MOFs synthesis. The most intuitive synthetic pathway is the combination of organic linkers of the same kind but bearing different functional groups (“tags”) during the MOF synthesis; this leads to the so-called MIXMOFs or multivariate MOFs.⁵ A high-throughput approach has been exploited to obtain MIXMOFs with up to eight different tags. Albeit being easy to pursue, this method suffers from a severe lack of control of the functionalization extent. Looking for alternatives, organic chemistry allows for the introduction of new functional groups within the main molecular skeleton even *after* the MOF synthesis, through the post-synthetic modification (PSM) route.⁶ As a result, a series of isorecticular MOFs having the same network topology can be prepared. PSM popularity is witnessed by a number of seminal papers appeared in the literature in the last few years,^{5,7} but an extensive investigation of the real potential of this synthetic method in combination with a variety of organic and organometallic reagents has not been addressed yet. PSM provides high flexibility in the material design; nonetheless PSM is still rather complicated and requires multistep procedures, with a careful screening of the synthesis conditions to have a precise control of the amount of functional groups introduced in the final material. One desired target is to impart multimodality to these porous materials by the covalent anchoring of different molecules to the reactive sites present in the pores of the reticular MOF network possibly under mild reaction conditions, avoiding conflicting side-reactions and preserving the crystalline texture of the starting material. While selected PSM procedures like the vapor-phase PSM (VP-PSM) are simple and extremely clean approaches to reach a high functionalization degree (particularly in the case of small

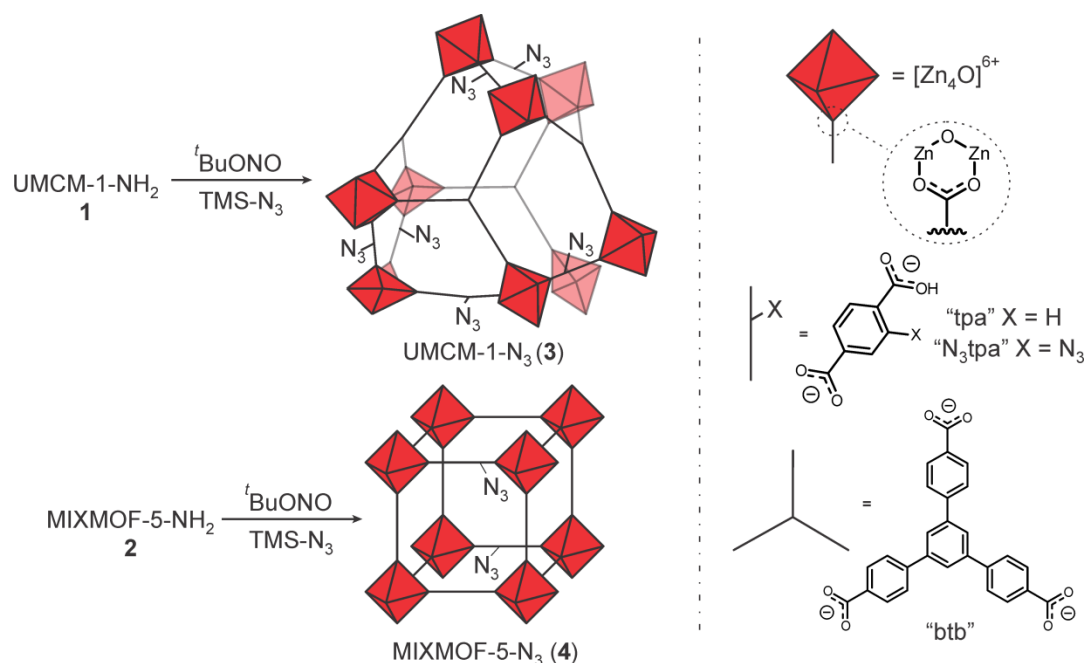
and volatile reactive molecules),⁸ “click chemistry” is an alternative powerful tool capable of introducing complex organic and organometallic moieties into MOFs.⁹

In this chapter is described the PSM of two novel N₃-decorated MOFs starting from the related NH₂-functionalized analogues: UMCM-1-N₃ [Zn₄O(N₃tpa)(btb)_{4/3}; N₃tpa²⁻ = 2-azidoterephthalate; btb³⁻ = 4,4',4''-benzene-1,3,5-triyl-tribenzoate], showing **muo** (UMCM-1) network topology,¹⁰ and MIXMOF-5-N₃ [Zn₄O(N₃tpa)_{0.4}(tpa)_{2.6}; tpa²⁻ = terephthalate], with the same **pcu** (primitive cubic lattice) network topology as that of MOF-5.¹¹ A versatile and efficient organometallic approach to the (multi)functionalization of these MOFs by their exposure to terminal acetylenes under Cu^I-mediated conditions (CuAAC reaction) is reported. This experimental methodology allows for the use of relatively mild reaction conditions, following the well consolidated “click chemistry” protocol and starting from a variety of reactive alkynes or mixtures thereof. Additionally, the azide-alkyne cycloaddition reaction is compatible with various solvents and functional groups^{12,13} and the produced triazole functionality is chemically stable, with structural and functional properties similar to those of the (more common) amide bond. We have already exploited this copper-mediated protocol successfully in the derivatization of carbon nanomaterials like carbon nanotubes (see chapter 2).¹⁴ Single organic/organometallic terminal acetylenes or defined binary and ternary acetylene mixtures have been employed for the homo- and hetero-decoration of the MOF network, respectively. Noteworthy, a precise tuning of the grafted organic/organometallic groups within the MOF's tridimensional network is simply achieved through a fine control of the relative amount of each terminal acetylene in the binary or ternary reactive mixture. This translates into a facile and convenient MOFs engineering and constitutes a real breakthrough in MOFs PSM procedures. Finally, the use of an acetylene end-capped dye has been employed for the first time as both model polycyclic reagent and fluorescent probe for the monitoring of the guest molecule distribution within the tridimensional MOF's network.

3.3 Results and Discussion

The selection of the appropriate MOF topologies suitable for PSM is the starting point of our study. The ideal candidates should have large channels capable of hosting bulky dangling substituents. The efficiency on a fully decorated MOF framework (*i.e.*, all the

organic linkers in the framework carrying one reactive group available for PSM) is dramatically limited by the scarce diffusion of the reagent throughout the MOF crystals.¹⁵ On the contrary, a reduced loading of the reactive functional groups (MIXMOF-5 case) combined with large pore and channels size (UMCM-1 case) can guarantee a high diffusion rate of the reactive molecules throughout the material tridimensional network.¹⁵ On this basis, two NH₂-decorated MOFs, UMCM-1-NH₂ (**1**)¹⁶ and MIXMOF-5-NH₂ (**2**)⁸ with a relatively low density of NH₂ reactive groups (43 % for **1** and 12 % for **2**, as determined by ¹H NMR spectroscopy after sample digestion) and large pores and high surface areas have been chosen as starting materials for the present study.¹⁷ **1** and **2** have been straightforwardly prepared in gram scale *via* solvothermal synthesis following the literature procedures^{8,16} (see also section 3.5). PXRD spectra and BET surface area measurements (**1**: 3780 m²/g; **2**: 3350 m²/g) were in line with literature data. The as prepared NH₂-decorated materials have been converted into the corresponding N₃-derivatives UMCM-1-N₃ [Zn₄O(N₃tpa)(btb)_{4/3}; N₃tpa²⁻ = 2-azidoterephthalate; btb³⁻ = 4,4',4''-benzene-1,3,5-triyl-tribenzoate, **3**] and MIXMOF-5-N₃ [Zn₄O(N₃tpa)_{0.4}(tpa)_{2.6}; tpa²⁻ = terephthalate, **4**, Scheme 3.1] using a highly efficient one-step literature procedure (Scheme 3.1).^{9c}



Scheme 3.1. Synthesis of UMCM-1-N₃ (**3**) and MIXMOF-5-N₃ (**4**) materials *via* PSM of their NH₂-decorated precursors (**1** and **2**, respectively).

In a typical procedure (Scheme 3.1), crystals of **1** or **2** are suspended in a CHCl_3 solution of *tert*-butylnitrite (7 equiv.) and azidotrimethylsilane (TMS-N_3 - 6 equiv.) while being gently shaken overnight (see section 3.5). The $-\text{NH}_2$ conversion into the azido ($-\text{N}_3$) group occurred without loss of the framework integrity, and it was ascertained for each sample through FT-IR spectroscopy (KBr pellets); evidence for the azido formation is given by the appearance of a relatively intense asymmetric stretching $\nu(\text{N}_3)^{18}$ band close to 2120 cm^{-1} (2131 cm^{-1} for **3**, Figure 3.1 and 2117 cm^{-1} for **4**, Figure 3.2) and confirmed by ^1H NMR spectroscopy of the digested samples (see section 3.5 and Figure 3.3).

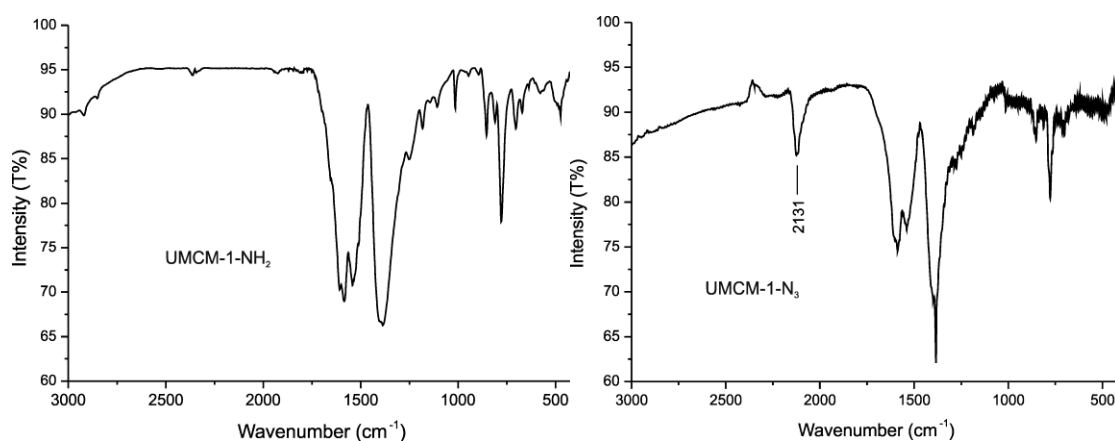


Figure 3.1. FT-IR spectra [KBr pellet] of the UMCM-1- NH_2 (**1**) (left) and UMCM-1- N_3 (**3**) (right).

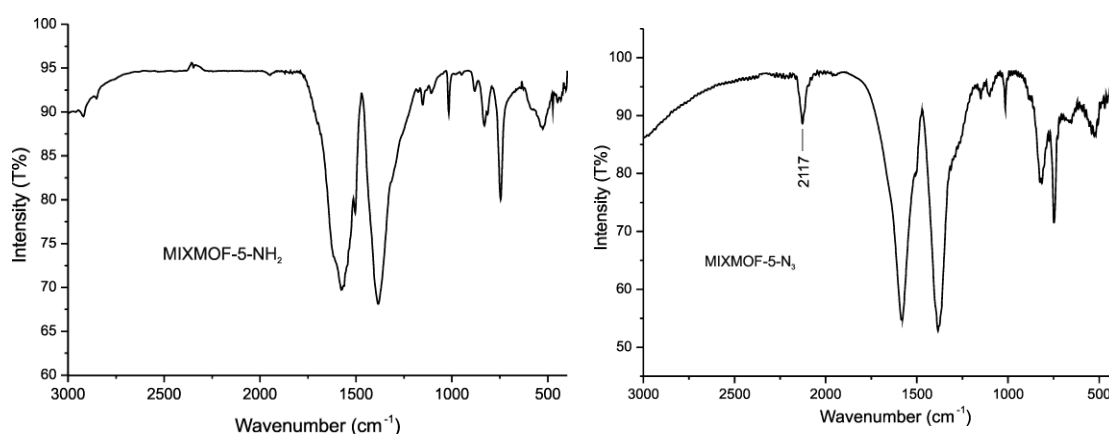


Figure 3.2. FT-IR spectra [KBr pellet] of the MIXMOF-5- NH_2 (**2**) (left) and MIXMOF-5- N_3 (**4**) (right).

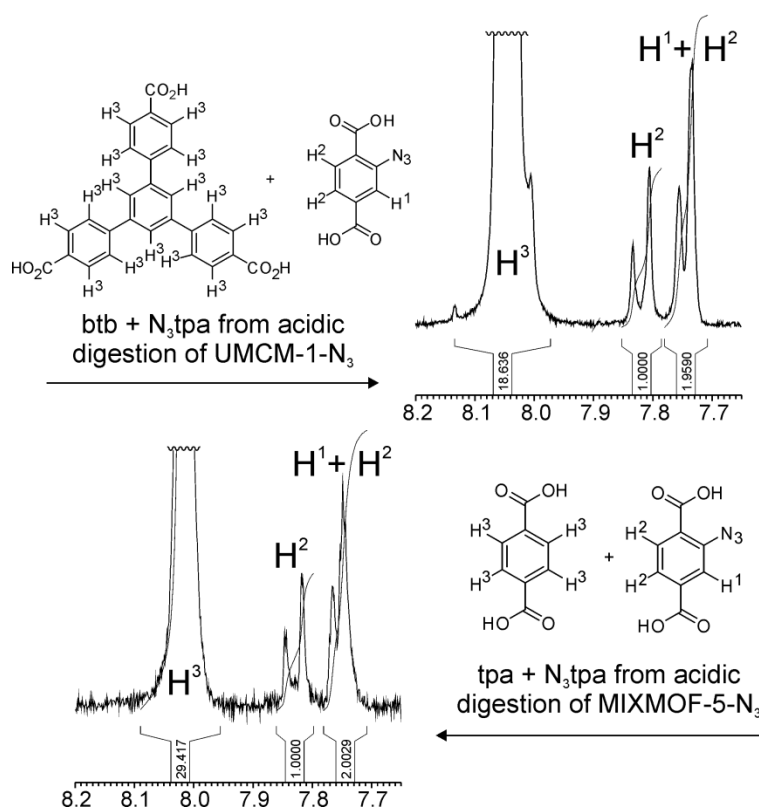
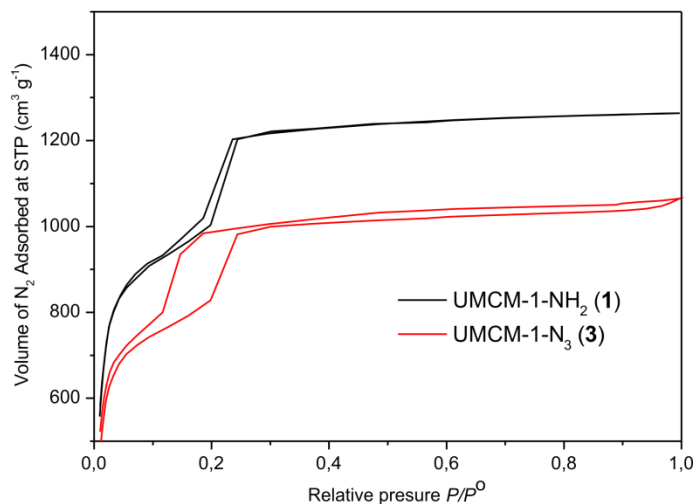


Figure 3.3. Low-fields ^1H NMR spectra of the digested UCMCM-1- N_3 (top) and MIXMOF-5- N_3 samples (bottom).

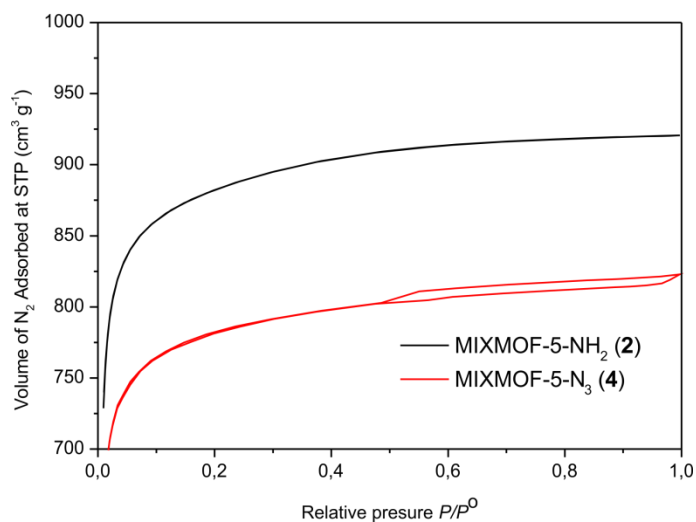
The distinctive low-fields ^1H NMR signals from the aromatic building-blocks [2-azidoterephthalate ($\text{N}_3\text{tpa}^{2-}$), terephthalate (tpa^{2-}) and 4,4',4''-benzene-1,3,5-triyl-tribenzoate (btb^{3-})] show the quantitative conversion of the $-\text{NH}_2$ into $-\text{N}_3$ for both **3** and **4** (Figure 3.3).

Accordingly, the calculated molecular formulae for **3** and **4** are $\text{Zn}_4\text{O}(\text{N}_3\text{tpa})(\text{btb})_{4/3}$ and $\text{Zn}_4\text{O}(\text{N}_3\text{tpa})_{0.4}(\text{tpa})_{2.6}$ respectively, matching those of the NH_2 -containing starting materials and confirming the quantitative $-\text{NH}_2 \rightarrow -\text{N}_3$ conversion. As a matter of fact, the N_3tpa molar loading for **3** is almost 2.5 times higher than that found in **4**. The larger size of the azido group compared with the amino substituent is witnessed by the lower BET surface area of **3** and **4** when compared with that of **1** and **2** (3090 vs. 3780 m^2/g and 2980 vs. 3350 m^2/g for **1-3** and **2-4**, respectively – see Figures 3.4 and 3.5).



MOFs	BET Surface area (m ² /g)	Langmuir Surface area (m ² /g)
UMCM-1-NH ₂ (1)	3777	4317
UMCM-1-N ₃ (3)	3092	3526

Figure 3.4. N₂ adsorption isotherms of UMCM-1-NH₂ (1) and UMCM-1-N₃ (3) and relative SSA values.



MOFs	BET Surface area (m ² /g)	Langmuir Surface area (m ² /g)
MIXMOF-5-NH ₂ (2)	3347	3833
MIXMOF-5-N ₃ (4)	2977	3400

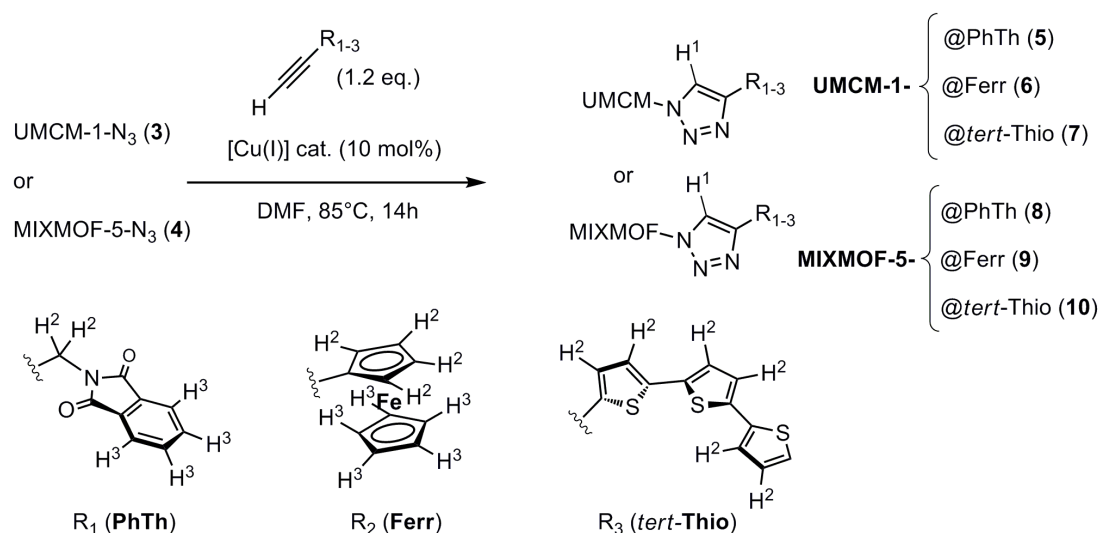
Figure 3.5. N₂ adsorption isotherms of MIXMOF-5-NH₂ (2) and MIXMOF-5-N₃ (4) and relative SSA values.

The as-prepared crystalline samples are indefinitely stable once stored in the dark and kept wet with toluene at room temperature.¹⁹ Each N₃-MOF sample is recovered as a solid and semi-dry material by filtration of a toluene suspension on a sintered glass frit (pore size 4-5.5 μm) and drying to constant weight under a stream of N₂.²⁰ As semi-dry microcrystalline powders, both N₃-MOF samples maintain relatively high lifetimes when stored under N₂ atmosphere and they can be handled in air for short time periods with no apparent decomposition.

Our strategy for the PSM of **3** and **4** relies upon the efficient azide-alkyne cycloaddition protocol (CuAAC) by using CuI[P(OEt)₃] as catalyst.^{12,21} Related Cu-mediated approaches to the MOF's PSM have already been reported in the literature: from the pioneering work of Sada *et al.*^{9a} to the recent contributions by Farrusseng and co-workers.^{9c} Despite the conceptual similarities of our approach to these studies, our contribution is focused on the unprecedented use of complex mixtures of model organic/organometallic alkyne-end-capped reagents (including a selected fluorescent probe) and their capillary distribution into the MOF reticular network. The controlled MOF's decoration is a remarkable key tool for a versatile and convenient MOF engineering.

3.3.1 MOF homo-decoration

Our initial approach to the homo-PSM of **3** and **4** is summarized in Scheme 3.2.



Scheme 3.2. CuAAC reaction between N₃-MOFs (**3** and **4**) with different alkyne-end-capped organic/organometallic reagents.

In a typical PSM procedure, the semi-dry solid N₃-MOF samples are suspended in dry and degassed DMF (1 mL) and treated, in sequence, with the selected alkyne (1.2 equiv. with respect to the estimated N₃ loading for semi-dry samples containing an average 60 wt. % of N₃-MOF)²⁰ and the copper catalyst CuI[P(OEt)₃] (10 mol% with respect to the alkyne). Each addition step (DMF, alkyne and catalyst) is followed by an impregnation time during which solvent and reagents are allowed to diffuse homogeneously throughout the material network. After each addition, the suspension undergoes three degassing cycles before being purged with nitrogen. The final catalyst addition is followed by heating in an oil bath at 85 °C while gently shaking it overnight (14 h). Successive washing cycles/filtration (over a 0.2 μm PTFE filter) with freshly distilled and degassed toluene give the post-modified material that is isolated and stored under N₂ atmosphere. The simplicity of the employed modification protocol and the quantitative conversion of the N₃ functional groups under the conditions used, together with the easy material handling (before and after PSM) and its relatively high stability under controlled conditions, make this approach highly convenient for running processes on a relatively large scale (up to 500 mg of N₃-MOF *per run*).

The post-functionalized materials **5-10** have been characterized by different spectroscopic/spectrometric (FT-IR, TGA-MS, NMR) and powder X-ray diffraction techniques whose combination has unambiguously provided evidence of the quantitative PSM.

FT-IR spectra recorded on all the functionalized materials show the complete suppression of the intense $\nu(\text{N}_3)$ asymmetric stretching (close to 2120 cm⁻¹; see Figures 3.1 and 3.2 *vs.* 3.6 and 3.7 for two selected examples) together with the appearance of relatively intense and distinctive stretching bands of selected functionalities present on the triazole-containing dangling group [for example, a characteristic band/shoulder around 1730 cm⁻¹ ascribed to the $\nu(\text{C}=\text{O})$ vibrational modes of the phthalimide moiety in **5** and **8**, see Figures 3.6 and 3.7].

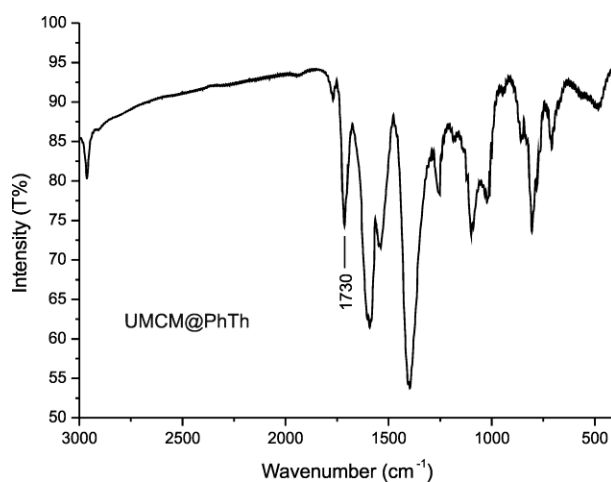


Figure 3.6. FT-IR spectrum [KBr pellet] of the **UCMCM@PhTh (5)** sample.

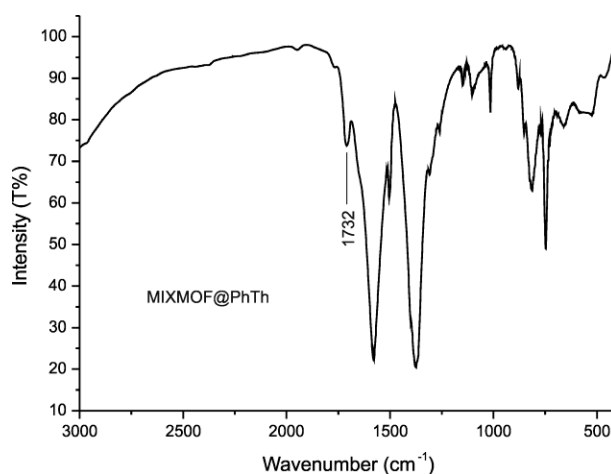


Figure 3.7. FT-IR spectrum [KBr pellet] of the **MIXMOF@PhTh (8)** sample.

TGA profiles of **5-7** and **8-10** *vs.* **3** and **4**, respectively, gives an additional proof of the occurred Cu-mediated azide-alkyne cycloaddition (see Figures 3.8 and 3.9). From a thorough analysis of the TGA profiles, one main distinctive feature is represented by a moderate weight loss measured only for samples **3** and **4** in the 170-220 °C temperature range and tentatively ascribed to the thermal N₃ decomposition followed by N₂ evolution. While the azide-alkyne cycloaddition transforms those thermally “labile” N₃ groups with the formation of the stable triazole systems (no weight loss is measured in the 170-220 °C temperature range for derivatives **5-7** and **8-10**), the post-functionalization process leads to an increase of carbonaceous residues that gradually decomposes at higher temperatures (over 500 °C).

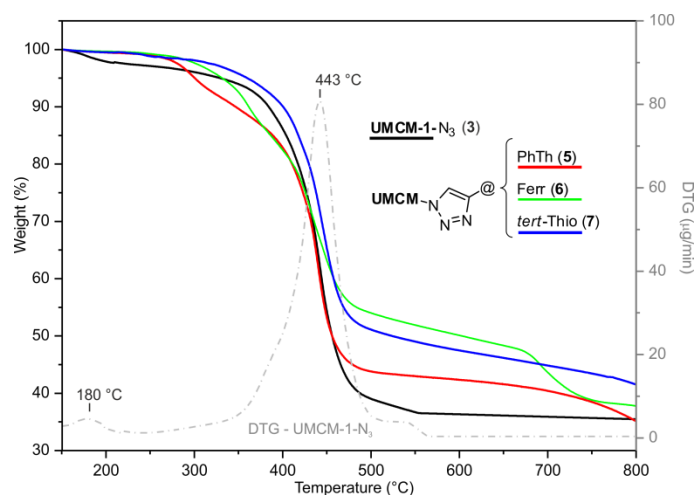


Figure 3.8. Normalized TGA profiles at comparison (N_2 , 50 mL/min) of **5-7** vs. **3** in the 150-800 °C temperature range.

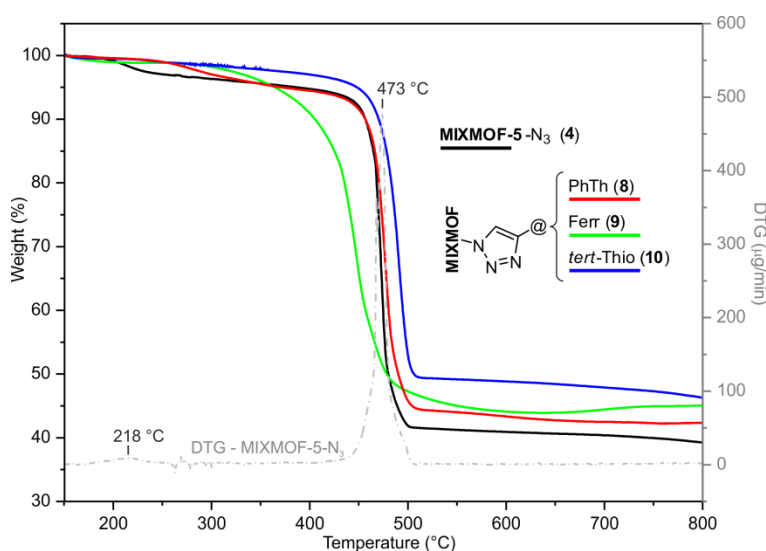


Figure 3.9. Normalized TGA profiles at comparison (N_2 , 50 mL/min) of **8-10** vs. **4** in the 150-800 °C temperature range.

The PXRD diffractograms of the homo-functionalized UMCM-based samples **5-7** do not show any significant change of the crystalline texture with respect to **3** after the functionalization process (Figure 3.10); in the case of the homo-functionalized MIXMOF-based materials **8-10**, new peaks appear for the phthalimide decorated (**8**) only (at $2\theta = 7.8, 14.7, 15.9, 24.4$ and 26.8° , corresponding to a d -spacing of 11.3, 6.0, 5.6, 3.6 and 3.3 \AA , respectively - Figure 3.11); this is likely due to the ability of phthalimide to form extended and *periodic* π -stacking interactions with the benzene rings of the MOF scaffold. In fact, similar $d(\text{phenyl-phenyl})$ distances have been found in other crystalline structures of phthalimide-containing organic compounds.²² The

same peaks also appear in the diffractograms of the phthalimide-containing MIXMOF hetero-functionalized samples (*vide infra*).

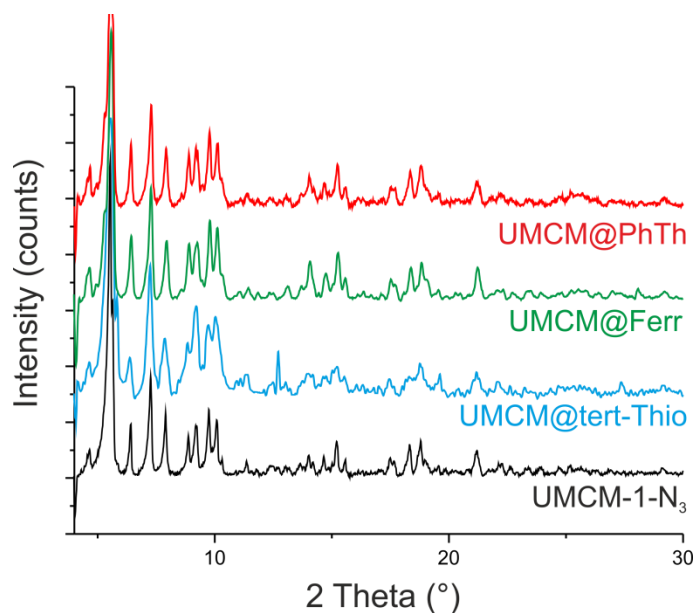


Figure 3.10. PXRD diffractograms of the homo-functionalized UMCM derivatives **5** (red), **6** (green) and **7** (light-blue). The diffractogram of **3** (black) is also reported for the sake of comparison.

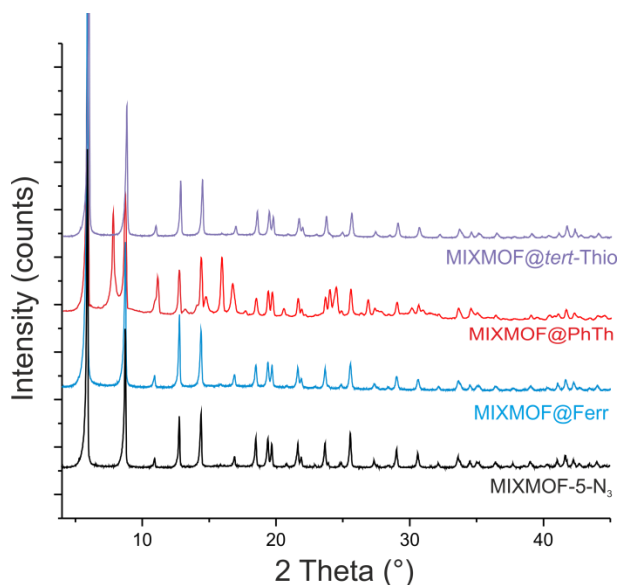


Figure 3.11. PXRD patterns of the homo-functionalized MIXMOF derivatives **8** (red), **9** (light-blue) and **10** (violet). The pattern of **4** (black) is also reported for the sake of comparison.

Although a direct comparison of the two different pristine MOFs textures (Figures 3.10 and 3.11, **3** vs. **4**) reveals that the crystallinity degree of UMCM is consistently lower than that of MIXMOF-5, as confirmed by other reports,²³ the post-synthetic

modification treatment does not affect the crystalline texture of the final derivatives significantly (Figures 3.10, **3** vs. **5-7** and 3.11, **4** vs. **8-10**).

A direct evidence of the successful post-functionalization process is unambiguously given by the ^1H NMR spectroscopy of the digested MOF samples (Figures 3.12 and 3.13). Each sample is digested in an acidic DMSO- d_6 solution (DMSO- d_6 /D $_2$ O/DCI) before being analyzed by ^1H NMR spectroscopy at room temperature. The resulting spectra reveal the complete disappearance of the aromatic signals between 7.70 and 7.85 ppm, attributed to the $\text{N}_3\text{tpa}^{2-}$ component present in both N_3 -MOFs.

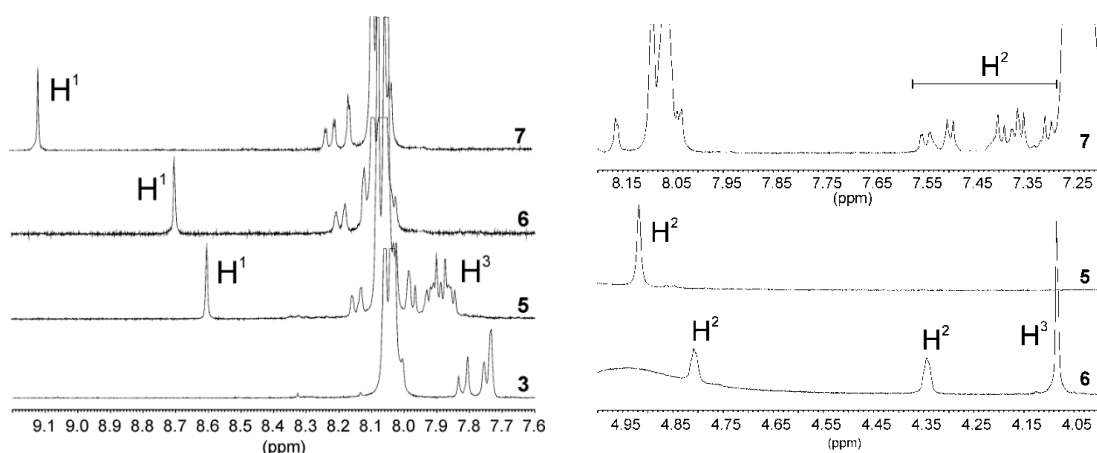


Figure 3.12. Left: low-field ^1H NMR spectra [300 MHz, (DMSO- d_6 /DCI/D $_2$ O), 298 K, $9.2 \geq \delta$ (ppm) ≥ 7.6] of digested samples **3**, **5-7**. Right: high-field ^1H NMR regions of digested samples **5-7**. For H atoms labelling see above Scheme 3.2.

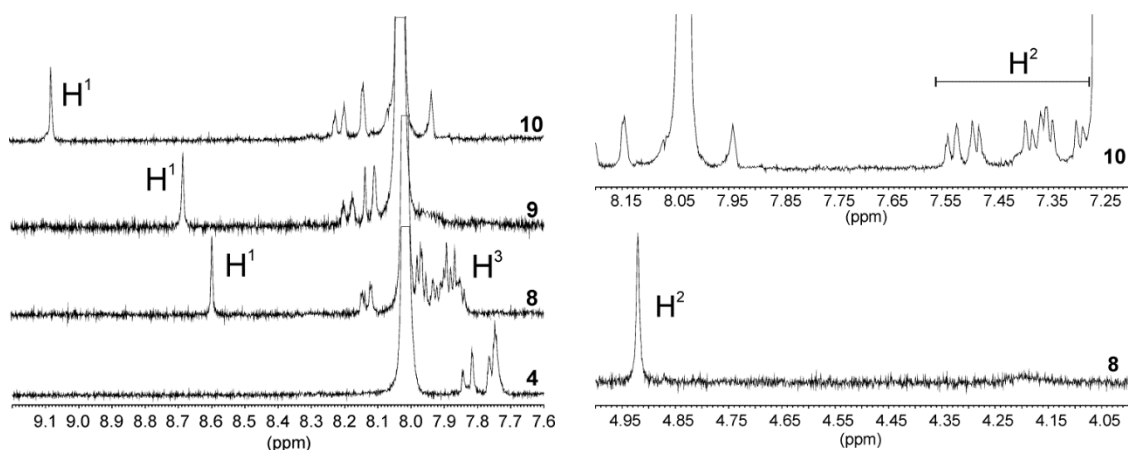


Figure 3.13. Left: low-field ^1H NMR spectra [300 MHz, (DMSO- d_6 /DCI/D $_2$ O), 298 K, $9.2 \geq \delta$ (ppm) ≥ 7.6] of digested samples **4**, **8-10**. Right: high-field ^1H NMR regions of digested samples **8** and **10**. For H atoms labelling see above Scheme 3.2.

The simultaneous appearance (in all derivatives) of new distinctive lower-field signals and, more importantly, of a singlet (H^1 in Figures 3.12 and 3.13) attributed to the triazole moiety (**5**: 8.59 ppm; **6**: 8.70 ppm; **7**: 9.11 ppm; **8**: 8.60 ppm; **9**: 8.68 ppm; **10**: 9.08 ppm), confirms the formation of the cycloaddition product as the unique species. Upper-field 1H NMR spectra show the presence of characteristic signals attributed to the ferrocene (**6**), *tert*-thiophene (**7** and **10**) and phthalimide methylene bridge moieties (**5** and **8**), respectively (see Figures 3.12 and 3.13 right).

The homogeneous functionalization of **7** and **10** has been ascertained spectroscopically, following the fluorescence of the *tert*-thiophene pendant arm by means of Laser Scanning Confocal Fluorescence Microscopy. Figure 3.14 (left) shows a maximum intensity projection (MIP) obtained for **7** upon excitation at 405 nm. The confocal fluorescence spectra of **7** (obtained from images recorded with the spectral module of the confocal microscope for excitation at 405 and 488 nm, respectively) are shown in Figure 3.14 (right). The fluorescence pattern obtained upon sample excitation at 488 nm presents a maximum around 540 nm; it is close to that measured on triazole-*tert*thiophene derivatives in solution upon sample excitation at 440 nm.²⁴ For the fluorescently labeled derivatives **7** and **10**, images reveal a homogeneous fluorescent probe diffusion into the bulk material.

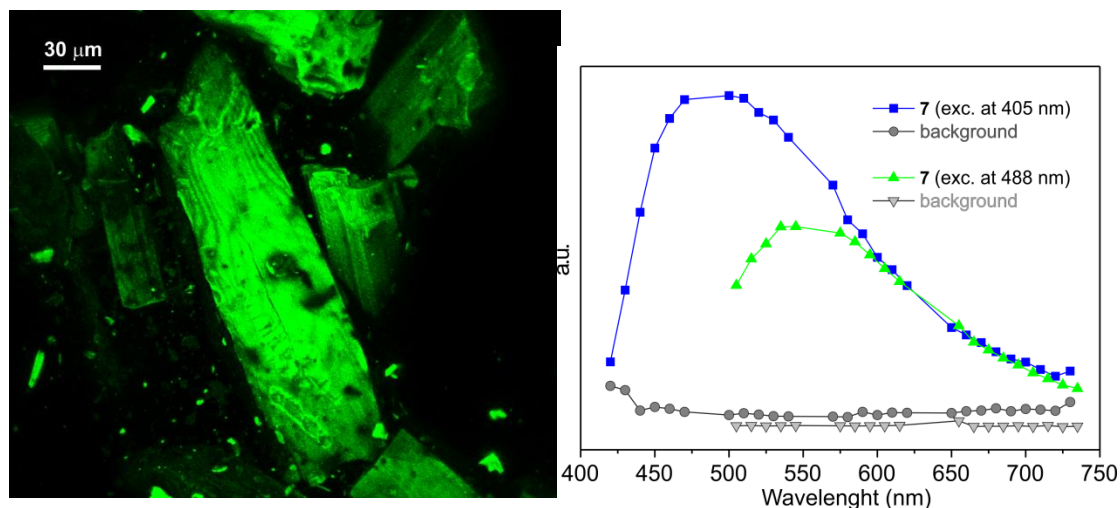


Figure 3.14. Left: Maximum intensity projection (MIP) obtained for crystals of **7** upon excitation at 405 nm. Right: Fluorescence spectra of **7** for excitation at 405 (-■-) and 488 nm (-▲-), respectively.

For the sake of completeness, the absorption and fluorescence properties of both pristine MOF-N₃ (**3**, **4**) and fluorescently labeled (**7**, **10**) samples have also been investigated through the respective acidic “digested” DMSO solutions (see Figure 3.15). This study has been carried out with the aim of distinguishing the triazole-based dye fluorescence emission from that of the MOF organic building blocks. As far as absorption spectra are concerned, a solution of **3** shows only one band centered at 273 nm (Figure 3.15, left); a red-shifted peak (280 nm), together with a lowest energy absorption band centered at 388 nm, is instead recorded for the digested terthiophene-containing sample **7** (Figure 3.15, right). The digested sample **3** solution shows, upon excitation at 282 and 365 nm, fluorescence centered at 361 and 436 nm, respectively (Figure 3.15, left), and no fluorescence for excitation at 440 nm. Differently, the solution from digested sample **7** shows three distinctive emission bands centered at 360, 443 and 538 nm for excitations at 282, 365 and 440 nm, respectively (Figure 3.15, right).²⁵ While the origin of the fluorescence centered at 538 nm is not totally clear, the weakly structured fluorescence emission centered at 443 nm unambiguously originates from the S₀→S₁ absorption of the terthiophene moiety, according to the excitation spectra. Red-shift of the main peaks in the absorption and fluorescence spectra are consistent with the generation of triazole α -substituted terthiophene moieties.²⁶ All the fluorescence spectra of the digested samples have been corrected and the excitation spectra were recorded for solutions absorbing less than 0.1 > 300 nm.

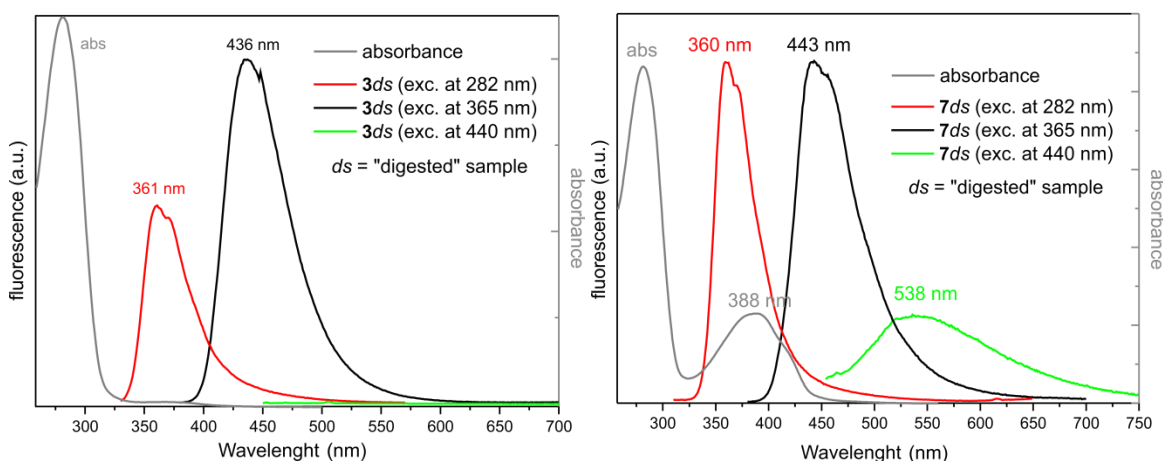


Figure 3.15. Left: Absorbance and fluorescence spectra of an acidic DMSO solution of the digested sample **3** in a 1 cm cuvet (**3ds**). Fluorescence is recorded upon sample excitation at 282, 365 and 440 nm. Right: Absorbance and fluorescence spectra of an acidic DMSO solution of the digested sample **7** in a 1 cm cuvet (**7ds**). Fluorescence is recorded upon sample excitation at 282, 365 and 440 nm.

Z-stack imaging has also been performed on a sample thickness varying from 10 to 20 μm . Figure 3.16 shows the fluorescence of **10** on a selected area (about 75 x 75 μm) along the z axis with a progression of about 0.9 μm from image Z1 to Z12. Z-stack images have been also acquired on **7** on a similar z-range.

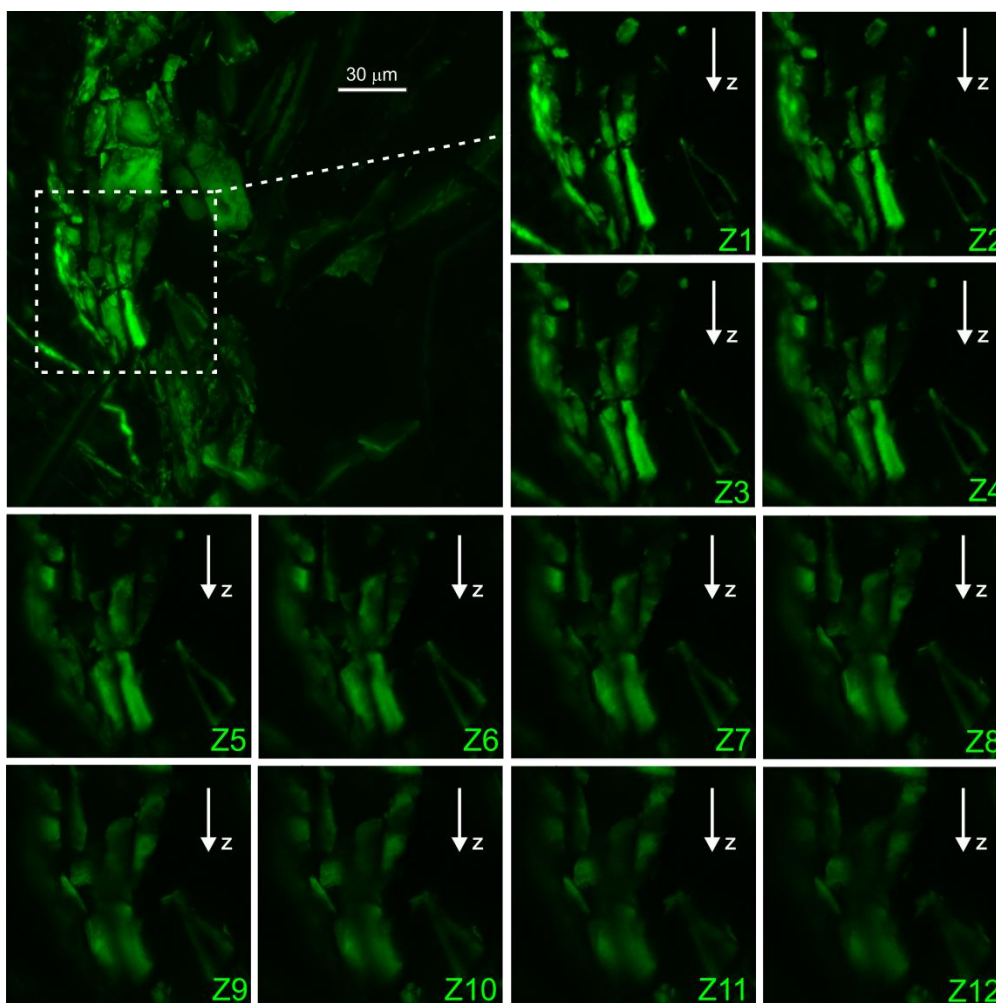


Figure 3.16. Z-stack images recorded on sample **10** for a section of 10 μm (along the z-axis, twelve z values) of a detail (white dashed box) of the top-left MIP image. Fluorescence is collected in the 500-550 nm range upon material excitation at 488 nm.

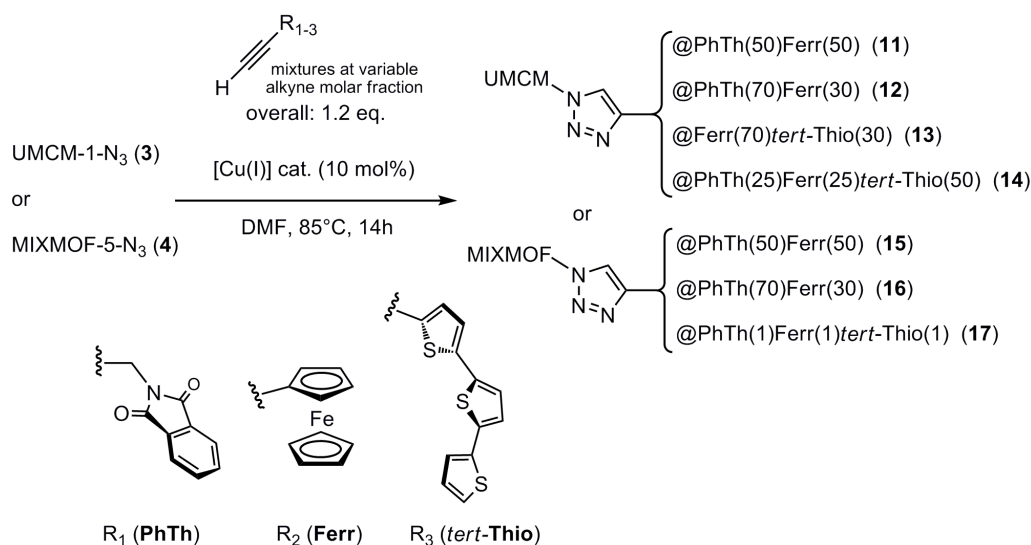
As Figure 3.16 shows, the fluorescence intensity is almost unchanged in this z-range, highlighting a homogeneous dye functionalization throughout the tridimensional network of the MOF sample.

All these characterization data taken together prove that the reaction conditions used for the PSM protocol lead to a full conversion of the N_3 groups into the corresponding

cycloadducts. As a matter of fact, each reactive alkyne and the Cu-catalyst smoothly diffuse through the channels of the reticular MOF networks.

3.3.2 MOF hetero-decoration

The introduction of multimodality into porous organic-inorganic materials under “mild” and “controlled” “click” conditions is accomplished following the same approach described above. The strategy to the hetero-PSM of N_3 -MOFs is summarized in Scheme 3.3.



Scheme 3.3. CuAAC reaction between N_3 -MOFs (3 and 4) with variable mixtures of alkyne-end-capped organic/organometallic reagents.

Hetero-functionalized samples are prepared via CuAAC chemistry using binary or ternary mixtures of acetylene end-capped reagents. The overall amount (equiv.) of acetylenes in the reactive mixture is maintained equal to that used in the homo-PSM experiments and constant to 1.2 equiv. with respect to the azido group content. In a typical experiment, equimolar binary mixtures of reactive alkynes (0.6 + 0.6 eq.; *cfr.* with the N_3 loading) are dissolved in DMF, and the resulting solutions are then used to impregnate the solid N_3 -MOF sample before adding the Cu catalyst $\text{Cu}[\text{P}(\text{OEt})_3]$ (10 mol% with respect to the alkyne). Similarly to the homo-PSM procedure, each addition step [DMF, alkyne(s) and catalyst] is followed by an impregnation time, during which solvent and reagents are allowed to diffuse homogeneously throughout the material network. After each addition, the suspension undergoes three degassing cycles before being purged with nitrogen. The final mixture is then heated in an oil bath at 85 °C,

while gently shaking it overnight (14 h). Successive washing cycles/filtrations (over a 0.2 μm PTFE filter) with freshly distilled and degassed toluene give the expected hetero-modified materials that are isolated and stored under N_2 atmosphere. As for the other binary and ternary reactive alkyne mixtures, the PSM protocol employed is the same reported above; the only difference is the variable molar fractions of the reactive alkynes in the mixture [70:30, 1:1:1 or 25:25:50; overall 1.2 alkyne(s) equiv. with respect to the azido group content].

Likewise homo-functionalized samples, the final semi-dry hetero-functionalized materials are recovered by washing/filtration processes and dried under a stream of N_2 to constant weight before being handled in air with no apparent decomposition for hours.

The characterization of the hetero-functionalized samples **11-17** has been accomplished similarly to that of **5-10**. All FT-IR spectra of the hetero-PSM materials show the complete suppression of the intense $\nu(\text{N}_3)$ asymmetric stretching (close to 2120 cm^{-1}), together with the appearance of relatively intense and distinctive stretching bands ascribable to functionalities present on the triazole-containing dangling group. The analysis of the TGA profiles do not reveal any distinctive thermal behavior,²⁷ except for the *tert*-thiophene-decorated samples (**14** and **17**) where the MS analysis of volatiles shows a characteristic peak at $m/z = 84$ attributed to the thiophene framework (TGA-MS profile of sample **17** is reported on Figure 3.17).

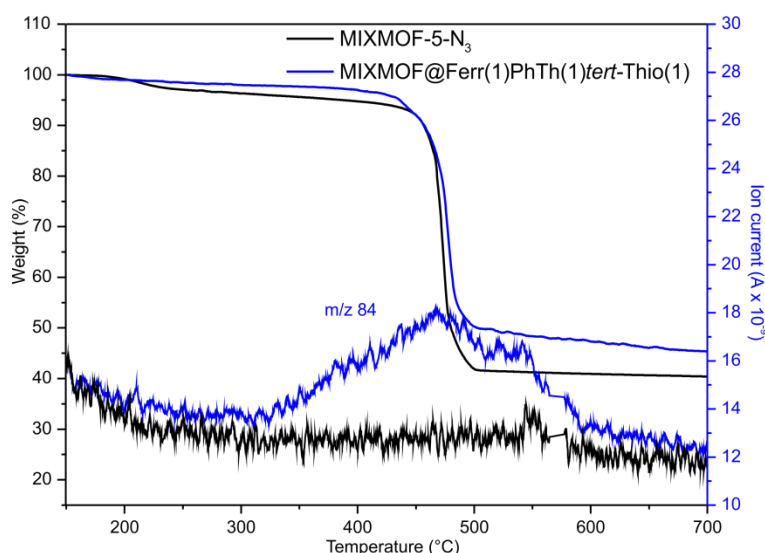


Figure 3.17. TGA/DTG profiles (N_2 , 50 mL/min) of MIXMOF@Ferr(1)PhTh(1)*tert*-Thio(1) (**17**) and MIXMOF-5- N_3 (**4**) samples at comparison (150-700 $^\circ\text{C}$ temperature range) associated with the MS analysis of volatiles [m/z ($\text{C}_4\text{H}_4\text{S}$) = 84 a.m.u.].

As for the homo-decorated samples, a more precise qualitative and quantitative analysis is achieved through ^1H NMR spectroscopy carried out on the digested samples.

Each MOF-derivative is then digested in an acidic $\text{DMSO-}d_6$ solution ($\text{DMSO-}d_6/\text{D}_2\text{O}/\text{DCI}$) before being analyzed through ^1H NMR spectroscopy. As Figures 3.18 and 3.19 show, the spectra reveal the complete disappearance of the aromatic signals attributed to the N_3tpa component present in both N_3 -decorated MOFs (Figure 3.18, **3** vs. **11-14**; Figure 3.19, **4** vs. **15-17**). Once again, the appearance of new aromatic signals, together with distinctive low-field singlets typical of the triazole aromatic moieties (Figure 3.18, **11**: 8.68 ppm and 8.61 ppm in a 1:1 ratio; **12**: 8.68 ppm and 8.61 ppm in a 3:7 ratio; **13**: 9.09 ppm and 8.68 ppm in a 3:7 ratio; **14**: 9.09 ppm, 8.68 ppm and 8.60 ppm in a 50:25:25 ratio; Figure 3.19, **15**: 8.62 ppm and 8.54 ppm in a 1:1 ratio; **16**: 8.60 ppm and 8.53 ppm in a 3:7 ratio, **17**: 9.06 ppm, 8.61 ppm and 8.53 ppm in a 1:1:1 ratio) is indicative of the presence of the cycloaddition product as the unique species. Finally, upper-field ^1H NMR spectra (Figures 3.18 and 3.19, right) show the presence of characteristic signals attributed to the ferrocene (**11-17**), *tert*-thiophene (**13**, **14** and **17**) and phthalimide methylene bridge moieties (**11**, **12**, **14** and **15-17**), respectively.

From a thorough and quantitative analysis of all ^1H NMR spectra acquired on the hetero-functionalized samples, it is evident that the applied protocol allows for a full control of the relative percentages of the hetero-groups covalently grafted on the MOF reticular network. Indeed, the simple adjustment of the relative molar fraction of the alkynes in the reactive mixtures (binary or ternary) *is entirely maintained in the post-synthetically modified material*.

As a result, a material impregnation with either 50:50 or 70:30 binary alkyne mixtures leads to hetero-modified MOFs with an identical molar ratio of the functional groups grafted to the MOF's network (Figure 3.18, spectra **11-13**; Figure 3.19, spectra **15-16**). Notably, a complete control on the MOF's network grafting is also achieved in the presence of selected and variable *ternary* mixtures of alkynes.

As shown in Figures 3.18 (spectrum **14**) and 3.19 (spectrum **17**), the material impregnation with either a 25:25:50 or 1:1:1 ternary mixture of alkynes ultimately *shows the same molar ratio as that of the starting mixture*.

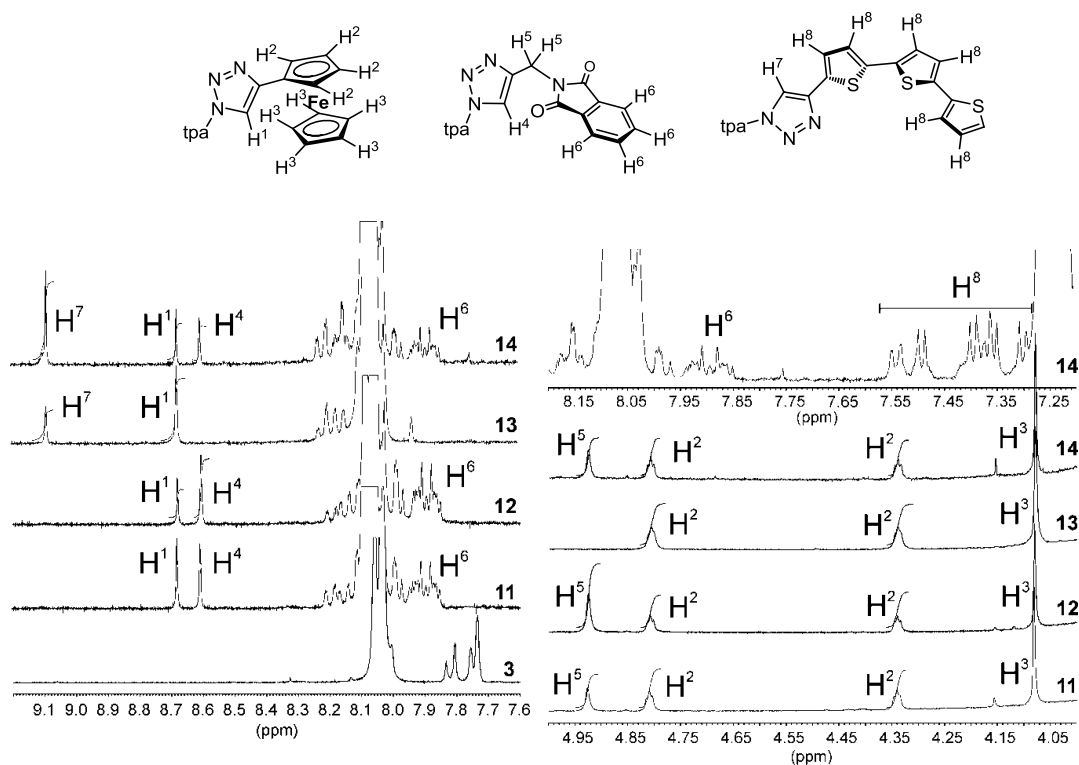


Figure 3.18. Left: low-field ^1H NMR spectra [300 MHz, ($\text{DMSO}-d_6/\text{DCI}/\text{D}_2\text{O}$), 298 K, $9.2 \geq \delta$ (ppm) ≥ 7.6] of digested samples **3**, **11-14**. Right: most representative high-field ^1H NMR regions of digested samples **11-14**.

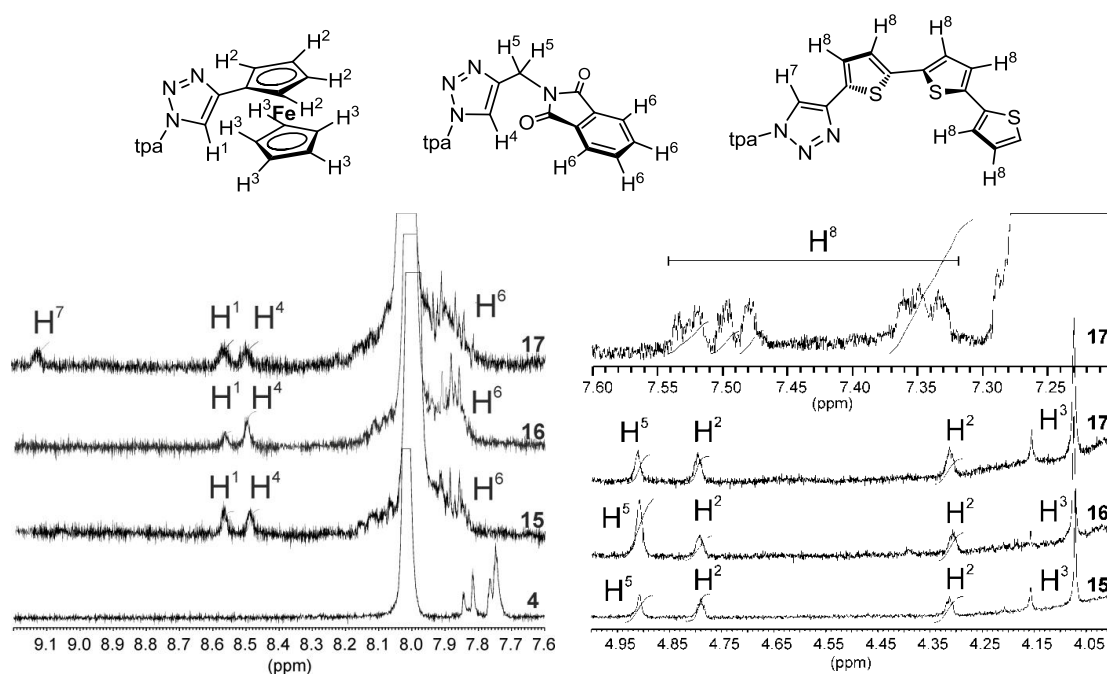


Figure 3.19. Left: low-field ^1H NMR spectra [300 MHz, ($\text{DMSO}-d_6/\text{DCI}/\text{D}_2\text{O}$), 298 K, $9.2 \geq \delta$ (ppm) ≥ 7.6] of digested samples **4**, **15-17**. Right: high-field ^1H NMR regions of digested samples **15-17**.

The hetero-functionalization procedure highlights the general character, the high functional groups tolerance, selectivity and orthogonality of the adopted Cu-mediated protocol, besides being an experimental proof of the homogeneous and smooth diffusion of the alkyne reagents in the MOF reticular network. As a matter of fact, a proper material impregnation with mixtures of different terminal alkynes can be employed to tune the specific functional group loading into the accessible channels of porous MOFs.²⁸

As for the UMCM-based samples **5-7**, no significant changes of the PXRD patterns are observed for the hetero-decorated derivatives **11-14**. As Figure 3.20 shows, hetero-derivatized samples do not vary their crystalline texture with respect to the starting N₃-MOF reagents except for phthalimide-containing MIXMOFs (**15-17**). Similarly to sample **8**, diffractograms of samples **15-17** present additional peaks due to the contribution of the phthalimide substituent.²²

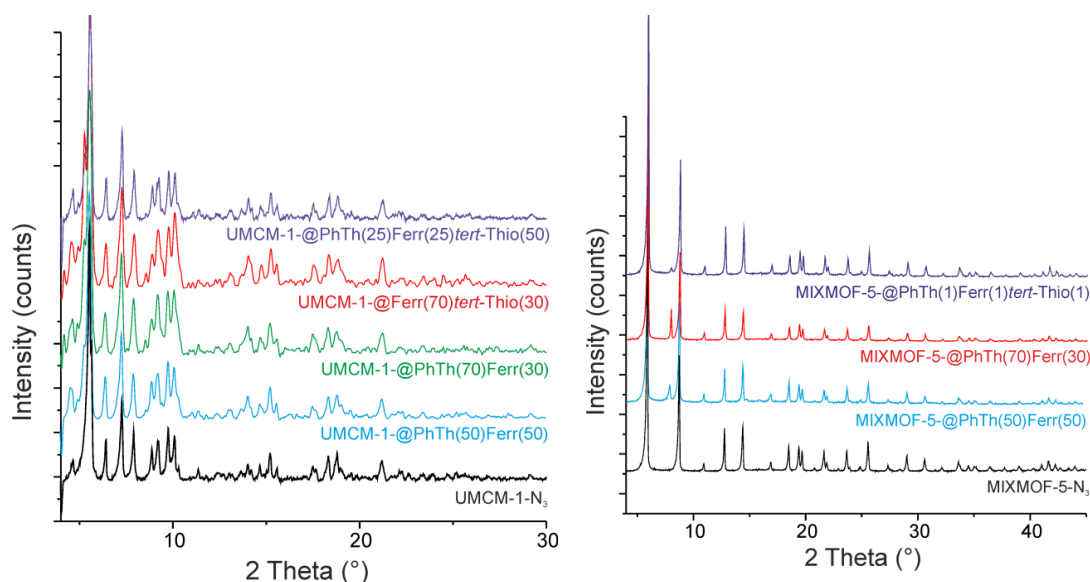
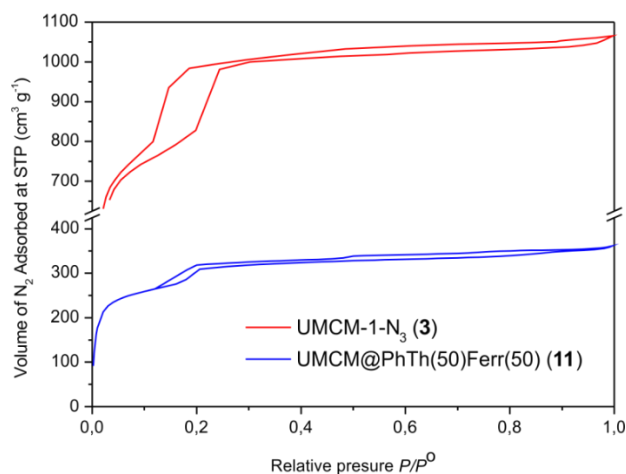


Figure 3.20. (left) PXRD spectra of the hetero-functionalized UMCM derivatives **11** (light-blue), **12** (green), **13** (red) and **14** (violet). Spectrum of **3** (black) is also reported for the sake of comparison. (right) PXRD spectra of the hetero-functionalized MIXMOF derivatives **15** (light-blue), **16** (red) and **17** (violet). Spectrum of **4** (black) is also reported for the sake of comparison.

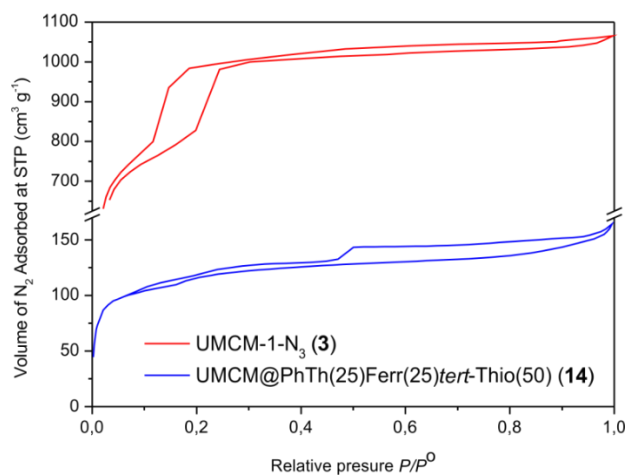
The BET surface area (SA) of selected hetero-functionalized samples has also been measured and compared. In general, the SA values recorded for the post-synthetically modified MOFs are always lower than those of the corresponding N₃-based starting material; the higher the functional group loading, the lower the SA value obtained within the same MOF topology (*cfr.* Figures 3.21 and 3.22 for an example from the

UMCM-1 family). This is in line with the increased steric hindrance created within the pores when filled with bulky dangling groups.



MOFs	BET Surface area (m ² /g)	Langmuir Surface area (m ² /g)
UMCM-1-N ₃ (3)	3092	3526
UMCM@PhTh(50)Ferr(50) (11)	757	1487

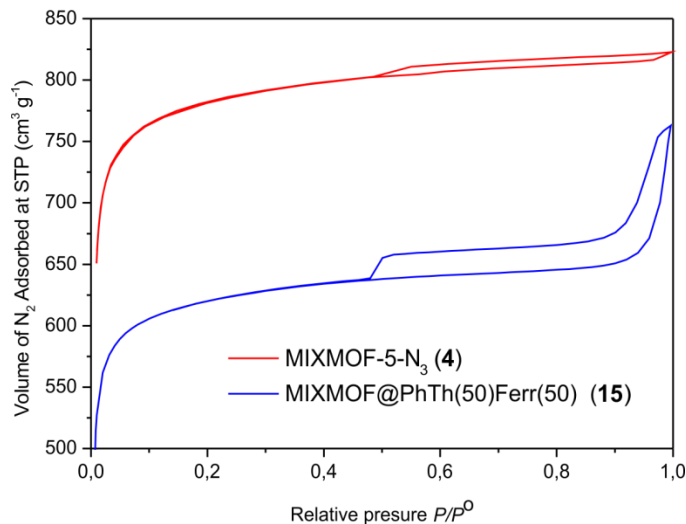
Figure 3.21. N₂ adsorption isotherms of UMCM-1-N₃ (**3**) and UMCM@PhTh(50)Ferr(50) (**11**) and relative SSA values.



MOFs	BET Surface area (m ² /g)	Langmuir Surface area (m ² /g)
UMCM-1-N ₃ (3)	3092	3526
UMCM@PhTh(25)Ferr(25) <i>tert</i> -Thio(50) (14)	334	589

Figure 3.22. N₂ adsorption isotherms of UMCM-1-N₃ (**3**) and UMCM@PhTh(25)Ferr(25)*tert*-Thio(50) (**14**) and relative SSA values.

When considering different MOFs topologies at comparable loading degree, the SA decrease observed within the UMCM-1 family is more pronounced than that of the MIXMOF-5 class (*cfr.* Figures 3.21 and 3.23). This mirrors the higher functionalization degree of UMCM-1 when compared with MIXMOF-5.



MOFs	BET Surface area (m ² /g)	Langmuir Surface area (m ² /g)
MIXMOF-5-N ₃ (4)	2977	3400
MIXMOF@PhTh(50)Ferr(50) (15)	1618	2814

Figure 3.23. N₂ adsorption isotherms of MIXMOF-5-N₃ (**4**) and MIXMOF@PhTh(50)Ferr(50) (**15**) and relative SSA values.

The quantitative material impregnation and functionalization is proved for the hetero-functionalized samples as well, exploiting the same confocal microscope spectroscopy tools in the presence of a fluorescent dye. The confocal fluorescence spectra recorded on sample **13** (Figure 3.24 right) are similar to those measured for the digested sample solutions, even though they have an appreciably red-shifted maximum.

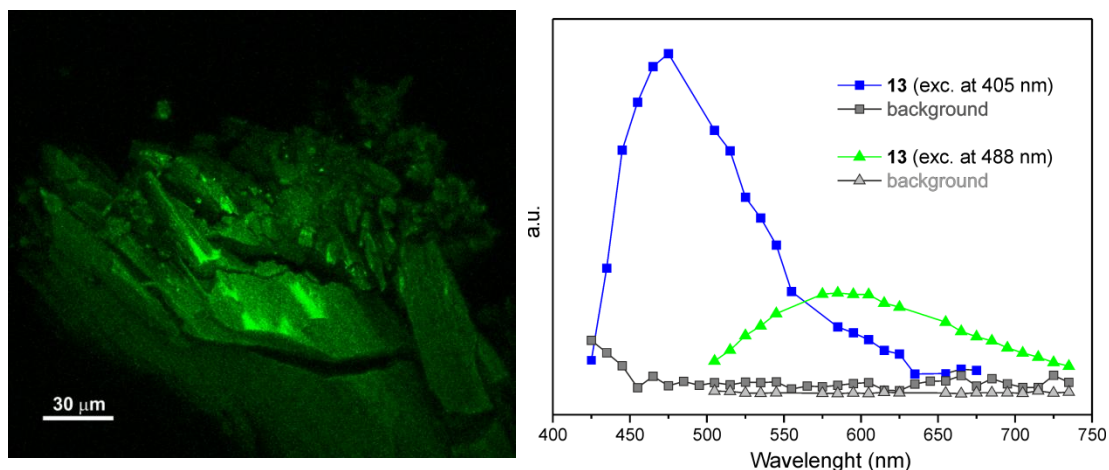


Figure 3.24. Left: Maximum intensity projection (MIP) obtained for sample **13** upon material excitation at 405 nm (fluorescence image collected in the 500-550 nm). Right: Fluorescence spectra of **13** upon sample excitation at 405 (-■-) and 488 nm (-▲-), respectively.

Z-stack imaging has been performed also in this case (sample thickness ca. 10 μm), and it confirms the homogeneous dye distribution in the bulk material (Figure 3.25). The same conclusions also holds for sample **14**.

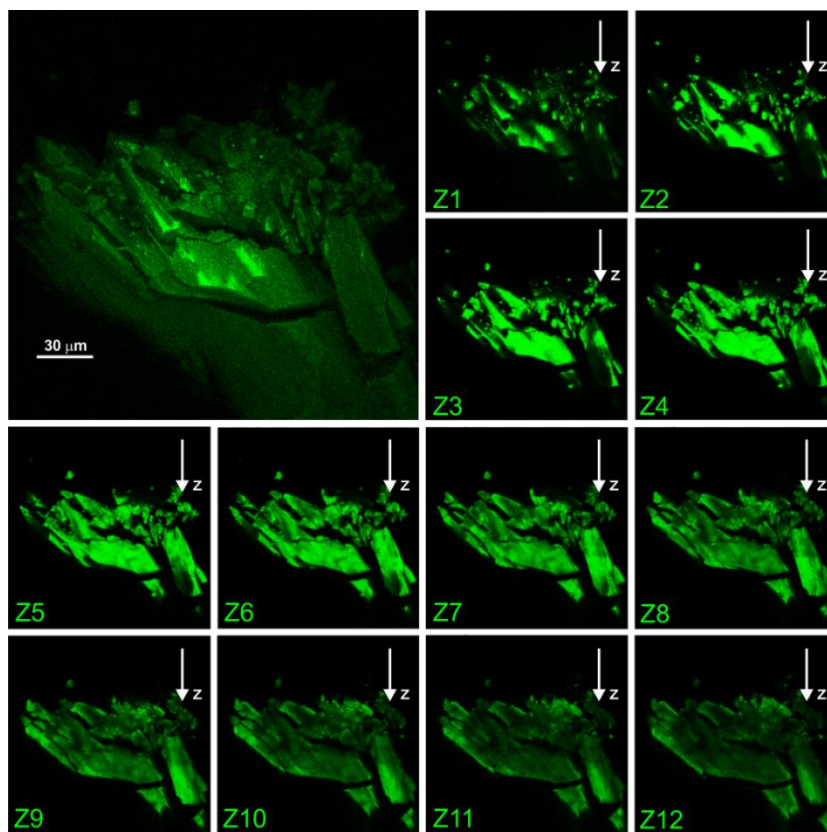


Figure 3.25. Z-stack images recorded on sample **13** for a section of 12 μm (along z-axis, progression of about 1 μm from Z1 to Z12) of the top-left MIP image. Fluorescence is collected in the 500-550 nm range upon material excitation at 488 nm.

3.4 Conclusions

Post-synthetic functionalization methods have been successfully exploited for the preparation of novel multi-decorated MOFs through the simple “click” chemistry procedure (CuAAC). In particular, more than one functional group is introduced into the MOF scaffold *at once*, through the employment of mixtures of alkyne reagents on a well-defined stoichiometric ratio, *that is maintained within the decorated products*. Therefore, a variation of the alkynes molar ratio in the reactive mixture results in a facile and efficient tuning of the grafted functional groups in the final material. Smooth reagents and catalyst diffusion into the material channels, together with the general character of the CuAAC chemistry (*i.e.* its high selectivity and functional group tolerance), play a fundamental role in the achieved control. Both the relatively mild reaction conditions used and the relatively large material pore size contribute to the success and control of the functionalization process. Such a precise control on the functional group loading on the final material network constitutes a key tool for the simple and versatile MOF’s engineering.

3.5 Experimental Section

3.5.1 General Considerations

All manipulations were carried out under dry nitrogen atmosphere using standard Schlenk-type techniques. Nitrogen (> 99.999%; Rivoira) was dried through a CaCl₂ column and deoxygenated with an oxysorb cartridge from Messer Griesheim prior to use. DMF was degassed and stored at room temperature over 4 Å molecular sieves under nitrogen atmosphere. Toluene was obtained by means of a MBraun solvent purification system. 5-ethynyl-*tert*-thiophene was prepared from the 5-bromo-*tert*-thiophene²⁹ in 95 % isolated yield according to a literature procedure.³⁰ All the other chemicals were purchased from commercial suppliers and used as received without further purification. Samples sonication was carried out using an Elma S15 Elmasonic sonicator bath (37 kHz). Filtration was accomplished by using PTFE filter (Whatman) with 0.2 µm pore size.

3.5.2 Material Characterization and Analyses Conditions

Thermogravimetric analysis (TGA) were performed under N₂ atmosphere (50 mL/min) on an EXSTAR Thermo Gravimetric Analyzer (TG/DTA) Seiko 6200 coupled with a ThermoStar™ GSD 301 T (TGA-MS) for the MS analysis of volatiles.

FT-IR spectroscopy was performed on a Perkin-Elmer Spectrum BX FT-IR spectrophotometer and all samples were prepared by mixing spectroscopic grade KBr with either N₃-MOFs or MOF derivatives (3-5 wt. %) and analyzed in the 400-4000 cm⁻¹ range with a resolution of 1 cm⁻¹.

¹H NMR spectra of all the digested MOF samples were recorded on an Avance 300 MHz instrument (300.13 MHz for ¹H). Chemical shifts are reported in ppm (δ) relative to TMS, referenced to the chemical shifts of residual solvent resonances.

Powder X-ray diffraction (PXRD) measurements were carried out in a Bragg-Brentano geometry either with a Panalytical X'PERT PRO powder diffractometer equipped with a PIXcel[®] solid state detector or with a D8 Advance Bruker AXS diffractometer. The diffractograms were recorded at room temperature in the 5-60 ° 2θ region, operating with Cu K_α radiation (λ = 1.5418 Å). A 7.5 mm height anti-scatter slit was used on the diffracted beam. The 2θ step size was 0.0263 °, with a counting time of 317 s/step. The measurements were carried out in air at ambient pressure and temperature.

Fluorescence imaging was performed on an inverted Nikon A1 laser scanning confocal microscope equipped with a 405 nm pulsed/CW diode laser (Picoquant, Germany) and a 488 nm CW Argon ion laser (Melles Griot).

Confocal fluorescence imaging was carried out on the samples at 20 °C. The 5215 x 512 or 1024 x 1024 pixel images were collected using a Nikon PLAN APO VC 60 oil immersion objective with NA 1.40. With this imaging configuration, pixel side dimension ranged from 100 to 250 nm. Z-stack fluorescence imaging was performed on 0.5-1 μm sections for a total thickness of 20-30 μm. Fluorescence was collected in several spectral windows. In front of the photomultiplier we used bandpass filters centered at 450 nm (50), and 525 nm (50). Spectral imaging has been performed using the Nikon A1 spectral detector consisting of a multi-anode photomultiplier with an array of 32 anodes. A wavelength range of 6 or 10 nm per anode has been applied.

BET surface area measurements. N₂ adsorption isotherms were recorded at 77 K (liquid nitrogen bath) on a Micromeritics® ASAP 2020 instrument. Prior to the measurements, the samples were degassed at 100 °C for 16 h.

3.5.3 Preparation of MIXMOF-5-NH₂⁸

2-Aminoterephthalic acid (0.045 g, 0.25 mmol), terephthalic acid (0.125 g, 0.75 mmol) and Zn(NO₃)₂·4H₂O (0.784 g, 3.00 mmol) were dissolved in DMF (50 mL), and the clear solution was divided and transferred into five 20 mL scintillation vials. The vessels were placed in a sand bath and heated into a programmable oven to 105 °C using a gradient of 2.0 °C/min. The temperature was held for 24 h, and after that time the oven was slowly cooled to room temperature. The solvent was decanted, and crystals of MIXMOF-5-NH₂ were washed with DMF (3 x 5 mL) rinsed and soaked in CHCl₃ for 3 days, replacing the solvent every 24 h with fresh one. Finally, the solvent was decanted and the crystals soaked and stored in toluene until needed.

3.5.4 Preparation of UMCM-1-NH₂³¹

2-Aminoterephthalic acid (0.490 g, 2.7 mmol), Zn(NO₃)₂·4H₂O (2.83 g, 10.8 mmol), and 4,4',4''-benzene-1,3,5-triyl-tribenzoic acid (btb, 0.424 g, 0.97 mmol) were dissolved in 100 mL of DMF. The solution was divided into 10 mL portions and transferred into 10 scintillation vials (20 mL capacity each). The vials were placed in a sand bath, and the bath was transferred to an isothermal oven heated at 85 °C. After 48 h, the vials were removed from the oven and left to cool at room temperature. The mother liquor was decanted, and crystals of UMCM-1-NH₂ were washed with DMF (3 x 12 mL) and soaked in CHCl₃ (12 mL) for 24 h. The crystals were then rinsed with fresh CHCl₃ (3 x 10 mL) and left to soak for 3 days in CHCl₃, replacing the solvent every 24 h. The crystals were finally stored wet under CHCl₃ until needed.

3.5.5 Preparation of MIXMOF-5-N₃

Freshly dried MIXMOF-5-NH₂ (28 mg, 0.36 mmol of -NH₂) was placed into a dried vial (20 mL capacity) with 3.0 mL of CHCl₃, 0.29 mL (2.52 mmol, 7 eq) of *tert*-butyl nitrile and 0.26 mL (2.16 mmol, 6 eq) of azidotrimethylsilane under an argon atmosphere. The sample was reacted overnight at room temperature to convert MIXMOF-5-NH₂ into MIXMOF-5-N₃ (quantitative). The reaction was quenched by

decanting the solvent. Excess reactants were removed by washing with CHCl_3 (6 x 4 mL). The crystals were stored in toluene until needed.

3.5.6 Preparation of UMCM-1- N_3

Freshly dried UMCM-1- NH_2 (47 mg, 0.71 mmol equiv of $-\text{NH}_2$) was placed into a dry vial (20 mL capacity) with 6.0 mL of CHCl_3 , 0.58 mL (4.97 mmol, 7 eq) of *tert*-butyl nitrite and 0.52 mL (4.26 mmol, 6 eq) of azidotrimethylsilane (TMSN_3) under an argon atmosphere. The sample was left to react overnight at room temperature to get UMCM-1- N_3 (quantitative). The reaction was quenched by decanting the solvent. Excess reactants were removed by washing with CHCl_3 (6 x 6 mL). The crystals were stored in toluene until needed.

3.5.7 General procedure for the homo-(hetero)-PSM of N_3 -MOFs via CuAAC chemistry

All manipulations were carried out in the dark or keeping all MOF reagents and products away from the direct contact with the light as much as possible. In a typical homo-PSM procedure, crystals of N_3 -MOFs (50 mg) were filtered on a sintered glass frit (pore size 4-5.5 μm) and dried under a stream of N_2 up to constant weight. The semi-dry samples (45 wt. % and 50 wt. % of residual toluene in the UMCM-1- N_3 and MIXMOF-5- N_3 samples, respectively) were then transferred under N_2 atmosphere in a 10 mL Schlenk-tube and suspended in dry and degassed DMF (1 mL). The suspension was then treated with a DMF solution (0.5 mL) of the selected alkyne (1.2 equiv. with respect to the azido groups) or alkynes mixture (in case of hetero-decoration procedure – overall 1.2 equiv. with respect to the azido groups) and maintained at room temperature for 5 hours (impregnation time) while being gently shaken. Afterwards, $\text{CuI}[\text{P}(\text{OEt})_3]$ (0.12 equiv. cat. 10 mol%) was added as a DMF solution (0.3 mL), and the resulting suspension underwent three degassing cycles before being purged with nitrogen. The reaction mixture was finally heated at 85 $^\circ\text{C}$ for 14 h while being gently shaken. The mixture was allowed to cool to room temperature and crystalline derivatives were recovered by successive washing cycles/filtration (over a 0.2 μm PTFE filter) and dried under a stream of N_2 up to constant weight. All homo- (hetero)-decorated materials were stored in the dark as semi-dry samples under N_2 atmosphere, with no apparent decomposition for weeks.

3.5.8 ^1H NMR characterization of MOF's reagents and derivatives

All semi-dried MOF reagents and derivatives were characterized by liquid ^1H NMR spectroscopy after material's "digestion". In a typical procedure, 6 mg of MOF crystals were dissolved in $\text{DMSO-}d_6$ (500 μL) and diluted DCI (100 μL of a solution prepared as follows: 23 μL of 35 % DCI in D_2O diluted with 1 mL of $\text{DMSO-}d_6$) with sonication for a few minutes. After complete MOF dissolution, the clear solution was analyzed by ^1H NMR (d1 = 8 s).

References and Notes

- ¹ a) S. Kitagawa, R. Kitaura, S. Noro, *Angew. Chem. Int. Ed.* **2004**, *43*, 2334. b) J. L. C. Rowsell, O. M. Yaghi, *Microporous Mesoporous Mater.* **2004**, *73*, 3. c) G. Férey, *Chem. Soc. Rev.* **2008**, *37*, 191.
- ² a) D. Britt, D. Tranchemontagne, O. M. Yaghi, *Proc. Natl. Acad. Sci. U. S. A.* **2008**, *105*, 11623. b) J.-R. Li, R. J. Kuppler, H.-C. Zhou, *Chem. Soc. Rev.* **2009**, *38*, 1477. c) A. Rossin, B. Di Credico, G. Giambastiani, L. Gonsalvi, M. Peruzzini, G. Reginato, *Eur. J. Inorg. Chem.* **2011**, 539. d) A. Rossin, B. Di Credico, G. Giambastiani, M. Peruzzini, G. Pescitelli, G. Reginato, E. Borfecchia, D. Gianolio, C. Lamberti, S. Bordiga, *J. Mater. Chem.* **2012**, *22*, 10335.
- ³ a) J. Lee, O. K. Farha, J. Roberts, K. A. Scheidt, S. T. Nguyen, J. T. Hupp, *Chem. Soc. Rev.* **2009**, *38*, 1450. b) A. Corma, H. García, F. X. Llabrés i Xamena, *Chem. Rev.* **2010**, *110*, 4606. c) M. Ranocchiari, J. A. van Bokhoven, *Phys. Chem. Chem. Phys.* **2011**, *13*, 6388.
- ⁴ R. C. Huxford, J. Della Rocca, W. Lin, *Curr. Opin. Chem. Biol.* **2010**, *14*, 262.
- ⁵ a) W. Kleist, M. Maciejewski, A. Baiker, *Thermochim. Acta* **2010**, *499*, 71. b) W. Kleist, F. Jutz, M. Maciejewski, A. Baiker, *Eur. J. Inorg. Chem.* **2009**, 3552. c) S. Marx, W. Kleist, J. Huang, M. Maciejewski, A. Baiker, *Dalton Trans.* **2010**, *39*, 3795. d) T. Lescouet, E. Kockrick, G. Bergeret, M. Pera-Titus, S. Aguado, D. Farrusseng, *J. Mater. Chem.* **2012**, *22*, 10287. e) H. Deng, C. J. Doonan, H. Furukawa, R. B. Ferreira, J. Towne, C. B. Knobler, B. Wang, O. M. Yaghi, *Science* **2010**, *327*, 846. f) M. Kim, J. A. Boissonnault, P. V. Dau, S. M. Cohen, *Angew. Chem., Int. Ed.* **2011**, *50*, 12193.
- ⁶ a) Z. Wang, S. M. Cohen, *Chem. Soc. Rev.* **2009**, *38*, 1315. b) S. M. Cohen, *Chem. Rev.* **2012**, *112*, 970.
- ⁷ a) Z. Wang, S. M. Cohen, *J. Am. Chem. Soc.* **2007**, *129*, 12368. b) K. K. Tanabe, Z. Wang, S. M. Cohen, *J. Am. Chem. Soc.* **2008**, *130*, 8508. c) M. Kandiah, S. Usseglio, S. Svelle, U. Olsbye, K. P. Lillerud, M. Tilset, *J. Mater. Chem.* **2010**, *20*, 9848. d) T. Ishiwata, Y. Furukawa, K. Sugikawa, K. Kokado, K. Sada, *J. Am. Chem. Soc.* **2013**, *135*, 5427.
- ⁸ M. Servalli, M. Ranocchiari, J. A. van Bokhoven, *Chem. Commun.* **2012**, *48*, 1904.
- ⁹ a) Y. Goto, H. Sato, S. Shinkai, K. Sada, *J. Am. Chem. Soc.* **2008**, *130*, 14354. b) T. Gadzikwa, O. K. Farha, C. D. Malliakas, M. G. Kanatzidis, J. T. Hupp, S. T. Nguyen, *J. Am. Chem. Soc.* **2009**, *131*, 13613. c) M. Savonnet, D. Bazer-Bachi, N. Bats, J. Perez-Pellitero, E. Jeanneau, V. Lecocq, C. Pinel, D. Farrusseng, *J. Am. Chem. Soc.* **2010**, *132*, 4518. d) H.-L. Jiang, D. Feng, T.-F. Liu, J.-R. Li, H.-C. Zhou, *J. Am. Chem. Soc.* **2012**, *134*, 14690. e) M. Savonnet, E. Kockrick, A. Camarata, D. Bazer-Bachi, N. Bats, V. Lecocq, C. Pinela, D. Farrusseng, *New J. Chem.* **2011**, *35*, 1892. f) M. Savonnet, A. Camarata, J. Canivet, D. Bazer-Bachi, N. Bats, V. Lecocq, C. Pinela, D. Farrusseng, *Dalton Trans.* **2012**, *41*, 3945.
- ¹⁰ K. Koh, A. G. Wong Foy, A. J. Matzger, A. G. Wong-Foy, *Angew. Chem. Int. Ed.* **2008**, *47*, 677.
- ¹¹ H. Li, M. Eddaoudi, M. O'Keeffe, O. M. Yaghi, *Nature* **1999**, *402*, 276.

-
- 12 a) V. V. Rostovtsev, L. G. Green, V. V. Fokin, K. B. Sharpless, *Angew. Chem.* **2002**, *114*, 2708; *Angew. Chem. Int. Ed.* **2002**, *41*, 2596. b) X. Li, *Chem. Asian J.* **2011**, *6*, 2606.
- 13 a) C. W. Tornøe, M. Meldal, in *The Wave of the Future* (Ed.: M. Lebl, R. A. Houghten), San Diego: American Peptide Society and Kluwer Academic Publishers, **2001**, 263. b) C. W. Tornøe, C. Christensen, M. Meldal, *J. Org. Chem.* **2002**, *67*, 3057.
- 14 G. Tuci, C. Vinattieri, L. Luconi, M. Ceppatelli, S. Cicchi, A. Brandi, J. Filippi, M. Melucci, G. Giambastiani, *Chem. Eur. J.* **2012**, *18*, 8454.
- 15 M. Ranocchiaro, C. Lothschütz, D. Grolimund, J. A. van Bokhoven, *Proc. R. Soc. A* **2012**, *468*, 1985.
- 16 a) K. K. Tanabe, S. M. Cohen, *Angew. Chem. Int. Ed.* **2009**, *48*, 7424. b) Z. Wang, K. K. Tanabe, S. M. Cohen, *Chem. Eur. J.* **2010**, *16*, 212.
- 17 PSMs with anhydrides and aldehydes have been already documented with both materials. See also refs. 8, 16.
- 18 E. Lieber, C. N. Ramachandra Rao, T. S. Chao, C. W. W. Hoffman, *Anal. Chem.* **1957**, *29*, 916.
- 19 The high (C+O)/N ratio of **3** and **4** makes these MOFs absolutely safe, handling and harmless materials. See also S. Bräse, C. Gil, K. Knepper, V. Zimmermann, *Angew. Chem. Int. Ed.* **2005**, *44*, 5188.
- 20 This treatment does not allow for a complete removal of toluene from the material pores and channels. An average residual content of toluene (calculated on three separate batches) of 45 wt. % and 50 wt. % is measured by ¹H NMR spectroscopy (of the digested samples).
- 21 F. Himo, T. Lovell, R. Hilgraf, V. V. Rostovtsev, L. Noodleman, K. B. Sharpless, V. V. Fokin, *J. Am. Chem. Soc.* **2005**, *127*, 210.
- 22 a) D. G. Hamilton, D. E. Lynch, K. A. Byriel, C. H. L. Kennard, *Aust. J. Chem.* **1997**, *50*, 439. b) M. M. Bishop, L. F. Lindoy, B. W. Skelton, A. H. White, *J. Chem. Soc., Dalton Trans.* **2002**, 377. c) J. Janczak, R. Kubiack, *Acta Cryst. E* **2007**, *63*, o2627.
- 23 J. Hafizovic, M. Bjørgen, U. Olsbye, P. D. C. Dietzel, S. Bordiga, C. Prestipino, C. Lamberti, K. P. Lillerud, *J. Am. Chem. Soc.* **2007**, *129*, 3612.
- 24 A. Shaygan Nia, C. Enders, W. H. Binder, *Tetrahedron* **2012**, *68*, 722.
- 25 Terephthalic acid is known to emit only weakly, with a maximum at 360 nm. Substituents on the α position of the aromatic ring generate a red-shifted unstructured emission with a maximum at ca. 436 nm. See also ref. K. Ishibashi, A. Fujishima, T. Watanabe, K. Hashimoto, *J. Photochem. Photobiol. A: Chemistry* **2000**, *134*, 139.
- 26 α -terthiophene has an absorption maximum at ca. 353 nm with $\epsilon \approx 22000$ and a vibronically structured fluorescence spectrum with maxima at 407 and 426 nm (see ref. R. S. Becker, J. S. de Melo, A. L. Macüanita, F. Elisei, *J. Phys. Chem.* **1996**, *100*, 18683); imidazole and triazole α -substituted terthiophene display red-shifted absorption and fluorescence peaks (see ref. A. Shaygan Nia, C. Enders, W. H. Binder, *Tetrahedron* **2012**, *68*, 722.)

-
- 27 As reported for the homo-functionalized samples, one main distinctive feature of the hetero-functionalized MOFs is represented by the disappearance of initial weight loss in the 170-220 °C temperature range and ascribable to the thermal N₃ decomposition followed by N₂ evolution.
- 28 For the sake of completeness, the hetero-functionalization study has been carried out on both selected N₃-MOFs. Although the outcomes unambiguously demonstrate the general applicability of the protocol irrespective of the N₃-MOF system used, the reduced N₃ loading in **4** translates into ¹H NMR spectra featured by relatively low signal/noise ratio.
- 29 M. Melucci, G. Barbarella, M. Zambianchi, P. Di Pietro, A. Bongini, *J. Org. Chem.* **2004**, *69*, 4821.
- 30 X. Zhao, C. Piliago, B.-S. Kim, D. A. Poulsen, B. Ma, D. A. Unruh, J. M. J. Fréchet, *Chem. Mater.* **2010**, *22*, 2325.
- 31 Z. Wang, K. K. Tanabe, S. M. Cohen, *Inorg. Chem.* **2009**, *48*, 296.

4. A Hetero-bi-Functional Spacer for the Smart Engineering of Carbon-based Nanostructures

4.1 Abstract

Big efforts have been made in recent years to develop novel functionalization protocols aimed at imparting multimodality and improved properties to complex carbon-based nanostructures. Relatively unexplored is the incorporation of cleavable bonds to the nanomaterial surface for the controlled release (or exchange) of specific molecules under appropriate chemical and biological settings. In this chapter, we describe the design and synthesis of a hetero-bi-functional linker joining a “cleavable” disulfide moiety for the covalent anchoring of a wide range of thiol end-capped (bio)molecules and a “clickable” terminal acetylene group. The strategy lies on the well-established Cu-mediated acetylene-azide coupling (CuAAC) reaction between the acetylene linker and single-walled carbon nanotubes (SWCNTs) decorated with phenylazido pendant arms. This chemical approach is very versatile and it allows for a fine control of the carbon nanomaterial functionalization and post-derivatization degree. Indeed, the disulfide “bond cleavage”, operated by sulfhydryl containing molecules, occurs with the *controlled release* of a pyridine-dye whose concentration is proportional to the extent of cleavage or conjugation by an incoming thiol end-capped molecule. A controlled CNT hetero-decoration with the bi-functional linker in mixture with selected terminal acetylene molecules is exploited to impart multimodality (*i.e.* multifunctionality) to the final carbon nanohybrids. As a result, easily “post-derivatizable” and traceable nanostructured platforms containing a linking group potentially available for a wide range of biological probes are prepared and completely characterized.

4.2 Introduction

Many efforts have been devoted in the last two decades to the development of effective and simple functionalization schemes for 1D and 2D carbon nanostructures with the final aim of improving their processability and handling as well as imparting

multimodality to the resulting hybrids.¹ In particular, carbon nanotubes (CNTs) have been widely explored as substrates for a number of functionalization protocols to afford decorated nanostructured systems with unique chemico-physical properties.² Potential applications of the as prepared CNT-based hybrids are envisaged in different technological fields: from the preparation of nanocomposite materials with improved properties³ and their exploitation in nanomedicine for drug delivery,⁴ therapy and imaging,⁵ to their use as catalytic materials in specific fields of renewable energies technology.⁶ In spite of a number of well-established CNT functionalization protocols,⁷ the development of new synthetic methodologies that lead to a more efficient integration of these nanomaterials into complex functional structures still represents a challenging research matter in the field. In particular, the incorporation of functionalities containing cleavable bonds (under appropriate chemical and/or biological settings) represents a step-forward towards the smart engineering of these nanostructures.⁸ A controlled molecular exchange at the CNT surface is still a relatively unexplored field; on the other hand it can offer a unique strategy to the *controlled release* of specific guest molecules initially linked to the surface of the nanomaterial carrier (CNT). For instance, Dai and co-workers have demonstrated how the intracellular delivery of CNT-based bioconjugates and the subsequent release of the biological probe from the nanocarrier (CNT) can be smartly triggered by a selective disulfide bond cleavage operated by thiol reducing enzymes.⁹ Similarly, You *et al.* have demonstrated how chemically decorated CNTs can easily conjugate and release biological molecules at will, according to specific biological or chemical stimuli.¹⁰ Both technologies conceptually lie on the design and synthesis of a “cleavable” linker for the covalent anchoring of a wide range of thiol end-capped biomolecules (including DNA, RNA and proteins).

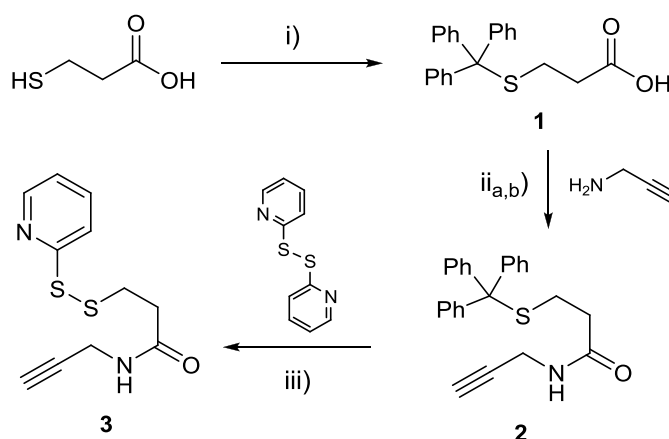
In chapter 2 we have already exploited the preparation of flexible and versatile “CNT platforms” chemoselectively decorated with aryl-azido pendant arms;¹¹ their exploitation in combination with variably substituted terminal acetylenes (or mixtures thereof), under classical bioorthogonal CuAAC conditions,¹² has provided a valuable protocol for a controlled single-step homo- and hetero-functionalization of the SWCNT sidewalls.¹³ In this chapter, the easy-to-scale-up synthesis of a simple organic linker joining a “cleavable” disulfide moiety and a “clickable” terminal acetylene group is described. Its chemistry is fully investigated in the homogeneous phase by means of model reaction protocols before being “clicked” at the surface of the above mentioned

f_{N3} -SWCNT platforms. The data reported hereafter describe a functionalization scheme capable of imparting multimodality (*i.e.* multifunctionality) to 1D carbon nanostructures while they operate as nanocarriers for potential biological probes. The CNT conjugation with thiol end-capped biomolecules is conveniently followed spectroscopically by monitoring the appearance of a characteristic absorbance peak(s) due to the release in solution of the pyridine-2-thiol (or pyridine-2-thione) as side-reaction product(s). While simple UV-vis measurements allow for a precise estimation of the CNT-covalently grafted biomolecule loading, an appropriate hetero-decoration of the nanomaterial with a selected fluorescence dye (BODYPy-derivative) generates an optically traceable bioconjugate. In addition, this study offers interesting insights on the role of the grafted molecules on the ultimate material morphology while providing a clear evidence of the distribution of the phenyl-azido groups at the CNT surface as a consequence of the aryl-diazonium salts regiochemistry.

4.3 Results and Discussion

4.3.1 Synthesis of the hetero-bi-functional spacer **3**

The approach to this study starts with the gram-scale synthesis of the hetero-bi-functional cross-linker **3**. Scheme 4.1 illustrates the stepwise procedure developed to prepare the desired acetylene derivative in fairly good yield (51 % over three steps).

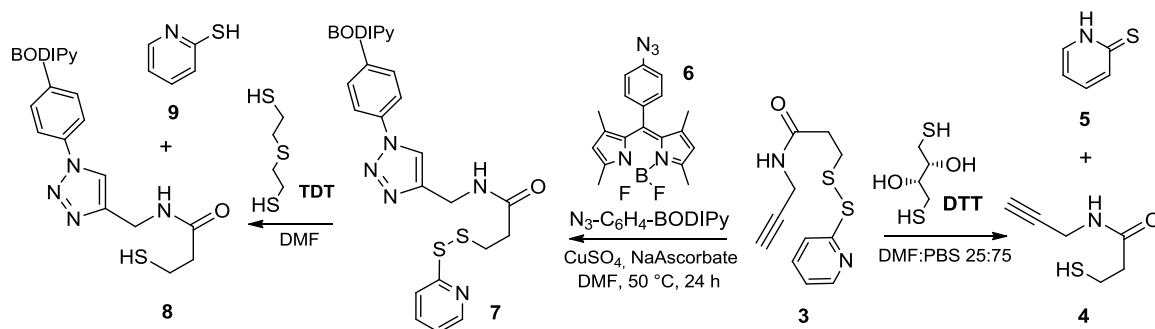


Scheme 4.1. Synthesis of the acetylene spacer **3**. Reagents and conditions: i) Ph_3CCl , CH_2Cl_2 , r.t., overnight;¹⁴ ii_a) DCC, HOBT, DMF, r.t. 3h. ii_b) propargylamine, Et_3N , DMF, 24 h; iii) 1,2-di(pyridin-2-yl)disulfane (2-aldrithiolTM), Et_3SiH , TFA, CH_2Cl_2 , r.t. 5 h.

According to this synthetic path, the 3-tritylsulfanyl-propanamide (**2**) is straightforwardly prepared through an initial sulfhydryl trityl protection of the commercially available 3-mercaptopropionic acid followed by a one-pot activation/amidation of the carboxylic acid (DCC, HOBT, propargylamine) to give the acetylene intermediate as a white solid in 82 % isolated yield over two steps. At odds with several literature precedents,^{14,15,16,17} all our attempts to get the free alkyl-thiol intermediate by sulfhydryl deprotection of the isolated **2** failed. Indeed, the reaction of **2** with Et₃SiH and TFA gave, upon solvent evaporation, only untreatable rubbery materials. On the contrary, the one-pot addition¹⁸ of the 2-aldrithiolTM reagent to a CH₂Cl₂ solution of **2**, followed by treatment with Et₃SiH and TFA, gives the desired product **3** as a viscous pale yellow oil in 62 % isolated yield after chromatographic purification.

4.3.2 Reactivity study on the hetero-bi-functional cross-linker **3** in homogeneous phase

Before applying **3** to the homo- and hetero-decoration of complex carbon nanostructures, the reactivity of its terminal functionalities is scrutinized and optimized in homogeneous phase in combination with model reactants (Scheme 4.2). To verify the reactivity at the disulfide linkage in **3**, a solution of dithiothreitol (DTT) is added to cleave and reduce the disulfide bridge, leading to the free sulfhydryl derivatives **4** with the simultaneous release of one equivalent of pyridine-2-thione (**5**). The reaction is performed in a 25:75 DMF:PBS (dimethylformamide:phosphate buffer saline) solution at pH 7.2, where the cleavage proceeds quantitatively. DMF is used to improve the solubility of **3** and the reaction course is conveniently followed by UV-vis measurements.



Scheme 4.2. Reactivity tests on the hetero-bi-functional cross-linker **3**. Optimized conditions for the S-S cleavage and CuAAC reaction in homogeneous phase.

Two solutions at different concentration of **3** ($1 \cdot 10^{-4}$ and $5 \cdot 10^{-5}$ M) have been prepared and treated with DTT. The UV-vis measurements on the solutions, before (blank samples – dashed lines) and after DTT treatment (solid lines), show the appearance of a clear absorbance (A) peak at 343 nm (Figure 4.1A), typical of the pyridine-2-thione moiety, whose intensity is proportional to the extent of occurred disulfide cleavage (see section 4.5).

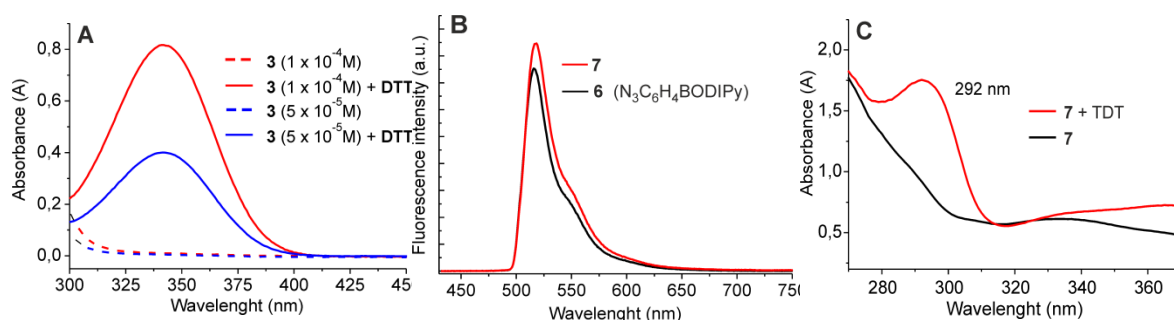
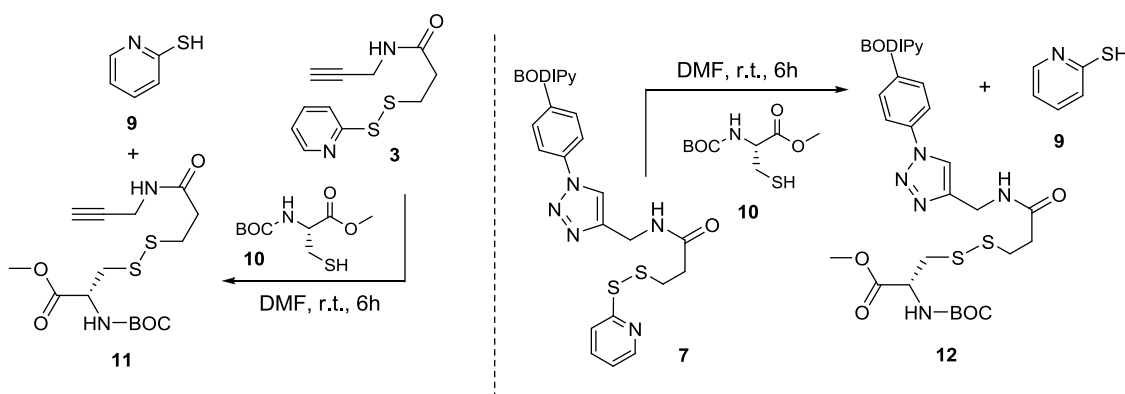


Figure 4.1. A) UV-vis measurements on **3** solutions at different concentration, before and after DTT (20-fold excess) treatment. B) Fluorescence measurements on **6**, before and after (**7**) CuAAC reaction; the excitation scattering light is eliminated by means of a long-pass filter setup (cut-on 500 nm) – see section 4.5. C) UV measurements on a **7** solution, before and after TDT (20-fold excess) treatment.

According to the UV-vis measurements, for both solutions a quantitative disulfide cleavage takes place already at room temperature within few minutes. Optimized CuAAC conditions have also been set-up in homogeneous phase between the terminal acetylene moiety on **3** and the model BODIPy phenylazido derivative **6**. Different Cu^I , Cu^{II} -based catalysts have been systematically scrutinized under classical reaction protocols to afford the cycloaddition product in fairly good yields. Among these, both $CuSO_4/Na$ -ascorbate/DMF and $(EtO)_3P/CuI/DMF$ gave almost identical yields, while other soluble Cu^I sources like $CuI/DBU/DMF$ resulted into moderately lower chemical yields for **7**. A fluorescence study is performed on **6**, before and after the CuAAC reaction (**7**) as to assess the effect of the triazole “linker” on the dye fluorescence emission properties. As Figure 1B shows, the fluorescence of the dye is invariably maintained in the cycloaddition product **7**.¹⁹ Finally, the cleavage of the disulfide bridge is quantitatively achieved at room temperature in a few minutes upon treatment with 2,2'-thiodiethanethiol (**TDT**) as reagent (Scheme 4.2). The scarce solubility of **7** in protic media requires a modification of the cleavage conditions as well as the use of the more lipophilic **TDT**. The reaction is performed in pure DMF and the process is

systematically followed by UV measurements. A clear absorbance peak at 292 nm, due to the preferred pyridine-2-thiol isomer (**9**) in aprotic solvents,²⁰ is observed, without any interference with the absorbance wavelengths of the BODIPy dye (Figure 4.1C).

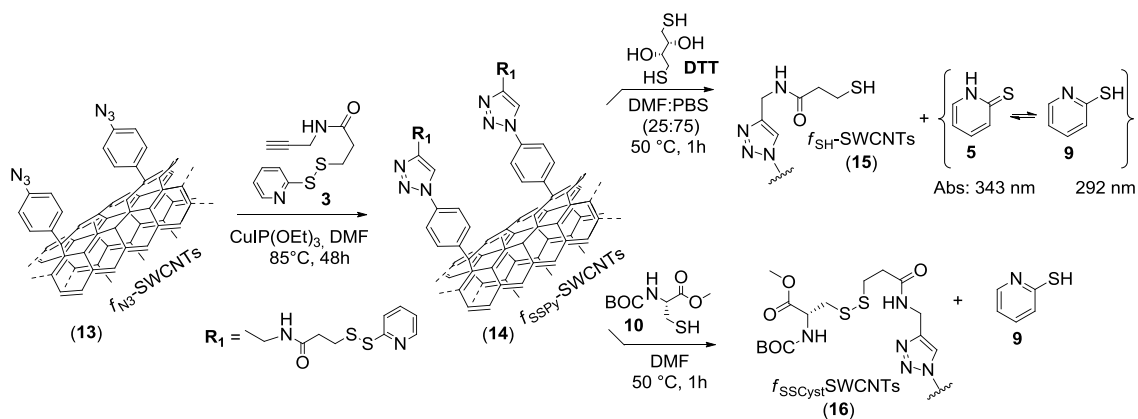
For the sake of completeness, both the spacer **3** and the intermediate **7** have been reacted with the protected natural L-aminoacid **10** [*N*-(*tert*-Butoxycarbonyl)-L-cysteine methyl ester] selected as a mimic of a sulfhydryl terminating residue of a more complex protein chain (Scheme 4.3). On both systems, the reaction with **10** proceeds smoothly, leading to a complete conjugation of the protected L-aminoacid through the disulfide bond after stirring the mixture in DMF at r.t. over 6 h. Similarly to above, the reaction course is followed spectroscopically till completeness by monitoring the appearance of the absorbance peak at 292 nm due to the generation of the pyridine-2-thiol species (**9**). Reactions work-up and chromatographic purification of the crude mixtures gave the conjugated compounds **11** and **12** in 62 % and 39 % isolated yield, respectively.



Scheme 4.3. Reaction of a model sulfhydryl terminating aminoacid **10** [*N*-(*tert*-Butoxycarbonyl)-L-cysteine methyl ester] on **3** and **7** and isolation of the respective conjugated compounds **11** and **12**.

4.3.3 Homo- and hetero-decoration of f_{N3} -SWCNTs; towards multifunctional carbon nanotube platforms

As a natural step forward towards the covalent homo and hetero-decoration of complex carbon nanostructures, the hetero-bi-functional cross-linker **3** is employed in combination with “CNT platforms” decorated with aryl-azido pendant arms according to the protocol developed in chapter 2. The exploited post-functionalization methodology relies on the preliminary covalent anchoring of **3** to the CNT sidewalls using a Cu^I-mediated azide-alkyne cycloaddition protocol (CuAAC) (Scheme 4.4).



Scheme 4.4. CuAAC reaction between the arylazido-decorated f_{N_3} -SWCNTs (**13**) and the alkyne-terminated spacer **3**. Post-derivatization of the **14** intermediate by either disulfide cleavage (**14** \rightarrow **15**) or conjugation with a HS-terminating aminoacid residue of a model protein chain (**14** \rightarrow **16**).

In a typical procedure, **3** and the f_{N_3} -SWCNTs (**13**) are reacted in degassed DMF at 85 °C for two days in the presence of a catalytic amount (10 mol% respect to **3**) of the soluble Cu^I source $\text{CuI}[\text{P}(\text{OEt})_3]$. No appreciable changes (in terms of either chemical conversion or work-up/purification procedures) are observed when the reaction was run using CuSO_4/Na -ascorbate as catalyst. The reaction stoichiometry was arbitrarily fixed to 1 : 5 mol% between the estimated azido groups at the CNTs and the acetylene moiety of **3**, respectively. The catalyst amount was more precisely tuned and fixed to 10 mol% with respect to the reactive terminal alkyne. Finally, the functionalized material (**14**) undergoes successive sonication/centrifugation/washing cycles and filtration through a 0.2- μm -pore inorganic membrane before being dried under vacuum to constant weight. Afterwards, a selective disulfide bond chemical cleavage is performed on **14**, upon treatment with **DTT** in a 25:75 DMF:PBS solution (Scheme 4.4). The reaction is followed spectroscopically by monitoring the evolution of **9** (and **5** - *vide infra*) till completeness after 1 h at 50 °C. In opposition to the homogeneous process, the disulfide cleavage in **14** does not proceed quantitatively at room temperature, even after several hours, while a gentle heating of the reaction mixture rapidly drives the process to completeness (Scheme 4.4; **14** \rightarrow **15**). Similarly to the disulfide cleavage, the CNT conjugation with a natural L-aminoacid **10** [*N*-(*tert*-Butoxycarbonyl)-L-cysteine methyl ester] containing a sulfhydryl moiety (selected as a HS-terminating residue of a model protein chain) is achieved upon reaction under almost identical conditions (Scheme 4.4; **14** \rightarrow **16**). The reaction course is again followed spectroscopically, on the basis of the

dyes evolution (**5**, **9**). In a typical procedure, the crude mixture containing either f_{SH} -SWCNTs (**15**) or $f_{SS_{Cyst}}$ -SWCNTs (**16**) is centrifuged to remove the suspended solid material, and the reaction course is monitored by sampling 1 mL of the clear supernatant and analyzing it by UV-vis spectroscopy. Figure 4.2 shows the UV-vis measurements on the solutions before (gray dashed lines) and after treatment with a thiol (red solid lines for treatment with **DTT** and **10**). In the case of **DTT**, the red line highlights the appearance of two absorbance peaks at 292 and 343 nm (Figure 4.2A), due to the coexistence of the two tautomeric forms of the pyridine-based dye in solution (**5** and **9**); the relative intensities measured account for the complete cleavage/conjugation processes (see section 4.5). As expected for aprotic reaction media, only **9** results from the treatment of **14** with **10** (Figure 4.2B).

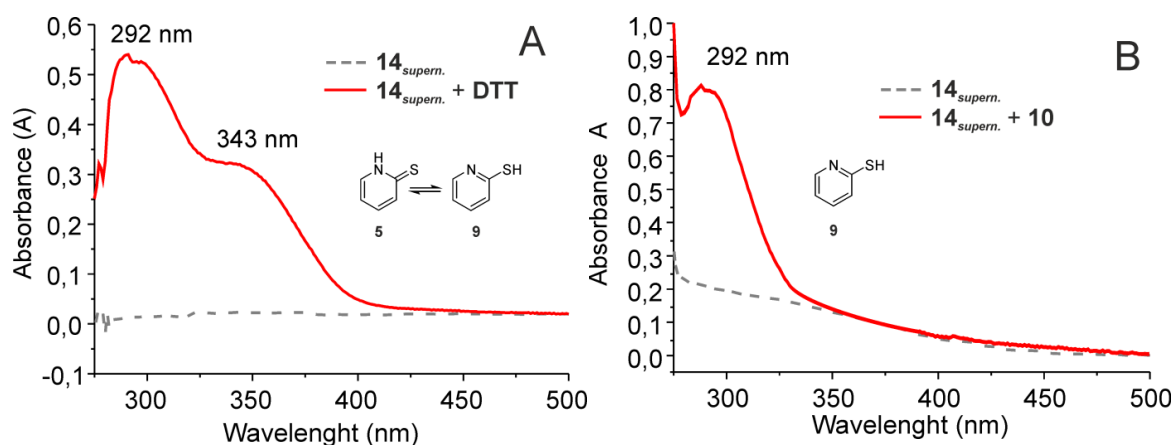


Figure 4.2. UV-vis measurements on the reaction supernatant before and after treatment of **14** with a selected thiol: (A), **DTT**, 20-fold excess or (B), **10**, 5-fold excess.

The functionalized nanomaterials **14** and **16** have been characterized through different chemical (elemental analysis) spectroscopic/spectrometric (FT-IR, TGA-MS) and morphological (TEM) techniques. A first evidence of the occurred Cu-mediated azide-alkyne cycloaddition to give **14** is qualitatively achieved by comparing the TGA-MS profile of **14** with that of the starting material f_{N_3} -SWCNTs (**13**) (Figure 4.3). For the sake of consistency, all comparative measurements have been done on a starting material (**13**) that underwent identical reaction conditions and reagents except for the use of the copper catalyst (“blank sample”).

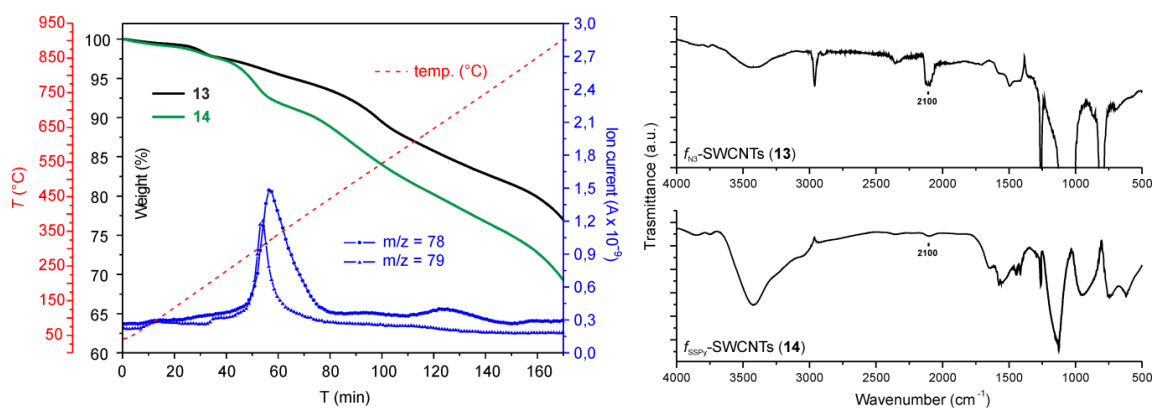


Figure 4.3. (left) TGA profiles (N_2 atm., 50 mL min^{-1}) of **13** and **14** associated with the MS analysis of volatiles (m/z 78 and m/z 79) from **14**. (right) FT-IR spectra of **13** and **14**.

As Figure 4.3 (left) shows, a weight loss of 13.7 % has been measured on sample **14** in the 200-450 °C temperature range (calculated as the weight difference between the TGA profiles of **13** and **14**). Most importantly, the analysis of volatiles in the same temperature range reveals the appearance of two distinctive fragmentation peaks, typical of pyridine units (m/z 79 M^+ ; m/z 78 M^+-1) and exclusively present in sample **14**. At higher temperatures (> 450 °C), only gradual, comparable and not distinctive weight losses are observed for the two materials. The N and C quantitative elemental analysis [f_{N_3} -SWCNTs (**13** - blank sample): N, 2.67; C, 87.71; S, 0.06; f_{SSPy} -SWCNTs (**14**): N, 3.31; C, 77.99; S, 2.70) also provides evidence of the occurred functionalization.²¹ From the TGA measurements, it can be inferred that about 0.543 mmol of $-C_6H_4-(C_2HN_3)-CH_2NHCO(CH_2)_2S_2(C_6H_5N)$ pendant arm *per g* of **13** are consumed in the 200-450 °C temperature range.²² This is in good agreement with the functionalization loading measured from the elemental analysis, where 0.412 and 0.473 mmol are calculated from the S and N contents, respectively. In addition, FT-IR spectrum of sample **14** clearly shows an almost complete suppression of the relatively intense $\nu(N_3)$ asymmetric stretching close to 2100 cm^{-1} (Figure 4.3, right), accounting for an only minor residual amount of $-C_6H_4-N_3$ groups, not reactive under the adopted CuAAC conditions.

For the reaction with **10**, a qualitative evidence of the occurred L-aminoacid grafting is similarly provided by the comparison of the TGA profiles of **14** and **16** and the respective MS analysis of volatiles. As shown in Figure 4.4, the TGA profile of **16** do not show any distinctive weight loss in the 40-900 °C temperature range but only a gradual decomposition takes place. If only an extra and not distinctive 6.4 % weight loss can be measured at the end of the TGA analysis on **16**, the MS analysis of volatiles

gives more clear evidence of the L-cysteine conjugation. Indeed, MS peaks due to the pyridine units (m/z 79 M^+ ; m/z 78 M^+-1) are totally suppressed in **16**, while two new and distinctive fragmentation peaks due to the thermal decomposition and rearrangement of the *tert*-butoxyl groups of the *N*-Boc protecting moieties (m/z 56 M^+ ; m/z 55 M^+-1 relative to the isobutene evolution) clearly grow-up (Figure 4.4).

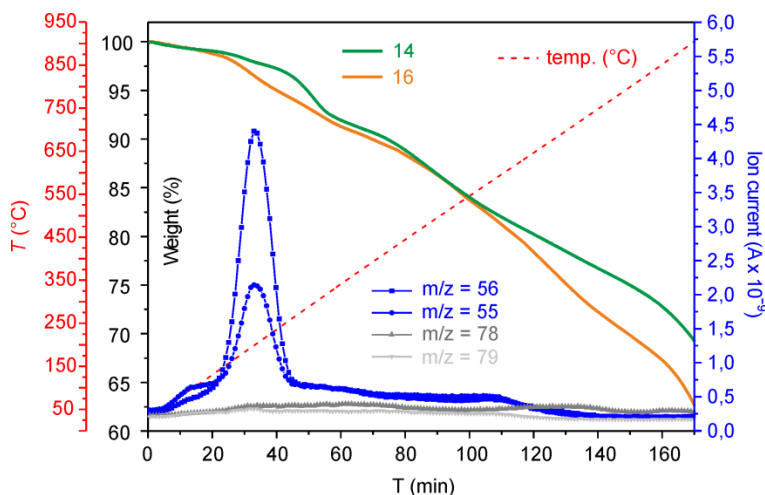
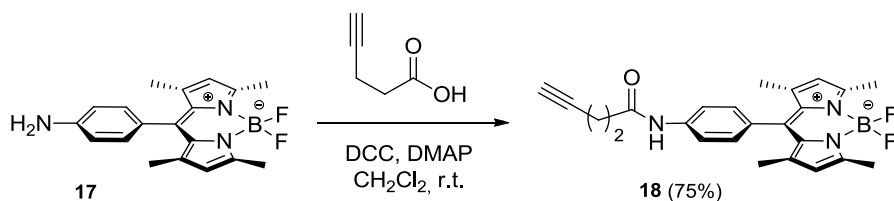


Figure 4.4. TGA profiles (N_2 atm., 50 mL min^{-1}) of **14** and **16** associated with the MS analysis of volatiles (m/z 55, m/z 56, m/z 78 and m/z 79) from **16**.

Similarly to above, the CNT hetero-decoration is performed by reacting the f_{N3} -SWCNTs (**13**) with a controlled mixture of selected alkyne end-capped molecules. At odds with our previous outcomes in the field, the final goal of this study goes beyond the production of complex carbon nanostructures with broad chemical diversity, but it aims at providing functional nanomaterials as easily and cleanly post-derivatizable macromolecular fluorescent probes. With this aim, the alkyne derivative **18** of the fluorescent BODIPy scaffold is conveniently prepared in fairly good yield and in a single reaction step from the BODIPy aniline²³ **17** and 4-pentynoic acid, under classical amidation conditions (Scheme 4.5).



Scheme 4.5. Synthesis of an alkyne terminated BODIPy scaffold from the BODIPy aniline **17**.

Similarly to related BODIPy derivatives,^{23d} the amidation reaction does not affect significantly the fluorescent properties of the BODIPy core (Figure 4.5).^{23a}

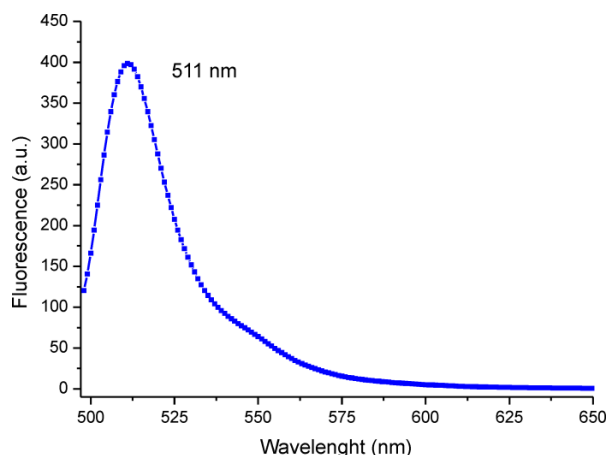
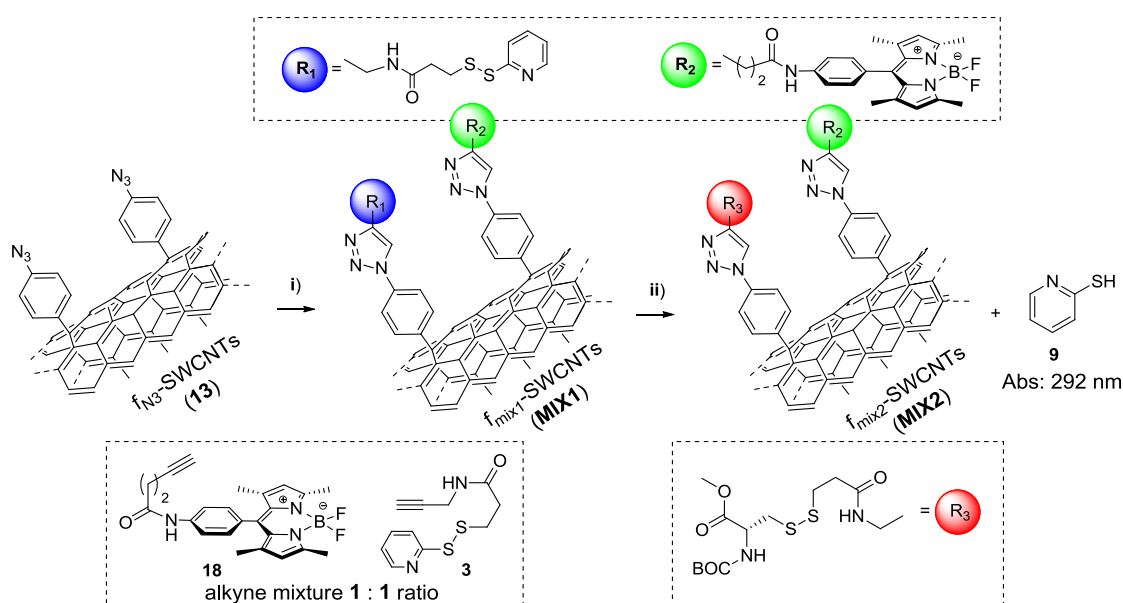


Figure 4.5. Fluorescence spectrum of the alkyne-BODIPy derivative **18**.

The chemical approach to the CNT hetero-decoration via CuAAC chemistry consists in the use of an equimolar mixture of the two acetylene end-capped molecules **18** and **3** (Scheme 4.6); the total amount (mmol) of the acetylene reactants is kept equal to that used in the homo-decoration experiment.²⁴



Scheme 4.6. Hetero-decoration via CuAAC reaction between the arylazido-functionalized f_{N_3} -SWCNTs (**13**) and a 1:1 ratio mixture of the alkyne-terminated spacer **3** and BODIPy fluorescent derivative **18**. (i) **13** (0.020 g), **18:3** = 1:1 ratio (0.17 mmol overall), Cu[P(OEt)₃] (0.017 mmol), DMF, 85 °C, 48 h. Post-derivatization of the f_{MIX1} -SWCNTs via conjugation with a HS-terminating amino acid residue (f_{MIX1} -SWCNTs → f_{MIX2} -SWCNTs). (ii) **10** (0.05 mmol), DMF, 50 °C, 1 h.

In a typical procedure, **18**, **3** and the f_{N3} -SWCNTs (**13**) are reacted in degassed DMF at 85 °C for two days in the presence of a catalytic amount (10 mol% respect to the alkynes content) of the soluble Cu^I source CuI[P(OEt)₃]. Successive and multiple sonication/centrifugation/washing cycles are accomplished on the hetero-functionalized material **MIX1** to remove the unreacted alkynes and physisorbed reagents. Filtration/washing through a 0.2- μ m-pore inorganic membrane is used to recover the sample and the solid is finally dried under vacuum up to constant weight. Afterwards, **MIX1** undergoes reaction with the sulfhydryl-containing L-aminoacid **10** under a gentle heating and the process (**MIX1** vs. **MIX2**) is followed spectroscopically on the basis of the formation of the by-product **9**. The UV-vis measurements on the reaction solutions, before (gray dashed lines) and after treatment with **10** (blue solid line), clearly show the appearance of an absorbance peak at 292 nm (Figure 4.6 left), due to the release of the pyridine-based dye **9**; assuming a complete covalent grafting of **10** to the nanotubes through the disulfide bridge (*vide infra*), the measured absorbance intensity accounts for the functionalization loading of **3**. The fluorescence spectra (Figure 4.6 right) recorded upon excitation of the solid samples at 488 nm, before (**MIX1**) and after (**MIX2**) addition of **10**, are consistent with samples which maintain their fluorescence properties almost unchanged.

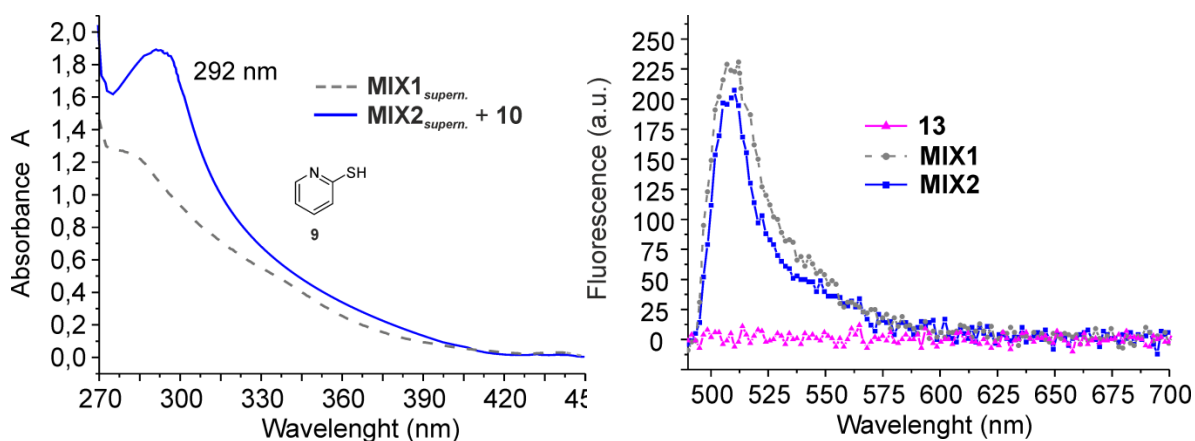


Figure 4.6. (left) UV-vis measurements on the reaction supernatant before (dashed gray line) and after (blue solid line) treatment of **MIX1** with **10**. (right) Fluorescence spectra of **MIX1** and **MIX2**.

For the sake of completeness, the effect of the dye covalent grafting to the surface of SWCNTs on its fluorescence properties, has been discussed in brief. A remarkable decrease of the dye fluorescence signal is commonly observed on nanotube-dye hybrids,

where the support itself (CNT) as well as the presence of metal impurities (coming from the CNT synthesis) can dramatically compromise (quench) the fluorescence dye emission.²⁵ As Figure 4.7 shows, in the case of sample **MIX1**, the fluorescence emission is reduced up to 80 % compared to that recorded for free dye **18** (assuming equal dye concentrations in **MIX1** and **18**).

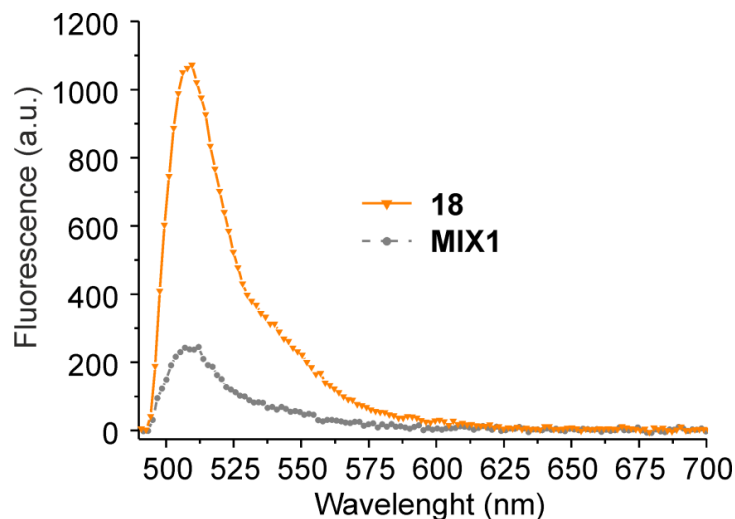


Figure 4.7. Fluorescence spectra of **18** and **MIX1** assuming an equal concentration of the BODYPy dye on both systems.

TGA-MS analyses and IR spectra of **MIX1** and **MIX2** samples account for a complete conversion of the azido groups on **13** (Figures 4.8 and 4.9). Although only a gradual thermal decomposition takes place on both samples with no really distinctive weight losses, the measured weight loss difference and the MS analysis of volatiles give clear evidence of the occurred transformations. As shown in Figure 4.8 (left), a weight loss of 21.3 % is measured on the **MIX1** sample in the 40-875 °C temperature range (calculated as the weight difference between the TGA profiles of **13** and **MIX1**). In addition to that, the analysis of volatiles in the 200-450 °C temperature range shows again the appearance of two fragmentation peaks due to pyridine units (m/z 79 M^+ ; m/z 78 M^+-1) and ascribed to a partial material functionalization with the spacer **3**. Notably, the MS analysis of the **MIX2** sample reveals the complete suppression of the pyridine peaks, while distinctive fragmentations ascribed to the thermal decomposition/rearrangement of the protecting *tert*-butoxyl groups (*isobutene* - m/z 56 M^+ ; m/z 55 M^+-1) can be clearly observed in the narrower 125-275 °C temperature range (Figure 4.8, right); these results represent a clear evidence of an occurred ligand exchange at the disulfide bridge between the pyridine-2-thiolate group and the incoming *N*-Boc-L-cysteine methyl ester (**10**).

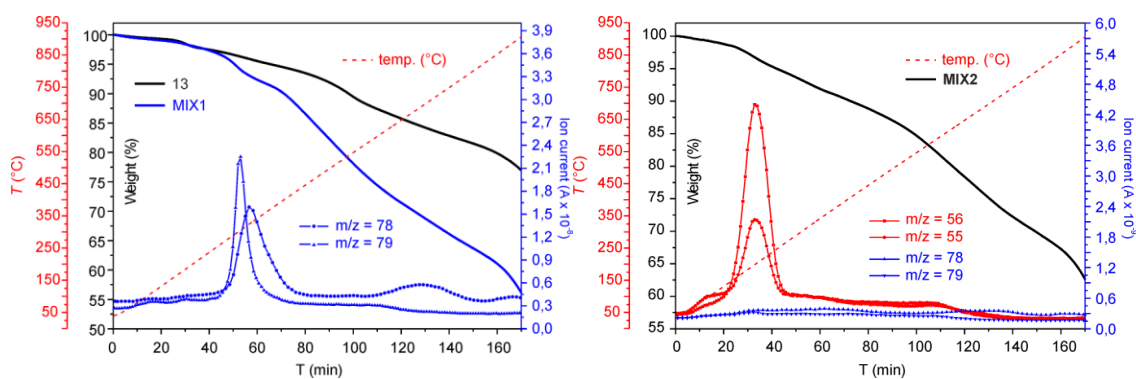


Figure 4.8. (left) TGA profiles (N_2 atm., 50 mL min^{-1}) of **13** and **MIX1** associated with the MS analysis of volatiles (m/z 78 and m/z 79) from **MIX1**. (right) TGA profiles (N_2 atm., 50 mL min^{-1}) of **MIX2** associated with the MS analysis of volatiles (m/z 55 and m/z 56, m/z 78 and m/z 79).

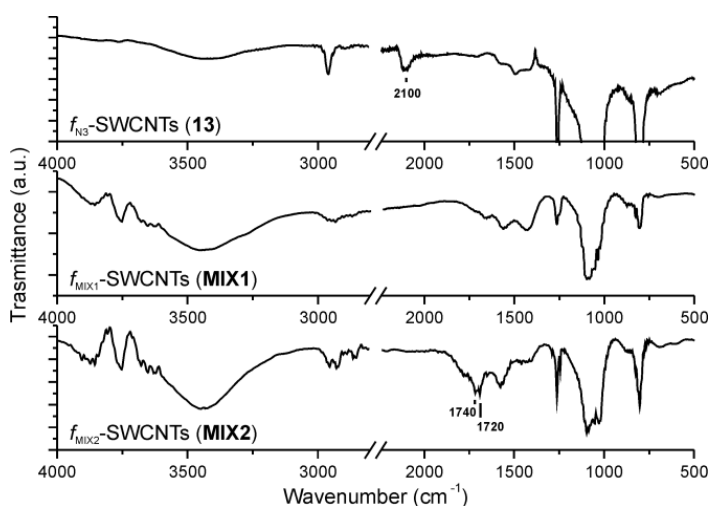


Figure 4.9. FT-IR spectra of **13**, **MIX1** and **MIX2**.

The N, C, S elemental analysis [f_{N_3} -SWCNTs (**13** - blank sample): N, 3.07; C, 84.55; S, 0.03; f_{MIX1} -SWCNTs (**MIX1**): N, 4.73; C, 74.98; S, 1.82; f_{MIX2} -SWCNTs (**MIX2**): N, 3.25; C, 77.81; S, 0.95] do not offer more than a qualitative outlook on the two successive reaction pathways (**13** \rightarrow **MIX1** \rightarrow **MIX2**) with a trend of the C, N, S ratio lying on the expected values for a roughly 50:50 **3:18** functionalization in **MIX1** and the expected ligand exchange in **MIX2**.

A morphological study based on TEM analysis of **13** and **MIX2** unveils a higher tubes aggregation degree on the multidecorated sample, with the generation of highly ordered and straight bundles made of tens of SWCNTs (Figure 4.10 A vs. B).

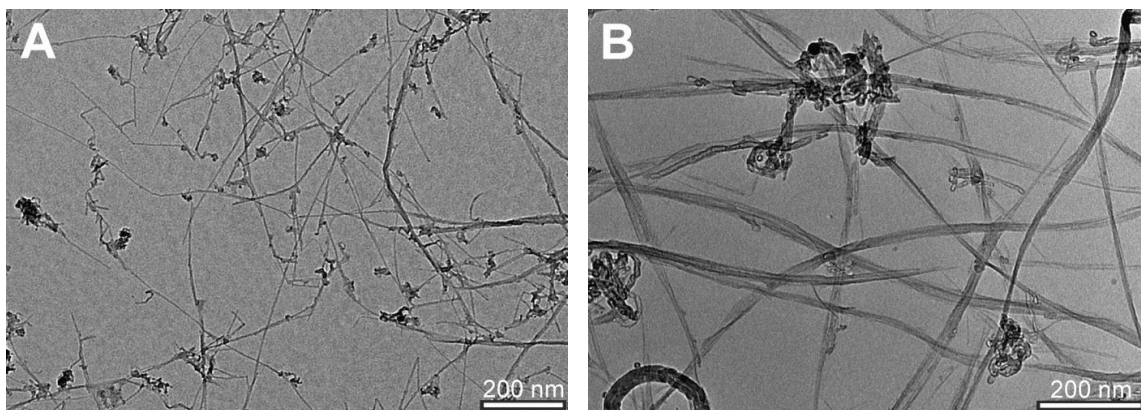


Figure 4.10. TEM micrographs of samples **13** (A) and **MIX2** (B).

Although any reasonable explanation to this morphological change lies on a merely speculative ground, a cohesive effect driven by CNTs surface modification/decoration with highly conjugated polyaromatic frameworks can be invoked. The fluorescently labeled sample **MIX2** has also been analyzed by Confocal Laser Scanning Fluorescence Microscopy, in order to evaluate the dye distribution at the material surfaces. As Figure 4.11 shows, the confocal image obtained upon material excitation at 488 nm, reveals a prevailing spot-like distribution of the dye on the CNT bundles.

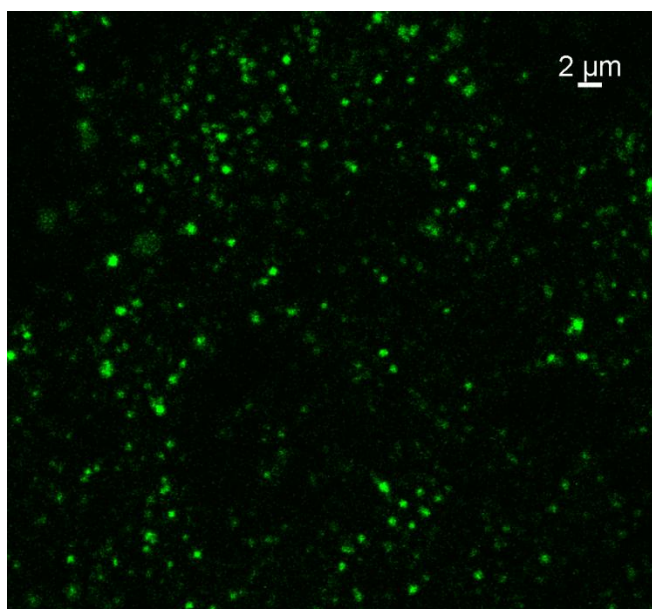


Figure 4.11. Confocal Laser Scanning Fluorescence microscopy of sample **MIX2**: fluorescence image collecting photons in the range 500-550 nm.

The as-generated $(Ar)_{n-1}$ -CNT radical species can be rapidly intercepted and trapped by a second aryl radical reagent, thus allowing a close distribution of the chemically

grafted functionalities. In addition, the sp^2 -network perturbation due to the aryl radical attack induces the local generation of high-energy sites (defects), potentially suitable for an additional (and proximal) chemical attack. Moreover, the observed spot-like distribution of the BODIPy dye derivative can also originate from a multilayer aryl coating of the CNT surface. Menna and Pignataro have recently demonstrated how a simple modulation of the aryldiazonium salt concentration under classical Tour conditions can promote the growth of multilayered structures.²⁶ This process, also named CNT superfunctionalization, is expected to increase the concentration of the aryl functionalities locally; as a consequence, their subsequent post-derivatization (click chemistry) will result in a spatially confined fixation of the newly introduced functionalities (*i.e.* formation of dye “spots” throughout the material).

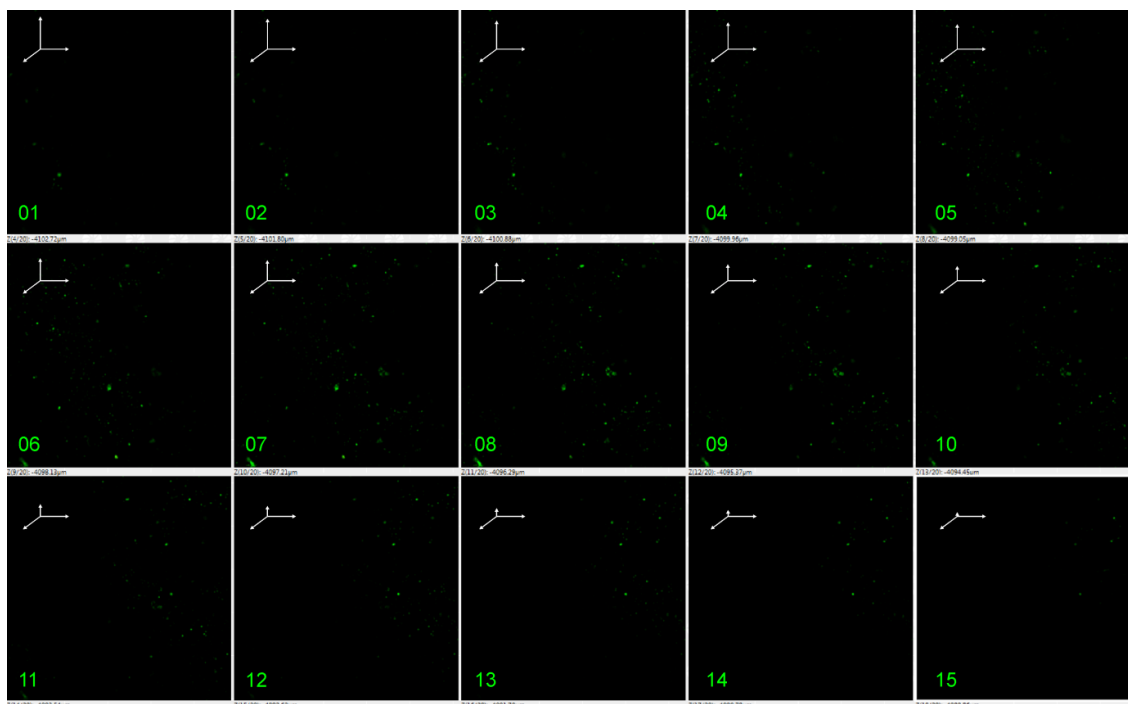


Figure 4.12. Z-stack of sample **MIX2**, for a section of 12 μm (along z-axis, progression of about 1 μm from Z01 to Z15); the images show the distribution of the fluorescent spots throughout the material thickness

Fluorescence lifetime measurements on sample **MIX2** have revealed the co-existence of two different fluorescence decays. In particular, lifetimes of 4.2 and 0.5 ns (with the former being strongly dominating) have been measured (Figure 4.13).²⁷ The shorter lifetime may be reasonably due to the close proximity of dyes in a spot, as well as fluorescence quenching effects due to the CNTs.

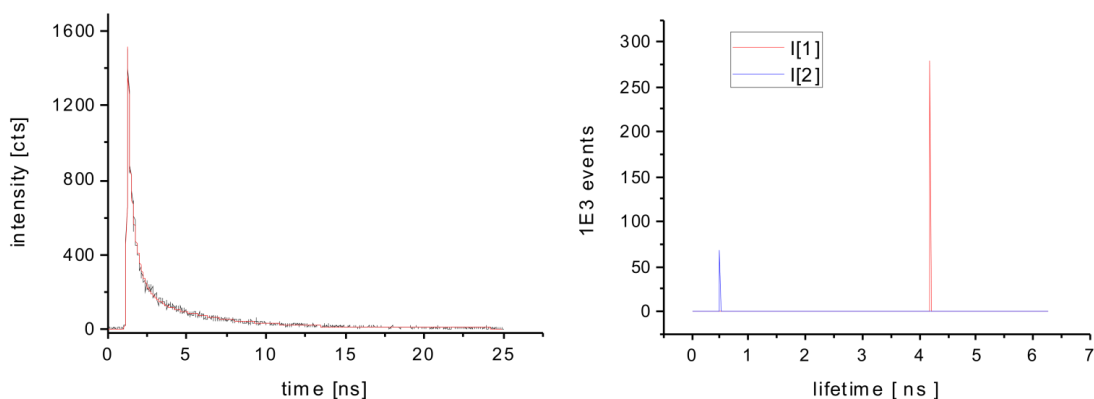


Figure 4.13. (left) Fit of the fluorescence decay calculated for the scanned area with bi-exponential function and (right) lifetime frequency of the fitted image.

4.4 Conclusions

In this chapter we describe the synthesis of a linear hetero-functional cross-linker featured by a “cleavable” disulfide moiety for the covalent anchoring of a wide range of thiol end-capped (bio)molecules and by a “clickable” terminal acetylene group for the CuAAC reaction at the surface of phenylazido-decorated carbon-based nanostructures. The bio-orthogonal character of the click reaction makes it highly desirable for conjugating CNTs and biomolecules.^{12,28} The adopted methodology generates “multifunctional CNT platforms” where the disulfide “bond cleavage” operated by sulfhydryl containing molecules occurs with the *controlled release* of a pyridine-dye, whose concentration is proportional to the extent of cleavage or conjugation by an incoming thiol end-capped molecule. As a result, the cleavage/functionalization scheme provides a useful tool for the chemical linkage of a wide range of thiol-terminating probes to the carbon nanomaterial surface, while a precise functionalization loading is simple assessed by UV-vis measurements. A controlled CNT hetero-decoration through a one-step CuAAC reaction with an acetylene mixture composed by the bi-functional linker and an acetylene fluorescence dye (BODYPy-derivative) is used to impart multifunctionality at the final carbon-nanohybrid. This approach generates optically traceable nanocarriers, whose conjugation with sulfhydryl containing (bio)molecules is allowed through a simple ligand exchange at the disulfide bridge; most importantly, each functionalization and post-derivatization step can be precisely followed by spectroscopic measurements (UV-vis) of the reaction solutions by monitoring the release of a pyridine dye. A morphological study of the as prepared hetero-decorated

nanohybrids has provided interesting insights on the ultimate distribution of the functional groups at the nanomaterial surface, as a consequence of the regiochemical attack of radical species generated from aryl-diazonium intermediates.

4.5 Experimental Section

4.5.1 General Considerations

All reactions were performed under dry nitrogen atmosphere using standard Schlenk-type techniques. Nitrogen (> 99.999%; Rivoira) was dried through a CaCl₂ column and deoxygenated with an oxysorb cartridge from Messer Griesheim prior to use. Dichloromethane was freshly distilled over CaH₂ prior to use, dry DMF (dimethylformamide) and triethylamine were purified according to literature procedure²⁹ and stored over 4 Å molecular sieves under nitrogen atmosphere. Pristine SWCNTs (90 % C) were purchased from NanoAmor and used without further purification. Phenyl-azido decorated SWCNTs (*f*_{N₃}-SWCNTs, **13**),¹¹ amino- (**17**)³⁰ and azido-phenyl-BODIPy (**6**)³¹ compounds were prepared according to literature procedures. Unless otherwise stated, all other chemicals/solvents were purchased from commercial suppliers and used as received without further purification.

Sample sonication was carried out by using an Elma S15 Elmasonic sonicator bath (37 kHz) while cooling samples in a water/ice mixture throughout the whole treatment. CNTs filtration was accomplished by using PTFE membranes/filters (Whatman) with 0.2 µm pore size. All measurements carried out on pristine SWCNTs and functionalized materials (*f*-SWCNTs) were conducted on samples which underwent identical washing/sonication/filtration workup procedures.

4.5.2 Material characterization and analyses conditions

Thermogravimetric analyses (TGA) were performed under N₂ atmosphere (50 mL min⁻¹) on an EXSTAR thermogravimetric analyzer (TG/DTA) Seiko 6200 coupled with a ThermoStar GSD 301T (TGA-MS) for MS analysis of volatiles.

FT-IR spectroscopy was performed on a Perkin–Elmer Spectrum BX FT-IR spectrophotometer and CNT samples were prepared by mixing spectroscopic grade KBr with pristine SWCNTs or *f*-SWCNTs (2–3 wt. %) and analyzed in the 400 – 4000 cm⁻¹ range with a resolution of 1 cm⁻¹. IR spectra of pristine SWCNTs (2–3 wt. %)/KBr was

used as background and directly subtracted from the spectra of the functionalized (*f*-SWCNTs) samples.

^1H - and ^{13}C -NMR spectra of all organic products and intermediates were obtained on a Bruker Avance 300 MHz instrument. Chemical shifts are reported in ppm (δ) relative to TMS and referenced to the chemical shifts of residual solvent resonances.

Elemental analysis were performed on a Thermo FlashEA 1112 Series CHNS-O elemental analyzer with an accepted tolerance of 0.4 units on C, H, N and S.

UV-vis measurements were performed on a Perkin Elmer UV/VIS/NIR Lambda 19 Spectrometer.

Esi-MS was acquired on a LCQ-Fleet Thermo Scientific Ion Trap Mass Spectrometer using diluted MeOH sample solutions (10^{-5} M).

Fluorescence measurements were performed on a laboratory setup by using, for the excitation, a Nichia NDS1113E laser diode with emission at 486 nm, filtered by means of an interference band pass optical filter Andover 488FS10 (central wavelength: 488 nm; bandwidth: 10 nm FWHM). The emitted fluorescence was collected by means of a multimode optical fiber coupled with a collimating GRIN lens, filtered by means of an interference long-pass optical filter Semrock BLP01-488R-25 (cut-on wavelength: 500 nm) for blocking the excitation scattered light, and detected on a spectrometer Andor Shamrock 303i.

Confocal fluorescence imaging was performed on an inverted Nikon A1 laser scanning confocal microscope equipped with a CW argon ion laser for excitation at 457, 488 and 514 nm (Melles Griot, 40 mW), and a diode laser for excitation at 485 nm (LDH-D-C-405 of Picoquant GmbH Berlin, Germany) operating both in continuous mode (50 mW) and pulsed at 40 MHz (1.0 mW average power for pulse FWHM of 120 ps). Confocal fluorescence imaging was carried out on the samples at room temperature. The images were collected using a Nikon PLAN APO VC 20 \times or Nikon PLAN APO VC 60 \times oil immersion objective with NA 0.95 and 1.40, respectively. Images of 512*512 pixels have been acquired and pixel dimension of the xy plane falls in the range 0.1-0.4 μm . Hexagonal pinhole dimension was set to 1.0 au corresponding to 38 μm and optical thickness of 440 nm. Two dichroic mirrors reflecting either 405 and 488 nm or 405, 488, 541 and 640 nm were used. Bandpass filters in front of the PMT selected fluorescence in the ranges 500-550 nm and 570-620 nm. Spectral imaging was done with Nikon 32-PMT array detector with resolution varying from 6 to 10 nm per channel. For fluorescence lifetime imaging a time-correlated single photon counting

(TCSPC) system of Picoquant GmbH Berlin was used exciting at 485 nm. Photons were detected in TTTR mode with two Single Photon Avalanche Diodes manufactured by Micro Photon Devices (MPD), Bolzano, Italy. Fluorescence was filtered with the opportune fluorescence SEMROCK bandpass filters 520/40 nm, and 585/40 nm. PicoHarp 300 photon processor completes the TCSPC system. SymPhoTime v. 5.1 analysis software was used for image processing and lifetime fitting. A tail fit with multi-exponential functions was performed to analyze fluorescence decays of selected ROI. The system allowed measurement of fluorescence lifetimes from 300 ps up to several nanoseconds.

4.5.3 Synthesis of 3-(tritylthio)propionic acid (1)

The carboxylic acid derivative **1** was prepared according to literature procedure¹⁴ and the final product was isolated in 90 % yield as analytically pure white crystals. ¹H NMR (300 MHz, CDCl₃, selected data) δ (ppm): 2.25 (t, ³J = 7.2 Hz, 2H), 2.48 (t, ³J = 7.2 Hz, 2H), 7.23-7.33 (9H), 7.33-7.45 (6H). Elem. Anal. for C₂₂H₂₀O₂S: calc. (%): C 75.83, H 5.78, S 9.20; found: C 76.09, H 5.91, S 9.05. For additional characterization data see ref. 14.

4.5.4 Synthesis of N-(prop-2-ynyl)-3-(tritylthio)propanamide (2)

To a solution of **1** (6 g, 17.2 mmol) in dry and degassed DMF (120 mL), *N*-Hydroxybenzotriazole (HOBt, 2.56 g, 18.9 mmol) and *N,N'*-dicyclohexylcarbodiimide (DCC, 3.90 g, 18.9 mmol) were added in sequence and the resulting mixture was maintained under stirring at room temperature for 3 h till completeness. The reaction course was followed by TLC chromatography (eluent: petroleum ether/AcOEt = 60/40), monitoring the progressive disappearance of the starting acid **1**. Afterwards, Et₃N (2.88 mL, 20.6 mmol) and propargylamine (1.4 mL, 20.6 mmol) were added and the resulting mixture was stirred at room temperature for further 24 h. The reaction was quenched by adding a diluted HCl solution (0.05 M, 120 mL) followed by 120 mL of CH₂Cl₂. The organic mixture was then extracted and the aqueous phase was treated with additional 120 mL of brine. The aqueous mother liquors were then extracted three times with CH₂Cl₂ (3 x 90 mL). The collected organic phases were dried over Na₂SO₄ and evaporated to dryness under reduced pressure. The crude semisolid material was purified by flash chromatography (SiO₂, petroleum ether:AcOEt = 60:40) to give **2** as a white solid in 91 % isolated yield. ¹H NMR (300 MHz, CDCl₃) δ (ppm): 2.03 (t, ³J =

7.3 Hz, 2H), 2.23 (t, $^3J = 2.4$ Hz, 1H), 2.53 (t, $^3J = 7.3$ Hz, 2H), 3.99 (m, 2H), 7.23-7.26 (10H), 7.33-7.46 (5H). $^{13}\text{C}\{^1\text{H}\}$ NMR (75 MHz, CDCl_3) δ (ppm): 27.5, 29.2, 35.4, 66.9, 71.7, 79.4, 126.8, 128.0, 129.6, 144.6, 170.6. Elem. Anal. for $\text{C}_{25}\text{H}_{23}\text{NOS}$: calc. (%): C 77.89, H 6.01, N 3.63, S 8.32; found: C 78.01, H 5.91, N 3.68, S 8.35. IR (KBr): 1636.4 cm^{-1} (ν , C=O).

4.5.5 Synthesis of N-(prop-2-ynyl)-3-(pyridin-2-yl)disulfanylpropanamide (3)

To a solution of **2** (6 g, 15.6 mmol) in dry and degassed CH_2Cl_2 (140 mL), 1,2-di(pyridin-2-yl)disulfane (10.3 g, 46.8 mmol) and Et_3SiH (2.75 mL, 17.2 mmol) were added in sequence. To the resulting mixture, trifluoroacetic acid (35 mL) was added dropwise and the system was maintained under stirring at room temperature for 4 h. Afterwards, the mixture was concentrated to reduced volume and was treated with 550 mL of a $\text{AcOEt}:\text{Et}_3\text{N}$ (1:1) solution. The solution was stirred at room temperature overnight before being diluted with water (550 mL). The resulting phases were separated and the aqueous liquor was extracted three times with AcOEt (3 x 500 mL). The collected organic layers were dried over Na_2SO_4 and the solvent removed under reduced pressure. The crude product was purified by flash chromatography (SiO_2 , $\text{AcOEt}:\text{petroleum ether} = 80:20$) to give **3** in 62 % isolated yield as a pale yellow oil. ^1H NMR (300 MHz, CDCl_3) δ (ppm): 2.26 (t, $^4J = 2.6$ Hz, 1H), 2.64 (t, $^3J = 6.7$ Hz, 2H), 3.10 (t, $^3J = 6.7$ Hz, 2H), 4.10 (m, 2H), 7.17 (1H), 7.62 (1H), 7.69 (1H), 8.56 (1H). $^{13}\text{C}\{^1\text{H}\}$ NMR (75 MHz, CDCl_3) δ (ppm): 29.2, 35.1, 35.5, 71.6, 79.8, 120.7, 121.2, 137.5, 149.3, 159.2, 170.7. Elem. Anal. for $\text{C}_{11}\text{H}_{12}\text{N}_2\text{OS}_2$: calc. (%): C 52.35, H 4.79, N 11.10, S 25.41; found: C 52.41, H 4.65, N 10.77, S 25.07. IR (KBr): 1647.6 cm^{-1} (ν , C=O). MS-Esi: $m/z = 275$ ($\text{M} + \text{Na}^+$).

4.5.6 Synthesis of the alkyne-BODIPy derivative 18

To a solution of N,N'-dicyclohexylcarbodiimide (0.254 g, 1.23 mmol) in CH_2Cl_2 (5 mL) was added 4-pentynoic acid (0.076 g, 0.79 mmol) in CH_2Cl_2 (5 mL) followed by the addition of the aniline-BODIPy derivative **17** (0.268 g, 0.79 mmol) in CH_2Cl_2 (4 mL). Anhydrous 4-dimethylaminopyridine (DMAP, 0.010 g, 0.079 mmol) was then added and the resulting solution stirred under nitrogen for 24 h at room temperature. The reaction mixture was then diluted with CH_2Cl_2 , washed in sequence with water, a 0.5 M HCl solution (2 x 40 mL), a saturated NaHCO_3 solution (2 x 40 mL) and brine. After drying over anhydrous Na_2SO_4 , the solvent was evaporated and the crude product

was purified by flash chromatography on silica gel, eluting first with EtOAc/hexane (1:3) and then with EtOAc/hexane (1:2) to afford the compound **18** as an orange gummy solid in 75 % yield. ^1H NMR (300 MHz, CDCl_3) δ (ppm): 1.41 (s, 6H), 2.54 (s, 6H), 2.63 (m, 4H), 5.97 (s, 2H), 7.23 (2H), 7.69 (2H), 7.83 (1H). $^{13}\text{C}\{^1\text{H}\}$ NMR (75 MHz, CDCl_3) δ (ppm): 14.6, 24.9, 25.5, 33.9, 36.3, 49.3, 53.4, 69.8, 82.8, 120.0, 121.7, 128.7, 130.6, 131.6, 138.7, 141.2, 143.1, 155.4, 169.4. Elem. Anal. for $\text{C}_{25}\text{H}_{29}\text{BF}_2\text{N}_3\text{O}$: calc. (%) N 9.63, C 68.82, H 6.70; found: N 9.76, C 68.65, H 6.91. IR (KBr): 1658.6 cm^{-1} (v, C=O).

4.5.7 Homogeneous CuAAC reaction on **3** with the azido-BODYPy-derivative **6**

To a solution of **6** in dry and degassed DMF (2 mL), **3** (0.55 mmol), CuSO_4 (0.02 mmol) and Na-ascorbate (0.04 mmol) were added in sequence. The mixture was stirred for 24 h at $50\text{ }^\circ\text{C}$ under nitrogen atmosphere. Afterwards, distilled water (20 mL) was added and the mixture extracted with AcOEt (3 x 15 mL). The collected organic phases were washed twice with water (2 x 30 mL) before being dried over Na_2SO_4 and concentrated under reduced pressure. The crude material was purified by flash chromatography over silica gel (eluent: AcOEt/petroleum ether : 80/20) to afford **7** as dark-red crystals in 45 % isolated yield (93 % yield if we consider the recovery of the azido reagent **6** during the chromatographic purification). The reaction has been also performed using $\text{Cu}[\text{P}(\text{OEt})_3]$ as alternative soluble CuAAC catalyst under identical experimental conditions, without any appreciable improvement of the isolated chemical yields. ^1H NMR (300 MHz, CDCl_3) δ : 1.44 (s, 6H), 2.58 (s, 6H), 2.66 (t, $^3J = 6.7\text{ Hz}$, 2H), 3.11 (t, $^3J = 6.7\text{ Hz}$, 2H), 4.66 (d, $^3J = 5.8\text{ Hz}$, 2H), 6.00 (s, 2H), 7.13 (1H), 7.46 (2H), 7.55-7.65 (3H), 7.90 (2H), 8.15 (1H), 8.51 (1H). $^{13}\text{C}\{^1\text{H}\}$ NMR (75 MHz, CDCl_3) δ : 14.5, 14.7, 34.7, 35.6, 120.6, 120.9, 121.3, 121.7, 130.0, 131.3, 135.5, 137.1, 137.4, 139.5, 142.9, 146.2, 149.9, 156.2, 159.1, 171.1. Elem. Anal. for $\text{C}_{30}\text{H}_{30}\text{BF}_2\text{N}_7\text{OS}_2$: calc. (%): C 58.35, H 4.90, N 15.88, S 10.38; found: C 58.41, H 4.65, N 15.77, S 10.07. IR (KBr): 1647.6 cm^{-1} (v, C=O).

4.5.8 General procedure for the homo- and hetero-derivatization of phenyl-azido decorated SWCNTs via CuAAC reaction

The CuAAC protocol used for the homo- and hetero-derivatization of f_{N_3} -SWCNTs (**13**) to give f_{SSPy} -SWCNTs (**14**), f_{MIX1} -SWCNTs (**MIX1**) and f_{MIX2} -SWCNTs (**MIX2**) hybrids follows that already described in chapter 2.¹¹ In a typical procedure, f_{N_3} -

SWCNTs (20 mg) were suspended in dry and degassed DMF (3 mL) and sonicated for 15 min. The resulting suspension was treated in sequence with the acetylenic derivative **3** (0.17 mmol) or an equimolar mixture of **3/18** (0.17 mmol overall), and CuI[P(OEt)₃] (6 mg, 0.017 mmol). The mixture was then sonicated for 30 min and heated at 85 °C while being stirred under nitrogen atmosphere for 48 h. After cooling to room temperature the suspension was diluted with ethyl acetate, sonicated for additional 10 min and centrifugated in order to recover the solid residue by simple decantation. The solid was washed and sonicated three times with AcOEt and CH₂Cl₂ (1 x 10 mL AcOEt, 2 x 10 mL CH₂Cl₂) and the supernatant solution was removed after centrifugation. Finally, the solid residue was suspended in CH₂Cl₂ (15 mL), sonicated for 10 min and filtered through an inorganic membranes/filters (Whatman) with 0.2 μm pore size before being dried under vacuum at 50 °C to constant weight.

4.5.9 General procedure for the disulfide cleavage on **3, **7** and the SWCNT composite **14** by a model dithiol and subsequent monitoring of the reaction course by UV-vis measurements**

In a typical procedure, 0.5 - 1 mg of the disulfide **3** was accurately weighted using a Sartorius 4503 microbalance (d = 0.001 mg) and dissolved in 2 mL of a mixture of DMF:PBS (phosphate buffered saline) = 25:75 (pH = 7.2). The solution was divided into two portions; the first was directly analyzed by UV-vis spectroscopy (“blank” sample), while the second was treated with a 20-fold excess of a solution of model thiol (DTT - dithiotreithol). After 15 min at room temperature, the solution was analyzed by UV-vis spectroscopy in the same condition used for the “blank” sample. The difference, in terms of absorbance values, measured between the two samples at 343 nm was correlated with the amount of pyridin-2-thione (**5**) released from the spacer using the Lambert-Beer equation (eq. 1):

$$C \text{ (mol L}^{-1}\text{)} = [A_{\text{sample}} - A_{\text{blank}}] / [\epsilon \text{ (M}^{-1} \text{ cm}^{-1}\text{)} b \text{ (cm)}] \quad (\text{eq. 1})$$

where ϵ is the molar extinction coefficient of pyridin-2-thione **5** (8080 M⁻¹ cm⁻¹) and b is the optical path (1 cm).

The same procedure was followed on sample **7** except for using the 2,2'-thiodiethanethiol (**TDT**) as model cleaving agent (for solubility reasons) in pure DMF as solvent, to give **8** and **9**.

An identical procedure to that described for the homogeneous disulfide cleavage on **3** was employed on the SWCNT samples containing the disulfide spacer (samples **14** → **15**) except for keeping, after the DTT addition, the well sonicated samples under heating (50 °C) for 1 h to bring the cleavage process to completeness. The resulting suspension was centrifuged and the supernatant analyzed by UV-vis spectroscopy.

4.5.10 Covalent grafting of the L-aminoacid **10** [*N*-(*tert*-Butoxycarbonyl)-L-cysteine methyl ester] on **3** to give **11**

A solution of **3** (0.02 g, 0.08 mmol) in 1.5 mL of dry and degassed DMF was treated with a DMF solution (0.5 mL) of the *N*-(*tert*-Butoxycarbonyl)-L-cysteine methyl ester (0.025 mL, 0.12 mmol) and the resulting solution was maintained under stirring at room temperature for 6 h. The reaction was then quenched with 20 mL of distilled water and extracted with CH₂Cl₂ (3 x 25 mL). The collected organic phases were dried over Na₂SO₄ and concentrated at reduced pressure. The crude product was purified by flash chromatography (SiO₂, AcOEt:petroleum ether = 50:50) affording **11** as a colourless oil in 62 % isolated yield. ¹H NMR (300 MHz, CDCl₃) δ: 1.45 (s, 9H), 2.22 (s, 1H), 2.61 (m, 2H), 2.93-3.19 (4H), 3.77 (s, 3H), 4.07 (m, 2H), 4.60 (m, 1H), 5.36 (m, 1H), 6.32 (s, 1H). ¹³C{¹H} NMR (75 MHz, CDCl₃) δ: 28.3, 29.3, 34.0, 35.9, 41.9, 52.7, 53.2, 71.6, 79.4, 80.5, 155.2, 170.5, 171.2. Elem. Anal. for C₁₅H₂₄N₂O₅S₂: calc. (%): C 47.85, H 6.43, N 7.44, S 17.03; found: C 47.41, H 6.55, N 7.77, S 17.07. IR (KBr): 1744.2 cm⁻¹ (v, MeO-C=O), 1708.3 cm⁻¹ (v, ^tBuO-C=O), 1653.1 cm⁻¹ (v, NH-C=O).

4.5.11 Covalent grafting of the L-aminoacid **10** [*N*-(*tert*-Butoxycarbonyl)-L-cysteine methyl ester] on **7** to give **12**

A solution of **7** (0.035 g, 0.06 mmol) in 1.5 mL of dry and degassed DMF was treated with a DMF solution (0.5 mL) of the *N*-(*tert*-Butoxycarbonyl)-L-cysteine methyl ester (0.02 mL, 0.08 mmol) and the resulting mixture was maintained under stirring at room temperature for 6 h. Afterwards, the reaction was quenched with 20 mL of distilled water and extracted with AcOEt (3 x 25 mL). The collected organic phases were dried over Na₂SO₄ and concentrated at reduced pressure. The crude product was purified by flash chromatography (SiO₂, AcOEt:petroleum ether = 80:20) to give **12** as red crystals in 39 % isolated yield. ¹H NMR (300 MHz, CDCl₃) δ: 1.44 (15 H), 2.57 (s, 6H), 2.65 (m, 2H), 3.00-3.14 (4H), 3.77 (s, 3H), 4.62 (3H), 5.36 (1H), 6.01 (2H), 6.67 (1H), 7.49 (2H), 7.93 (2H), 8.15 (1H). ¹³C{¹H} NMR (75 MHz, CDCl₃, selected data) δ: 14.1,

28.3, 29.4, 29.7, 30.9, 31.9, 52.7, 53.2, 121.8, 122.8, 129.8, 169.8. Elem. Anal. for $C_{34}H_{42}BF_2N_7O_5S_2$: calc. (%): C 55.06, H 5.71, N 13.22, S 8.65; found: C 54.81, H 5.65, N 13.37, S 8.27. IR (KBr): 1749.1 cm^{-1} (v, MeO-C=O), 1711.1 cm^{-1} (v, ^tBuO-C=O), 1649.1 cm^{-1} (v, NH-C=O).

4.5.12 Covalent grafting of the L-aminoacid 10 [*N*-(*tert*-Butoxycarbonyl)-L-cysteine methyl ester] on 14 to give f_{SSCy} -SWCNTs (16)

20 mg of f_{SSPy} -SWCNTs were suspended in 1.5 mL of dry and degassed DMF and sonicated for 15 minutes. A solution of the *N*-(*tert*-Butoxycarbonyl)-L-cysteine methyl ester (0.010 mL, 0.05 mmol) in DMF (0.5 mL) was added in sequence and the resulting suspension was sonicated for further 10 minutes before being stirred at 50 °C for 1 h. After cooling down the mixture to room temperature, AcOEt (10 mL) was added and the suspension sonicated for further 10 min. The solid residue was separated from the mother liquor by centrifugation and submitted to the following work-up procedure. The recovered solid residue underwent three successive washing/sonicating cycles (2 x AcOEt, 1 x CH_2Cl_2) each time recovering the solid compound by centrifugation. Afterwards, the solid residue was suspended in dichloromethane, sonicated for additional 10 min and filtered through 0.2 μm filter (Whatman) before being dried under vacuum at 50 °C to constant weight.

References and Notes

- ¹ a) A. Krüger, in *Carbon Materials and Nanotechnology* (Ed.: A. Krüger), Wiley-VCH, Weinheim, **2010**, p. 490. b) V. Georgakilas, M. Otyepka, A. B. Bourlinos, V. Chandra, N. Kim, K. C. Kemp, P. Hobza, R. Zboril, K. S. Kim, *Chem. Rev.* **2012**, *112*, 6156. c) D. M. Guldi, N. Martín, in *Carbon Nanotubes and Related Structures: Synthesis Characterization, Functionalization, and Applications* (Eds.: D. M. Guldi, N. Martín), Wiley-VCH, Weinheim, **2010**, p. 562.
- ² a) D. Tasis, N. Tagmatarchis, A. Bianco, M. Prato, *Chem. Rev.* **2006**, *106*, 1105. b) P. Singh, S. Campidelli, S. Giordani, D. Bonifazi, A. Bianco, M. Prato, *Chem. Soc. Rev.* **2009**, *38*, 2214. c) V. Sgobba, D. M. Guldi, *Chem. Soc. Rev.* **2009**, *38*, 165. d) K. Dirian, M. Angeles Herranz, G. Katsukis, J. Malig, L. Rodríguez-Perez, C. Romero-Nieto, V. Strauss, N. Martín, D. M. Guldi, *Chem. Sci.* **2013**, *4*, 4335.
- ³ a) T. Kashiwagi, E. Grulke, J. Hilding, R. Harris, W. Awad, J. Douglas, *Macromol. Rapid Commun.* **2002**, *23*, 761. b) C. F. Kuan, W. J. Chen, Y. L. Li, C. H. Chen, H. C. Kuan, C. L. Chiang, *J. Phys. Chem. Solids* **2010**, *71*, 539. c) M. T. Byrne, Y. K. Gun'ko, *Adv. Mater.* **2010**, *22*, 1672. d) S. H. Park, P. R. Bandaru, *Polymer* **2010**, *51*, 5071. e) N. G. Sahoo, S. Rana, J. W. Cho, L. Li, S. H. Chan, *Prog. Polym. Sci.* **2010**, *35*, 837.
- ⁴ a) Z. Liu, K. Chen, C. Davis, S. Sherlock, Q. Cao, X. Chen, H. Dai, *Cancer Res.* **2008**, *68*, 6652. b) Z. Liu, S. Tabakman, K. Welsher, H. Dai, *Nano Res.* **2009**, *2*, 85. c) M. Prato, K. Kostarelos, A. Bianco, *Acc. Chem. Res.* **2008**, *41*, 60.
- ⁵ a) Z. Liu, A. C. Fan, K. Rakhra, S. Sherlock, A. Goodwin, X. Chen, Q. Yang, D. W. Felsher, H. Dai, *Angew. Chem. Int. Ed. Engl.* **2009**, *48*, 7668. b) K. Kostarelos, A. Bianco, M. Prato *Nat. Nanotechnol.* **2009**, *4*, 627. c) A. Ruggiero, C. H. Villa, J. P. Holland, S. R. Sprinkle, C. May, J. S. Lewis, D. A. Scheinberg, M. R. McDevitt, *Int. J. Nanomedicine* **2010**, *5*, 783.
- ⁶ a) G. Tuci, C. Zafferoni, P. D'Ambrosio, S. Caporali, M. Ceppatelli, A. Rossin, T. Tsoufis, M. Innocenti, G. Giambastiani, *ACS Catal.* **2013**, *3*, 2108 b) G. Tuci, C. Zafferoni, A. Rossin, A. Milella, L. Luconi, M. Innocenti, L. Truong Phuoc, C. Duong-Viet, C. Pham-Huu, G. Giambastiani, *Chem. Mater.* **2014**, *26*, 3460.
- ⁷ a) N. Karousis, N. Tagmatarchis, D. Tasis, *Chem. Rev.* **2010**, *110*, 5366. b) A. Hirsch, O. Vostrowsky, *Top. Curr. Chem.* **2005**, *245*, 193.
- ⁸ a) C. Samorì, H. Ali-Boucetta, R. Sainz, C. Guo, F. M. Toma, C. Fabbro, T. da Ros, M. Prato, K. Kostarelos, A. Bianco, *Chem. Commun.* **2010**, *46*, 1494. b) J. Chen, S. Chen, X. Zhao, L. V. Kuznetsova, S. S. Wong, I. Ojima, *J. Am. Chem. Soc.* **2008**, *130*, 16778.
- ⁹ N. Wong Shi Kam, Z. Liu, H. Dai, *J. Am. Chem. Soc.* **2005**, *127*, 12492.
- ¹⁰ Y.-Z. You, C.-Y. Hong, C.-Y. Pan, *J. Phys. Chem. C* **2007**, *111*, 16161.
- ¹¹ G. Tuci, C. Vinattieri, L. Luconi, M. Ceppatelli, S. Cicchi, A. Brandi, J. Filippi, M. Melucci, G. Giambastiani, *Chem. Eur. J.* **2012**, *18*, 8454.
- ¹² J. M. Baskin, C. R. Bertozzi, *QSAR Comb. Sci.* **2007**, *26*, 1211.

-
- 13 For a conceptually similar approach to the homo- and hetero-decoration of MOF materials see also:
G. Tuci, A. Rossin, X. Xu, M. Ranocchiari, J. A. van Bokhoven, L. Luconi, I. Manet, M. Melucci,
G. Giambastiani, *Chem. Mater.* **2013**, *25*, 2297.
- 14 E. L. Ruggles, P. B. Decker, R. J. Hondal, *Tetrahedron* **2009**, *65*, 1257.
- 15 D. A. Pearson, M. Blanchette, M. L. Baker, C. A. Guindon, *Tetrahedron Lett.* **1989**, *30*, 2739.
- 16 Y. Lin, A. Favre-Re'guillon, S. Pellet-Rostainga, M. Lemaire, *Tetrahedron Lett.* **2007**, *48*, 3463.
- 17 J. C. Kaila, A. B. Baraiya, A. N. Pandya, H. B. Jalani, K. K. Vasu, V. Sudarsanam, *Tetrahedron
Lett.* **2009**, *50*, 3955.
- 18 P. A. Wender, E. A. Goun, L. R. Jones **2010**, US2010/0255499 A1
- 19 The variation of intensity measured in Figure 4.1B falls within the repeatability error of the
fluorescence measurement setup.
- 20 a) P. Beak, *Acc. Chem. Res.* **1977**, *10*, 186. b) S. Stoyanov, I. Petkov, L. Antonov, T. Stoyanova, P.
Karagiannidis, P. Aslanidis, *Can. J. Chem.* **1990**, *68*, 1482.
- 21 The elemental analysis provides an overestimated functionalization loading falling within the same
order of magnitude of that calculated from the TGA profile. N, C, and S contents are calculated as
average values over three independent runs. Sulfur (and nitrogen) contaminations on sample **13** are
due to minor physisorbed residues of **3** in the "blank sample".
- 22 According to the elemental analysis on sample **13** (f_{N_3} -SWCNTs), we estimate a functionalization
loading of 0.635 mmol of $-C_6H_4-N_3$ per 1g of material.
- 23 a) A. Cui, X. Peng, J. Fan, X. Chen, Y. Wu, B. Guo, *J. Photochem. Photobiol. A* **2007**, *186*, 85. b)
H. Lu, S. S. Zhang, H. Z. Liu, Y. W. Wang, Z. Shen, C. G. Liu, X. Z. You, *J. Phys. Chem. A* **2009**,
113, 14081. c) S. Mula, K. Elliott, A. Harriman, R. Ziesse, *J. Phys. Chem. A* **2010**, *114*, 10515. d)
A. Vázquez-Romero, N. Kielland, M. J. Arévalo, S. Preciado, R. J. Mellanby, Y. Feng, R. Lavilla,
M. Vendrell, *J. Am. Chem. Soc.* **2013**, *135*, 16018.
- 24 For both homo- and hetero-functionalization, the amount of terminal alkynes is kept in excess
respect to the estimated azido-groups available at the SWCNT sidewalls ($\approx 5 : 1$).
- 25 C. F. Chiu, N. Dementev, E. Borguet, *J. Phys. Chem. A* **2011**, *115*, 9579 and refs cited therein.
- 26 P. Salice, E. Fabris, C. Sartorio, D. Fenaroli, V. Figà, M.-P. Casaletto, S. Cataldo, B. Pignataro, E.
Menna, *Carbon* **2014**, *74*, 73.
- 27 Similar fluorescence lifetimes (ranging from 3.0 to 3.14 ns) have been reported for related BODIPy
derivatives in CH_2Cl_2 . See ref. S. Mula, G. Ulrich, R. Ziesse, *Tetrahedron Lett.* **2009**, *50*, 6383.
- 28 J. A. Prescher, C. R. Bertozzi, *Nat. Chem. Biol.* **2005**, *1*, 13.
- 29 D. D. Perrin, W. L. F. Armarego, D. R. Perrin, *Purification of Laboratory Chemicals*, Vol. 1, 2nd
ed., Pergamon, **1980**.
- 30 E. Maligaspe, N. V. Tkachenko, N. K. Subbaiyan, R. Chitta, M. E. Zandler, H. Lemmetyinen, F.
D'Souza, *J. Phys. Chem. A* **2009**, *113*, 8478.
- 31 M. J. Leonardi, M. R. Topka, P. H. Dinolfo, *Inorg. Chem.* **2012**, *51*, 13114.

5. Tailoring Carbon Nanotube N-Dopants while Designing Metal-Free Electrocatalysts for the Oxygen Reduction Reaction in Alkaline Medium

5.1 Abstract

A straightforward, energy- and atom-saving process to the production of tailored N-doped and catalytically active metal-free carbon nanostructures, has been set up. The N-decoration of multi-walled carbon nanotubes (MWCNTs) occurs *via* chemical functionalization under mild reaction conditions and our *ex-situ* approach generates effective catalysts for the oxygen reduction reaction (ORR) in alkaline environment. The adopted methodology lists a number of remarkable technical advantages, among which the full exposure of the N-containing functionalities to the nanomaterial outer side where the catalytic process takes place, an absolutely remarkable electrocatalytic activity and long-term stability of selected N-doped metal-free samples for ORR in basic medium and an easy tailoring of the N-containing functional groups. This latter aspect contributes to elucidate the complex structure-reactivity relationship of N-doped carbon nanomaterials in ORR, providing fundamental insights on the nature of the N-active sites as well as on the role of neighboring carbons. The protocol described hereafter offers an excellent basis for the development of more active metal-free electrocatalysts for the ORR.

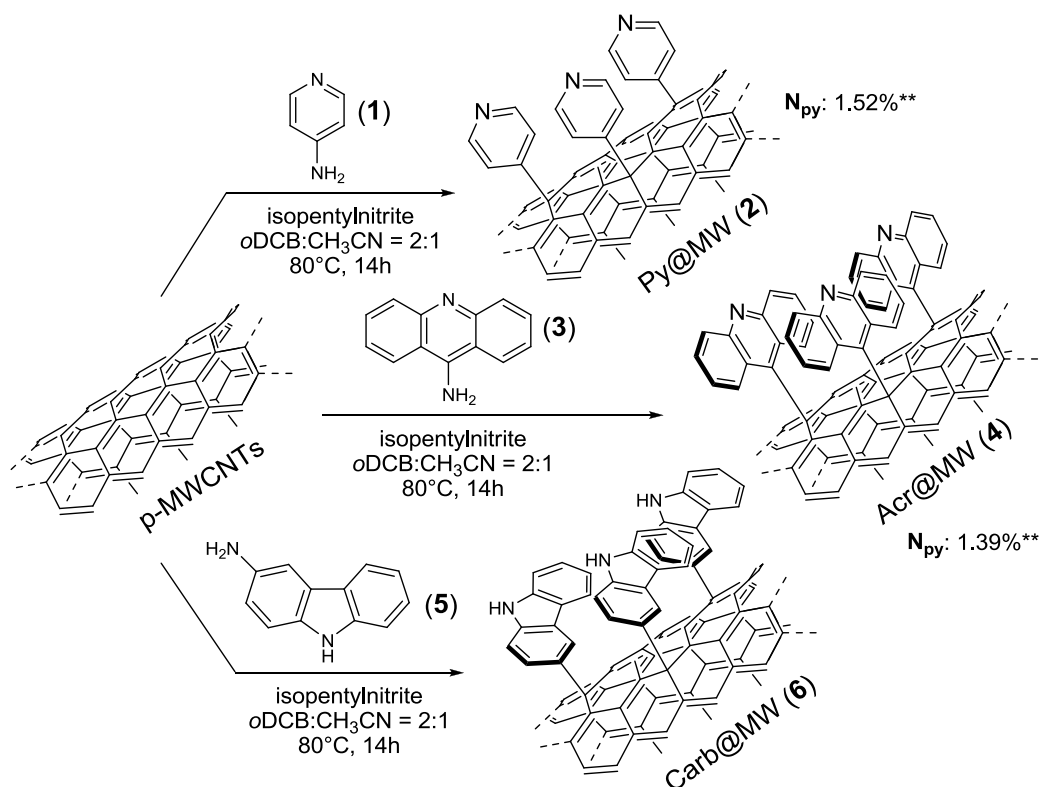
5.2 Introduction

Intensive research efforts have been devoted in the last few years to the development of efficient, durable and inexpensive alternatives to precious-metal based electrocatalysts (typically containing Pt and its alloys) for the Oxygen Reduction Reaction (ORR) in fuel cells (FC) cathodes.¹ Typically, the ORR can proceed either through a four-electron process to combine oxygen with electrons and protons into water as the final product, or through a less efficient two-step, two-electron pathway involving the formation of the hydroperoxide ions as intermediates.¹ On this ground,

nitrogen-doped 1D and 2D carbon nanomaterials (occasionally combined with non-noble metal nanoparticles) have recently emerged as valuable candidates capable of promoting this reaction efficiently.² It is generally accepted that N-doped carbon nanostructures can favor the surface O₂ chemisorption/activation improving their catalytic performance in the ORR remarkably.^{2a,3} While a relatively high number of N-doped carbon nanostructures showing catalytic activity in ORR have been prepared by the *in-situ* CVD approach,² much less work has been done for the obtainment of catalytically active N-decorated carbon nanomaterials using milder and easily tunable *ex-situ* (exohedral) organic functionalization techniques. The latter imply a number of important issues whose achievement may represent a real breakthrough in the development of novel nanostructured metal-free catalysts. Indeed, besides leading to a fine tuning of the chemical identity of the N-dopants, an *ex-situ* approach better matches the requirements for energy- and atom-saving processes than the classical CVD approach. In addition, N-dopants are entirely present at the nanotube surface, where the catalytic process takes place. Last but not least, an *ex-situ* approach can contribute to answer the widely debated question related to the intrinsic ability of different N-containing groups, randomly embedded in the sp² CNT network, at promoting ORR.⁴ Although the real nature of the active sites in N-doped carbon nanomaterials still remains unclear, it is generally accepted that pyridine and pyrrole nitrogen atoms contribute differently to the ORR, the former playing a key role in promoting the process.⁴ In this regard, a puzzling question arises: what is the effect of the neighboring atomic environment on the ability of pyridinic nitrogen atoms to promote ORR?

5.3 Results and discussion

Trying to shed light on which is the effect of the neighboring atomic environment on the ability of pyridinic nitrogen atoms to promote ORR, we took advantage from the well consolidated aryldiazonium salt (*Tour*) functionalization protocol⁵ as a convenient synthetic methodology for the *ex-situ* N-doping of MWCNTs with pyridine- and pyrrole-containing dangling groups (Scheme 5.1).



Scheme 5.1. CNTs *ex-situ* functionalization via aryl diazonium salt (*Tour*) conditions. **The N_{py} content ($N_{py}\%$) is calculated for sample **2** and **4** via acid-base titration and reported as average value over the three independent runs (see Table 5.2).

As shown in Scheme 5.1, 4-aminopyridine (**1**), 9-aminoacridine (**3**) and 3-aminocarbazole (**5**) are selected as N-containing candidates, **3** and **5** being selected as mimics of pyridine and pyrrole frameworks, respectively, embedded in a conjugated Csp^2 network. All reactions proceed smoothly under mild conditions, providing the expected functionalized samples **2**, **4** and **6**. Careful work-up procedures and parallel “blank-tests” (carried-out in the absence of the isopentyl nitrite reagent) have been used to rule out any possible reagent contamination resulting from simply physisorbed molecules (see section 5.5).

The as synthesized N-doped materials have been spectroscopically [XPS (Figure 5.2) Raman (Figure 5.3) and morphologically (TEM, Figure 5.4) characterized (*vide infra*)].

CHN elemental analysis on **2**, **4** and **6** is used to calculate the functionalization loading (2.0 N wt. % for **2**, 1.7 N wt. % for **4** and 2.8 N wt. % for **6**, see Table 5.1), while an acid-base titration for the more basic samples **2** and **4** provides a well matching response on the pyridine-group content (see Table 5.2).⁶

Table 5.1. Elemental analyses for samples **2**, **4** and **6** and relative “blank tests”. “Blank tests” are performed using identical reaction conditions and reagents except for the use of the isopentyl nitrite reagent. The N% content of each “blank sample” is subtracted from the N-content % of the respective sample.

	C%	N%		C%	N%		C%	N%
Sample 2	87.19	2.05	Sample 4	92.60	1.87	Sample 6	92.45	2.91
MWCNTs (blank test)	92.58	0.08	MWCNTs (blank test)	92.81	0.14	MWCNTs (blank test)	93.71	0.15

Table 5.2. Acid-base titration for the more basic samples **2** and **4**.

	N _{py} %		N _{py} %
Sample 2 (1° run)	1.64	Sample 4 (1° run)	1.28
Sample 2 (2° run)	1.44	Sample 4 (2° run)	1.52
Sample 2 (3° run)	1.49	Sample 4 (3° run)	1.38
Sample 2 (average)	1.52	Sample 4 (average)	1.39

Finally, thermogravimetric analyses (TGA) give additional evidence of the occurred functionalization process (Figure 5.1). More gradual decomposition profiles observed for all N-doped samples are indicative of a substantial sidewall perturbation as consequence of the functionalization procedure.

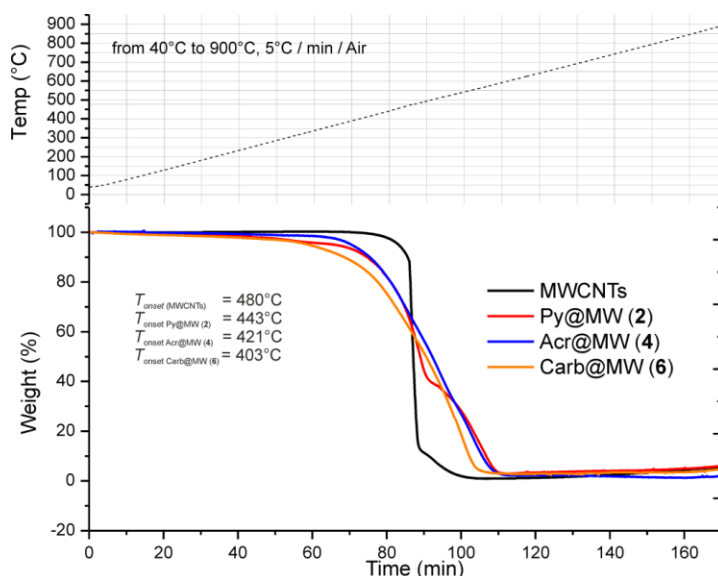


Figure 5.1. TGA profiles of pristine MWCNTs (black-line) and N-decorated CNT samples **2** (red-line), **4** (blue-line) and **6** (orange-line). Thermal program: 40–900 °C, 5 °C/min; air atmosphere, 100 mL min⁻¹.

XPS spectra of the N-containing samples present characteristic N 1s profiles. Peaks at 398.6 eV for **2** and **4**, and 400.2 eV for **6** (Figure 5.2) are attributed to pyridinic nitrogen⁷ and pyrrole-type containing groups, respectively. Minor components at higher binding energy values arise from the N 1s spectra of both pyridine containing samples and are ascribed to commonly observed surface contaminations.^{5e,g,7}

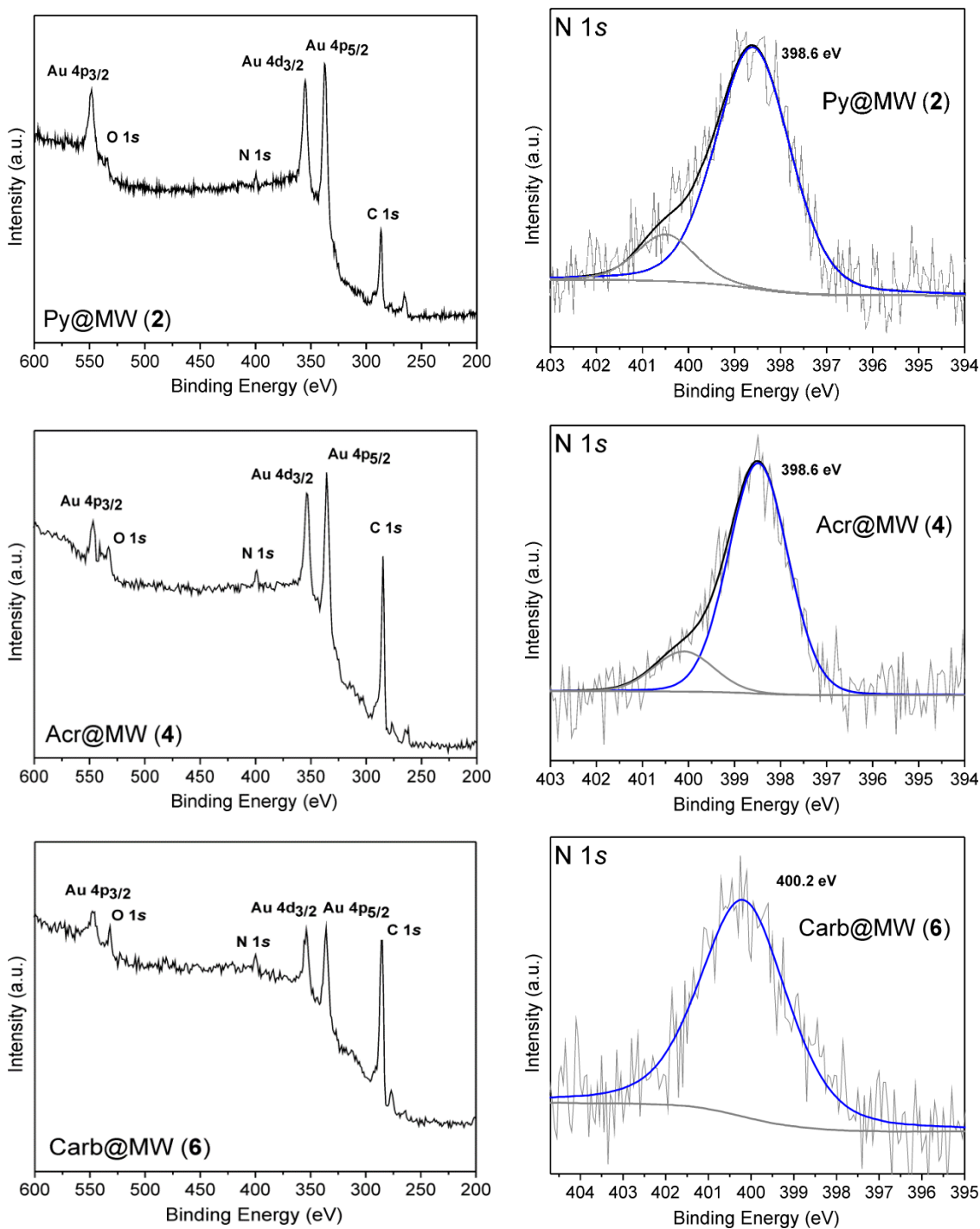


Figure 5.2. Survey core level regions (left) and high resolution N 1s (right) core level regions and their relative fits for the XPS spectra of samples **2**, **4** and **6**, respectively.

Raman spectra of all the N-decorated materials (Figure 5.3) do not show any significant change in the I_D/I_G values compared to the pristine sample, thus revealing only negligible crystallite and defect sites surface density alterations.

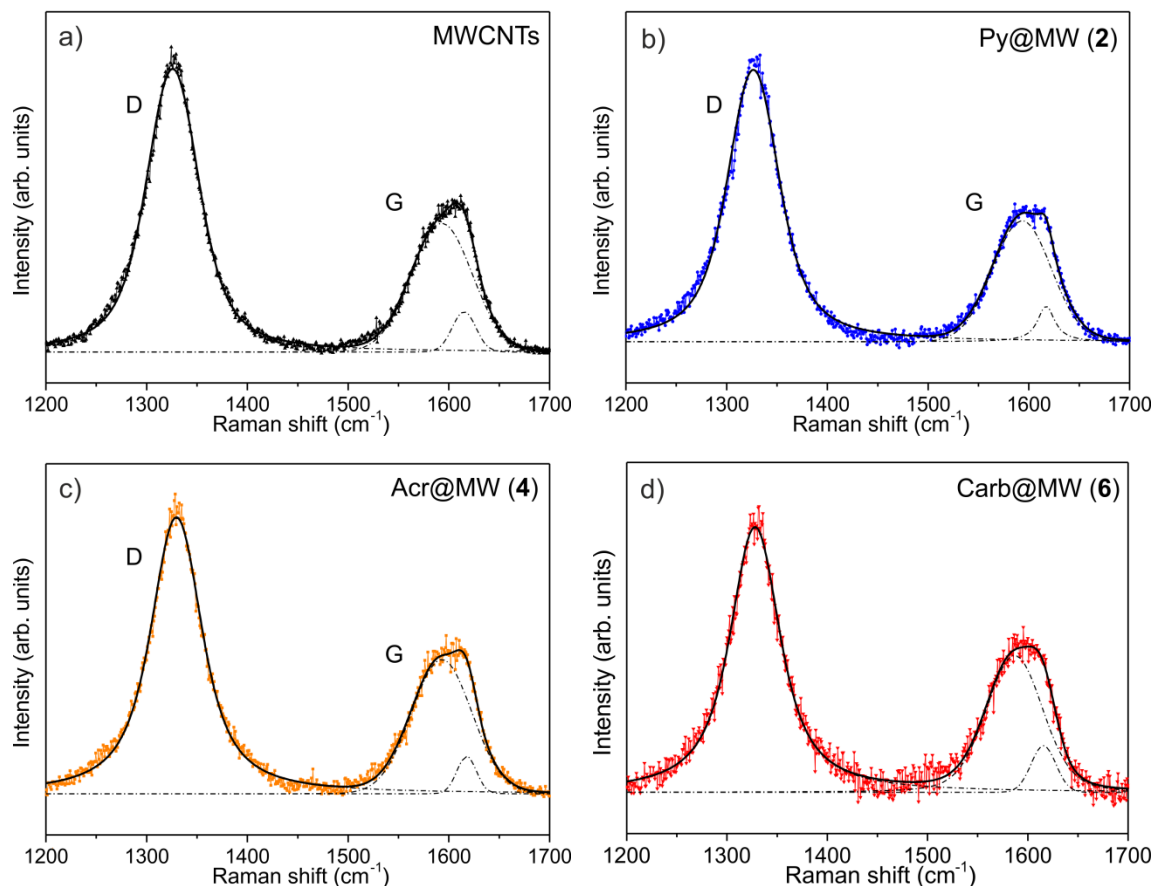


Figure 5.3. Raman spectra of a) pristine MWCNTs, b) Py@MW (2), c) Acr@MW (4) and d) Carb@MW (6) and their relative fits. Colored dots represent the experimental points. The single peak fittings are reported as dot-dashed lines, while the full line represents the total spectrum fit. All recorded curves were fitted using Lorentzian lineshapes and the intensity ratios (namely, I_D/I_G) were calculated from the fitted total curve parameters.¹⁶⁻¹⁸ Calculated I_D/I_G ratios are 2.3 and 2.1 for MWCNTs, 2, 4 and 6, respectively.

Similarly, TEM images of the N-decorated samples do not reveal any significant morphological difference in terms of tube length and diameter compared to the pristine one; slightly deaggregated tube bundles appear for the functionalized samples throughout the whole scanned area (Figure 5.4).

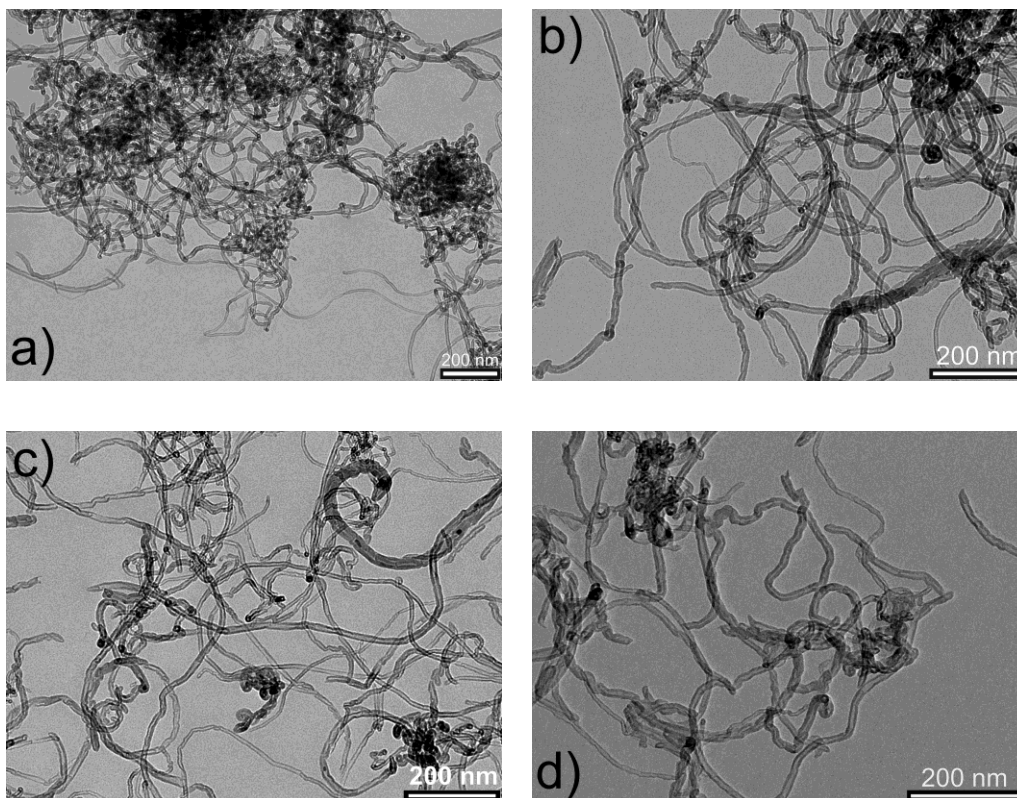


Figure 5.4. TEM images of a) pristine MWCNTs, b) Py@MW (2), c) Acr@MW (4) and d) Carb@MW (6).

The as prepared N-decorated CNT samples have been scrutinized with respect to their catalytic performance in ORR.² To evaluate their electrocatalytic activity, N-CNTs/Nafion films deposited on a rotating glassy carbon (GC) electrode have been preliminarily investigated by cyclic voltammetry (CV) using a three electrode cell operating in O₂ saturated 0.1 M KOH solution. Under O₂-saturated conditions, the N-decorated samples show an irreversible ORR peak not present under N₂-saturated electrolyte conditions (Figure 5.5).

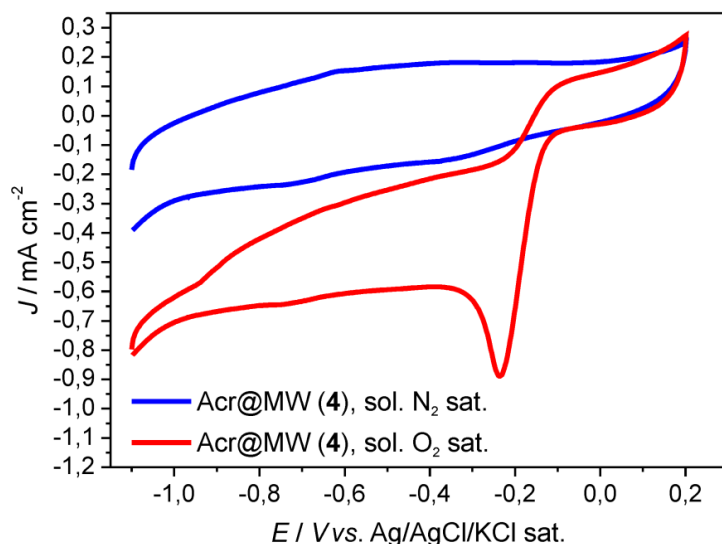
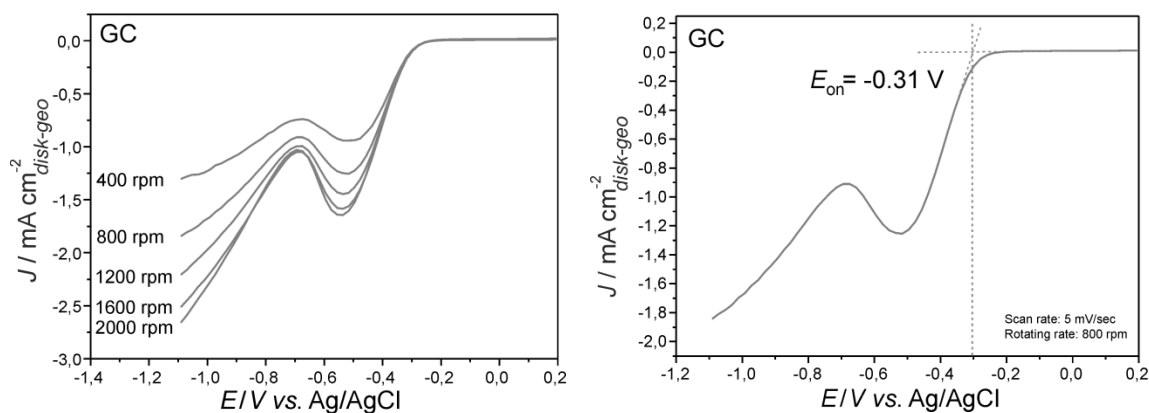
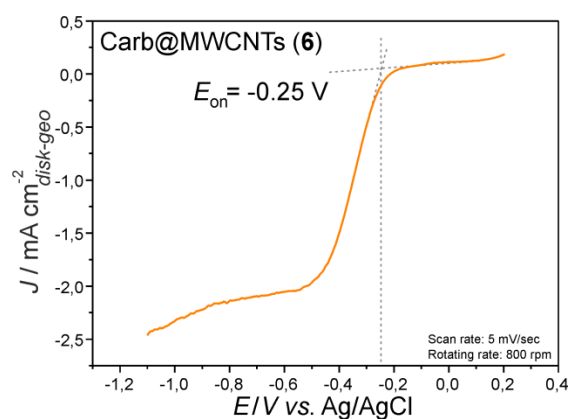
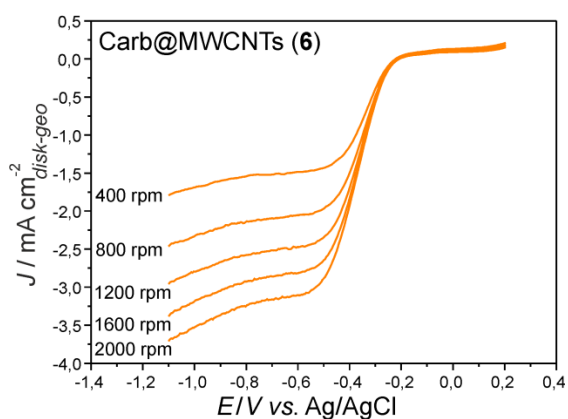
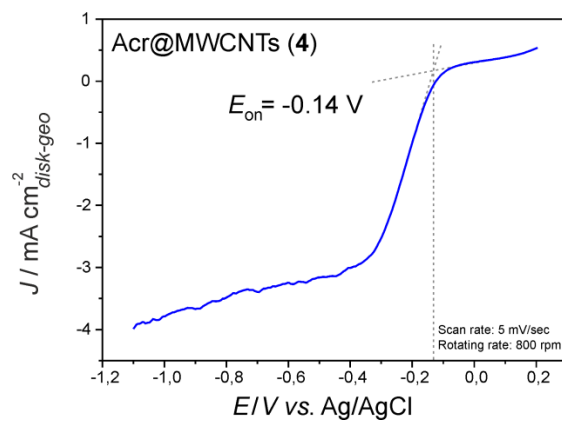
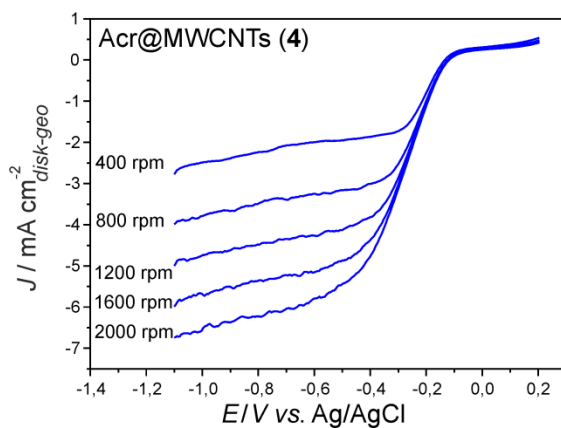
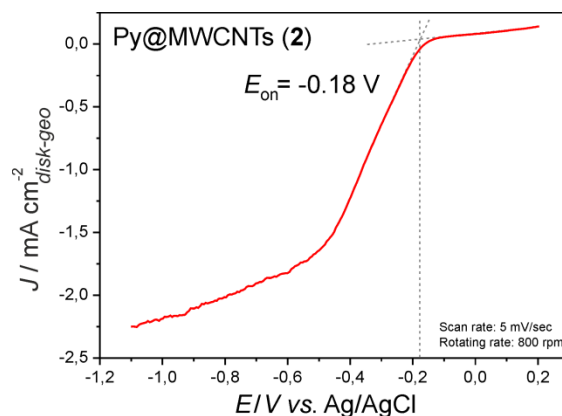
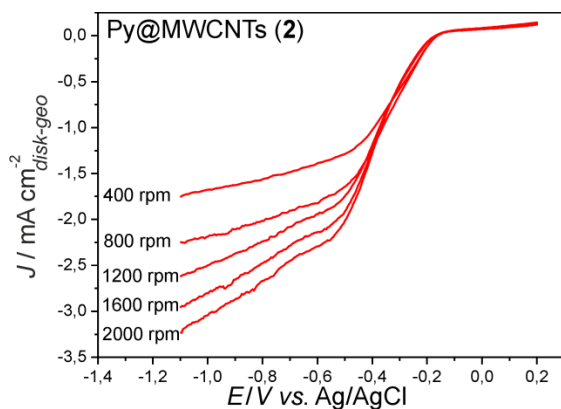
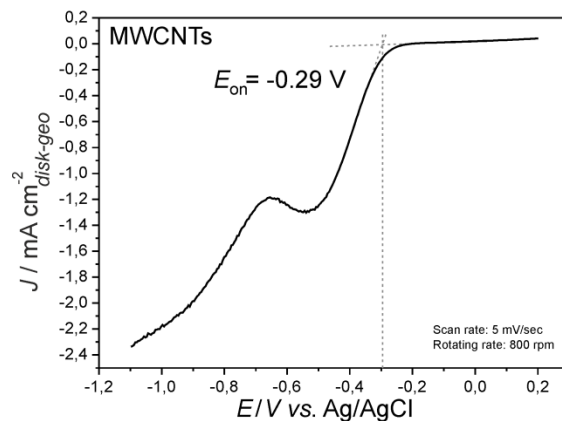
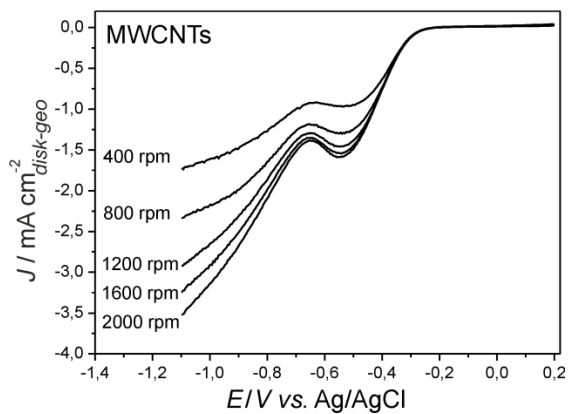


Figure 5.5. Cyclic Voltammograms for sample Acr@MW (4) in N_2 -saturated (blue-line) and O_2 -saturated solutions (red-line). The potential was linearly swept from -1.1 V to 0.2 V with a scan rate of 5 mV s^{-1} . Ag/AgCl/KCl sat. was employed as reference electrode.

To gain further insights on the ORR electrochemical performance of the *ex-situ* N-doped samples, rotating ring disk electrode (RRDE) voltammograms have been systematically acquired (Figure 5.6). The amount of the N-decorated material deposited on the RRDE is maintained constant and fixed to the optimal value measured on sample 4 (see section 5.5.5).

Linear-sweep voltammograms (LSVs) for each sample at different spin rates are shown in Figure 5.6. Potentials are linearly swept from -1.1 V to 0.2 V and finally reversed against an Ag/AgCl/KCl sat. as reference electrode with a scan rate of 5 mV s^{-1} .





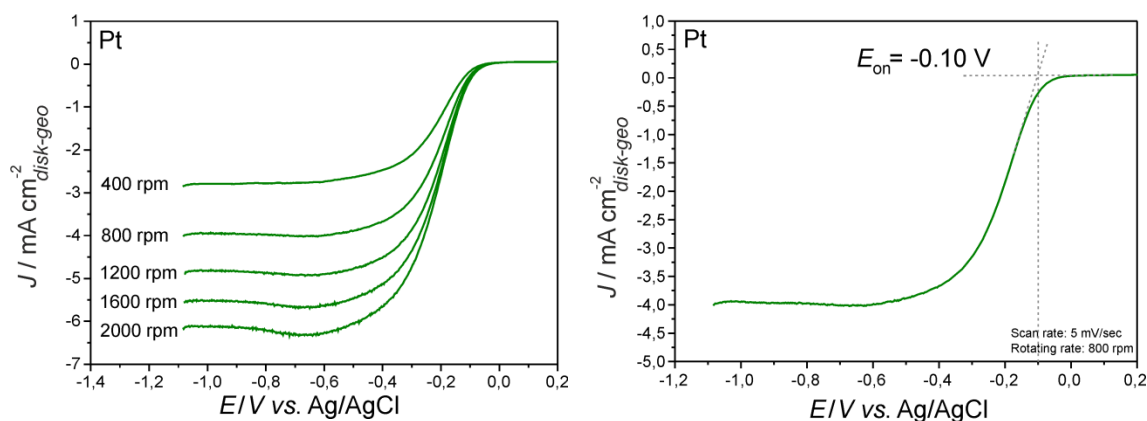


Figure 5.6. Polarization curves at different rotation rates recorded for ORR in O₂-saturated 0.1 M KOH solution for (from up to bottom): GC, MWCNTs, Py@MWCNTs (**2**), Acr@MWCNTs (**4**), Carb@MWCNTs (**6**) and Pt samples. Scan rates: 5 mV s⁻¹, catalyst loading 358 μg cm⁻².

Figure 5.7 illustrates the ORR polarization curves of the three N-doped samples (**2**, **4**, **6**), compared with pristine MWCNTs, GC and Pt-based electrocatalysts, along with the respective H₂O₂ production.⁸ For all ORR profiles reported on Figure 5.7, background currents, measured under saturated N₂ conditions, are subtracted from the respective curves to eliminate all capacitive contributions.

As Figure 5.7 shows, the onset potentials (E_{on}) of all C-based catalysts are negatively shifted from the E_{on} value measured for the Pt electrocatalyst. Noteworthy, while ORR starts at -0.181 V (E_{on}) on **2**, corresponding to an overpotential of ca. 80 mV compared to Pt, less than 40 mV (overpotential) are measured for **4**. Compared to pristine CNTs and samples **2** and **6**, the ORR onset potential measured for **4** is shifted to a more positive value featuring a remarkably higher electrocatalytic activity (Figure 5.7). The average number of electrons ($n_{E = -1 \text{ V}}$) transferred for O₂ molecule in the ORR process is calculated according to the Koutecky-Levich (*K-L*) equation and relative values are outlined in Table 5.3.^{9,10}

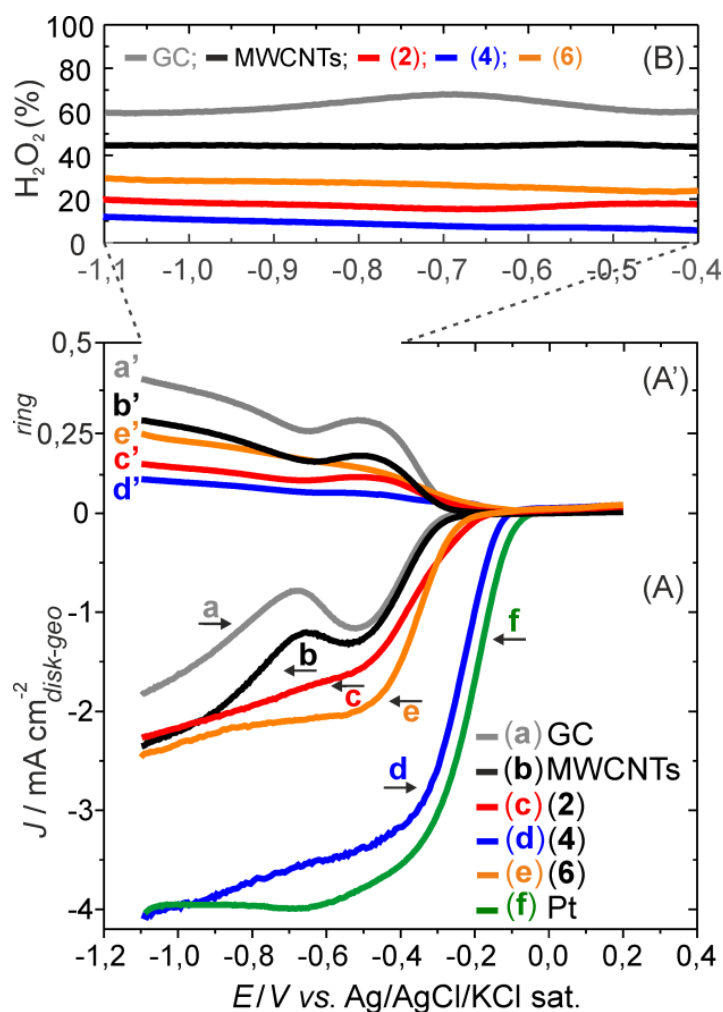


Figure 5.7. (A) Current-potential curves at 293 K for ORR in O_2 saturated 0.1 M KOH solution for the disk electrode [0.196 cm^2 GC rotating-disk electrode] and (A') for the ring electrode [0.11 cm^2 Pt rotating-ring electrode]. All samples are measured at an angular rotation rate (f) of 800 rpm. (B) H_2O_2 production (%) for all N-doped and undoped samples.

The K - L plots (J^1 vs. $f^{-1/2}$) of each catalyst, obtained from LSVs according to J values measured at -1 V, show good linearity at various rotation speeds (Figure 5.8) implying a first-order reaction towards dissolved O_2 .

The calculated n value for the ORR catalyzed by **4**, as measured at high overpotential ($E = -1 \text{ V}$), suggests a largely prevailing four-electron process. This is further confirmed by the moderate ring current recorded for this catalyst at the Pt rotating ring-disk electrode along with the modest percentage of H_2O_2 produced (Figure 5.7B).¹⁰

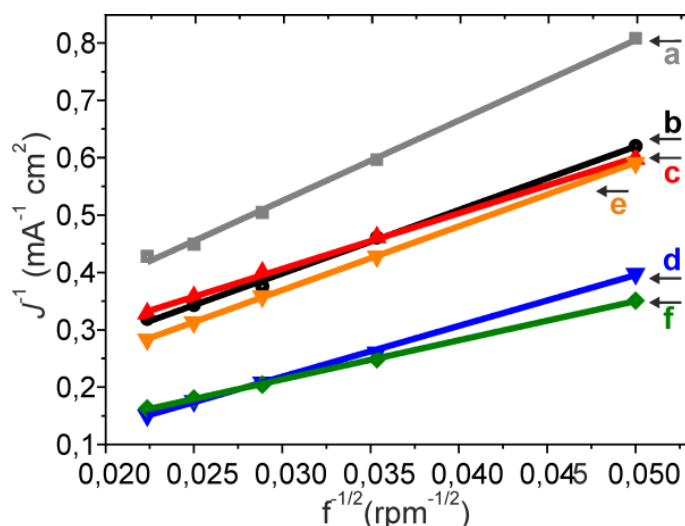


Figure 5.8. *K-L* plots for **2**, **4**, **6**, GC, MWCNTs and Pt catalysts as obtained from the respective LSVs.⁹ Parameters used: O₂ concentration (*C*), 1.15 10⁻³ mol L⁻¹; O₂ diffusion coefficient (*D*), 1.95 10⁻⁵ cm² s⁻¹; kinematic viscosity (*ν*) of the electrolyte solution, 0.008977 cm² s⁻¹.

Table 5.3. *E*_{on} values (V), average number of electrons transferred (*n*_{E=-1 V}) for O₂ molecule and average yield of hydrogen peroxide formation in 0.1 KOH. Data derived from Figures 5.7 and 5.8.

Catalyst	<i>E</i> _{on} (V)	<i>n</i> _{E=-1 V}	H ₂ O ₂ (%) [§]
GC	-0.307	2.0	64
MWCNTs	-0.299	2.5	48
Py@MW (2)	-0.181	2.9	24
Acr@MW (4)	-0.139	3.2	10
Carb@MW (6)	-0.250	2.5	32
Pt	-0.101	4.1	-

[§] average values calculated in the -0.4 ÷ -1 *E/V* range.

As it can be inferred from these data, pyridinic nitrogen sites are responsible in part of the final catalyst performance whereas neighboring carbon atoms seem to play an essential role on the catalyst ability to perform ORR efficiently.⁴ Indeed, pyridine units embedded in a conjugated (although spatially limited) sp² carbon network dramatically improve the catalyst performance both in terms of *E*_{on} and diffusion-limited current density values (*J*) (Table 5.3, catalyst **4** vs. **2** and Figure 5.7). Such a result contributes to shed light on the complex structure-reactivity relationship of N-doped carbon

nanomaterials with respect to their catalytic performance in ORR and evidences the central role played by the N-chemical environment.

In line with literature precedents for variably *in-situ* prepared N-doped carbon nanomaterials containing relatively high N-pyrrolic fractions,^{4,11} our carbazole-based system **6** shows only moderate electrocatalytic performance together with a relatively high H₂O₂ production (Figures 5.7 and 5.8). Additionally, the catalytic activity gap measured between **4** and **6** is even more remarkable while considering the higher surface N-loading on **6** as it results from the experimental data (> 50 % based on N-elemental analysis – see Table 5.1).

For the sake of completeness, any electrochemical activity (RRDE measurements) potentially associated to reagent and solvent contaminations has been properly ruled out using a blank test conducted on a “blank-test” for sample **4**. (Figure 5.10).

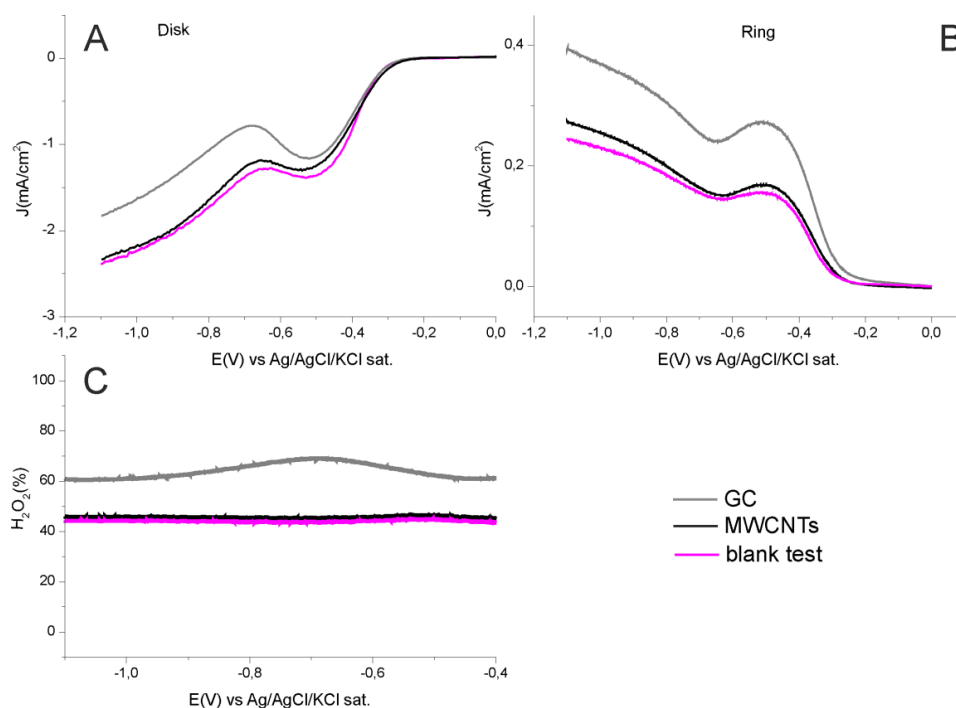


Figure 5.10. RRDE “blank test” A) Polarization curves at 800 rpm of GC (gray line), MWCNTs (black line) and “blank-test” for sample **4** (pink line) [MWCNTs and acridine in mixture - in the absence of the isopentyl nitrite reagent – after regular work-up procedure] at comparison. B) Current-potential curves at the ring electrode [0.11 cm² Pt rotating-ring electrode]. C) H₂O₂ production (%) for GC (gray line), MWCNTs (black line) and “blank-test” for sample **4** (pink line).

5.4 Conclusion

In summary, a straightforward single step and reproducible approach to the production of tailored N-doped and catalytically active carbon nanostructures, has been set up. Compared to the classical *in-situ* approach our *ex-situ* method, besides providing fundamental insights on the complex structure-reactivity relationship of N-doped carbon nanomaterials in ORR, lists a number of remarkable advantages: 1) mild reaction conditions required to N-decorate the CNTs surface (energy saving process); 2) easy tailoring of the N-containing functional groups and 3) their full exposure (atom saving) to the nanomaterial outer side where the catalytic process takes place; 4) absolutely remarkable electrocatalytic activity and long-term stability of selected N-doped metal-free samples for ORR in basic medium. As for the latter point, ink of catalyst **4** presents a complete reproducibility of its electrochemical performance in successive CV cycles, while maintaining its electrochemical properties almost unchanged when simply stored at room temperature for months. Owing to the established versatility of the *Tour* functionalization protocol with both 1D and 2D nanomaterials,¹² the methodology developed in this study can be conveniently applied to the *ex-situ* hetero-decoration of different nanocarbon materials with light-elements for the production of metal-free catalysts.

5.5 Experimental Section

5.5.1 General Considerations

All manipulations were carried out under dry nitrogen atmosphere using standard Schlenk-type techniques. Nitrogen (> 99.999%; Rivoira) was dried through a CaCl₂ column and deoxygenated with an oxysorb cartridge from Messer Griesheim prior to use. *o*DCB (ortho-dichlorobenzene) was dried according to the literature procedures¹³ and stored under nitrogen atmosphere. Dry acetonitrile (CH₃CN) was obtained by means of an MBraun Solvent Purification System. MWCNTs (98 % in C) were purchased from Sigma-Aldrich (Lot# MKBH5811V). Unless otherwise stated, all other chemicals were purchased from commercial suppliers and used as received without further purification.

Samples sonication was carried out using an Elma S15 Elmasonic sonicator bath (37 kHz) while cooling the samples in a water/ice mixture throughout the treatment. CNTs

filtration was accomplished by using inorganic PTFE filter (Whatman) with 0.2 μm pore size.

All measurements carried out on pristine MWCNTs and functionalized samples (2, 4, 6) were conducted on samples which underwent identical washing/filtration/sonication/work-up procedures. For each functionalized sample (2, 4, 6) a “blank functionalization test” was performed using identical reaction conditions and reagents except for the use of the isopentyl nitrite reagent. For RRDE of a blank sample see Figure 5.10. Furthermore, any electrochemical activity (RRDE measurements) potentially associated to reagent and solvent contaminations has been properly ruled out using a blank test conducted on MWCNTs treated with the isopentyl nitrite in oDCB/CH₃CN mixture.

5.5.2. Material Characterization and Analyses Conditions

Thermogravimetric analysis (TGA) was performed under air (100 mL/min) on an EXSTAR Thermo Gravimetric Analyzer (TG/DTA) Seiko 6200.

X-ray photoelectron spectroscopy (XPS). For XPS measurements, the samples were dispersed in ethanol and after short sonication a small drop of the suspension was drop-casted onto gold coated (about 50 nm) glass and left to dry at room temperature. Then samples were introduced in the UHV system via a loadlock and kept in the introduction chamber for at least 12 hours, allowing for the removal of volatile substances such as water and organic solvents, as confirmed by the pressure value achieved (2×10^{-10} mbar), just above the instrument base pressure. The spectra were collected at normal emission using a non-monochromated Mg-K α X-ray source (1253.6 eV) and a VSW HAC 5000 hemispherical electron energy analyzer operating in the constant-pass-energy mode at $E_{pas} = 44$ eV. The overall energy resolution was 1.2 eV as measured as a full-width at half maximum (FWHM) of the Ag 3d_{5/2} line of a pure silver reference. The binding energies of the obtained spectra were referenced to C 1s peak at 285.0 eV.¹⁴ Prior to the elemental scans, a survey scan was measured for all the samples in order to detect all the elements present. Spectroscopic analysis included a Shirley background subtraction and peak separation by using mixed Gaussian–Lorentzian functions in a least-squares curve-fitting software (Winspec)¹⁵ developed in the LISE at the Facultés Universitaires Notre-Dame de la Paix, Namur, Belgium.

Raman spectra were recorded using the 647.1 nm emission of a Kr ion laser source and each CNTs sample was prepared by gently pressing the carbon powder into the

cavity of the sample holder. The scattered radiation was collected in a back scattering geometry, dispersed using the single stage configuration of a triple Raman spectrometer (Trivista TR555) equipped with a 900 grooves/mm grating and recorded by a liquid nitrogen cooled CCD detector. The beam profile was cleaned by a spatial filter and Rayleigh scattering was filtered out using Notch filters. The spectral resolution was 1 cm^{-1} . The incident laser power on the sample was lower than 0.3 mW and any damage of the sample due to the laser was carefully checked and excluded. The Raman spectra were collected in order to detect the presence and strength of the G and D modes.¹⁶ The G mode, which is located at around 1590 cm^{-1} , is characteristic of the sp^2 in-plane bond-stretching motion of pairs of carbon atoms in graphite-like structures. The D mode is found at around 1320 cm^{-1} and becomes active only in the presence of disorder.¹⁶ All recorded curves were fitted using Lorentzian line-shapes and the intensity ratios (namely I_D/I_G) were calculated from the fitted areas of the D and G bands.^{16,17,18} According to the literature,¹⁸ D- and G-peak intensities were used for the calculation of the I_D/I_G ratios.

Transmission Electron Microscopy (TEM) analysis of modified and unmodified CNTs was performed by a Philips CM12 microscope operating at 120 kV, on samples prepared by drop casting previously sonicated suspensions (EtOH) over copper grids coated with a Formvar film (FF200-Cu - Formvar film only). TEM images were recorded with a CCD camera (Gatan 791).

Rotating-ring disk electrode (RRDE) measurements were performed using a ring-disk electrode from Pine instrument consisting of a glassy carbon (GC) disk insert ($\text{Ø } 5\text{mm}$; $A = 0.196 \text{ cm}^2$) and a Pt ring ($A = 0.11 \text{ cm}^2$) The RRDE measurements were carried out using a Modulated Speed Rotator (MSR) from Pine Instruments. All the measurements were carried out using an Autolab potentiostat/galvanostat in a single compartment glass cell using a three electrode arrangement. The working electrode was prepared as follows: a proper amount of CNTs (10 mg) was dispersed in 0.220 g of water, 0.112 g of ethanol and 0.084 g of a Nafion solution (5 wt. % in lower aliphatic alcohols and water). The resulting ink was sonicated for 30 - 45 min and drop-casted onto the glassy carbon electrode (3 mg). The as-prepared electrode was then dried at room temperature and its final loading was calculated in $358 \mu\text{g}/\text{cm}^2$. A platinum wire was used as counter electrode, and a double junction Ag/AgCl/KCl sat. electrode served as reference electrode. All CV and RRDE experiments were carried out at a scan rate of 5 mV/s in the potential range of + 0.2 to - 1.2 V. Nitrogen or oxygen were used to purge the

solution to achieve oxygen-free or oxygen-saturated electrolyte solution. Commercial Metrohm Pt electrode (\varnothing 3 mm) was used for comparison. All measurements were repeated at least four times for verification and all CNT inks resulted indefinitely stable in air for months.

Elemental analyses were performed using a Thermo FlashEA 1112 Series CHNS-O elemental analyzer. The average values are calculated over three independent runs.

5.5.3 General procedure for the *ex-situ* MWCNTs functionalization via aryldiazonium salt chemistry

In a typical procedure, MWCNTs (40 mg) were weighed into a two-necked 100 mL flask and suspended in 32 mL of dry and degassed *o*DCB. The suspension was sonicated for 30 min and then treated with a degassed acetonitrile solution (16 mL) of the corresponding aniline (**1**, **3**, **5**, 0.86 mmol). Isopentyl nitrite (0.17 mL, 1.30 mmol) was added *via* syringe and the suspension was further sonicated for 10 min. The mixture was heated at 80 °C for 14 hours under stirring and nitrogen atmosphere. Afterwards, the mixture was cooled to room temperature, diluted with ethylacetate (20 mL) and sonicated for 20 minutes before being centrifugated in order to recover the solid residue. The latter was then washed with ethylacetate and then twice with dichloromethane, each time sonicated for 10 min and separated from the supernatant by centrifugation. The solid residue was finally suspended in dichloromethane, sonicated for 20 min and filtered through a 0.2 μm -pore PTFE filter. The collected material was dried at 50 °C under vacuum to constant weight and stored on air at room temperature.

5.5.4 Acid-base titration of N-decorated samples 2 and 4

5 mg of the selected N-decorated material (**2** or **4**) were suspended in 7 mL of a standard HCl solution (2.8×10^{-3} M, standardized with Na_2CO_3 as primary standard), sonicated for 30 min and maintained in the dark at room temperature under stirring for 48 h. Afterwards, the suspension was centrifugated and three aliquots of the supernatant solution were titrated with a standardized solution of NaOH (2×10^{-3} M). The pyridine content (N_{Py} %) was calculated for each sample as the average value over the three independent runs.⁶

5.5.5 Electrochemical data processing

The amount of the N-decorated material deposited on the RRDE is maintained constant and fixed to the optimal value [catalyst loading (μg of N-MWCNTs cm^{-2})] measured on sample 4.

Table 5.4. Number of exchange electrons for RRDE measurements carried out at different catalyst loadings (298, 358 and 430 $\mu\text{g cm}^{-2}$).

Catalyst loading (mg of ink)	2.5	3	3.6
Catalyst loading ($\mu\text{g cm}^{-2}$)	298	358	430
Catalyst loading (μg) ^a	58	70	84
Exchange electrons (n)	2.94	3.24	3.13

^a 0.196 cm^2 GC rotating-disk electrode

The ORR is studied through the RRDE measurements as described before. The Pt Ring electrode potential is kept constant at a value of 0.5 V *vs.* Ag/AgCl/KCl_{sat.} while the potential of the Disk electrode is swept from -1.1 V to 0.2 V and reversed against an Ag/AgCl/KCl_{sat.} as reference electrode with a scan rate of 5 mV s^{-1} . The Ring potential value is chosen to allow only the oxidation of H_2O_2 .¹⁰ While the total Disk current I_D is the sum of the O_2 reduction current to H_2O ($I_{\text{H}_2\text{O}}$) and to H_2O_2 ($I_{\text{H}_2\text{O}_2}$) (eq. 5.1), the Ring current I_R is due to the H_2O_2 oxidation ($I_{\text{H}_2\text{O}_2}$) exclusively (eq. 5.2).

$$I_D = I_{\text{H}_2\text{O}} + I_{\text{H}_2\text{O}_2} \quad (\text{eq. 5.1})$$

$$I_R = I_{\text{H}_2\text{O}_2} N \quad (\text{eq. 5.2})$$

N is the Collection Efficiency¹⁹ and it is the fraction of the material from the disk which subsequently flows at the ring electrode. It can be expressed as a fraction between 0.0 and 1.0 and depends on the electrode geometry. In this work we make use of the theoretical Collection Efficiency of 0.256 as reported for the employed Pine RRDE electrode.

Accordingly, the molar fraction of H_2O_2 ($X_{\text{H}_2\text{O}_2}$) produced in the process is calculated from the number of moles of H_2O ($n_{\text{H}_2\text{O}}$) and H_2O_2 ($n_{\text{H}_2\text{O}_2}$) using equations 5.3, 5.4 and 5.5:

$$n_{H_2O} = \frac{I_{H_2O}}{4F} \quad (\text{eq. 5.3})$$

$$n_{H_2O_2} = \frac{I_{H_2O_2}}{2F} \quad (\text{eq. 5.4})$$

$$X_{H_2O_2} = \frac{n_{H_2O_2}}{n_{H_2O_2} + n_{H_2O}} \quad (\text{eq. 5.5})$$

Replacing moles with the experimental currents (I_D and I_R) as calculated from equations. 5.1 and 5.2 we obtain eq. 5.6:

$$X_{H_2O_2} = \frac{2I_R/N}{I_D + I_R/N} \quad (\text{eq. 5.6})$$

The number of electrons transferred per O_2 molecule in the ORR for the different catalysts has been calculated by the Koutecky-Levich equation applied to the ORR curves obtained at different rotation rates (rpm).²⁰ The Koutecky-Levich equation is given by equation 5.7:

$$\frac{1}{j} = \frac{1}{j_{cc}} + \frac{1}{nK_f\sqrt{f}} \quad (\text{eq. 5.7})$$

With:

$$K_f = 0.2FC_0D_0^{2/3}\nu^{-1/6}$$

Where, j is the current density, j_{cc} is the kinetic current density, n is the number of exchanged electrons, F is the Faraday constant, D_0 is the oxygen diffusion coefficient ($1.95 \times 10^{-5} \text{ cm}^2 \text{ s}^{-1}$), f is the angular rotation rate of the electrode (rpm), ν is the kinematic viscosity of the solution ($0.008977 \text{ cm}^2 \text{ s}^{-1}$) and C_0 is the O_2 concentration in solution ($1.15 \times 10^{-3} \text{ mol dm}^{-3}$).¹⁰ With these parameters, the value of K_f constant is 0.03538. The average number of electrons n exchanged during the ORR has been extrapolated from the slop of the plot of j^{-1} versus $f^{-1/2}$ at a specific potential value. We have recorded cyclic voltammeteries from -1.1 V to 0.2 V at different rotation rates (from 400 to 2000 rpm) and calculated the n values at -1 V.

References

- ¹ a) S. Minhua, in: *Electrocatalysis in Fuel Cells, A Non- and Low-Platinum Approach*, S. Minhua (Ed.), Springer, London **2013**, p 327. b) D. S. Su, J. Z. Zhang, B. Frank, A. Thomas, X. Wang, J. Paraknowitsch, R. Schlögl, *ChemSusChem* **2010**, *3*, 169. c) N. M. Markovic, T. J. Schmidt, V. Stamenkovic, P. N. Ross, *Fuel Cells* **2001**, *1*, 105. d) Z. Chen, D. Higgins, A. Yu, L. Zhang, J. Zhang, *Energy Environ. Sci.* **2011**, *4*, 3167. e) M. Chisaka, Y. Suzuki, T. Iijima, Y. Sakurai, *J. Phys. Chem. C* **2011**, *115*, 20610.
- ² a) K. Gong, F. Du, Z. Xia, M. Durstock, L. Dai, *Science* **2009**, *323*, 760. b) K. Chizari, A. Deneuve, O. Ersen, I. Florea, Y. Liu, D. Edouard, I. Janowska, D. Begin, C. Pham-Huu, *ChemSusChem* **2012**, *5*, 102. c) A. Morozan, P. Jégou, M. Pinault, S. Campidelli, B. Jusselme, S. Palacin, *ChemSusChem* **2012**, *5*, 647. d) Y. Li, W. Zhou, H. Wang, L. Xie, Y. Liang, F. Wei, J.-C. Idrobo, S. J. Pennycook, H. Dai, *Nature Nanotech.* **2012**, *7*, 394. e) D. Geng, Y. Chen, Y. Chen, Y. Li, R. Li, X. Sun, S. Ye, S. Knights, *Energy Environ. Sci.* **2011**, *4*, 760. f) K. Parvez, S. Yang, Y. Hernandez, A. Winter, A. Turchanin, X. Feng, K. Müllen, *ACS Nano* **2012**, *6*, 9541. g) D. Yu, E. Nagelli, F. Du, L. Dai, *J. Phys. Chem. Lett.* **2010**, *1*, 2165. h) S. M. Unni, S. Devulapally, N. Karjule, S. Kurungot, *J. Mater. Chem.* **2012**, *22*, 23506. i) L. Qu, Y. Liu, J.-B. Baek, L. Dai, *ACS Nano* **2010**, *4*, 1321. j) C. V. Rao, Y. Ishikawa, *J. Phys. Chem. C.* **2012**, *116*, 4340.
- ³ a) W. An, C. H. Turner, *J. Phys. Chem. C* **2009**, *113*, 7069. b) M. Kaukonen, A. V. Krasheninnikov, E. Kauppinen, R. M. Nieminen, *ACS Catal.* **2013**, *3*, 159. c) H. Kim, K. Lee, S. I. Woo, Y. Jung, *Phys. Chem. Chem. Phys.* **2011**, *13*, 17505.
- ⁴ a) S. Kuroki, Y. Nabae, M. Chokai, M.-A. Kakimoto, S. Miyata, *Carbon* **2012**, *50*, 153. b) L. Feng, Y. Yan, Y. Chen, L. Wang, *Energy Environ. Sci.* **2011**, *4*, 1892. c) C. V. Rao, C. R. Cabrera, Y. Ishikawa, *J. Phys. Chem. Lett.* **2010**, *1*, 2622.
- ⁵ a) J. L. Bahr, J. M. Tour, *Chem. Mater.* **2001**, *13*, 3823. b) C. A. Dyke, J. M. Tour, *J. Am. Chem. Soc.* **2003**, *125*, 1156. c) C. A. Dyke, J. M. Tour, *Nano Lett.* **2003**, *3*, 1215. d) J. L. Hudson, M. J. Casavant, J. M. Tour, *J. Am. Chem. Soc.* **2004**, *126*, 11158. e) C. A. Dyke, M. P. Stewart, F. Maya, J. M. Tour, *Synlett* **2004**, *1*, 155. f) B. K. Price, J. L. Hudson, J. M. Tour, *J. Am. Chem. Soc.* **2005**, *127*, 14867. g) B. K. Price, J. M. Tour, *J. Am. Chem. Soc.* **2006**, *128*, 12899. h) C. D. Doyle, J. M. Tour, *Carbon* **2009**, *47*, 3215.
- ⁶ For related titration procedures see: a) B. Ballesteros, G. de la Torre, C. Ehli, G. M. Aminur Rahman, F. Agulló-Rueda, D. M. Guldi, T. Torres, *J. Am. Chem. Soc.* **2007**, *129*, 5061. b) E. Moaseri, M. Baniadam, M. Maghrebi, M. Karimi, *Chem. Phys. Lett.* **2013**, *555*, 164.
- ⁷ M. K. Daletoua, F. Paloukisa, A. Stefopouloa, *ECS Trans.* **2009**, *25*, 1915.
- ⁸ M. Neergat, V. Gunasekar, R. Rahul, *J. Electroanal. Chem.* **2011**, *658*, 25.
- ⁹ A. J. Bard, L. R. Faulkner, in: *Electrochemical Methods: Fundamentals and Applications*, 2nd Edition, John Wiley & Sons, Inc.: New York, **2001**, pp. 856.
- ¹⁰ Y. Wang, D. Zhang, H. Liu, *J. Power Sources* **2010**, *195*, 3135.

-
- ¹¹ a) D. Yu, Q. Zhang, L. Dai, *J. Am. Chem. Soc.* **2010**, *132*, 15127. b) S. Shanmugam, T. Osaka, *Chem. Commun.* **2011**, *47*, 4463. c) S. Kundu, T. C. Nagaiah, W. Xia, Y. Wang, S. Van Dommele, J. H. Bitter, M. Santa, G. Grundmeier, M. Bron, W. Schuhmann, J. Muhler, *J. Phys. Chem. C* **2009**, *113*, 14302.
- ¹² a) T. Kuila, S. Bose, A. K. Mishra, P. Khanra, N. H. Kim, J. H. Lee, *Prog. Mater. Sci.* **2012**, *57*, 1061. b) J. Liu, J. Tang, J. J. Gooding, *J. Mater. Chem.* **2012**, *22*, 12435.
- ¹³ D. D. Perrin, W. L. F. Armarego, D. R. Perrin, in: *Purification of Laboratory Chemicals*, Vol. 1, 2nd ed., Pergamon, **1980**.
- ¹⁴ T. Tsoufis, G. Tuci, S. Caporali, D. Gourmis, G. Giambastiani, *Carbon* **2013**, *59*, 100.
- ¹⁵ a) T. Tsoufis, J.-F. Colomer, E. MacCallini, L. Jankovič, P. Rudolf, D. Gourmis, *Chem. Eur. J.* **2012**, *18*, 9305. b) I. V. Pavlidis, T. Vorhaben, T. Tsoufis, P. Rudolf, U. T. Bornscheuer, D. Gourmis, H. Stamatis, *Bioresource Technol.* **2012**, *115*, 164.
- ¹⁶ A. C. Ferrari, J. Robertson, *Phys. Rev. B* **2000**, *61*, 14095.
- ¹⁷ A. C. Ferrari, J. Robertson, *Phys. Rev. B* **2001**, *64*, 075414.
- ¹⁸ M. M. Lucchese, F. Stavale, E. H. Martins Ferreira, C. Vilani, M. V. O. Moutinho, R. B. Capaz, C. A. Achete, A. Jorio, *Carbon* **2010**, *48*, 1592.
- ¹⁹ W. J. Albery, S. Bruckenstein, *Trans. Faraday Soc.* **1966**, *62*, 1920.
- ²⁰ S. Treimer, A. Tang, D. C. Johnson, *Electroanalysis* **2002**, *14*, 165.

6. Chemically Functionalized Carbon Nanotubes with Pyridine Groups as Easily Tunable N-decorated Nanomaterials for the Oxygen Reduction Reaction in Alkaline Medium

6.1 Abstract

We report on the N-decoration of multi-walled carbon nanotubes (MWCNTs) *via* chemical functionalization under mild reaction conditions. The introduction of tailored pyridinic functionalities as N-containing edge-type group mimics, generates effective catalysts for the oxygen reduction reaction (ORR) in alkaline environment. The adopted methodology lists a number of remarkable technical advantages, among which an easy tuning of the electronic properties of N-containing groups. The latter aspect further increases the level of complexity for the rationalization of the role of the N-functionalities on the ultimate electrochemical performance of the as-prepared metal-free catalysts. Electrochemical outcomes crossed with the computed electronic charge density distributions on each scrutinized pyridine group have evidenced the central role played by the N-chemical environment on the final catalyst performance. Notably, little variations of the atomic charges on the N-proximal carbon atoms of the chemically grafted heterocycles change the overpotential values at which the oxygen reduction reaction starts. The protocol described hereafter offers an excellent basis for the development of more active metal-free electrocatalysts for the ORR. Finally, the as-prepared catalytically active materials represent a unique model for the in-depth understanding of the underlying ORR mechanism.

6.2 Introduction

Efficient and low-cost electrocatalysts capable of facilitating the sluggish cathodic oxygen reduction reaction (ORR) are at the heart of renewable energy technologies based on fuel cells and other electrochemical energy devices. The prohibitive cost of the

platinum-group metal (PGM)-based electrocatalysts, together with their limited reserves in nature, constitute the major drawback to their sustainable commercial application in several technological fields. In spite of their outstanding electrocatalytic performance in the ORR, Pt-based electrocatalysts can suffer from severe poisoning effects (such as gas adsorption or fuels cross-over) which affect their durability and limit their practical application sphere.¹ Along with recent intensive research efforts in reducing or replacing Pt-based electrocatalysts in ORR,² light-heteroelement doped carbon nanomaterials (CNMs) with at least one dimension tailored at the nanometer scale have raised the interest of the catalysis and material science community.³ In particular, nitrogen-doped CNMs (N-CNMs) have been intensively investigated, in light of their remarkable electrochemical properties for the ORR in alkaline environment.^{3c,4} Moreover, the presence of an adequate number of catalytically active sites exposed on materials typically featured by high surface area and excellent electrical conductivity makes them attractive single-phase catalysts with no need of any additional conductive support. Although the ORR in alkaline media is catalyzed by a wide variety of pure carbon-based electrocatalysts such as glassy carbon (GC),⁵ active carbon,⁶ carbon nanotubes,⁷ graphene and other related carbon-based materials,^{3,8} the absence of alien atoms in the sp^2 C-network translates into a simple $2e^-$ reduction process featured by moderate current densities (J) and low onset potentials, with the generation of HO_2^- ions as the main oxidation product. On the contrary, an appropriate CNMs engineering through a light-heteroelement doping (mostly N-doping) has led to the obtainment of more performing metal-free electrocatalysts fostering a prevalent $4e^-$ reduction process with OH^- ions as the major oxidation product. Intensive studies in the field have contributed to the discovery of excellent N-CNM-based, metal-free systems active in the ORR, showing similar and even better electrocatalytic activity, long-term stability and tolerance to crossover effects than expensive platinum-based electrocatalysts.^{3d,4a,9} Since the first seminal report by Dai and co-workers in 2009,^{9a} a huge effort has been done to prepare either mono-dimensional (1D) or bi-dimensional (2D) N-CNMs and to fully exploit their catalytic ability on both a theoretical¹⁰ and experimental³ ground. Among the synthetic methods used for their preparation, Chemical Vapor Deposition (CVD) still remains the most effective and widely used technique,¹¹ although other approaches like CNMs annealing in the presence of different nitrogen sources,^{22,12} chemical reduction/doping with selected N-containing reducing agents^{3b,13} or direct carbonization of N-containing organic precursors^{14,24e} constitute valuable and

alternative synthetic paths. However, none of the above mentioned approaches fulfills the requirement of a protocol for an effective tailoring of the introduced N-functionalities.

Although the role of nitrogen doping and the nature of the “catalytically active” nitrogen sites in these complex carbon nanostructures still represent an intensive matter of debate,³ it seems clear that the inclusion of nitrogen(s) in the honeycomb carbon structure, besides inducing remarkable modifications of the physico-chemical properties of the undoped 1D and 2D materials (such as structure, electrical conductivity, surface properties and oxidation stability), breaks the electroneutrality of the Csp^2 network, thus generating carbon active sites proximal to the heteroatom¹⁵ which take part in the molecular oxygen activation and subsequent O-O bond breaking.^{9a,16} Indeed, a net redistribution of the charge density around the nitrogen atoms improves the material oxygen adsorption properties and facilitates the occurrence of the electrochemical oxygen reduction;^{22,17} an appropriate balance between a moderate oxygen binding energy and a highly localized electron density around the active site, seems to be crucial for getting highly performing ORR catalysts.^{9a,18} Independent research groups have recently discussed how the introduction of N-atoms into the network of a carbon-based nanomaterial would increase the electronic density of states near the Fermi level, thus facilitating the electron transfer from the electronic bands of the C network to the O_2 antibonding orbitals.¹⁹ As a matter of fact, the polarization of the C-N bond as well as the net atomic electronic charge distribution on selected N-containing heterocycles, can be invoked as a descriptor for the catalyst/substrate interaction, *provisio* that a fine tuning of the N-dopants in the carbon nanostructures can be achieved.

The type of nitrogen functional groups and the nitrogen doping level strongly depend on the applied synthetic conditions;^{3,20} a precise control of these factors still remains far from being exhaustively accomplished. If a partial control on the degree and type of N-doping in 1D N-CNMs is achieved through an accurate optimization of the CVD synthetic conditions,²¹ a similar goal seems to be more efficiently approached in the case of 2D N-CNMs through the annealing of undoped CNMs in the presence of well defined N-containing precursors.²² Irrespective of the method used, different N-functionalities (such as pyridinic N, pyrrolic N, quaternary N, etc...) often co-exist in the as-synthesized N-CNMs; a simple adjustment of their relative concentration in the material remains the only tunable parameter. As a consequence, the role of the different N-functionalities on the catalytic efficiency of the as-synthesized N-CNMs still remains

rather elusive and it is at the origin of controversial debates in the scientific community, sometimes producing even conflicting literature results.^{3,22}

Wågberg and co-workers have recently demonstrated how a thermal post-synthetic treatment on CVD-prepared N-doped MWCNTs can result in the transformation of pyrrolic and pyridinic nitrogen sites into quaternary nitrogen sites (N-Qs), with an overall improvement of the electrocatalytic performance in ORR.²³ Although any conclusion on the electrocatalytic contribution of pyridinic and quaternary N-functionalities still remains difficult to draw up,^{9c,d,16a,23,24,25,26} and the role of the total N-loading on the ORR activity looks like rather uncertain,^{27,28} it is accepted that nitrogen sites located at the graphitic edge planes^{23,27a} exhibit the highest catalytic efficiency in ORR. Accordingly, a $4e^-$ reduction path takes place prevalently on the nitrogen *edge* defects [*i.e.* on the pyridinic and on the quaternary N-sites (the so-called “valley graphitic-N”)], while a less efficient $2e^-$ process preferentially occurs on the *in-plane* nitrogen defects.^{27a,29}

Taking advantage from these fundamental concepts, the chemical functionalization candidates as a valuable and alternative approach to the nitrogen decoration of complex carbon nanostructures by means of tailored “edge-type” N-containing functionalities.³⁰ Compared with the classical CVD approach, chemical functionalization offers a unique tool to the rationalization of the fundamental structure-reactivity relationship of N-doped carbon nanomaterials active in ORR. Moreover, it lists a number of remarkable technical advantages: (i) the energy-saving conditions required for the CNTs decoration with well defined N-containing functional groups; (ii) their easy chemical and structural tuning; (iii) a substantial atom-economy decoration strategy (full exposure of the N-containing groups to the nanomaterial outer side where the catalytic reaction takes place); (iv) a remarkable electrocatalytic activity and long-term stability of the as-prepared N-doped carbon nanostructure employed as metal-free systems for the ORR in basic environment. In chapter 5,³⁰ we have demonstrated how simple pyridine groups embedded in a conjugated (although spatially limited) sp^2 carbon network and covalently linked to the CNT sidewalls can guarantee remarkable catalytic performance in ORR, in terms of both onset potentials (E_{on}) and diffusion-limited current density (J) values. The interest for tailored electron-poor N-containing groups as mimics of “nitrogen edge-type defects” stems from their postulated ability to improve the onset potential values in the electrochemical mediated ORR.²² Here, we report a full account on the synthesis, characterization and electrocatalytic activity of a series of MWCNTs

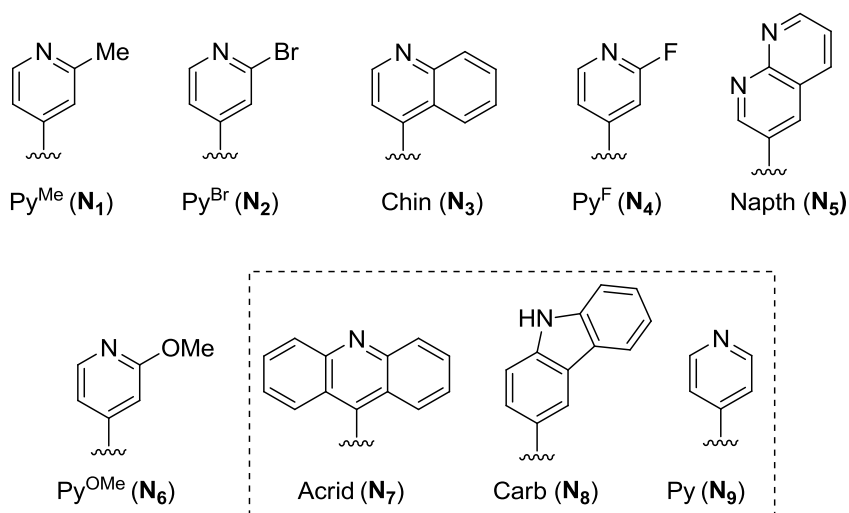
functionalized with a variety of well defined pyridine groups. This study highlights the central role played by the pyridine moiety on the electrocatalytic activity of these N-decorated MWCNTs in the ORR. Most importantly, a clear-cut evidence of the role of the electronic charge density distribution at the chemically grafted N-heterocycles on the final catalyst performance in the ORR is given. Such a result introduces an additional level of complexity to the rationalization and comprehension of the ultimate role of the pyridine groups on the electrocatalytic performance in the ORR promoted by these nanomaterials.

6.3 Results and Discussion

The main objective of the present study is to provide a clear-cut understanding of the complex structure-reactivity relationship which drives the electrocatalytic performance of carbon nanomaterials decorated with well-defined N-containing functionalities (*i.e.* pyridinic-N sites). Besides offering a definitive answer to the widely debated question dealing with the role played by pyridine groups on the electrocatalytic activity of N-functionalized/doped carbon nanomaterials in the ORR, the obtained results suggest the existence of a coherent descriptor of the catalyst performance (at least in terms of onset potential values) based on the electronic charge density distribution at the N-neighboring carbon atoms as well as on the related N–C_α bond polarization.

On a merely speculative ground, the concept of “doping” is more properly referred to those CNMs featured by “implanted” heteroelements in the sp^2 carbon network; therefore it should be kept distinguished from that of “chemical functionalization” with heteroelement-containing functionalities attached to the carbon basal or edge planes. On the other hand, selected “dopants” or “hetero-functionalities”, like those containing pyridine or pyrrole groups, are conceivable as “edge-type” groups only, and therefore “chemical functionalization” can be proposed as a valuable alternative path to bring N-containing functionalities on the CNM’s board as edge-type defect mimics. Such an approach offers a unique tool to the unambiguous understanding of the catalytic role exerted by selected N-containing groups in the ORR, paving the way to the development of tailored and more catalytically active metal-free electrocatalysts for the ORR and providing a simplified model for the in-depth understanding of the underlying reaction mechanisms.

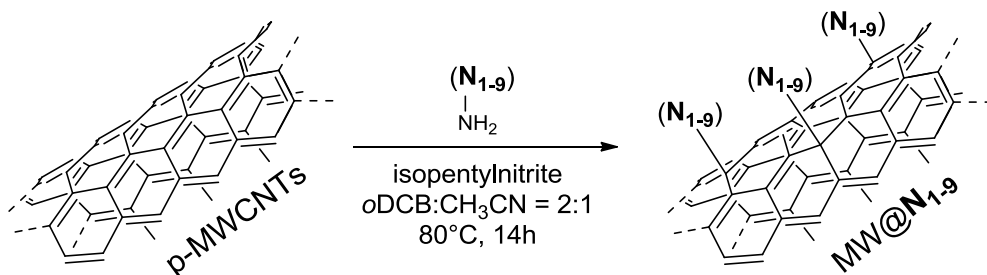
Following our preliminary studies on Acridine and Pyridine-functionalized MWCNTs (see chapter 5),³⁰ a series of variably substituted pyridine groups have been selected as candidates for the chemical functionalization of MWCNTs (Scheme 6.1). A control on the electronic properties of the heterocycles as well as on the polarization of the N–C $_{\alpha}$ bond is made possible through a selection of either electron donating (EDG) or electron withdrawing (EWG) groups attached to the α -position of the pyridine ring.



Scheme 6.1. N-containing heterocycles used for the MWCNTs decoration (N_{1-6} this chapter). Functional groups N_{7-9} (included in the dashed frame) have already been discussed in chapter 5³⁰ and cited here for completeness.

6.3.1 Synthesis and characterization of the N-functionalized MW@ N_{1-6} samples

The adopted procedure for the N-decoration of the MWCNTs is based on the classical aryl-diazonium salt chemistry (*Tour* protocol).³¹ The functionalization is conveniently performed under relatively mild reaction conditions (Scheme 6.2), starting from pristine MWCNTs and one aniline derivative chosen among the selected N-containing moieties (Scheme 6.1).



Scheme 6.2. MWCNTs N-decoration via aryl diazonium salt (*Tour*) protocol (MW@N_{1-6} this chapter). Samples $\text{MW@N}_{7,9}$ have been already discussed in chapter 5³⁰ and cited here for completeness.

Each functionalized sample undergoes a careful workup procedure made of successive and multiple sonication/centrifugation and filtration cycles as to remove all the unreacted reagents. A blank functionalization test (a parallel reaction conducted in the absence of the isopentyl nitrite reagent) is carried out for each aniline sample, with the aim of quantifying the residual amount (traces) of physisorbed N-contaminants potentially deriving from the reaction procedure. All the as-prepared samples (MW@N₁₋₆) have been spectroscopically [XPS (Figure 6.4), Raman (Figure 6.2)] and morphologically (TEM, Figure 6.1) characterized.

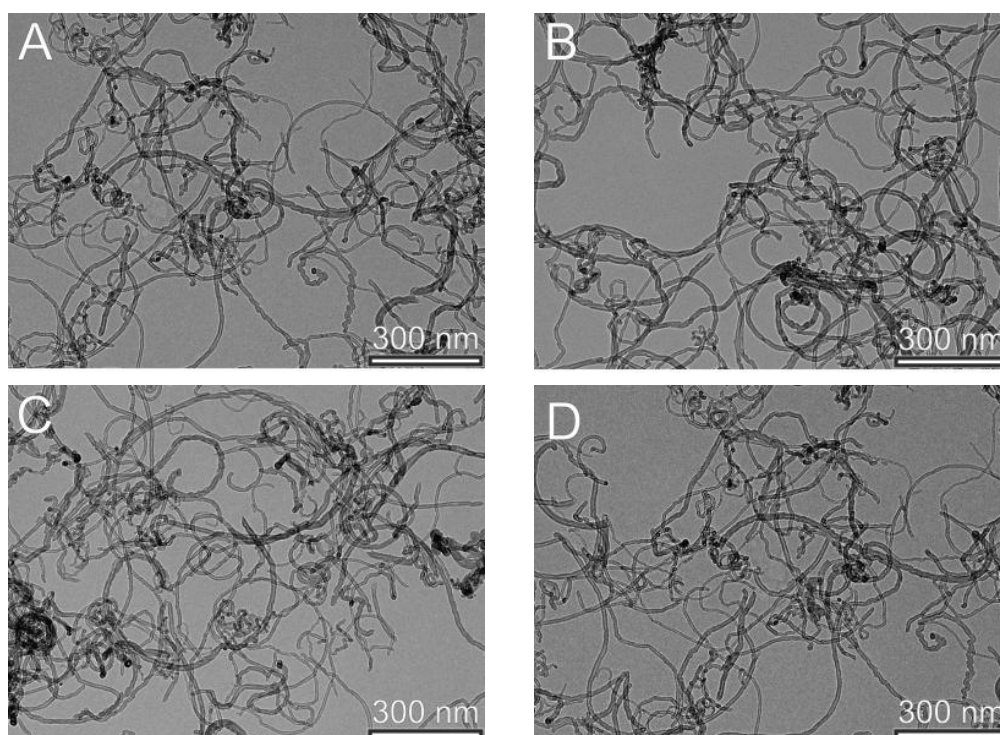


Figure 6.1. TEM images of pristine MWCNTs (A) and MW@N₂ (B), MW@N₃ (C), MW@N₄ (D) samples.

In the TEM analyses, all the functionalized materials (MW@N₁₋₆) don't present any appreciable morphological change in terms of either tubes length and diameter or bundles aggregation on the whole scanned area. Figures 6.1B-D show TEM pictures recorded on a selection of the most representative functionalized samples (Figure 6.1B: MW@N₂; Figure 6.1C: MW@N₃; Figure 6.1D: MW@N₄) compared with the pristine ones (Figure 6.1A).

Similarly, Raman spectra of all the MW@N samples do not reveal any major change in the intensity ratio of the D and G modes (I_D/I_G), this parameter being commonly used as a benchmark of the crystallite and defect sites surface density alteration (Figure 6.2).

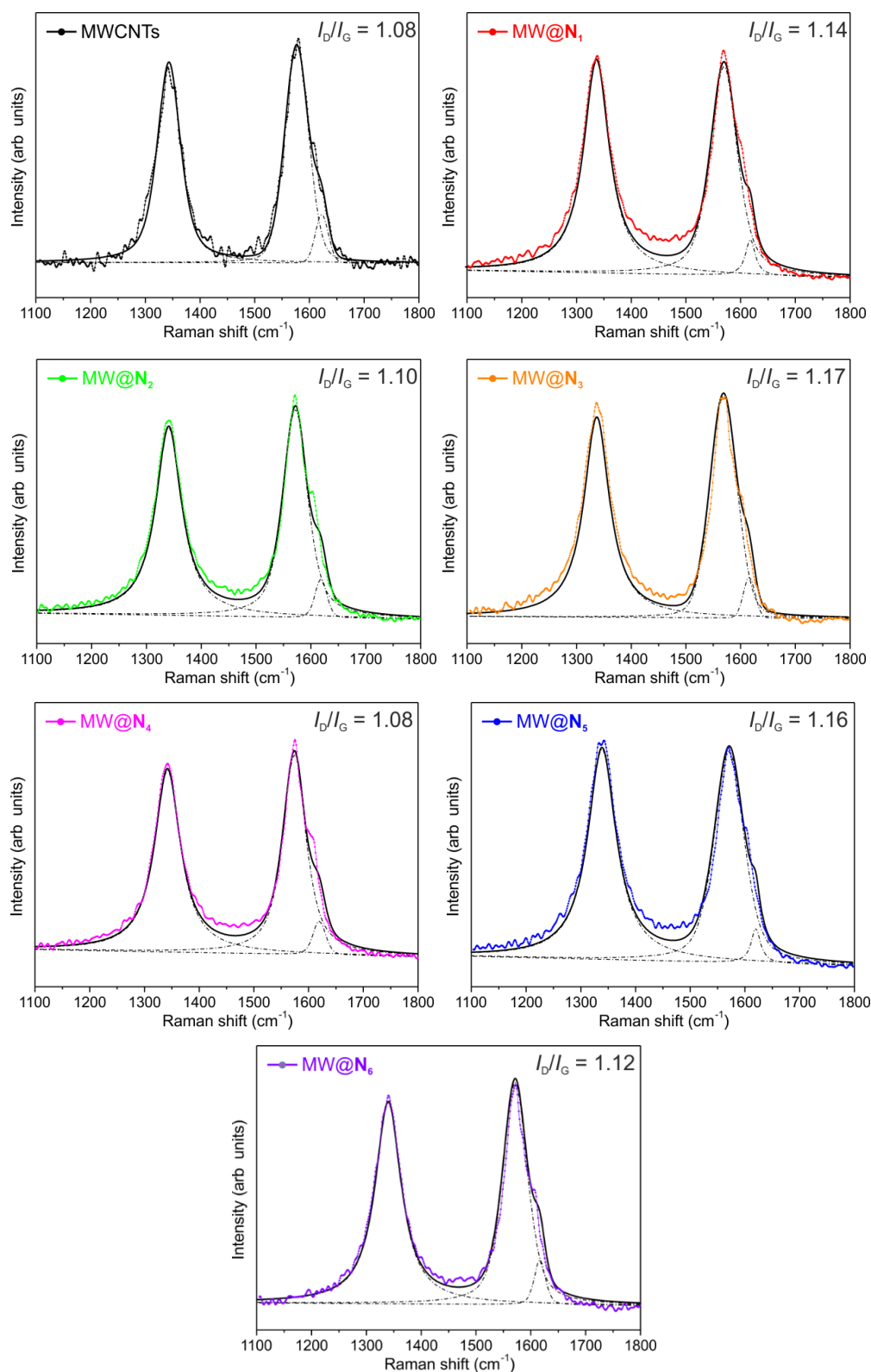


Figure 6.2. Raman spectra of pristine MWCNTs and all N-functionalized samples MW@N₁₋₆ and their relative fits. Colored dots represent the experimental points. The single peak fittings are reported as dot-dashed lines, while the full line represents the total spectrum fit. All recorded curves were fitted using Lorentzian lineshapes and the intensity ratios (namely, I_D/I_G) were calculated from the fitted total curve parameters. Calculated I_D/I_G ratios range from 1.08 for p-MWCNTs to 1.17 for one of the most functionalized sample (MW@N₃).

The Raman and TEM issues are consistent with a non-invasive N-decoration procedure which leaves the main physico-chemical properties of the functionalized materials unchanged while grafting tailored pyridine-based dangling groups to their outer surface.

A preliminary evidence of the occurred functionalization is given by the analysis of the thermogravimetric profiles (TGA). All samples are heated in air within the same temperature range (40-900 °C); a more gradual decomposition profile is evidenced for all the N-decorated samples when compared with the pristine ones (Figure 6.3). Such a trend, indicative of a slightly increased “sidewall roughness” as a consequence of the functionalization procedure, does not give more than a qualitative indication of the occurred CNTs decoration.

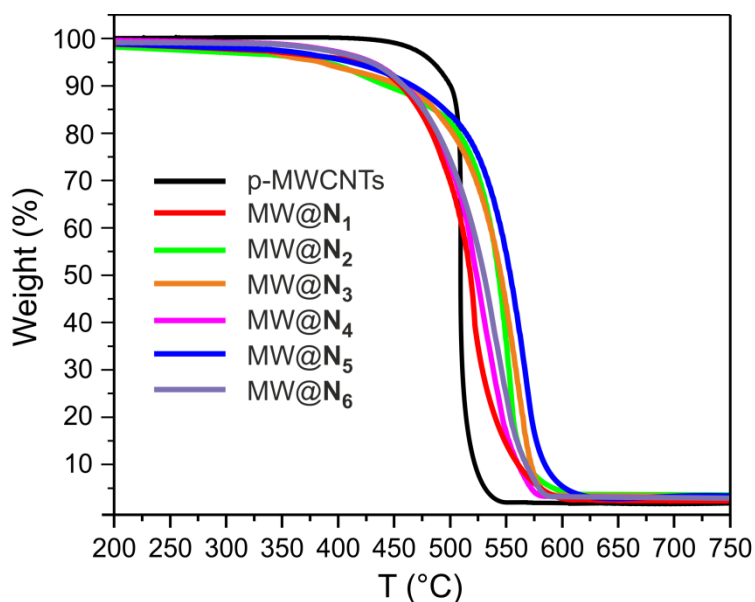


Figure 6.3. TGA profiles of pristine MWCNTs (black-line) and N-decorated CNT samples MW@N₁₋₆. Thermal program: 40-900 °C, 5 °C/min; air atmosphere, 100 mL min⁻¹.

A quantitative loading of the N-containing heterocycles is provided by the crossed comparison of the CHN elemental analysis and the acid-base titration of the pyridinic basic sites (Table 6.2). The acid-base titration guarantees the most reliable and accurate quantification of the N-loading, restricting the measurement to those N-containing groups really available and/or chemically accessible at the CNT surface (Table 6.1).

Table 6.1. Acid-base titrations on the MW@N₁₋₆ samples.

	N _{Py} ^{Me} (N%)		N _{Py} ^{Br} (N%)		N _{Py} ^{Chin} (N%)
MW@N ₁ (1° run)	0.77	MW@N ₂ (1° run)	0.23	MW@N ₃ (1° run)	1.37
MW@N ₁ (2° run)	1.04	MW@N ₂ (2° run)	0.41	MW@N ₃ (2° run)	1.03
MW@N ₁ (3° run)	0.86	MW@N ₂ (3° run)	0.41	MW@N ₃ (3° run)	1.23
MW@N ₁ (average)	0.89	MW@N ₂ (average)	0.35	MW@N ₃ (average)	1.21

	N _{Py} ^F (N%)		N _{Py} ^{Naph} (N%)		N _{Py} ^{OMe} (N%)
MW@N ₄ (1° run)	0.38	MW@N ₅ (1° run)	1.28	MW@N ₆ (1° run)	0.99
MW@N ₄ (2° run)	0.16	MW@N ₅ (2° run)	1.61	MW@N ₆ (2° run)	0.52
MW@N ₄ (3° run)	0.24	MW@N ₅ (3° run)	1.53	MW@N ₆ (3° run)	0.76
MW@N ₄ (average)	0.26	MW@N ₅ (average)	1.47	MW@N ₆ (average)	0.76

Table 6.2. Calculation of the N-functional loading on each MW@N sample.

	Elemental Analysis ^a			Acid-base titration ^b	XPS analysis
	C %	N %	N (wt.%) ^c ; [mmol/g] ^d	N _{Py} (wt.%) ^e ; [mmol/g] ^d	N (at.%) ^f ; [mmol/g] ^f
p-MWCNTs ^e	93.83	0.20			
MW@N ₁	90.58	1.22	1.02 ; [0.73]	0.89 ; [0.64]	1.9 ; [1.50]
p-MWCNTs ^e	93.97	0.09			
MW@N ₂	92.65	0.51	0.42 ; [0.30]	0.35 ; [0.25]	0.6 ; [0.48]
p-MWCNTs ^e	95.30	0.17			
MW@N ₃	90.97	1.45	1.28 ; [0.91]	1.21 ; [0.86]	1.5 ; [1.13]
p-MWCNTs ^e	95.04	0.03			
MW@N ₄	92.05	0.44	0.41 ; [0.29]	0.26 ; [0.19]	0.6 ; [0.49]
p-MWCNTs ^e	92.75	0.33			
MW@N ₅	91.34	1.98	1.65 ; [1.18]	1.47 ; [1.05]	2.0 ; [1.54]
p-MWCNTs ^e	95.30	0.02			
MW@N ₆	91.99	0.74	0.72 ; [0.51]	0.76 ; [0.54]	1.1 ; [0.85]

^a Average C% and N% values calculated over three independent runs. ^b Average N_{Py}% values calculated over three independent runs. ^c The N% content calculated as difference between the N-content (%) of each functionalized sample (MW@N₁₋₆) and the respective “blank sample” (p-MWCNTs). ^d Relative functional group loading. ^e “Blank samples” prepared using identical reaction conditions, reagents and work-up procedure applied to the synthesis of MW@N₁₋₆ samples, except for the use of the isopentyl nitrite as reagent. ^f Relative functional group loading calculated from the extrapolated N (wt. %).

As Table 6.2 shows, Elemental Analysis provides N-contents for almost all the functionalized samples with slight overloadings (compared to the acid-base titration) ranging from 0.07 to 0.18 N%. The lower functionalization loading measured for materials containing pyridine functionalities substituted with inductive EWGs (samples MW@N₂, MW@N₄, MW@N₆) is in line with the electron poor character of these heterocycles and their subsequent ability to stabilize the postulated reactive aryl radical intermediates during the Tour reaction protocol.³²

XPS spectra of MW@N₁₋₆ show characteristic N 1s profiles featured by one main peak in the 398.8 ÷ 399.3 eV range, consistent with the presence of pyridine nuclei (Figure 6.4).^{21a,33} Although not catalytically relevant (see section 6.5), minor residues coming from solvents and/or reagents retained by the material porosity are not totally removed by the work-up procedure. Accordingly, minor N 1s shoulders at higher binding energy values and present in almost all functionalized samples (Figures 6.4B, C, E, G, H) are ascribed to commonly observed surface contaminations.^{30,31e,g,34} Figure 6.4D shows the typical Br 3d signal consisting of a doublet (Br 3d_{5/2} and Br 3d_{3/2}, respectively at 70.7 and 71.8 eV) due to spin-orbit coupling,³⁵ which position is indicative of a Br-pyridine group.

A little shoulder at higher Binding Energy values in the F 1s spectrum of MW@N₄ has been explained by invoking two different fluorine environments (Figure 6.4F); the main peak at 687.4 eV (85 %) is ascribed to the 2-fluoropyridine moiety, while the minor component at 689.6 eV (15 %) is indicative of a direct binding of F to the MWCNT sidewall.³²

From a quantitative point of view, the overall N-loading measured through XPS is typically much closer to the Elemental Analysis values than those coming from the acid-base titration (see Table 6.1 and Table 6.2). Apart from slightly overestimated N-loadings, the XPS technique provides unambiguous evidence of the surface material decoration with the expected N-containing heterocycles.

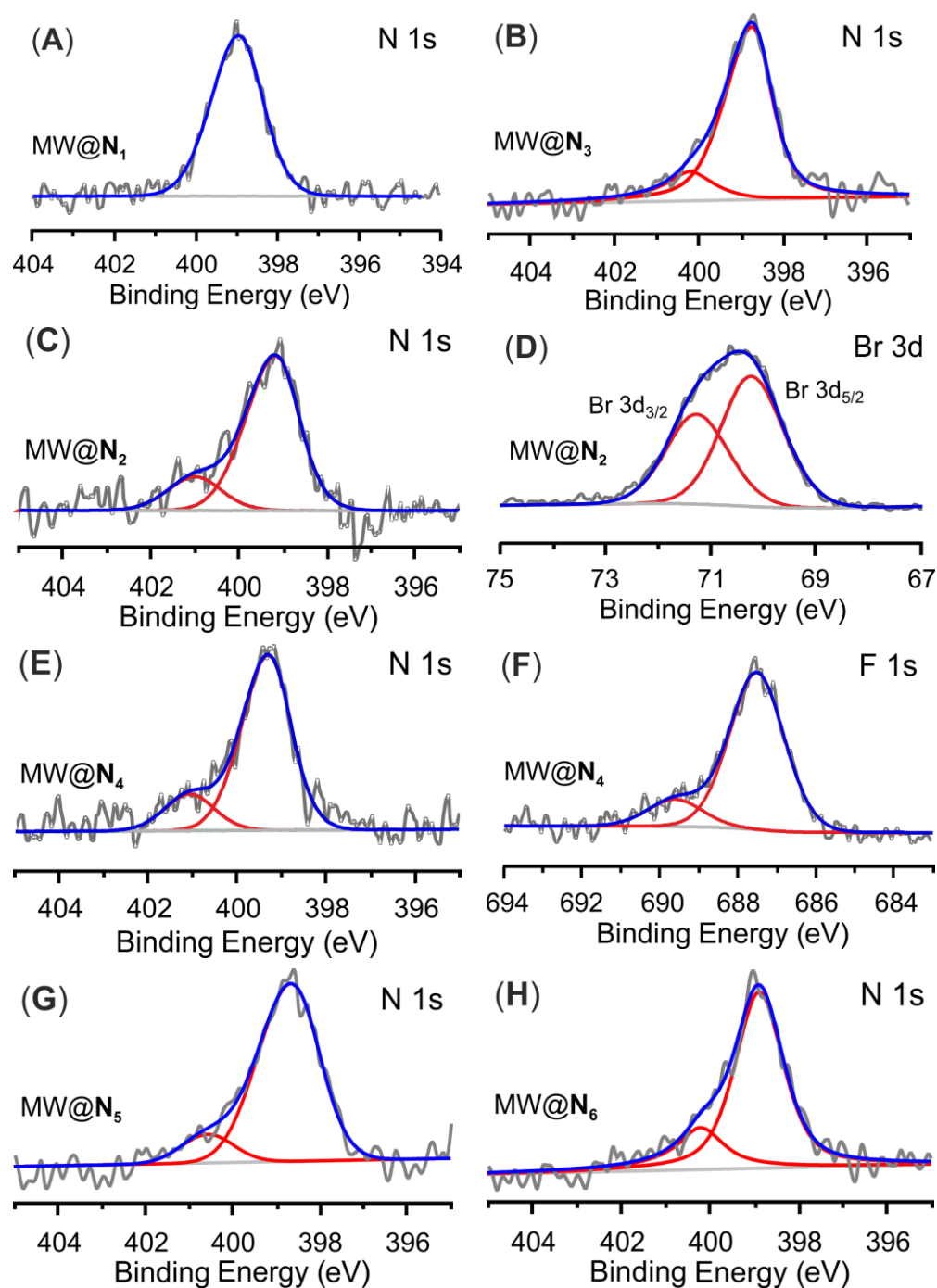


Figure 6.4. High resolution N 1s (A: MW@N₁; B: MW@N₃; C: MW@N₂; E: MW@N₄; G: MW@N₅; H: MW@N₆) Br 3d (D: MW@N₂) and F 1s (F: MW@N₄) core level regions and their relative fits for the XPS spectra of samples MW@N₁₋₆.

6.3.2 Electrochemical tests on MW@N₁₋₆ samples as electrocatalysts for the ORR

After the material characterization, the study of their electrocatalytic performance in the ORR has been performed. To this purpose, a MW@N/Nafion[®] ink is prepared for each functionalized sample and subsequently casted on a rotating glassy carbon (GC) electrode to give a thin and homogeneous film after solvent evaporation (see section

6.5). The as-prepared electrocatalysts have been investigated by cyclic voltammetry (CV) using a three-electrode cell consisting of an Ag/AgCl/KCl saturated reference electrode and a Pt counter electrode operating in a 0.1 M KOH solution (Figure 6.5).

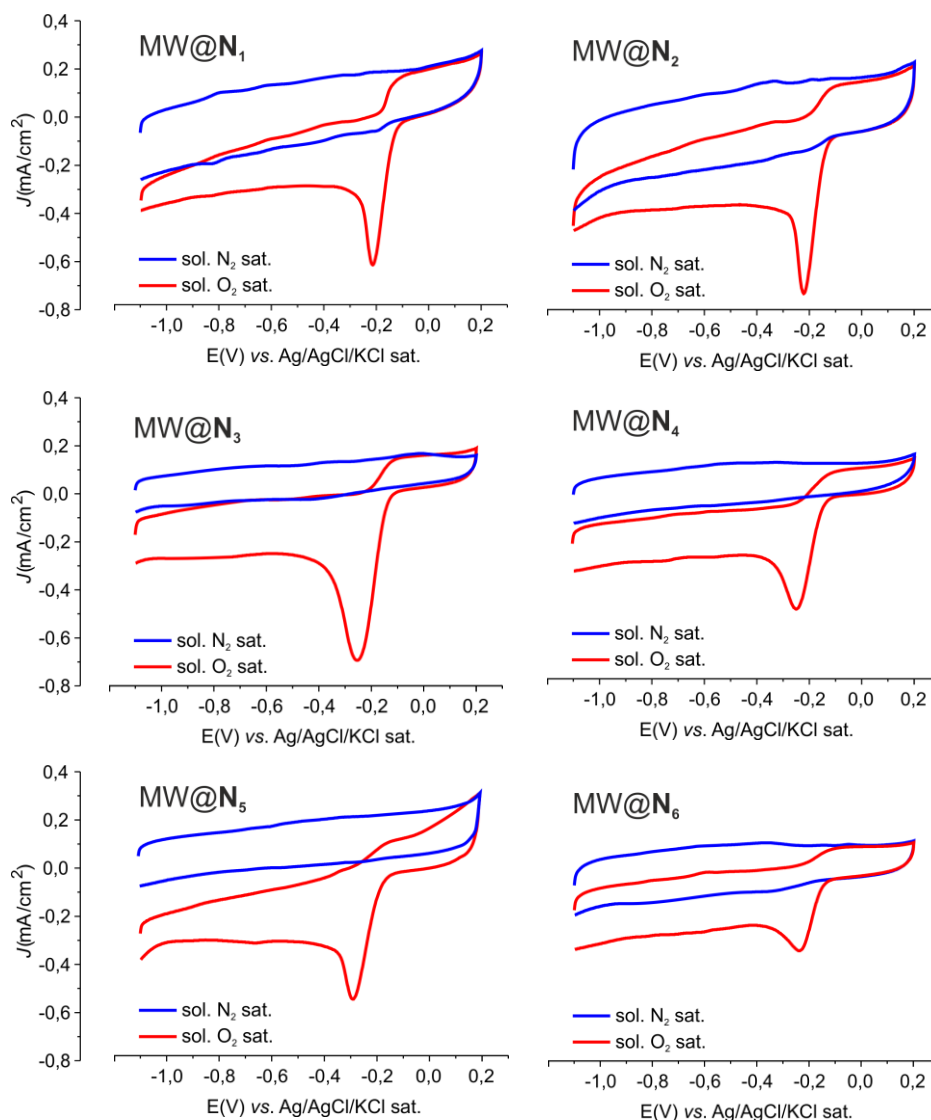


Figure 6.5. Cyclic voltammograms for MW@N₁₋₆ samples recorded under N₂-saturated (blue) and O₂-saturated solutions (red). The potential was linearly swept from -1.1 to 0.2 V at a scan rate of 5 mV s⁻¹ vs. Ag/AgCl/KCl sat. as the reference electrode.

As Figure 6.5 shows, under O₂-saturated conditions each N-decorated sample presents a well-defined ORR cathodic peak not present under a saturated N₂ environment. To gain further insights into the oxygen-reduction reaction, rotating ring disk electrode (RRDE) voltammograms are acquired in O₂-saturated 0.1 M KOH electrolyte solution and compared with the electrocatalytic performance of the pristine MWCNTs, the bare GC and a commercial Metrohm Pt-polycrystalline electrode (Ø 3 mm). For all CNMs,

the amount of the deposited catalyst is fixed to $358 \mu\text{g}/\text{cm}^2$ irrespective of the different N-loadings measured on the relative MW@N_{1-6} samples; such a value is assumed in accord with the highest number of exchanged electrons at variable N-CNM ink loadings (see also Table 6.5 in section 6.5.4), measured for one of the most performing system of this series (MW@N_2). Linear sweep voltammograms are firstly recorded for each sample at different spin rates (from 400 to 2000 rpm), while sweeping potentials linearly from -1.1 to 0.2 V and reversing them against Ag/AgCl/KCl sat. (Figure 6.6); for all the electrochemical profiles, background currents measured under saturated N_2 conditions at the same potential scan rate (5 mV s^{-1}) are subtracted from the respective curves to eliminate all the capacitive contributions.

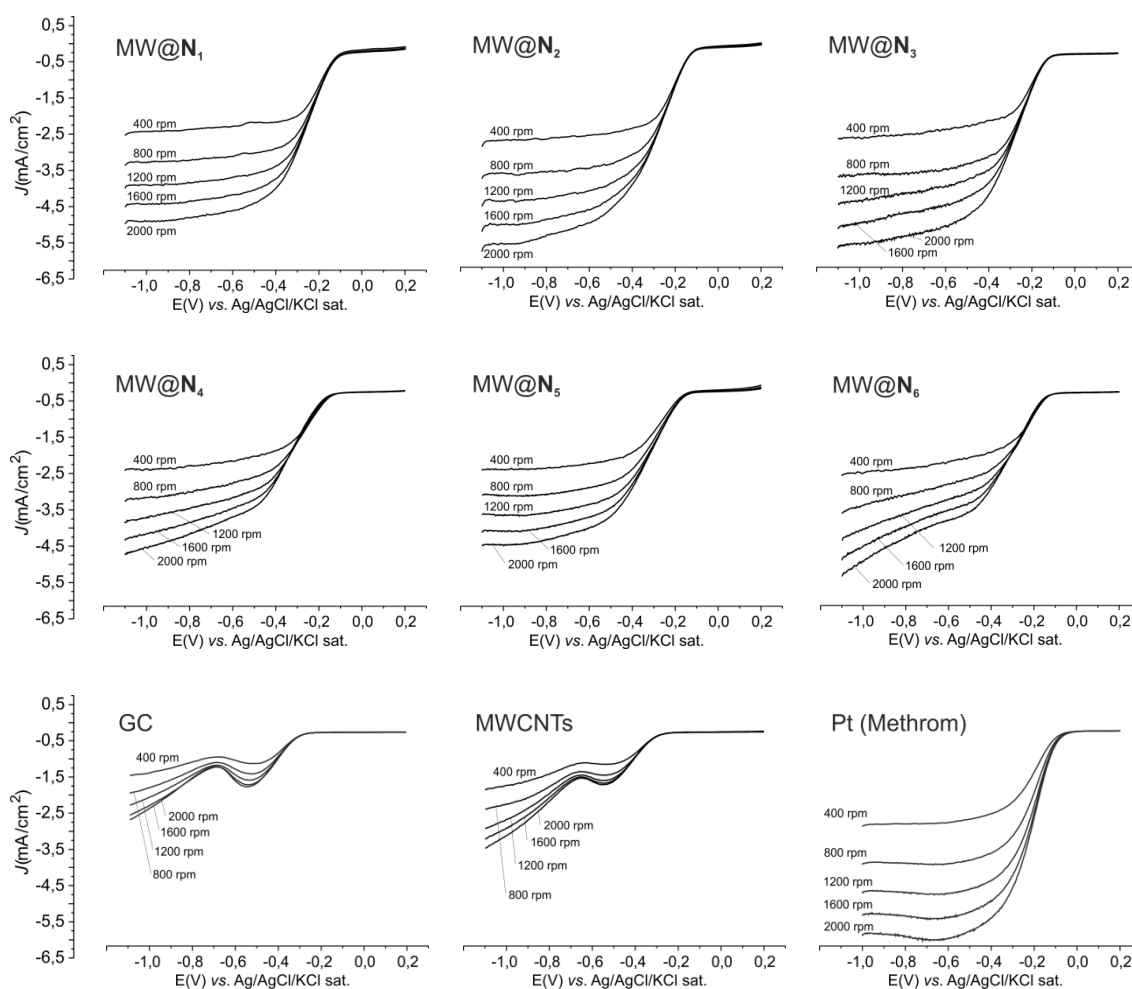


Figure 6.6. Linear sweep voltammograms (LSVs) for ORR in O_2 -saturated 0.1 M KOH solution for MW@N_{1-6} samples, GC, pristine MWCNTs and the Pt-based reference electrode, at variable spin rates (400, 800, 1200, 1600 and 2000 rpm). Scan rate: 5 mV s^{-1} , catalyst loading $358 \mu\text{g cm}^{-2}$.

Figure 6.7A shows the ORR polarization curves recorded at 800 rpm for each system, along with the respective ring current values relative to the oxidation of hydrogen peroxide ions (HO_2^-) measured at the Pt-ring electrode held at a potential of 0.50 V (Figure 6.7A').

As Figure 6.7A shows, the onset potentials (E_{on}) measured for all N-CNMs are negatively moved from that of Pt, while maintaining a remarkable and positive shift compared to the GC (a) and pristine MWCNTs (b). For the latter two catalysts only, a clear reduction pre-wave is observed at low overpotentials, followed by a second reduction wave starting around -0.7 V, this being indicative of a prevalent $2e^-$ reduction path.^{5a,7,9c,36} Accordingly, lower ring currents are measured for all N-decorated samples (Figure 6.7A') compared to pristine MWCNTs and GC. This reduced current is indicative of a decreasing amount of HO_2^- ions reaching the ring electrode under increasing negative potentials.

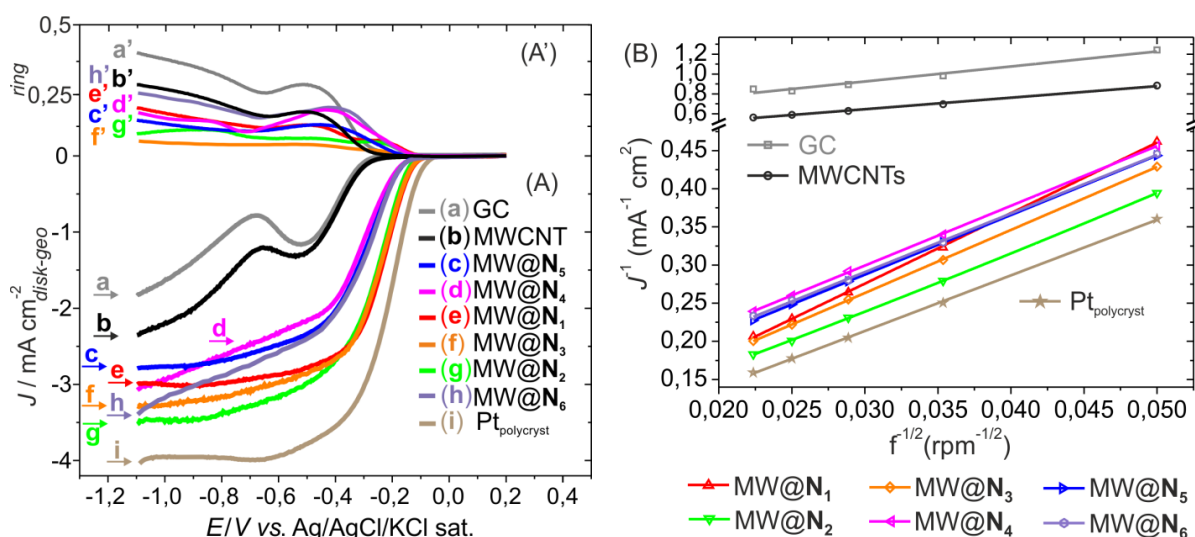


Figure 6.7. [Left] (A) RRDE current-potential curves at 293 K for ORR in O_2 saturated 0.1 M KOH solution recorded by using a rotating ring-disk GC electrode [GC disk, $A = 0.196 \text{ cm}^2$] with (A') Pt ring [$A = 0.11 \text{ cm}^2$]. All samples are measured at an angular rotation rate (f) of 800 rpm. [Right] (B) K - L plots for MW@ N_{1-6} , GC, MWCNTs and Pt catalysts as obtained from the respective LSVs at -0.75 V. Parameters used: O_2 concentration (C), $1.15 \cdot 10^{-3} \text{ mol L}^{-1}$; O_2 diffusion coefficient (D), $1.95 \cdot 10^{-5} \text{ cm}^2 \text{ s}^{-1}$; kinematic viscosity (ν) of the electrolyte solution, $0.008977 \text{ cm}^2 \text{ s}^{-1}$.

The onset potential (E_{on}) values measured for each catalyst are listed in Table 6.3. Noteworthy, while ORR starts at -0.299 V (E_{on}) on pristine MWCNTs, corresponding to an overpotential of ca. 200 mV compared to Pt (Table 6.3, entry 2 vs. 9; Figure 6.7A, b vs. i), overpotentials between 34 and 78 mV are measured for all the N-decorated samples. In particular, it is possible to identify two distinct classes of catalysts, each one characterized by similar E_{on} values in the ORR. Among these, the ORR onset potentials measured for MW@N₁, MW@N₂ and MW@N₃ (Table 6.3, entries 3-5; Figure 6.7A, curves e, f, g) are shifted to more positive values, thus featuring higher electrocatalytic activity compared to the other N-CNMs. Their ORR performance (number of transferred electrons *per* O₂ molecule) in the diffusion and kinetically limited regions (from -0.65 to -0.95 V) is evaluated on the basis of the Koutecky-Levich (K-L) equation.^{5a,37} K-L plots of each catalytic system obtained at different potential values (from -0.65 to -0.95 V) are reported on Figure 6.8.

All curves show excellent linearity thus implying a first-order reaction towards dissolved O₂. For the sake of comparison, the *K-L* plots (J^{-1} vs. $\nu^{-1/2}$) of each catalyst obtained at -0.75 V are reported in Figure 6.7B. The calculated average number of electrons ($n_{E = -0.75 \text{ V}}$) transferred *per* O₂ molecule in the ORR process are outlined in Table 6.3 (see section 6.5 for calculation details).

Table 6.3. E_{on} values (V) and average number of electrons transferred ($n_{E = -0.75 \text{ V}}$) for O₂ molecule as derived from plots in Figures 6.7A and 6.7B, respectively.

Entry	Catalyst	E_{on} (V)	$n_{E = -0.75 \text{ V}}$
1	GC	-0.307	1.9
2	MWCNTs	-0.299	2.5
3	MW@N ₁	-0.135	3.1
4	MW@N ₂	-0.144	3.7
5	MW@N ₃	-0.137	3.4
6	MW@N ₄	-0.179	3.5
7	MW@N ₅	-0.168	3.6
8	MW@N ₆	-0.169	3.5
9	Pt	-0.101	3.9

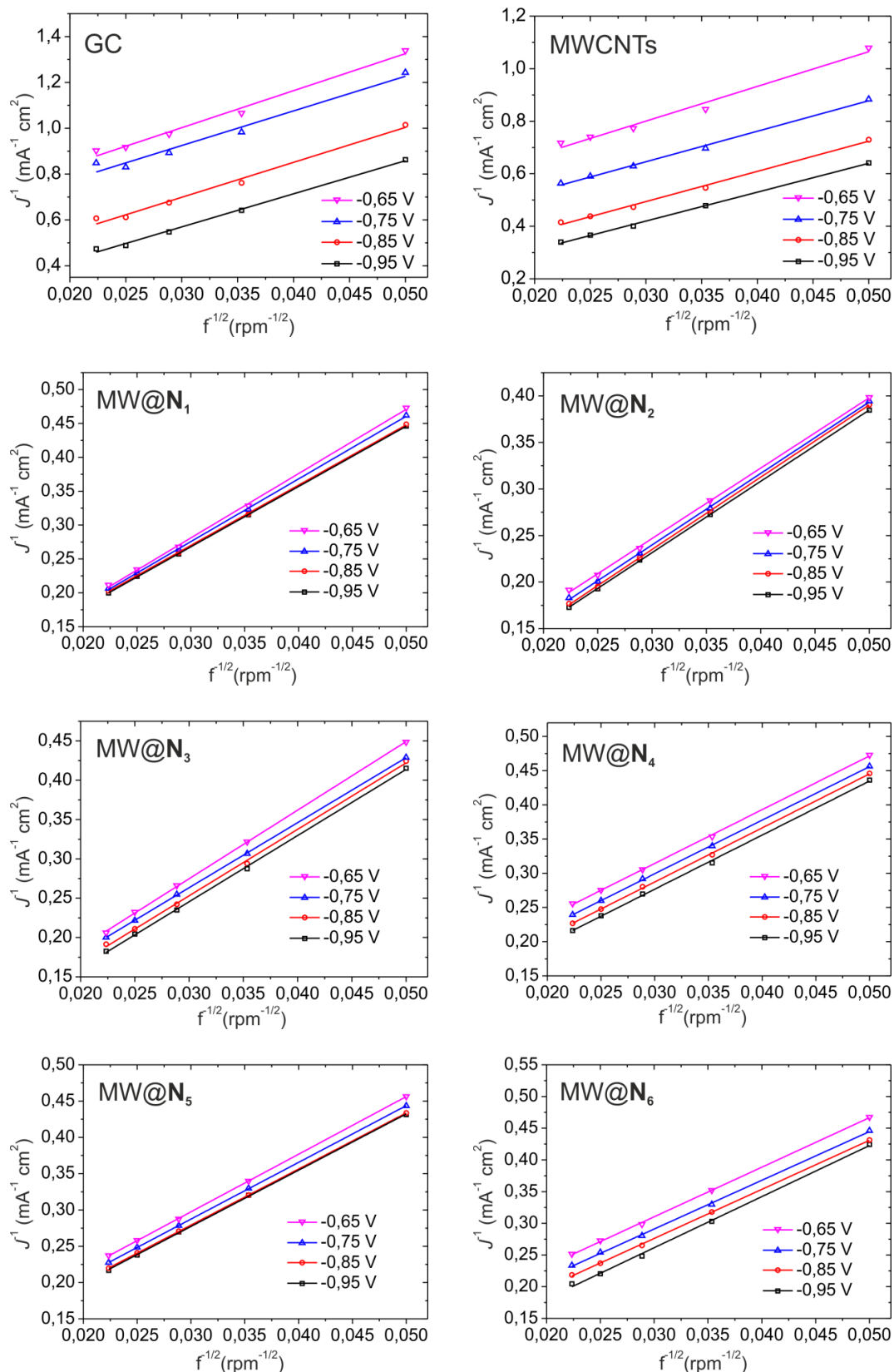


Figure 6.8. *K-L* plots for MW@N₁₋₆, GC, MWCNTs and Pt catalysts as obtained from the respective LSVs at -0.65 (pink line), -0.75 (blue line), -0.85 (red line) and -0.95 V (black line), respectively. Parameters used: O₂ concentration (*C*), 1.15 10⁻³ mol L⁻¹; O₂ diffusion coefficient (*D*), 1.95 10⁻⁵ cm² s⁻¹; kinematic viscosity (*ν*) of the electrolyte solution, 0.008977 cm² s⁻¹.

Notably, the N-functionalized materials show from good to excellent n values measured at -0.75 V for the ORR; this is indicative of a prevailing $4e^-$ reduction process for all these systems. Such a statement is further supported by the rather moderate ring current values recorded for all N-CNMs at the Pt ring electrode, consistent with a scarce amount of HO_2^- ions produced during the catalytic cycles (Figure 6.7A').

The E_{on} values for the already reported (see chapter 5)³⁰ N-decorated CNMs bearing different N-containing heterocycles (see Scheme 6.1, samples **N₇₋₉**) are shown for comparison in Table 6.4.

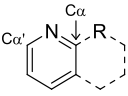
Table 6.4. E_{on} values (V) measured for samples MW@**N₇₋₉**.

Catalyst	E_{on} (V)
MW@ N₇	-0.139
MW@ N₈	-0.250
MW@ N₉	-0.181

Compared to the classical preparation protocol (CVD approach), chemical functionalization gives the rare opportunity to rationalize the structure-activity relationship of these metal-free catalysts systematically, through a fine tuning of the electronic properties of the N-containing heterocycle involved as “active site” in the catalytic process. All the substituted pyridine derivatives used in the study can be roughly conceived as mimics of edge-type N-defects with tunable chemical environment (substituents) that modifies the ring electronic charge density distribution. Most importantly, the functionalization protocol meets the fundamental requirement of maximizing the number of N-edge-sites at the nanomaterial surface, where the oxygen adsorption presents considerably lower energy barriers compared to equivalent undoped edge-sites as well as to in-plane N-sites.^{10e,3c} A comparison between the different N-containing heterocycles present at the CNT sidewalls and the voltammetric performance of the relative MW@**N₁₋₆** nanomaterials, highlights the influence of the electronic charge density distribution at the N-sites (as well as at the N-neighboring carbon atoms) on the ability of the N-CNMs to promote the kinetically sluggish dioxygen reduction reaction more or less efficiently. If electron-accepting nitrogen atoms are known to generate a highly positive charge density on the adjacent C_α atoms, electron-

withdrawing (EW) or electron-donating (ED) groups attached to the α -position of the heterocyclic ring certainly have a strong influence on the final atomic charge density redistribution. As a matter of fact, a tuning of the adsorption energy of the dioxygen species (substrate) and/or its reduction intermediates (products) onto the catalytically active sites (N-heterocycle) is expected. On this regard, we have proposed a rationale to the experimental outcomes in the ORR obtained with the MW@N₁₋₆ samples based on the calculation of the Bader atomic charges on each N-heterocycle.³⁸ After a DFT pre-optimization of the dangling substituents (N₁-N₆) at the B3LYP//6-31G** level of theory, a Bader charge analysis has been performed for each case to infer the Bader atomic charges on the N and C _{α} atoms,³⁹ whose values are outlined in Table 6.5.

Table 6.5. Net Bader charges (q) of the N and C _{α} atoms calculated on N₁₋₆ heterocycles. Bader analysis of the atomic charge density on previously reported N_{7,9} systems (see chapter 5)³⁰ has also been listed here for completeness.

Entry	N-heterocycle	q _N			N-C _{α} bond polarization [q _N + q _{Cα}]
			q _{Cα}	q _{Cα'}	
1	N ₁	-2.857	1.324	1.281	4.181
2	N ₂	-2.982	1.504	1.183	4.486
3	N ₃	-2.649	1.416	1.258	4.065
4	N ₄	-2.905	2.330	1.294	5.235
5	N ₅	-2.745	2.649	1.293	5.394
6	N ₆	-2.845	2.467	1.208	5.312
7	N ₇	-2.696	1.448	1.448	4.144
8	N ₈	-2.356	0.828	0.828	3.184
9	N ₉	-2.670	1.161	1.161	3.831

The analysis of the C _{α} atomic charges, together with that of the corresponding N-C _{α} bond polarization, show a rather well-matching trend with the onset potentials (E_{on}) measured on the respective N-CNMs. An increase of the q_{C α} value translates into worst E_{on} values (Table 6.5, entries 4-6 vs. Table 6.3 entries 6-8) while reduced charge densities on the C _{α} generate a better catalyst performance, at least in terms of E_{on} values (Table 6.5, entries 1-3 vs. Table 6.3 entries 3-5). Minor discrepancies, as little

deviations from the postulated $q_{C\alpha}$ vs. E_{on} trend within each of the two series of catalysts (MW@N₁₋₃ and MW@N₄₋₆), can be ascribed to the unsymmetrical nature of the N-containing groups. Indeed, a minor contribution from the C_{α} positions in the catalytic process cannot be definitively ruled out.

In the case of previously reported (see chapter 5)³⁰ N-decorated CNMs bearing different N-containing heterocycles (see also Scheme 6.1, samples N₇₋₉ and Table 6.4 for the relative E_{on} values), it can be noticed that reduced $q_{C\alpha}$ values [compared to the best performing systems (MW@N₁₋₃)] lead to even worst E_{on} values. Such results introduce an additional level of complexity to the original claim that pyridine-like moieties in N-doped CNMs improve the onset potential values of the ORR.²² According to our experimental evidence, it can be stated that the nature of the pyridine moieties in N-CNMs plays a fundamental role in favoring a predominant $4e^-$ reduction process, as well as in modulating the overpotential values at which the oxygen reduction starts. Indeed, the variation of the atomic charges on the N-proximal carbon atoms of the heterocycle is strongly linked to the dioxygen adsorption energy on the material “active sites”. According to this phenomenological model, an optimal $q_{C\alpha}$ value in the range of $1.32 \div 1.50$ (see also Table 6.5, entries 1-3,7) is calculated on the samples MW@N₁₋₃ and MW@N₇, while N-CNMs showing either higher (MW@N₄₋₆) or lower (MW@N₈₋₉) $q_{C\alpha}$ charges are featured by worse E_{on} performance. Notably, deviations from the optimal $q_{C\alpha}$ values (Table 6.5, entries 1-3,7) can also lead to alternative reduction paths, especially at high overpotentials. This is the case of the sample MW@N₈ (containing pyrrole groups) and the MW@N₉ sample (containing plain pyridine units), where rather moderate $q_{C\alpha}$ values (as well as the relative N- C_{α} bond polarization values) make a $2e^-$ reduction process highly competitive. In line with this observation, a significant amount of HO₂⁻ ions is detected during the ORR when using these samples as catalysts. For the two limit samples MW@N₄ and MW@N₆, a diffusion and kinetically limited process (at high overpotentials) seems to be significantly affected by the too high $q_{C\alpha}$ values (see Figure 6.7A, curves d and h). If any possible rationale to this behavior remains merely speculative, this experimental outcome can be tentatively justified by the presence of an “overcharge” at the C_{α} that makes the interaction with the reduction intermediates/products too strong for the reaction to proceed further; from this point of view, it can be seen as a sort of “catalyst poisoning”. Despite these data, no further discussion can be done on the way dioxygen adsorbs to the “active sites” (side-on mode - also known as the Yeager model and/or end-on mode - known as the Pauling model)⁴⁰

which is another largely debated issue on both an experimental and a theoretical ground. On the other hand, it seems generally accepted that *zigzag* edge structures (as our chemically grafted N-moieties can be considered) promote a preferential dioxygen *end-on* adsorption mode.^{10e}

6.4 Conclusions

MWCNTs decorated with tailored pyridine-containing groups are valuable materials to be used as ORR catalysts giving, at the same time, a unique perspective on some specific structure-reactivity relationship of these metal-free systems. In this chapter, a number of variably substituted pyridine moieties are brought on the CNTs board (basal or edge planes) through a well consolidated chemical functionalization approach. If it is accepted that pyridine nuclei in N-CNMs play an important role in the improvement of the overpotential values at which the oxygen reduction starts,²² a control on their electronic properties through inductive electron donating (EDG) or electron withdrawing (EWG) groups attached to the α -position of the pyridine ring adds another level of complexity to the rationalization of the electrochemical outcomes. Indeed, variations of the atomic charges on the α -carbon atoms of the heterocycles (as well as the related N-C $_{\alpha}$ bond polarization) translate into systems featured by different E_{on} values. One possible rationale to this phenomenological trend is attributed to the change of the adsorption energy of the dioxygen species (substrate) and/or its reduction intermediates (products) onto the catalytically active sites (N-heterocycle). The calculation of the Bader atomic charges on each substituted heterocycle has been used to rationalize the observed electrochemical trend. As a result, MW@N featured by the best onset potentials (E_{on} ranging from 0.135 to 0.144 V) are associated to $q_{C_{\alpha}}$ values measured in the 1.32 ÷ 1.50 range (and the respective N-C $_{\alpha}$ bond polarization values in the 4.0 ÷ 4.5 range). Out of this range, higher or lower $q_{C_{\alpha}}$ charges (or N-C $_{\alpha}$ bond polarization values) translate into catalytic systems showing worse E_{on} performance. In addition, the electrochemical results reveal how deviations from the optimal $q_{C_{\alpha}}$ values can trigger alternative reduction paths, especially at high overpotentials.

Overall, the results outlined in the chapter demonstrate that pyridine functionalized MWCNTs generate valuable electrocatalysts for the ORR. This alternative approach to the heterodecoration of carbon nanomaterials stresses the importance of the N-chemical surrounding on the catalytic performance of the N-functionalities, offering both an

excellent work basis to the development of more catalytically active metal-free electrocatalysts for the ORR and a unique model for the in-depth understanding of the underlying ORR mechanism. In addition, our conclusions can settle a complex and often controversial matter related to the catalytic role of the different N-functionalities present in N-doped carbon nanomaterials prepared by the classical approaches, like CVD or CNMs thermal annealing with different nitrogen sources. These latter synthetic methods do not provide any control of the chemical surrounding at the N atom, thus giving N-CNMs with N-functionalities “embedded” in a sp^2 network with totally unpredictable stereo-electronic environment. Moreover, the implanted nitrogen atoms are also present in the inner portions of the nanomaterial, not directly exposed to the dioxygen during the catalytic trials; this makes their catalytic contribution (if there is any) more and more unpredictable. These assumptions can contribute to justify many conflicting data reported in the recent literature and in particular the controversial catalytic role of specific N-functionalities present in differently prepared N-CNMs.

6.5 Experimental Section

6.5.1 General Considerations

All manipulations were carried out under dry nitrogen atmosphere using standard Schlenk-type techniques. Nitrogen (> 99.999%; Rivoira) was dried through a CaCl_2 column and deoxygenated with an oxysorb cartridge from Messer Griesheim prior to use. *o*DCB (ortho-dichlorobenzene) was dried according to the literature procedures⁴¹ and stored under nitrogen atmosphere. Dry acetonitrile (CH_3CN) was obtained by means of an MBraun Solvent Purification System. MWCNTs (98 % in C) were purchased from Sigma-Aldrich (Lot# MKBH5814V) and used as received. Unless otherwise stated, all other chemicals were purchased from commercial suppliers and used as received without further purification. Samples sonication was carried out using an Elma S15 Elmasonic sonicator bath (37 kHz) while cooling the samples in a water/ice mixture throughout the treatment. CNTs filtration was accomplished by using inorganic PTFE filter (Whatman) with 0.2 μm pore size. *All measurements carried out on pristine MWCNTs and functionalized samples (MW@N₁₋₆) were conducted on samples which underwent identical washing/filtration/sonication/work-up procedures. For each functionalized sample (MW@N₁₋₆) a “blank functionalization test” was performed using identical reaction conditions and reagents except for the use of the*

isopentyl nitrite reagent. RRDE measurements on the blank samples have excluded any electrochemical activity associated to potentially physisorbed N-containing heterocycles.³⁰ Furthermore, any electrochemical activity (RRDE measurements) potentially associated to reagent and solvent contaminations has been properly ruled out using a blank test conducted on MWCNTs treated with the isopentyl nitrite in *o*DCB/CH₃CN mixture.

6.5.2 Material Characterization and Analyses Conditions

Thermogravimetric analyses (TGA) were performed under air (100 mL/min) on an EXSTAR Thermo Gravimetric Analyzer (TG/DTA) Seiko 6200.

X-ray Photoelectron Spectroscopy (XPS) analyses were performed with a Thermo Fisher Theta Probe spectrometer equipped with a monochromatic Al K α X-ray source (1486.6 eV) with a spot size of 300 μ m, corresponding to a power of 70 W and at a take-off angle of 53 ° relative to the sample normal. Samples in form of powders were fixed on ultra high vacuum compatible Cu adhesive tape (3M) ensuring, as much as possible, an uniform coverage. Survey spectra (0 - 1300 eV) were acquired at a pass energy of 200 eV with an energy step size of 1 eV. High resolution spectra were recorded at a pass energy of 100 eV with a step size of 0.05 eV. In the set conditions the overall energy resolution was 0.9 eV. When needed, charge compensation for treated MWCNTs was accomplished by a low energy electron flood gun (1 eV). Charge correction of the spectra was performed by taking the sp² graphitic component of the C1s spectrum as internal reference (Binding Energy, BE = 284.6 eV). Special care was devoted during the analyses, to verify that no change in the samples was induced by exposure to the X-ray beam and the electron flood gun. XPS analysis was repeated on three different spots for each sample. High resolution spectra of detected elements were acquired for quantitative and detailed BE chemical shift analysis. Atomic percentages were calculated using the Scofield sensitivity factors set in the Thermo Advantage V4.87 software (Thermo Fisher Corporation) and a non-linear Shirley background subtraction algorithm. The high resolution spectra were fitted with mixed Gaussian-Lorentzian peaks after a Shirley background subtraction. The determined standard deviation in the peak position was ± 0.2 eV.

Raman spectra were recorded using LabRAM ARAMIS Horiba Raman spectrometer equipped with a 1200 grooves/mm grating and recorded by a peltier cooled CCD detector. Spectra were recorded over the range of 200 - 3200 cm⁻¹ using the 532 nm

emission of a YAG laser source with laser quantum MPC600 PSU. The beam profile was cleaned by a spatial filter and Rayleigh scattering was filtered out using EDGE filters. The spectral resolution was 1 cm^{-1} . The incident laser power on the sample was lower than 42 mV and any damage of the sample due to the laser was carefully checked and excluded. Samples were prepared by gently pressing CNTs and MW@N_{1.6} fine powders into a flat thin film on glass substrate, and each sample was recorded randomly on 3 different positions. Raman spectroscopy was employed to investigate a change in the structure during the CNT N-decoration by detecting the presence and strength of D and G modes.⁴² The Raman spectrum shows a D band at around 1360 cm^{-1} , and a G band at 1590 cm^{-1} , which correspond to the presence of sp^3 defects and tangential vibration of sp^2 carbon atoms in hexagonal plane of graphite-like structures, respectively. All recorded curves were baseline and fitted using Lorentzian line-shapes and the D- and G-peak intensities were used for the calculation of the I_D/I_G ratios.^{42, 43, 44}

Transmission Electron Microscopy (TEM) analysis of modified and unmodified CNTs was performed by a Philips CM12 microscope operating at 120 kV, on samples prepared by drop casting previously sonicated suspensions (EtOH) over copper grids coated with a Formvar film (FF200- Cu - Formvar film only). TEM images were recorded with a CCD camera (Gatan 791).

Rotating-ring disk electrode (RRDE) measurements were performed using a ring-disk electrode from Pine instrument consisting of a glassy carbon (GC) disk insert ($\text{Ø } 5\text{ mm}$; $A = 0.196\text{ cm}^2$) and a Pt ring ($A = 0.11\text{ cm}^2$). The RRDE measurements were carried out using a Modulated Speed Rotator (MSR) from Pine Instruments. All the measurements were carried out using an Autolab potentiostat/galvanostat in a single compartment glass cell using a three electrode arrangement. The working electrode was prepared as follows: a proper amount of CNTs (10 mg) was dispersed in 0.220 g of water, 0.112 g of ethanol and 0.084 g of a Nafion solution (5 wt. % in lower aliphatic alcohols and water). The resulting ink was sonicated for 30-45 min and drop-casted onto the glassy carbon electrode (3 mg). The as-prepared electrode was then dried at room temperature. A platinum wire was used as counter electrode, and a double junction Ag/AgCl/KCl sat. electrode served as reference electrode. All CV and RRDE experiments were carried out at a scan rate of 5 mV/s in the potential range from -1.1 to + 0.2 V vs. Ag/AgCl/KCl sat. Nitrogen or oxygen was used to purge the solution to achieve an oxygen-free or an oxygen-saturated electrolyte solution, respectively. Commercial Metrohm Pt electrode ($\text{Ø } 3\text{ mm}$) was used for comparison and all

measurements were repeated at least four times. Finally, the measurement set-up, the moderate electrolyte viscosity and the entity of the measured currents did not required any ohmic compensation.

All prepared CNT inks were indefinitely stable in air for months with neither any apparent decomposition nor alteration of their electrochemical performance. The number of electrons transferred per O₂ molecule (n) in the ORR for the different catalysts has been calculated by the Koutecky-Levich equation applied to the ORR curves obtained at different rotation rates (rpm).⁴⁵ The Koutecky-Levich is given by equation 6.1:

$$\frac{1}{j} = \frac{1}{j_{cc}} + \frac{1}{nK_f\sqrt{f}} \quad (\text{eq. 6.1})$$

With:

$$K_f = 0.2FC_0D_0^{2/3}\nu^{-1/6}$$

Where, j is the current density, j_{cc} is the kinetic current density, n is the number of exchanged electrons, F is the Faraday constant, D_0 is the oxygen diffusion coefficient ($1.95 \times 10^{-5} \text{ cm}^2 \text{ s}^{-1}$), f is the angular rotation rate of the electrode (rpm), ν is the kinematic viscosity of the solution ($0.008977 \text{ cm}^2 \text{ s}^{-1}$) and C_0 is the O₂ concentration in solution ($1.15 \times 10^{-3} \text{ mol dm}^{-3}$).⁵ With these parameters, the value of K_f constant is 0.03538. The average number of electrons (n) exchanged during the ORR has been extrapolated from the slope of the plot of j^{-1} versus $f^{-1/2}$ at a specific potential value. We have recorded the voltammetric curves from -1.1 V to 0.2 V at different rotation rates (from 400 to 2000 rpm) and calculated the n values in the diffusion and kinetically limited regions (from -0.65 to -0.95 V).

Elemental analyses were performed using a Thermo FlashEA 1112 Series CHNS-O elemental analyzer and elemental average values were calculated over three independent runs.

6.5.3 General procedure for the *ex-situ* MWCNTs functionalization via aryldiazonium salt chemistry

In a typical procedure, MWCNTs (40 mg) were weighed into a two-necked 100 mL flask and suspended in 32 mL of dry and degassed *o*DCB. The suspension was sonicated for 30 min and then treated with a degassed acetonitrile solution (16 mL) of

the corresponding aniline (0.86 mmol). Isopentyl nitrite (0.17 mL, 1.30 mmol) was added *via* syringe and the suspension was further sonicated for 10 min. The mixture was heated at 80 °C for 14 hours under stirring and nitrogen atmosphere. Afterwards, the mixture was cooled to room temperature, diluted with ethylacetate (20 mL) and sonicated for 20 minutes before being centrifugated in order to recover the solid residue. The latter was then washed with ethylacetate and then twice with dichloromethane, each time sonicated for 10 min and separated from the supernatant by centrifugation. The solid residue was finally suspended in dichloromethane, sonicated for 20 min and filtered through a 0.2 µm-pore PTFE filter. The collected material was dried at 50 °C under vacuum to constant weight and stored on air at room temperature.

6.5.4 Electrochemical data processing

The amount of the N-decorated material deposited on the RRDE is maintained constant and fixed to the optimal value [catalyst loading (µg of N-MWCNTs cm⁻²)] measured on the MW@N₂ sample (Table 6.6).

Table 6.6. Number of exchanged electrons for RRDE measurements carried out at different catalyst loadings (298, 358 and 418 µg cm⁻²).

Catalyst loading (mg of ink)	2.5	3	3.5
Catalyst loading (µg cm ⁻²)	298	358	418
Catalyst loading (µg) ^a	58	70	82
Exchange electrons (<i>n</i>)	3.41	3.72	3.52

^a 0.196 cm² GC rotating-disk electrode

6.5.5 Acid-base titration of N-CNMs MW@N_{1.6}

5 mg of the selected N-decorated material (MW@N_{1.6}) are suspended in 7 mL of a standard HCl solution (2.8 x 10⁻³ M, standardized with Na₂CO₃ as primary standard), sonicated for 30 min and maintained in the dark at room temperature under stirring for 48 h. Afterwards, the suspension is centrifugated and three aliquots of the supernatant solution are titrated with a standardized solution of NaOH (2 x 10⁻³ M). The pyridine content (N_{Py} %) was calculated for each sample as the average value over the three independent runs.^{46,47}

6.5.6 Computational Details

Density Functional Theory (DFT) calculations were performed in the gas phase using the *Gaussian09* program (revision C.01).⁴⁸ The real structures of the dangling groups on the CNTs were optimized with a B3LYP functional⁴⁹ using a 6-31G** basis set on all atoms. A Grimme D3 dispersion correction was also included in the optimization, through the Gaussian IOp(3/124 = 30) keyword.⁵⁰ Bader charge partitioning was made through the free algorithm developed at Texas University available here: <http://theory.cm.utexas.edu/bader/>. The Gaussian *.cube file coming from the optimizations was taken as starting point for the Bader analysis on a charge density grid.⁵¹

References and Notes

- ¹ a) E. Antolini, *Appl. Catal. B* **2009**, 88, 1. b) Y. Shao, G. Yin, Y. Gao, *J. Power Sources* **2007**, 171, 558. c) R. Borup, J. Meyers, B. Pivovar, Y. S. Kim, R. Mukundan, N. Garland, D. Myers, M. Wilson, F. Garzon, D. Wood, P. Zelenay, K. More, K. Stroh, T. Zawodzinski, J. Boncella, J. E. McGrath, M. Inaba, K. Miyatake, M. Hori, K. Ota, Z. Ogumi, S. Miyata, A. Nishikata, Z. Siroma, Y. Uchimoto, K. Yasuda, K.-I. Kimijima, N. Iwashita, *Chem. Rev.* **2007**, 107, 3904. d) S. Zhang, X. Yuan, H. Wang, W. Mérida, H. Zhu, J. Shen, S. Wu, J. Zhang, *Int. J. Hydrogen Energy* **2009**, 34, 388.
- ² A. Morozan, B. Josselme, S. Palacin, *Energy Environ. Sci.* **2011**, 4, 1238.
- ³ For critical review articles on the topic see: a) Y. Zheng, Y. Jiao, M. Jaroniec, Y. G. Jin, S. Z. Qiao, *Small* **2012**, 8, 3550. b) C. Z. Zhu, S. J. Dong, *Nanoscale* **2013**, 5, 1753. c) D.-W. Wang, D. Su, *Energy Environ. Sci.* **2014**, 7, 576 d) D. Yu, E. Nagelli, F. Du, L. Dai, *J. Phys. Chem. Lett.* **2010**, 1, 2165. e) C. Song, J. Zhang in: PEM Fuel Cell Electrocatalysts and Catalyst Layers, Fundamentals and Applications, - Electrocatalytic Oxygen Reduction Reaction, Zhang, JiuJun (Ed.), **2008**, Springer ISBN 978-1-84800-936-3
- ⁴ ORR based on metal-free or non-noble metal catalysts in acidic media are generally more critical. To the best of our knowledge only Pt and its alloys show the best ORR activity in an acidic electrolytes: see ref. a) Y. G. Li, W. Zhou, H. L. Wang, L. M. Xie, Y. Y. Liang, F. Wei, J. C. Idrobo, S. J. Pennycook, H. J. Dai, *Nat. Nanotechnol.* **2012**, 7, 394. Most importantly, kinetics for ORR in alkaline electrolyte are favored compared to those performed in acidic media, due to the lower overpotential associated to the first electron transfer to the O₂ adsorbed at the catalyst surface (${}_{\text{ad}}\text{O}_2 \rightarrow {}_{\text{ad}}\text{O}_2^{\bullet -}$; 0.7 V at pH = 14 vs. 1.53 V at pH = 0): see ref. b) B. B. Blizanac, P. N. Ross, N. M. Markovic, *Electrochim. Acta* **2007**, 52, 2264.
- ⁵ a) Y. Wang, D. Zhang, H. Liu, *J. Power Sources* **2010**, 195, 3135. b) M. Zhang, *Langmuir* **2004**, 20, 8781.
- ⁶ D. S. Su, J. Zhang, B. Frank, A. Thomas, X. Wang, J. Paraknowitsch, R. Schlögl, *ChemSusChem* **2010**, 3, 169.
- ⁷ I. Kruusenberg, J. Leis, M. Arulepp, K. Tammeveski, *J. Solid State Electrochem.* **2010**, 14, 1269.
- ⁸ H. Jin, H. Zhang, H. Zhong, J. Zhang, *Energy Environ. Sci.* **2011**, 4, 3389.
- ⁹ a) K. Gong, F. Du, Z. Xia, M. Durstock, L. Dai, *Science* **2009**, 323, 760. b) K. Chizari, A. Deneuve, O. Ersen, I. Florea, Y. Liu, D. Edouard, I. Janowska, D. Begin, C. Pham-Huu, *ChemSusChem* **2012**, 5, 102. c) A. Morozan, P. Jégou, M. Pinault, S. Campidelli, B. Josselme, S. Palacin, *ChemSusChem* **2012**, 5, 647. d) D. Geng, Y. Chen, Y. Chen, Y. Li, R. Li, X. Sun, S. Ye, S. Knights, *Energy Environ. Sci.* **2011**, 4, 760. e) K. Parvez, S. Yang, Y. Hernandez, A. Winter, A. Turchanin, X. Feng, K. Müllen, *ACS Nano* **2012**, 6, 9541. f) S. M. Unni, S. Devulapally, N. Karjule, S. Kurungot, *J. Mater. Chem.* **2012**, 22, 23506. g) L. Qu, Y. Liu, J.-B. Baek, L. Dai, *ACS Nano* **2010**, 4, 1321. h) C. V. Rao, Y. Ishikawa, *J. Phys. Chem. C.* **2012**, 116, 4340.

- 10 For a selection of recent theoretical reports on the topic see: a) K.-Y. Yeh, M. J. Janik, *J. Comput. Chem.* **2011**, *32*, 3399. b) L. Yu, X. Pan, X. Cao, P. Hu, X. Bao, *J. Catal.* **2011**, *282*, 183. c) M. Kaukonen, A. V. Krasheninnikov, E. Kauppinen, R. M. Nieminen, *ACS Catal.* **2013**, *3*, 159. d) S. Ni, Z. Li, J. Yang, *Nanoscale* **2012**, *4*, 1184. e) H. Kim, K. Lee, S. I. Woo, Y. Jung, *Phys. Chem. Chem. Phys.* **2011**, *13*, 17505.
- 11 a) D. M. Guldi, N. Martin in: Carbon Nanotubes and Related Structures Synthesis, Characterization, Functionalization, and Applications. Wiley-VCH, Weinheim, **2010**. b) Y. Zhang, L. Zhang, C. Zhou, *Acc. Chem. Res.* **2013**, *46*, 2329.
- 12 a) C. D. Higgins, J. Wu, W. Li, Z. Chen, *Electrochim. Acta* **2012**, *59*, 8. b) S. M. Unni, S. Devulapally, N. Karjulea, S. Kurungot, *J. Mater. Chem.* **2012**, *22*, 23506.
- 13 a) H. Yang, C. Shan, F. Li, D. Han, Q. Zhang and L. Niu, *Chem. Commun.* **2009**, 3880. b) S. Park, Y. Hu, Y. O. Hwang, S. E. Lee, L. B. Casabianca, W. Cai, J. R. Potts, H. W. Ha, S. Chen, J. Oh, S. O. Kim, Y. H. Kim, Y. Ishii, R. S. Ruoff, *Nature Commun.* **2012**, *3*, 638.
- 14 a) T.-P. Fellingner, F. Hasché, P. Strasser, M. Antonietti, *J. Am. Chem. Soc.* **2012**, *134*, 4072. b) K. Ai, Y. Liu, C. Ruan, L. Lu, G. Lu, *Adv. Mater.* **2013**, *25*, 998.
- 15 C. A. Leon y Leon, J. M. Solar, V. Calemma, L. R. Radovic, *Carbon* **1992**, *30*, 797.
- 16 T. Ikeda, M. Boero, S.-F. Huang, K. Terakura, M. Oshima, J.-I. Ozaki, *J. Phys. Chem. C* **2008**, *112*, 14706.
- 17 L. Zhang, J. Niu, L. Dai, Z. Xia, *Langmuir* **2012**, *28*, 7542.
- 18 M. Kaukonen, R. Kujala, E. Kauppinen, *J. Phys. Chem. C* **2012**, *116*, 632.
- 19 a) P. Wang, Z. Wang, L. Jia, Z. Xiao, *Phys. Chem. Chem. Phys.* **2009**, *11*, 2730. b) Z. Luo, S. Lim, Z. Tian, J. Shang, L. Lai, B. MacDonald, C. Fu, Z. Shen, T. Yu, J. Lin, *J. Mater. Chem.* **2011**, *21*, 8038.
- 20 a) T. Sharifi, F. Nitze, H. R. Berzaghui, C. W. Tai, M. Mazurkiewicz, A. Malopeszy, L. Stobinski, T. Wågberg, *Carbon* **2012**, *50*, 3535. b) S. Maldonado, S. Morin, K. J. Stevenson, *Carbon* **2006**, *44*, 1429. c) M. Glerup, M. Castignolles, M. Holzinger, G. Hug, A. Loiseau, P. Bernier, *Chem. Commun.* **2003**, 2542. d) M. Terrones, P. M. Ajayan, F. Banhart, X. Blase, D. L. Carroll, J. C. Charlier, R. Czerw, B. Foley, N. Grobert, R. Kamalakaran, P. Kohler-Redlich, M. Rühle, T. Seeger, H. Terrones, *Appl. Phys. A: Mater. Sci. Process* **2002**, *74*, 355.
- 21 a) K. Chizari, A. Vena, L. Laurentius, U. Sundararaj, *Carbon* **2014**, *68*, 369. b) S. van Dommele, A. Romero-Izquierdo, R. Brydson, K. P. de Jong, J. H. Bitter, *Carbon* **2008**, *46*, 138.
- 22 L. Lai, J. R. Potts, D. Zhan, L. Wang, C. K. Poh, C. Tang, H. Gong, Z. Shen, J. Linc, R. S. Ruoff, *Energy Environ. Sci.* **2012**, *5*, 7936.
- 23 a) T. Sharifi, G. Hu, X. Jia, T. Wågberg, *ACS Nano* **2012**, *10*, 8904. b) P. H. Matter, L. Zhang, U. S. Ozkan, *J. Catal.* **2006**, *239*, 83.
- 24 For a selection of recent papers dealing with N-doped carbon nanomaterials where pyridinic N atoms are assumed to be the most catalytically active sites in ORR see: a) S. Kundu, T. Chikka Nagaiah, W. Xia, Y. Wang, S. van Dommele, J. Hendrik Bitter, M. Santa, G. Grundmeier, M. Bron,

-
- W. Schuhmann, M. Muhler, *J. Phys. Chem. C* **2009**, *113*, 14302. b) C. V. Rao, C. R. Cabrera, Y. Ishikawa, *J. Phys. Chem. Lett.* **2010**, *1*, 2622. c) N. P. Subramanian, X. Li, V. Nallathambi, S. P. Kumaraguru, H. Colon-Mercado, G. Wu, J.-W. Lee, B. N. Popov, *J. Power Sources* **2009**, *188*, 44. d) K. Y. Park, J. H. Jang, J. E. Hong, Y. U. Kwon, *J. Phys. Chem. C* **2012**, *116*, 16848. e) H. B. Li, W. J. Kang, L. Wang, Q. L. Yue, S. L. Xu, H. S. Wang, J. F. Liu, *Carbon* **2013**, *54*, 249. f) C. Jeyabharathi, P. Venkateshkumar, M. S. Rao, J. Mathiyarasu, K. L. N. Phani, *Electrochim. Acta* **2012**, *74*, 171.
- 25 For a selection of recent papers dealing with N-doped carbon nanomaterials where graphitic N atoms are considered the most catalytically active sites in ORR see: a) H. Niwa, K. Horiba, Y. Harada, M. Oshima, T. Ikeda, K. Terakura, J.-I. Ozaki, S. Miyata, *J. Power Sources* **2009**, *187*, 93. b) B. Zheng, J. Wang, F. B. Wang, X. H. Xia, *Electrochem. Commun.* **2013**, *28*, 24. c) M. Chokai, M. Taniguchi, S. Moriya, K. Matsubayashi, T. Shinoda, Y. Nabae, S. Kuroki, T. Hayakawa, M. Kakimoto, J. Ozaki, S. Miyata, *J. Power Sources* **2010**, *195*, 5947.
- 26 For selected papers where both graphitic and pyridinic N atoms are suggested to be active in ORR see: refs. 22 and 23a.
- 27 For examples of N-CNMs active in ORR where the catalyst efficiency does not seem to be affected by the overall N-content see: E. J. Biddinger, U. S. Ozkan, *J. Phys. Chem. C* **2010**, *114*, 15306 and ref. 22.
- 28 For examples of N-CNMs active in ORR where the catalyst efficiency is affected by the overall N-content see: a) D. Deng, X. Pan, L. Yu, Y. Cui, Y. Jiang, J. Qi, W.-X. Li, Q. Fu, X. Ma, Q. Xue, G. Sun, X. Bao, *Chem. Mater.* **2011**, *23*, 1188. b) Y. Zhang, J. Ge, L. Wang, D. Wang, F. Ding, X. Tao, W. Chen, *Scientific Reports* **2013**, *3*, 2771.
- 29 R. A. Sidik, A. B. Anderson, N. P. Subramanian, S. P. Kumaraguru, B. N. Popov, *J. Phys. Chem. B* **2006**, *110*, 1787.
- 30 G. Tuci, C. Zafferoni, P. D'Ambrosio, S. Caporali, M. Ceppatelli, A. Rossin, T. Tsoufis, M. Innocenti, G. Giambastiani, *ACS Catal.* **2013**, *3*, 2108.
- 31 a) J. L. Bahr, J. M. Tour, *Chem. Mater.* **2001**, *13*, 3823. b) C. A. Dyke, J. M. Tour, *J. Am. Chem. Soc.* **2003**, *125*, 1156. c) C. A. Dyke, J. M. Tour, *Nano Lett.* **2003**, *3*, 1215. d) J. L. Hudson, M. J. Casavant, J. M. Tour, *J. Am. Chem. Soc.* **2004**, *126*, 11158. e) C. A. Dyke, M. P. Stewart, F. Maya, J. M. Tour, *Synlett* **2004**, *1*, 155. f) B. K. Price, J. L. Hudson, J. M. Tour, *J. Am. Chem. Soc.* **2005**, *127*, 14867. g) B. K. Price, J. M. Tour, *J. Am. Chem. Soc.* **2006**, *128*, 12899. h) C. D. Doyle, J. M. Tour, *Carbon* **2009**, *47*, 3215.
- 32 M. E. Lipińska, S. L. H. Rebelo, M. F. R. Pereira, J. A. N. F. Gomes, C. Freire, J. L. Figueiredo, *Carbon* **2012**, *50*, 3280.
- 33 K. Chizari, I. Janowska, M. Houllé, I. Florea, O. Ersen, T. Romero, P. Bernhardt, M. J. Ledoux, C. Pham-Huu, *Appl. Catal. A-Gen.* **2010**, *380*, 72.
- 34 M. K. Daletoua, F. Paloukisa, A. Stefopoulosa, *ECS Trans.* **2009**, *25*, 1915.
- 35 C. H. de Villeneuve, J. Pinson, M. C. Bernard, P. Allongue, *J. Phys. Chem. B* **1997**, *101*, 2415.

-
- 36 C. Song, J. Zhang, in: PEM Fuel Cell Electrocatalysts and Catalyst Layers: Fundamentals and Applications. J. Zhang (Ed.), **2008**, Springer ISBN 978-1-84800-936-3 - Chapter 2, Electrocatalytic Oxygen Reduction Reaction.
- 37 A. J. Bard, L. R. Faulkner, in: Electrochemical Methods: Fundamentals and Applications, 2nd Edition, John Wiley & Sons, Inc.: New York, **2001**, pp. 856.
- 38 R. Bader, in: Atoms in Molecules: A Quantum Theory. Oxford University Press. **1994**, ISBN 978-0-19-855865-1.
- 39 Calculations have been performed on the isolated heterocycles (N_1-N_6) as simplified models, focusing on N-charge and C_α charge values; none of the largely unpredictable electronic contributions of the CNM has been taken into account.
- 40 Z. Shi, J. Zhang, Z. Liu, H. Wang and D. Wilkinson, *Electrochim. Acta*, **2006**, *51*, 1905.
- 41 D. D. Perrin, W. L. F. Armarego, D. R. Perrin, in: *Purification of Laboratory Chemicals*, Vol. 1, 2nd ed., Pergamon, **1980**.
- 42 A. C. Ferrari, J. Robertson, *Phys. Rev. B* **2000**, *61*, 14095.
- 43 A. C. Ferrari, J. Robertson, *Phys. Rev. B* **2001**, *64*, 075414.
- 44 M. M. Lucchese, F. Stavale, E. H. Martins Ferreira, C. Vilani, M. V. O. Moutinho, R. B. Capaz, C. A. Achete, A. Jorio, *Carbon* **2010**, *48*, 1592.
- 45 S. Treimer, A. Tang, D. C. Johnson, *Electroanal.* **2002**, *14*, 165.
- 46 For titration procedures see: B. Ballesteros, G. de la Torre, C. Ehli, G. M. Aminur Rahman, F. Agulló-Rueda, D. M. Guldi, T. Torres, *J. Am. Chem. Soc.* **2007**, *129*, 5061 and ref. 34b.
- 47 E. Moaseri, M. Baniadam, M. Maghrebi, M. Karimi, *Chem. Phys. Lett.* **2013**, *555*, 164.
- 48 M. J. Frisch, G. W. Trucks, H. B. Schlegel, G. E. Scuseria, M. A. Robb, J. R. Cheeseman, G. Scalmani, V. Barone, B. Mennucci, G. A. Petersson, H. Nakatsuji, M. Caricato, X. Li, H. P. Hratchian, A. F. Izmaylov, J. Bloino, G. Zheng, J. L. Sonnenberg, M. Hada, M. Ehara, K. Toyota, R. Fukuda, J. Hasegawa, M. Ishida, T. Nakajima, Y. Honda, O. Kitao, H. Nakai, T. Vreven, J. A. Jr. Montgomery, J. E. Peralta, F. Ogliaro, M. Bearpark, J. J. Heyd, E. Brothers, K. N. Kudin, V. N. Staroverov, R. Kobayashi, J. Normand, K. Raghavachari, A. Rendell, J. C. Burant, S. S. Iyengar, J. Tomasi, M. Cossi, N. Rega, J. M. Millam, M. Klene, J. E. Knox, J. B. Cross, V. Bakken, C. Adamo, J. Jaramillo, R. Gomperts, R. E. Stratmann, O. Yazyev, A. J. Austin, R. Cammi, C. Pomelli, J. W. Ochterski, R. L. Martin, K. Morokuma, V. G. Zakrzewski, G. A. Voth, P. Salvador, J. J. Dannenberg, S. Dapprich, A. D. Daniels, Ö. Farkas, J. B. Foresman, J. V. Ortiz, J. Cioslowski, D. J. Fox, *Gaussian09*, Revision A.02, Gaussian Inc., Wallingford CT, **2009**.
- 49 A. D. Becke, *J. Chem. Phys.* **1993**, *98*, 5648.
- 50 S. Grimme, J. Antony, S. Ehrlich, H. Krieg, *J. Chem. Phys.* **2010**, *132*, 154104.
- 51 W. Tang, E. Sanville, G. Henkelman, *J. Phys.: Condens. Matter* **2009**, *21*, 084204.

List of abbreviations

BET	Brunauer-Emmett-Teller
btb	4,4',4''-benzene-1,3,5-triyl-tribenzoate
CNMs	Carbon nanomaterials
CNTs	Carbon nanotubes
CuAAC	Cu-mediated acetylene-azide coupling
CV	Cyclic Voltammetry
CVD	Chemical Vapour Deposition
DBU	1,8-diazobicyclo[5,4,0]-undecene
DCC	N-N'- dicyclohexylcarbodiimide
DFT	Density Functional Theory
DMAP	4-dimethylaminopyridine
DMF	Dimethylformamide
DMSO	Dimethylsulfoxide
DTT	Dithiothreitol
EDC	1-ethyl-3-(3-dimethylaminopropyl)carbodiimide
EDG	Electron donating group
EWG	Electron withdrawing group
FC	Fuel Cell
FT-IR	Fourier Transform Infrared Spectroscopy
GC	Glassy Carbon
HOBt	1-hydroxy-benzotriazole
K-L	Koutecky-Levich
LSVs	Linear-sweep voltammograms
<i>m</i>-CPBA	<i>meta</i> -chloroperbenzoic acid
MIP	Maximum intensity projection
MOFs	Metal Organic Frameworks
MWCNTs	Multi-walled carbon nanotubes
N₃tpa	2-azidoterephthalate
N-CNMs	Nitrogen-doped carbon nanomaterials
N-CNTs	Nitrogen-doped carbon nanotubes
NHS	N-hydroxy succinimide

NMR	Nuclear Magnetic Resonance
NPs	Nanoparticles
N-Qs	Quaternary nitrogen sites
<i>o</i>DCB	ortho-Dichlorobenzene
ORR	Oxygen Reduction Reaction
PBS	Phosphate buffer saline
pcu	Primitive cubic
PGMs	Platinum group metals
PSM	Post-synthetic modification
PTFE	Polytetrafluoroethylene
PXRD	Powder X-ray diffraction
RRDE	Rotating ring disk electrode
SA	Surface area
SSA	Specific Surface Area
SWCNTs	Single-walled carbon nanotubes
TDT	2,2'-thiodiethanethiol
TEM	Transmission Electron Microscopy
TFA	Trifluoroacetic acid
TGA	Thermogravimetric analysis
THF	Tetrahydrofuran
TMS	Tetramethylsilane
TMS-N₃	Azidotrimethylsilane
tpa	Terephthalate
UV-vis	Ultraviolet- visible
VA-MWCNTs	Vertically aligned multi-walled carbon nanotubes
VP-PSM	Vapor-phase post-synthetic modification
XPS	X-ray photoelectron spectroscopy

Acknowledgements

Innanzitutto il mio ringraziamento va a Giuliano che mi ha accolto nel suo gruppo e mi ha dato la possibilità di svolgere questo dottorato. In questi anni mi ha insegnato tantissimo e grazie al suo aiuto questo percorso è stato impegnativo ma anche pieno di soddisfazioni. Grazie mille di tutto.

Un grazie va al mio collega Lapo, che in questi anni è diventato un caro amico più che un semplice collega. Le giornate in laboratorio non sono mai monotone con lui e lo ringrazio oltre che per le risate anche per il prezioso aiuto e sostegno che mi ha dato fin dal primo giorno in cui sono arrivata.

Un grazie va anche ad Andrea sia per la sua preziosa collaborazione che per la sua simpatia e allegria contagiosa.

Un ringraziamento va anche a Claudio per il suo preziosissimo aiuto. Grazie per la pazienza e per la disponibilità ma anche per le risate e i bei momenti passati tra una misura e l'altra.

Un grazie va anche a tutti i ragazzi dell'ICCOM con i quali si è instaurato un bellissimo rapporto e con i quali le giornate passano in allegria.

Un ringraziamento va naturalmente alla mia famiglia che mi ha sempre sostenuto con fiducia e affetto in questo lungo percorso di studio fino al dottorato. Grazie per il vostro aiuto e supporto.

Un grazie va infine al mio fidanzato per il suo sostegno incondizionato e per i sacrifici che ha condiviso con me. Grazie mille per aver sempre creduto in me e per avermi supportato nei momenti difficili.

Grazie di cuore a tutti!